A CARBON NANOTUBE BEARING AND STODOLA ROTOR

by

Eugene Hightower Cook

B.S. Aerospace Engineering, 2006
University of Maryland, College Park, Maryland

Submitted to the Department of Aeronautics and Astronautics
in partial fulfillment of the requirements for the degree of

Master of Science in Aeronautics and Astronautics
at the

MASSACHVSETTS INSTITVTE OF TECHNOLOGY

September 2008

Author

Department of Aeronautics and Astronautics
20 August 2008

Certified by

Dr. David J. Carter
Principal Member of the Technical Staff
The Charles Stark Draper Laboratory, Inc.
Thesis Supervisor

Certified by

Prof. Zoltán S. Spakovszky
H.N. Slater Associate Professor of Aeronautics and Astronautics
Thesis Advisor

Accepted by

Prof. David L. Darmofal
Associate Department Head
Chairman, Committee on Graduate Students

[This page intentionally left blank.]

A CARBON NANOTUBE BEARING AND STODOLA ROTOR

by

Eugene H. Cook

Submitted to the Department of Aeronautics and Astronautics on 20 August 2008 in partial fulfillment of the requirements for the degree of Master of Science in Aeronautics and Astronautics

ABSTRACT

A nano-scale rotor supported on a cantilevered multi-wall carbon nanotube (MWNT) shaft (Stodola configuration) is proposed. The nanotube is also expected to function as the bearing, since individual walls of a MWNT are not strongly bonded and can slide on each other with low friction. While MWNT based rotors have been previously constructed, they have so far been limited to horizontally oriented nanotubes. The rotor uses a vertically aligned tube, which allows superior control of the rotor geometry, enabling improved rotor balancing and axisymmetric features such as electrodes or blades.

The rotor is proposed as a test stand for measuring inter-wall friction in MWNTs. The low friction in nanotubes has been studied with simulations and experiments, and while it is agreed that relative motion between walls is possible, there is much debate about the qualitative nature of the friction force between walls. Furthermore the reported quantitative values of friction vary by as much as ten orders of magnitude. The proposed rotor might be used to gather new friction data on rotating MWNT bearings at higher speeds that previously attempted. In addition, identical rotors fabricated on nanotubes of varying size, type, and crystalline quality might provide a large dataset that could be used to find correlations between friction behavior and these factors. Applications for the rotor beyond a friction testing apparatus could include pumps to work with existing micro-chemical sensors, gyroscopes, energy storage flywheels, and turbomachinery for power generation.

A fabrication process for the proposed rotor was developed, and is being refined. An isolated vertically aligned MWNT is grown by chemical vapor deposition (CVD), from a nickel catalyst dot defined with electron-beam lithography. A silicon dioxide sacrificial layer is applied, followed by a polysilicon layer from which to cut out the rotor. The rotor etch is performed by cryogenic reactive ion etching (RIE), patterned with electron-beam lithography. The rotor is released from the substrate by hydrofluoric acid vapor. One iteration of the fabrication process was completed, and further iterations are planned to complete a functional device. Actuation of the rotor would be achieved by directing jets of air at blades on the rotor, and an alternative electrostatic actuation concept is also proposed. A dynamic model of the rotor performance based on classical simple beam theory and rigid body dynamics indicates that speeds on the order of thousands to millions of revolutions per minute should be achievable, while avoiding the thirteen potential failure mechanisms analyzed.

Technical Supervisor: Dr. David J. Carter	Thesis Advisor: Prof. Zoltán S. Spakovszky
Principal Member of the Technical Staff	H.N. Slater Associate Professor of Aeronautics and Astronautics
The Charles Stark Draper Laboratory, Inc.	Massachusetts Institute of Technology

An electronic PDF version of this thesis, with color figures and hyperlinks, is available at http://dspace.mit.edu.

[This page intentionally left blank.]

ACKNOWLEDGMENTS

First I am greatly indebted to Dr. David J. Carter, my mentor at Draper Laboratory. This project was Dave's original brainchild, and his enthusiasm, knowledge, and dedication are the prime movers that continue to drive this research. Many thanks also go to Prof. Zoltán Spakovszky, whose contagious excitement and extremely valuable perspective have contributed immensely to this work and to my journey through MIT. I am also very thankful to Dr. Marc Weinberg, of Draper Laboratory, who provided so much wisdom and counsel on both things technical and the Ways of the Lab.

I would like to especially thank those people at Draper who contributed to this project with their own efforts, and without whom I could not have accomplished much. Parshant Kumar, Pete Miraglia, and Bill Teynor have my gratitude for taking their own time to contribute directly to the project. I am also indebted to everyone in the fab who has given me invaluable advice, including Mark April, Janis Aten, Jon Bernstein, Connie Cardoso, Dick Caruso, Amy Duwel, Biga Ganesh, Manuela Healey, Maria Holmboe, James Hsiao, Tom Langdo, John Le Blanc, Mark Mescher, Tony Monteiro, Tenzin Nyinjee, Mert Prince, Dan Pulver, Livia Racz, Henry Raczkowski, and Ricky Soong.

From the education office at Draper, I am very grateful to Linda Fuhrman and Gail DiDonato, as well as George Schmidt. These folks have been so very helpful to me in finding my footing and making sure I am taken care of. Thanks also to Mitch Hansberry, Ralph Pupa, and John Mahoney who helped with designing, machining, and rapid prototyping of various parts.

I would like to thank Dr. Yong Zhang and Dr. Anthony Garratt-Reed for much assistance with the microscopes at the MIT Electron Microscopy Shared Experimental Facility. I would also like to thank the people at Boston College who provided all the nanotube growth for this work. Thanks to Prof. Zhifeng Ren for bringing his nanotube growth expertise to bear, and thanks to Trilochan Paudel for doing so much nanotube growth. Thanks also to Dr. Dezhi Wang and Dr. Yucheng Lan for training and assistance with the Boston College TEM facility.

At the gas turbine laboratory at MIT, I am thankful to have met several delightful people. Thanks to Bernard Yen for graciously allowing the use of pictures of his permanent magnet turbine generator in this thesis. Thanks to Prof. Ed Greitzer, Dr. Choon Tan, and Holly Anderson for welcoming a Draper Fellow to the fold.

Personally I want to thank my good friends in the area. Thanks to my fellow Fellow Ryan Odegard for his outstanding ability to find interesting things to do, and for his "well aligned" sense of humor. I also want to thank Yong-yi Zhu. I have known him for a long time, and I consider any time with him well spent. Thanks as well to my officemates here at Draper: Jon Varsanik, Eli Weinberg, and Jonathon Cox, cool guys all.

I owe my parents more than I can measure, as it is their hard work that has brought me to the position where I can achieve this dream. Thank you for carrying me here. I want to thank my brother Gordon, whom I am very proud to count among my kin, and who is so much fun to be around. Finally I want to thank my incredible fiancée, Kyra. It is her love and support that I would turn to when my own steam seemed to be running low, and I believe there is as much of her sweat in here as my own. She is the best companion I could have asked for.

This thesis was prepared at The Charles Stark Draper Laboratory, Inc., under Internal Research and Development projects 21160-001: Carbon Nanotube Device Development, 21812-001: Carbon Nanotube Applications, and 23027-001: Carbon Nanotubes.

Eugene H. Cook
20 August 2008

CONTENTS

LIST OF FIGURES

LIST OF TABLES

NOMENCLATURE

Symbol	Description
A, B, C, D, E, F, G, H	Constants of integration
$A_1,\ A_2,\ A_3,\ A_4$	Components of forced response cosine term
A_{jk}	Rotation matrix from frame k to frame j (i.e. A_{32} rotates from frame 2 to 3)
A_{cap}	Overlapping area of two electrodes (a capacitor)
A_{cs}	Cross sectional area of a nanotube
$\mathcal{A}$	Control surface
$[A]$	Vector of forced response cosine term
$\vec{a}$	Misalignment of rotor center of mass from beam tip
a_x	x-misalignment of rotor center of mass in rotor-fixed frame
a_y	y-misalignment of rotor center of mass in rotor-fixed frame
a_z	z-misalignment of rotor center of mass in rotor-fixed frame
$B_1,\ B_2,\ B_3,\ B_4$	Components of forced response sine term
$[B]$	Vector of forced response sine term
C	Capacitance
C_{vdW}	Coefficient of van der Waals force
$[C_4]$	4x4 damping matrix for all 4 equations of motion
$[C_{X2}]$	Damping matrix for equations of motion in x-direction
$[C_{Y2}]$	Damping matrix for equations of motion in y-direction
$[CS]$	Vector of forcing function cosine term
c	Speed of light
$c_1,\ c_2$	Components of eigenvector
$c\phi,\ c\beta_X,\ c\beta_Y,\ c\alpha_x$	Cosine of ϕ, Cosine of β_X, Cosine of β_Y, cosine of α_x
D	Rotor disk diameter
d_c	Diameter of the interface between inner and outer nanotubes
d_{jet}	Diameter of glass pipette orifice and resulting jet
E	Young's modulus of carbon nanotube (including regular interwall spacing)
E_w	Young's modulus of single wall nanotube (based on graphene thickness)
e	Eccentricity of compressive load on column
F_{cent}	Centripetal force exerted by beam to keep rotor center of mass on circular path
F_{laser}	Force exerted by laser due to radiation pressure
F_{vdW}	Restoring spring force exerted by the van der Waals attraction between nanotube walls
F_x	Force in x-direction
$F_{x,\text{ applied}}$	Force applied to beam tip in x-direction
$F_{y,\text{ applied}}$	Force applied to beam tip in y-direction
g	Gap (clearance) between rotor and stator electrodes
h	Thickness of a single graphene layer; rotor-substrate clearance
$I_{xx},\ I_{yy},\ I$	Second moment of area for nanotube beam shaft cross section
$\tilde{J}$	Inertia tensor of rotor disk in frame 5
$\tilde{J}_{\text{principal}}$	Inertia tensor of rotor disk in principal axes
$J,\ J_{xx},\ J_{yy}$	Rotor disk diametral moments of inertia (about x- or y-axes)
$J_{xy},\ J_{xz},\ J_{yz}$	Rotor disk products of inertia

Symbol	**Description**
J_{zz}	Rotor disk axial moment of inertia (about nominal spin (z) axis)
KE	Kinetic energy
KE_{linear}	Kinetic energy of translation of rotor disk
$KE_{\text{linear, x}}$ $KE_{\text{linear, y}}$	Kinetic energy of x, y-translation of rotor disk
KE_{angular}	Kinetic energy of rotation
$KE_{\text{ang}, xx}$, $KE_{\text{ang}, yy}$	Kinetic energy of rotation components
$KE_{\text{ang}, zz}$, $KE_{\text{ang}, xy}$	Kinetic energy of rotation components
$KE_{\text{ang}, xz}$, $KE_{\text{ang}, yz}$	Kinetic energy of rotation components
$[K_4]$	4x4 stiffness matrix for all 4 equations of motion
$[K_{X2}]$	Stiffness matrix for equations of motion in x-direction
$[K_{Y2}]$	Stiffness matrix for equations of motion in x-direction
L	Cantilevered nanotube shaft length
$\mathcal{L}$	Lagrangian of the rotor and shaft system
l	Length of overlap between telescoping tubes
M_x	Beam internal moment about x-axis
$M_{x,\text{ applied}}$	Moment applied to beam tip about x-axis
M_y	Beam internal moment about y-axis
$M_{y,\text{ applied}}$	Moment applied to beam tip about y-axis
$[M_4]$	4x4 mass matrix for all 4 equations of motion
$[M_{X2}]$	2x2 Mass matrix for equations of motion in x-direction
$[M_{Y2}]$	2x2 Mass matrix for equations of motion in y-direction
m	Mass of the rotor disk
$\dot{m}$	Mass flow rate
n	Any whole number
$\hat{n}$	Unit normal to control surface
P	Compressive load applied to column
PE	Potential energy
PE_{cap}	Potential energy stored in a capacitor
PE_{elastic}	Potential energy stored in bent beam
$PE_{\text{elastic, x}}$	Potential energy stored in beam from bending in x-direction
$PE_{\text{elastic, y}}$	Potential energy stored in beam from bending in y-direction
PE_{vdW}	Potential energy of the van der Waals interaction between nanotube walls
$P_{\text{crit, Euler}}$	Critical compressive load to cause Euler buckling
$P_{\text{crit, shell}}$	Critical compressive load to cause shell buckling
P_{laser}	Laser power
p	Momentum; pressure
R	Reflectivity; radius of the rotor disk
$\vec{R}$	Position vector of nanotube beam tip in inertial frame
$\vec{\vec{R}}_C$	Position vector of rotor disk center of mass
R_{CX}	Instantaneous x-displacement of rotor center of mass
R_{CY}	Instantaneous y-displacement of rotor center of mass
R_{CZ}	Instantaneous y-displacement of rotor center of mass
R_X	Instantaneous x-displacement of nanotube beam tip
R_Y	Instantaneous y-displacement of nanotube beam tip
R_Z	Instantaneous y-displacement of nanotube beam tip

Symbol	**Description**
$[RB]$	State vector containing R_X, R_Y, β_X, and β_Y
r	Radius of a single layer of a multi-wall nanotube; polar coordinate
r_c	Radius of the interface between inner and outer nanotubes
r_{CM}	Radius of the circle travelled by the rotor center of mass
r_o	Outer radius of the nanotube
$[SN]$	Vector of forcing function sine term
$s\phi$, $s\beta_X$, $s\beta_Y$, $s\alpha_x$	Sine of ϕ, sine of β_X, sine of β_Y, sine of α_x
t	Rotor disk thickness; time
t_{coast}	Time taken for rotor to come to rest from initial speed due to friction
u	Transverse beam deflection in x-direction
V	Voltage
V_x	Beam internal shear in x-direction
V_y	Beam internal shear in y-direction
$\mathcal{V}$	Control volume
v	Transverse beam deflection in y-direction
v_{jet}	Velocity of air in jet
v_x	x-velocity (of air)
W	Weight of rotor disk
$\dot{W}$	Rate of mechanical work accomplished by laser
x	One of the coordinates of the nominal rotor plane
$\hat{x}$	Unit vector in x-direction
y	One of the coordinates of the nominal rotor plane
z	Coordinate along beam axis
α	Permanent angular misalignment of rotor
α_x	Permanent angular misalignment of rotor about x-axis
α_y	Permanent angular misalignment of rotor about y-axis
β_{dynamic}	Dynamic tilting angle of rotor due to forced response
β_{worst}	Worst case tilting angle of rotor
β_X	First Euler angle, describing tilting of the rotor around the x-axis
β_Y	Second Euler angle, describing tilting of the rotor around the y-axis
δ_{beam}	Transverse tip deflection of nanotube when subjected to transverse load
δ_{column}	Transverse tip deflection of nanotube when subjected to compressive load
δ_{dynamic}	Transverse tip deflection of nanotube under dynamic forced response
ε	Permittivity
$\tilde{\varepsilon}$	Strain tensor in nanotube
ε_{zz}	Axial strain in nanotube
η_{laser}	Laser “efficiency”
θ	Polar coordinate
θ_x	Angle of beam differential element about x-axis
θ_y	Angle of beam differential element about y-axis
λ	Free response eigenvalues (natural frequencies)
ν	Poisson’s ratio (of nanotube or rotor disk)
ρ	Density (of air or rotor disk)
$\tilde{\sigma}$	Stress tensor in nanotube
σ_{beam}	Axial stress in the nanotube at the root due to transverse load
σ_{cent}	Centrifugal stress in the rotor disk

Symbol	Description
σ_{column}	Axial stress in the nanotube at the root due to compressive load
$\sigma_{\mathrm{dynamic}}$	Axial stress in the nanotube at the root due to dynamic loads
σ_{fric}	Friction force per unit contact area within a nanotube
σ_{zz}	Axial stress in nanotube
τ_{cap}	Torque provided by capacitive electrostatic motor
τ_{fric}	Torque exerted by friction in the bearing
τ_{laser}	Torque provided by laser radiation pressure
$\varPhi_X,\ \varPhi_Y$	Eigenvectors for x- and y-equations of motion (Free response)
ϕ	Third Euler angle, describing rotation of the rotor about its nominal axis
$\varOmega$	Constant angular velocity of rotor disk
$\vec{\omega}$	Angular velocity vector of rotor disk (in rotating frame)
ω_x	Angular velocity of rotor disk about x-axis (in rotating frame)
ω_y	Angular velocity of rotor disk about y-axis (in rotating frame)
ω_z	Angular velocity of rotor disk about z-axis (in rotating frame)

ACRONYMS

Acronym	Meaning
a-Si	Amorphous Silicon
AFM	Atomic Force Microscopy, Microscope, Micrograph
CNT	Carbon Nanotube
C-CVD	Catalytic Chemical Vapor Deposition
CVD	Chemical Vapor Deposition
DC	Direct Current
DRIE	Deep Reactive Ion Etching
DWNT	Double-Wall Nanotube
e-beam	Electron Beam
EDX	Energy Dispersive X-ray Spectroscopy
ICP	Inductively Coupled Plasma
LPCVD	Low-Pressure Chemical Vapor Deposition
MD	Molecular Dynamics
MEMS	Micro-Electro-Mechanical Systems
MWNT	Multi-Wall Nanotube
NEMS	Nano-Electro-Mechanical Systems
p-Si	Polycrystalline Silicon
PECVD	Plasma-Enhanced Chemical Vapor Deposition
PEEK	Polyetheretherketone
PMMA	Polymethylmethacrylate
RF	Radio Frequency
RIE	Reactive Ion Etching
SEM	Scanning Electron Microscopy, Microscope, Micrograph
SWNT	Single-Wall Nanotube
TEM	Transmission Electron Microscopy, Microscope, Micrographj
VACNF	Vertically Aligned Carbon Nanotube Forest

[This page intentionally left blank.]

1 OVERVIEW

This project is about a rotating disk built on a cantilevered carbon nanotube (CNT) axle and bearing. Such a configuration is known as a “Stodola Rotor” [1]. Figure 1-1 illustrates all the major components, where the key component is a multi-wall carbon nanotube (MWNT). The MWNT is attached to a flat base, or substrate, and a disk is built onto the outermost shell of the MWNT. Because the concentric shells of MWNTs are not bonded, the disk and outer shells can rotate freely on the inner shells. No balls, gas flows, or electromagnetic fields are required for the bearing.

While the un-bonded shell structure of MWNT naturally provides “low” inter-layer friction, quantifying the friction has proved difficult. Current literature gives values ranging by ten orders of magnitude, from attonewtons to piconewtons per atom in contact. One of the goals of the project is to move towards resolution of this long-standing discrepancy, by providing a test stand on which to run nanotube friction experiments, and gather friction data for a variety of speeds, nanotube types, and sizes. Another goal is to provide a starting point for nanoscale rotating devices. Once the feasibility of MWNTs as a rotary bearing has been demonstrated, MEMS (Micro-Electro-Mechanical Systems) device

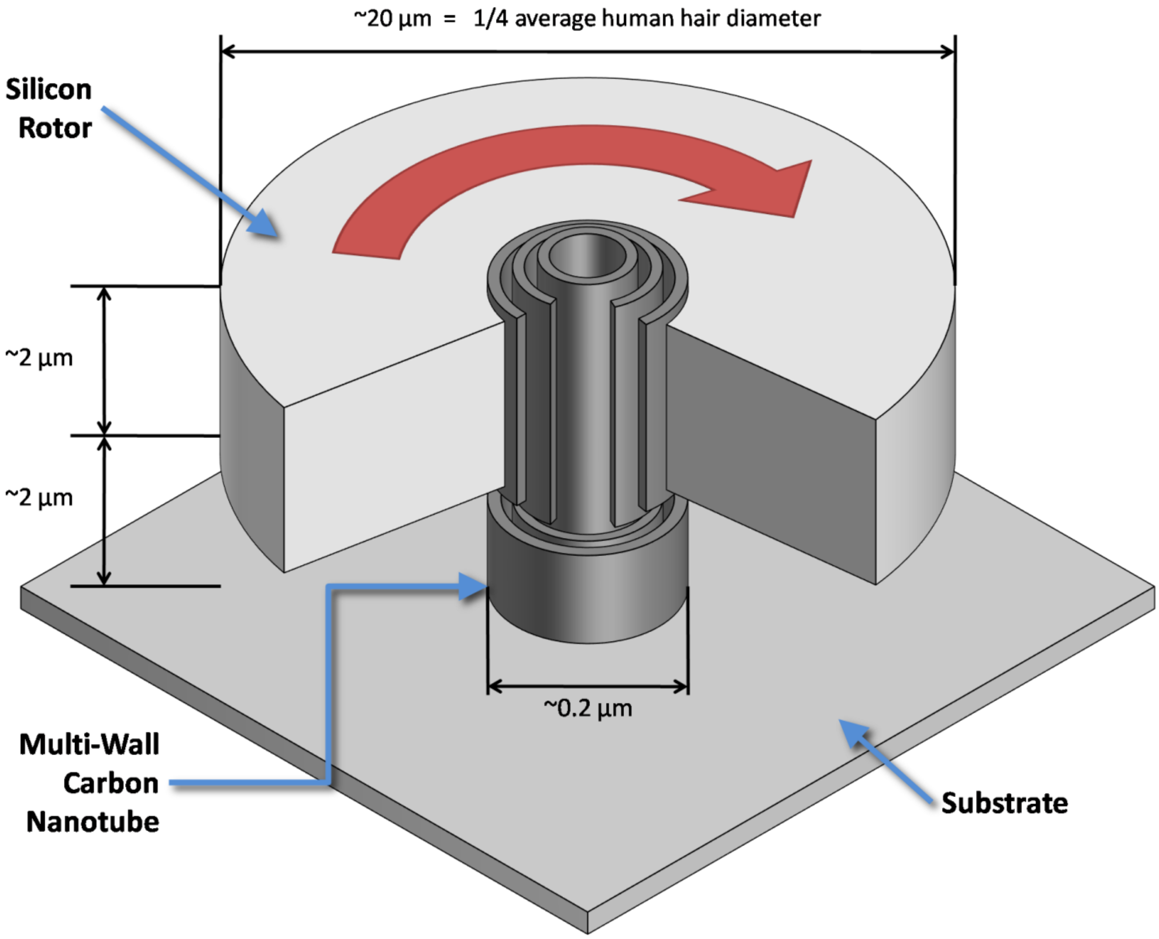

Figure 1-1: A schematic Illustration (not to scale) of the carbon nanotube rotor described here, with wedge-shaped cutaway to show the nanotube structure. A single cantilevered multi-wall carbon nanotube supports the rotor, acting as both the axle and bearing. This configuration is known as the Stodola Rotor [1].

designers can begin to take advantage of the architecture for myriad rotary devices, such as gyroscopes, pumps, flywheels, and turbomachinery. In addition, the friction data gathered could potentially inform the design choices made for these applications.

This is the first time a fabrication process for nanoscale MWNT based rotor in the Stodola configuration has been undertaken. Some researchers [2-4] have made microscopic seesaw-like rotating devices with nanotube axles, with horizontally oriented nanotubes, but this project is unique; here, the MWNT is vertically oriented – its axis is perpendicular to the substrate surface. Because micro-fabrication techniques have only limited ability to make shapes in the dimension perpendicular to the substrate, a horizontal MWNT could only be used for flat, paddle-like designs. This new approach makes entirely new geometries possible. In other words, a symmetric, disk-shaped rotor would be impossible to make without this fundamental change. There are significant challenges to overcome in order to build the device. Achieving vertically orientated MWNT requires nanotube growth by Chemical Vapor Deposition (CVD). This process is still being perfected, and in particular has difficulty producing tubes with few defects in the crystalline structure. This project is the first to use vertically oriented CNTs for a mechanical application, requiring high crystalline quality. In addition, the MEMS fabrication techniques required to build the other parts have not been thoroughly tested on CNTs, and this project pioneers some of those processes. However, if these challenges are overcome, the result would pave the way for all kinds of rotating micromechanical devices.

1.1 Goals of the Project

The overall goal of this work is to design, fabricate, and test a nanoscale axisymmetric mechanical rotor supported by a single cantilevered carbon nanotube. Such a configuration, referred to as a "Stodola Rotor" [1], provides an excellent starting point for observation and characterization of rotary MWNT bearings. Compared with other possible axisymmetric configurations, such as a Jeffcott Rotor [5] (which has both ends of the shaft supported), the Stodola Model is simpler to fabricate. Although the addition of a second support would dramatically increase the shaft stiffness, resulting in higher critical speeds, the dynamic model developed in section 3.3 shows that subcritical operation can be easily achieved, and displacements can be kept within acceptable margins even with the cantilevered shaft. As the simplest possible disk-shaped rotor design, the Stodola Rotor opens the door for CNT-supported micro-mechanical rotors. While it is well within the capability of current MEMS technology to fabricate, it contains all the basic dynamics that would be present in any CNT-supported rotary MEMS system. The idea is for the device built for this project to serve as a proof-of-concept for an entirely new MEMS bearing technology.

In working towards the primary goal, progress can be made on two secondary goals. First, data concerning what effects common microfabrication processes have on CNTs must be collected. CNTs are just beginning to be incorporated into micro-electronic [6-12], micro-mechanical [2-4, 13], and micro-fluidic [14-17] devices. Before using established MEMS fabrication procedures on CNTs, it is important to know what effects these procedures will have. For example, material deposited on top of nanotubes could react with the carbon, forming strong bonds, or it could refuse to bond and not adhere at all. Etching could cause damage to the CNTs; high-energy ions could sputter away the carbon, or harsh chemicals could attack it. Even if material is not removed, rearrangement of the atoms within the CNT could drastically alter its structure, reducing mechanical strength and stiffness, and inhibiting rotation. In order to ensure that the fabrication of the device will work as expected each individual process was tested on CNTs (results are described in Section 4.2.1). The knowledge gathered from these experiments towards this first secondary goal can be useful to future nanotube device fabrication efforts.

Besides the engineering-oriented goals of developing CNT processing capabilities and demonstrating MWNT rotary MEMS devices, there is a significant scientific objective. This new idea could allow friction in the rotating nanotube bearing to be measured experimentally. While it is clear that the shells of a MWNT slide on each other with very low friction, the literature to date disagrees widely about the quantitative value of that friction. Various theoretical [18-27] and experimental [2, 3, 18, 28-30] studies have reported friction ranging across ten orders of magnitude. Besides the quantitative differences, these studies even express substantial qualitative disagreement about the nature of friction in MWNTs, such as whether and to what extent such factors as sliding speed, contact area, commensurability, and the presence of defects affect the friction. Section 2.2 describes these prior works in detail. By achieving the goal of developing a friction test stand, this project aims at establishing the fundamental relations that govern the friction in rotating MWNTs. The data collected could potentially validate or refute theoretical friction models, and guide future nanotube device development with practical performance estimates.

1.2 New Accomplishments

The major difference between the current project and previous MWNT based rotary devices is the shift in geometry; the nanotube is oriented vertically to the substrate. All previous rotary MWNT devices have used a horizontally oriented nanotube. This seemingly simple change has powerful consequences, owing to the processing techniques that are currently available for micro-scale fabrication.

The fundamental mechanism for defining lateral shapes at the micro- and nano-scales is lithography. Photolithography involves exposing a surface coated with light-sensitive chemicals (called photoresist) to light through a mask, so that the surface is illuminated in the pattern on the mask. In the exposed areas, the photoresist reacts differently than the photoresist protected by the mask, and another chemical (called the developer) is used that dissolves only either the exposed or unexposed photoresist. The result is that although arbitrary shapes can be made, they can only be produced in two dimensions, since the features come from a projection of light through the mask. Any features in the dimension perpendicular to the substrate are made by depositing thin layers of different materials, or etching down through layers. Both of these techniques can also take advantage of lithography to generate layers that have patterns, but the thickness of the layer is typically uniform, thus fully three-dimensional shapes are not possible.

Previous rotating nanotube devices have so far placed the nanotube horizontally with respect to the substrate. In that configuration, one of the two dimensions of design freedom afforded by lithography is aligned with the tube axis. Consequently, the third dimension, in which fabrication is limited to uniform layers, is perpendicular to the tube axis. In other words, only flat rotating parts can be made, which rotate out of the plane in which they are flat. Round parts, like disks and rods cannot be made with an axis aligned to the tube axis. In contrast, this new approach aligns the tube axis with the dimension in which geometry is limited. The two “free” dimensions lie in the plane of rotation, enabling much more complex rotor geometries, and in particular axisymmetric geometries. Figure 1-2 shows what kind of rotors can be made with the horizontal tube process versus the vertical tube process.

The axisymmetric rotors that are made possible by this new approach are desirable for several reasons. First, the architecture theoretically enables high-speed rotation, because of its ability to reduce the rotor imbalance. As demonstrated by the dynamic model developed in section 3.3, imbalance in the rotor can quickly cause unacceptable deflections and stresses as the operating speed approaches the critical speed. Translational imbalance is the result of a body whose center of mass does not lie on the axis of rotation. With both dimensions of the imbalance accessible with photolithography (for the

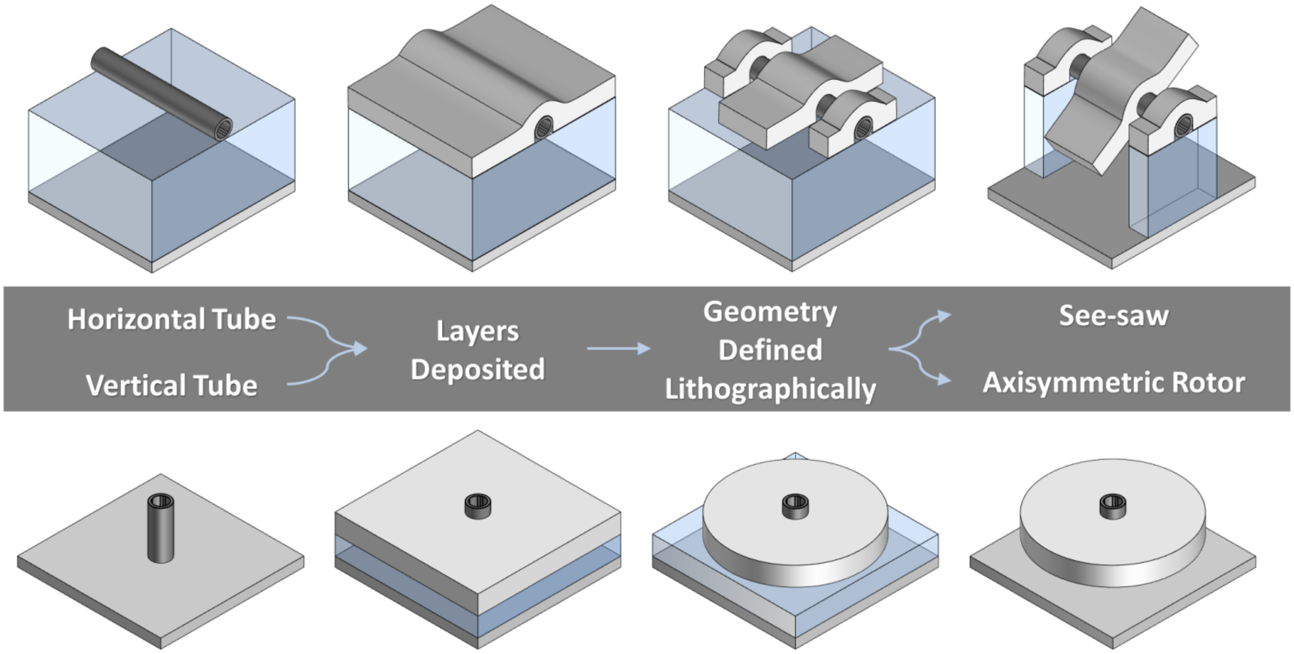

Figure 1-2: A vertically aligned tube allows axisymmetric geometry to be constructed. The grey material represents silicon, or whatever material is used for the device, while the blue material is a sacrificial support material, such as silicon dioxide.

present device), imbalance can be more easily controlled, and higher speeds can be achieved without damage to the device.

Besides allowing higher speed, the capability to construct axisymmetric geometry provides the opportunity for other features on the rotor. For example, the devices under development for the first proof of concept have simple paddle-wheel-type blades for actuation. The design calls for air jets to impinge on the paddles, and the rotation (the actuation is described in detail in section 4.3.1). With a horizontally oriented tube, only two paddles are possible, whereas an axisymmetric design enabled by the new vertical orientation can contain an arbitrary number of evenly spaced blades for extracting work from the surrounding airflow. In fact, the device qualifies as a nanoscale turbine. The MWNT bearing could enable further shrinking of previous microscale turbomachinery efforts, like the MIT micro-turbine [31-34]. For comparison, the entire rotor diameter for the present device is roughly the same as the diameter of the air supply nozzles for the hydrostatic thrust bearing in the previous micro-turbine, as shown in Figure 1-3.

This design freedom afforded by the vertical tube alignment extends far beyond the proof of concept device. Future devices could contain features such as electrodes or magnets for driving, sensing and power generation, gear teeth, and blades for pumping fluids or optical chopping. Furthermore, these features can be of arbitrary shape in the plane of rotation. For example, even airfoil shapes (as opposed to flat blades) for more advanced turbomachinery blading could be added to the rotor, like those used in the MIT micro-turbine.

In addition, the freedom extends off the rotor to the surrounding device, or stator. For example, previous rotary devices (all electrostatically actuated) contained only two or three stator electrodes. Each electrode beyond the first two requires multiple additional layers and lithography steps to make. Furthermore, these electrodes cannot be round with respect to the nanotube axis – they must be flat in a plane parallel to it. That means it is not possible to maintain a consistent distance between the rotor electrodes and stator electrodes for any significant portion of the complete rotation of the rotor, reducing the effectiveness of electrostatic actuation. Not only can the new approach provide arbitrary axisymmetric stator geometry, but also if desired, the stator geometry can be made in the same step and mask as the rotor. Besides electrostatic components, other rotating machinery would also benefit from axisymmetric stators, such as turbomachinery. Still other machines, such as a centrifugal pump, require smooth, curved, but not symmetric stationary components. The freedom afforded by this new approach to make arbitrary shapes in the plane of rotation, on both the rotor and the stator, enables a wide variety of possible devices.

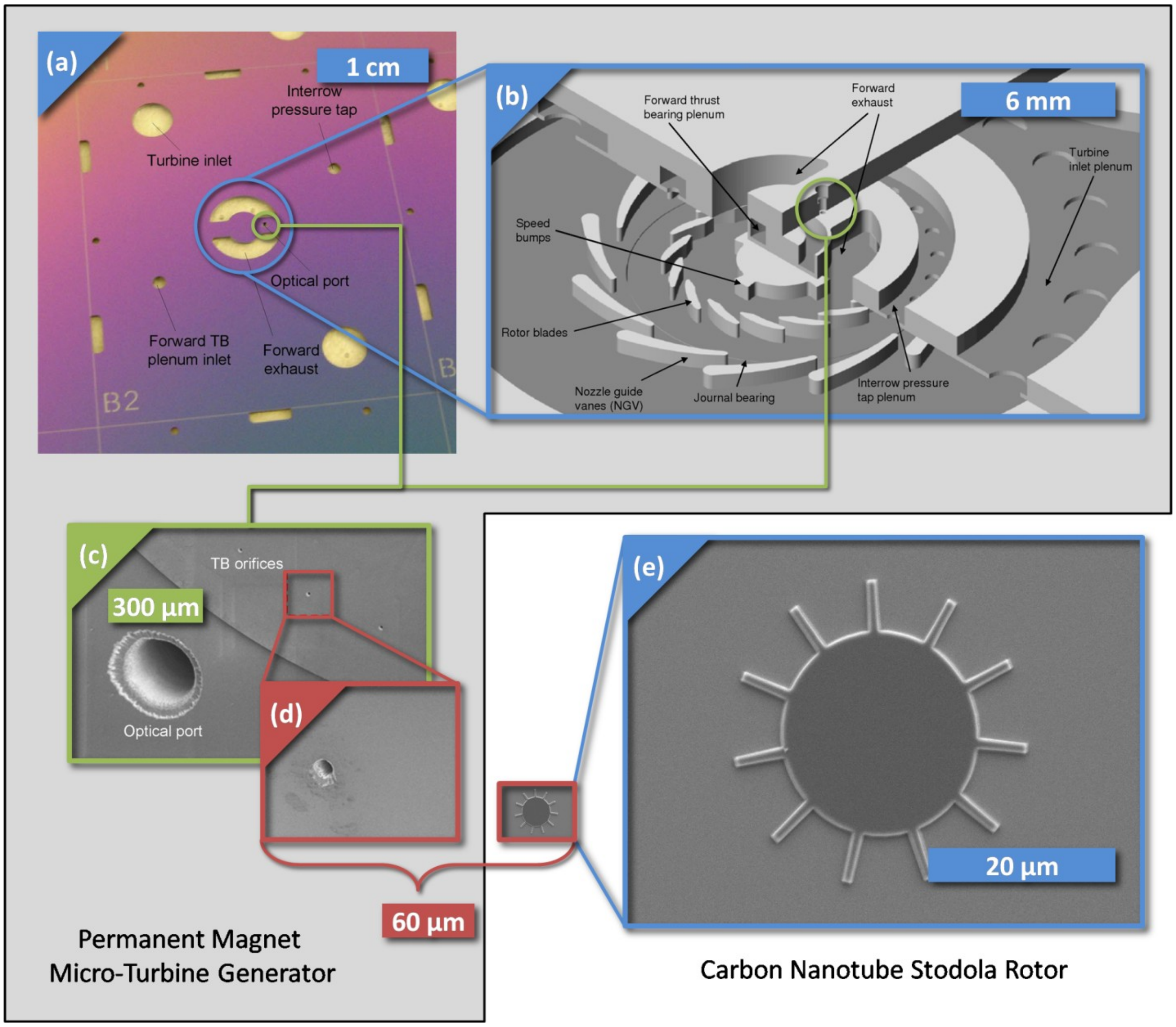

Figure 1-3: Size comparison of the present nano-turbine with a previous micro-turbine generator fabricated by Yen [34]. One layer of the die for that turbine generator is depicted in (a). The micro-turbine rotor (b) has a diameter of 12 mm, compared with the 20 µm diameter of the nano-Stodola rotor (e). The nano-Stodola rotor is closer to the size of the thrust bearing orifices in the micro-turbine (c,d) which are approximately 10 µm in diameter. Images of the micro-turbine in (a,b,c, and d) are provided courtesy of Bernard Yen [34].

An additional side benefit arises from the use of vertically aligned tubes. Previous studies [2, 3] have used MWNTs fabricated by the arc-discharge method. This method [35] is known to produce CNTs with a very high crystalline quality, i.e. free of defects, but the tubes are produced in deposit of mixed carbon materials, including CNTs, fullerenes, graphite, and amorphous carbon. The deposit must be refined and nanotubes of the desired size separated out. The refining process is well developed [35], but the resulting tubes are not attached to anything. In order to get them into MEMS devices, the tubes are typically scattered on a silicon substrate, which gives them their horizontal orientation, and then located in a microscope. The individual device is then designed and fabricated around one carefully hand-selected nanotube. (It should be noted that some work has been done on alignment of arc-discharge tubes in regular patterns [36, 37], but it is unclear how a vertical orientation could be achieved by these methods.)

In order to achieve vertically aligned tubes, this project has elected to use tubes grown by Chemical Vapor Deposition (CVD). In this technique, catalyst material is first deposited on the substrate, which is exposed to hydrocarbon gas at high temperature. The carbon in the gas dissolves into the molten catalyst, and precipitates out in the form of a nanotube. The orientation of the tubes grown this way is generally vertical, and the direction can be further controlled by introducing an electric field. The use of a catalyst material is the source of the side benefit; tubes will only grow where catalyst is present. Since the catalyst can be shaped and deposited by well-known MEMS techniques, tubes can be made in-place where they are needed. No painstaking hand tailoring of each device is required. Instead, devices can be batch fabricated in the manner of integrated circuits. While this benefit is not so critical in a research setting, the production cost savings of batch fabrication is crucial if such devices are ever to go into commercial production.

1.3 Challenges

The challenges that must be overcome for this project are mostly related to the fabrication process. Growing CNTs is a complex task involving finely tuned chemical reactions and precise nano-lithography. During and after growth, it is important to reduce defect formation in the tube, which could hinder or prevent rotation. Besides the tube, the rest of the MEMS fabrication techniques are used in a novel situation, *i.e.* in the presence of a CNT. That means all these techniques must be checked for compatibility with the CNT to ensure fabrication is possible.

While using CVD tubes is necessary to attain the required vertically oriented CNTs, one of the major challenges involved in building this rotating nanotube device is also a by-product of choosing to use CVD nanotubes: Growing the CVD tubes in the first place has proved difficult. In order to get a single tube isolated enough that it can serve as an axle, it is necessary to place a small (50-100 nm) piece of catalyst metal in the precise spot where the axle is intended to be. In order to attain the required catalyst size, e-beam lithography must be used. Instead of a mask, this method scans a beam of electrons across the photoresist, exposing only the areas specified in the program. This process is much more time consuming than photolithography, which can expose an entire wafer at once. In addition, it has been found that special surface treatments are required to get a single clean tube growth from the catalyst. For example, catalyst metal on bare silicon has tended to be scattered prior to growth, either by diffusion or by sputtering in the CVD CNT growth process, and a layer of chromium is necessary to improve the adhesion of the catalyst.

Additionally, CVD tubes tend to have more defects than arc-discharge tubes [35], primarily because of growth temperature. The growth temperatures used in chemical vapor deposition (300-1000°C) are far lower than those used in arc-discharge methods (3000-4000°C). Since atomic diffusion is strongly affected by temperature, the lower temperature reduces the ability of carbon atoms to migrate to ideal low-energy site before bonding, resulting in defects. While there are techniques to reduce the defect density of CVD tubes (discussed in section 2.1.2.4), these techniques are still being developed. Without adequate reduction of defects, by improving the crystalline quality of the nanotube structure, the friction of concentric shells in the MWNT rotating against each other could be high.

Besides the inherent defect-prone nature of the CVD CNTs used for this project, the project breaks new ground in terms of CNT integration with MEMS, and each step in the process to fabricate the device (discussed in section 4.2) must be checked to ensure that it does not cause damage to the tube. The first class of processing steps used to construct the device involves deposition of materials that form the rotor and support it during fabrication. These materials are deposited using Plasma-Enhanced Chemical Vapor Deposition (PECVD), a process in which a high RF bias is applied to feed gasses, ionizing them into a plasma. The bias also accelerates these ions onto the surface, where they adhere and build up the material. However, the high energy of the ions when they impact the surface also causes damage (in the form of defect introduction) and even some sputtering away of the underlying material. It is important to know that the CNTs will be able to withstand such a harsh environment. It is also important to ensure that the deposited material forms a coherent, conformal, even layer, instead of clumping into islands, or growing disproportionately on certain sides of the tube.

Even harsher than the deposition processes are the etching processes which are used to shape the rotor and release it from the support structure. The device must undergo Reactive Ion Etching (RIE), which uses the same plasma technique as PECVD. However, instead of gases that form deposits on the surface, gases that chemically attack the material are used. The nanotube must be able to withstand this environment as well. In addition to RIE, etching in liquid or vapor hydrofluoric acid is used to remove the support structure at the end of the process. The etch must be strong enough to remove all of the silicon dioxide support structure, without also removing nanotube material, or introducing defects in the tube.

The development of the processes used to create the device, as well as the integration of these individual steps is a significant hurdle to overcome in this project. Powerful tools are required to assess the success of the processing techniques used. Scanning Electron Microscopy (SEM) and Transmission Electron Microscopy were used heavily to observe nanotubes between growth, deposition, and etching steps, to assess the crystalline quality and look for signs of damage. These techniques are themselves non-trivial to implement. Altogether, the process of making the MWNT Stodola Rotor requires surmounting each of these distinct challenges.

1.4 Impact of the Project

Completion of the MWNT Stodola rotor would be an early step towards an entirely new rotary MEMS technology, and could have substantial scientific and engineering impact. The device could serve as a friction test stand, enabling collection of the first experimental data on dynamic friction in rotating MWNT bearings. This would be useful in potentially resolving the ongoing debate about the nature and value of MWNT friction. In addition, the device suggests a path towards the realization of numerous practical applications.

1.4.1 A Nanoscale Carbon Nanotube Friction Test Stand

The MWNT Stodola Rotor represents a rare opportunity to address a fundamental question of science: how does the friction between concentric carbon nanotubes behave? The literature does not express a consistent answer. Theoretical *ab initio* predictions are abundant [18-27], but their results vary by as much as ten orders of magnitude. Only one experimental measurement of rotary friction in MWNTs has been attempted [3]. Made with a seesaw-like device, this measurement determined the static friction for a particular nanotube.

With a procedure in place to make MWNT Stodola Rotors, the design can be used as a friction test stand. The concept is to use the device to gather data on MWNT friction, and to compare that data against prior experimental data and theoretical models. With data covering a sufficient portion of the parameter space, the gap between *ab initio* exercises and real world empiricism might be bridged.

Different methods of friction measurement are possible with the test stand, providing some confidence of accuracy. For example, allowing the rotor to coast down and recording speed vs. time data would allow the deceleration at each speed to be computed as the time derivative of the speed. With knowledge of the inertia and other damping influences, extraction of the frictional torque across the entire speed range is therefore possible. Alternatively, driving at a controlled constant speed while keeping track of the input drive power would provide a measure of the power dissipation – the frictional torque could then be determined as the power divided by the speed, if any other dissipative torques are appropriately accounted for.

However, the concept is to try to determine not only what the value of MWNT friction is, but also what the laws that govern its behavior are. To this end, multiple devices are envisioned, built on nanotubes with differing geometries and properties. Each individual device would provide points in the data space, which together might elucidate the important trends and mechanisms that govern friction.

The opportunity to correlate friction data with other factors of influence is the most important potential gain from the MWNT friction test stand. While data on the quantitative value of friction would be useful, the qualitative disagreement in the literature about what controls friction is an even more important question to address – this drives to the very core of the physical principals that govern friction. The test stand should enable the experiment to control as many parameters as possible to determine what factors influence the friction, and how. One parameter of interest is the speed at which the surfaces slide on one another. A single test stand would allow not only a static friction measurement, but also dynamic friction measurements across a range of speeds, potentially as high as a million revolutions per minute. Multiple test stands would enable investigation of the other factors. Contact area and tube size could be controlled from device to device. With different tube growth parameters or techniques, the effects of commensurability between nanotube layers and defect density could be assessed. Careful inspection of the tubes prior to incorporation into the device to evaluate the crystalline quality could be used to correlate friction performance with defect density.

1.4.2 Applications

The test device paves the way for a host of micromechanical devices. Any rotating mechanical device would be a candidate for miniaturization with MWNT bearings, but a few applications in particular stand to benefit significantly.

MEMS chemical and biological sensors have been in development for decades [38-43]. However, these systems typically rely on a pump to push analyte through them, or a vacuum pump to evacuate them. To date, no suitable MEMS vacuum pumps exist (to the author's knowledge), and other MEMS pumps have not proved capable of meeting the requirements of the sensors [40]. Therefore, in order to deploy these systems, bulky macro-scale pumping equipment has been needed. If a suitable MEMS pump could be developed, the entire system could be miniaturized to a convenient, portable size, while at the same time reducing power consumption. The MWNT bearing seems to be well suited to pumping applications, as its high stiffness can lead to high operating speeds. It is also capable of operating in a vacuum. Furthermore, it would not require an external electrical or compressed air supply, like some competing bearing technologies.

An additional application for which the MWNT bearing has promise is a microscale rotating gyroscope. Microscale gyroscopes exist based on the tuning fork design, but a true rotating disk could provide improved performance [44]. The ability of the bearing to provide very low "wobble" (angular displacement) could reduce the dominant cause of errors in dynamically tuned gyroscopes. The high stiffness could enable high-speed operation, leading to improved bandwidth and high sensitivity. In addition, the low friction suggests that the drive power to operate the gyroscope could be very low.

Another potential application is on-chip flywheel energy storage. The energy storage density capacity of a flywheel is limited primarily by the strength of the flywheel material. Any given flywheel can store energy per unit thickness scaling as the fourth power of the radius and the square of angular speed. However, to keep the stress below the material limit, the angular speed must vary inversely proportional to the radius. As a result the energy storage per unit thickness scales with disk area, or in other words the energy storage density (energy per unit mass) is completely independent of the disk size. Scaling flywheels down to the microscale doesn't hurt performance, and in fact could improve it since micro-sized materials can be made with fewer flaws, and hence higher material strength. Energy stored in silicon flywheels has comparable energy density to batteries, but could potentially be discharged much faster – in other words the power density of the flywheels could be high, providing short bursts of power on demand. The MWNT bearing could potentially make such flywheels feasible by enabling high speed rotation, and by providing a low-friction support that reduces unwanted energy dissipation over time.

The prototype device is a simple microturbine, extracting work from the airflow to overcome the friction. Further development of more advanced (and more useful) turbomachinery based on CNT bearings would be another interesting application. Turbomachines have been proposed [45, 46] for providing electrical power at a small scale, as an alternative to batteries. The fact that the power produced scales as the area (which controls the air flow rate) while device weight scales with the volume indicates that microturbomachinery could have a substantial advantage in power density. If successful, the MWNT bearing technology developed here might serve as a unique alternative to the gas bearings so far employed in microscale turbomachinery, by potentially allowing further size reduction and higher speed operation. Additionally, the presence of a physical (and electrically conducting) axle might enable electrical connection to the spinning rotor, which could prove beneficial for electricity-generating turbines.

While these applications are already being considered (see Section 5.2.3), many more applications are possible. The high speed, high stiffness, low friction and small size of the MWNT bearing could prove beneficial for all manner of rotating micro-electro-mechanical systems.

2 BACKGROUND – NANOTUBE PROPERTIES AND PRIOR WORK

Since their discovery [47], carbon nanotubes have been used for a remarkably wide variety of applications, each prompted by one or more of the unique properties of CNTs. The concentric-tube structure of multi-walled carbon nanotubes (MWNTs) makes them naturally suited for rotation. Combined with outstanding mechanical strength, and low friction between rotating tubes, this property makes CNTs an ideal candidate for nanoscale bearings. In other words, it is the properties of CNTs that make this project and all of its applications not just possible, but promising.

2.1 Atomic Structure of Carbon Nanotubes

2.1.1 The Ideal Carbon Nanotube Molecule

A single-wall carbon nanotube is a single molecule composed entirely of carbon in sp^2-hybridized bonds. In order to understand the structure of CNTs it is instructive to compare the structure of nanotubes with some other allotropes of carbon, depicted in Figure 2-1. Graphene is the simplest structure related to the nanotube. Graphene is a two-dimensional structure in which each carbon atom is sp^2-bonded to three other carbon atoms, forming a hexagonal lattice of carbon rings. A CNT is simply a graphene sheet rolled up[1] and joined to itself at the edge to form a tube. Multiple flat sheets of graphene stacked on each other form graphite, the most stable form of carbon at standard temperature and pressure. Likewise, multiple tubes of rolled graphene (SWNTs) can be found nested concentrically in each other, making a MWNT. MWNTs could also be thought of as a rolled piece of graphite, in the same way that a SWNT can be thought of as a single rolled graphene sheet.

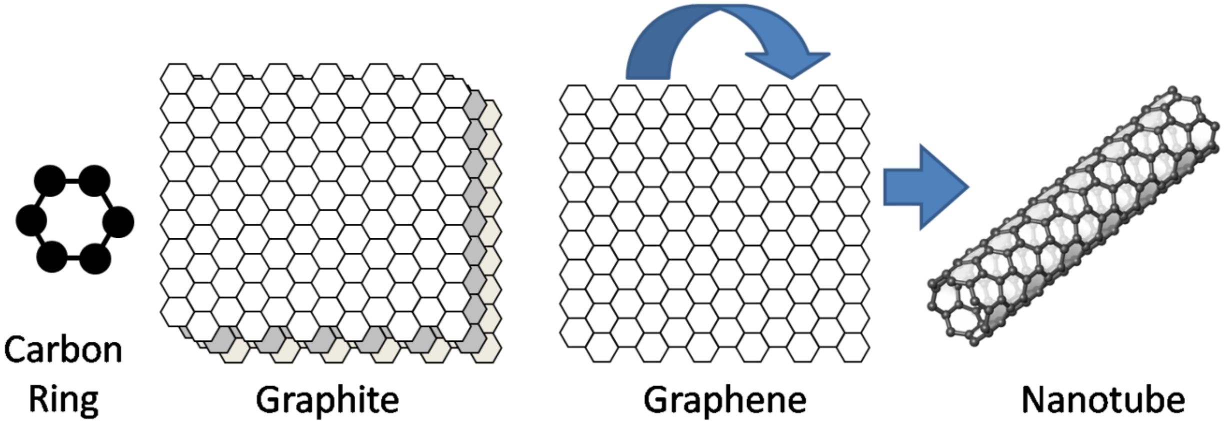

Figure 2-1: Terminology for carbon nanotubes and related structures. Note that nanotubes are not actually formed by rolling up graphene; this is only a helpful visualization tool.

Fullerenes are another carbon allotrope which is similar to CNTs. These structures are like nanotubes, in that they are composed of a single sheet of sp^2-bonded carbon, but the term covers more general shapes. Fullerenes are closed structures, and can be spherical, ellipsoidal, polyhedral, or irregularly shaped. Nanotubes are often observed with closed or capped ends, and can therefore be considered a type of fullerene.

---

[1] It is important to note that CNTs are not actually fabricated by rolling up graphene or graphite. This interpretation is only a useful mechanism for describing the structure.

Each graphene sheet, fullerene, or SWNT is a single molecule, with mostly satisfied bonds. Flat graphene sheets only have dangling bonds at the edges, and since a graphene sheet can extend up to four orders of magnitude farther than it is thick (for high-quality synthetic graphite [48]), the majority of the sheet has no incentive to bond with adjacent sheets. For fullerenes and CNTs, there are no edges or dangling bonds, since the sheet joins to itself forming a seamless tube (In fact, the edge energy saved by the lack of dangling bonds is what allows the tube to overcome the additional strain energy associated with the bending of the sheet.) Therefore graphite and MWNTs (in the absence of defects) experience little or no bonding between adjacent layers and SWNTs, respectively. There is only a van der Waals interaction holding the layers loosely together. This weak interaction is the source of low friction in both graphite and CNTs, and hence the reason that CNTs are an attractive material for MEMS & NEMS bearings.

Graphite and MWNTs share not only the same basic structural component – the physical dimensions that characterize their structures also match. The distance between two adjacent bonded carbon atoms is 0.144 nm for CNTs, and 0.142 nm for graphite. Similarly, the distance between stacked graphite layers and concentric nanotubes both vary around 0.34 nm. However, there are important differences between CNTs and graphite.

CNTs have a property called chirality, which describes the orientation of the hexagonal lattice with respect to the tube axis. It is helpful to consider again the idea of rolling up a graphene sheet. The sheet can be rolled up along many different angles, some of which are shown in Figure 2-2a. Because of the symmetry of the hexagonal lattice, angles between 0° and 30° cover all possible chiralities. Completely arbitrary angles are not possible, because the sheet must be rolled up in such a way that the carbon atoms making up the edges that will join match each other one-to-one. The chirality is conveniently specified by a vector, which describes (in terms of the two unit vectors shown in Figure 2-2b) which two lattice points in the flat sheet will be coincident at a single carbon atom when the tube is rolled up. In other words, the vector becomes a circumference of the nanotube it describes.

In any given MWNT, each layer has its own chirality. However, chirality and circumference are intimately linked – once the chirality is specified, so is the diameter. The reverse is also true: because only certain discrete chiral vectors are possible (those that terminate at an atom in the carbon lattice,) any given diameter corresponds to a certain chiral vector. The individual layers in the MWNT tend to be formed in order to satisfy the spacing requirement between layers, by having the appropriate diameters. As a consequence, the layers do not share the same chiral angle in general. This is in contrast to graphite, which is not subject to diameter restriction. While graphite can exist with adjacent layers rotated at arbitrary angles to each other, called turbostratic graphite [48], ideal defect-free graphite has a preferred stacking configuration, called ABAB stacking. Adjacent graphene layers are aligned at the same angle, and carbon atoms line up in the center of the hexagons of the adjacent layer, forming a fully three-dimensional crystal lattice.

The degree to which adjacent layers are aligned (the general case of graphite) or misaligned (the general case for MWNTs) is referred to as commensurability, and is significant to the study of friction between the layers of these materials. Aligned (commensurate) layers have a lower energy than incommensurate layers, when in contact. Consequently, a larger energy input is required to separate or move the layers past each other. In other words, commensurate layers should have higher friction. The effect is analogous to the friction between any two ridged surfaces: if the ridges align, they mesh like gear teeth and movement is difficult, whereas unaligned ridges could slide past each other more easily.

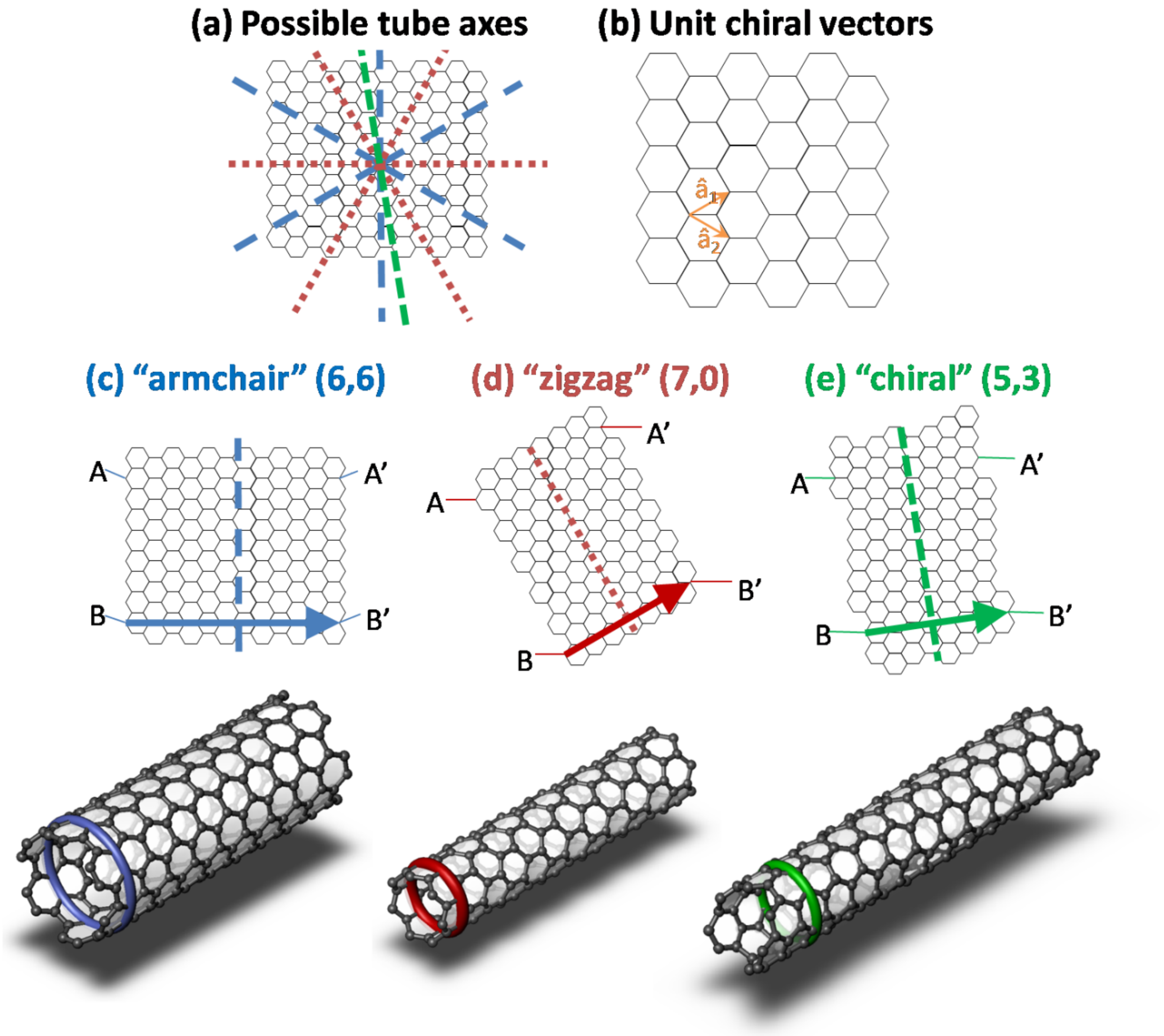

Figure 2-2: Carbon nanotube chirality. A graphene sheet can be rolled up around many different angles (a), by joining points A to A' and points B to B'. The angle is expressed as a vector, based on the two unit vectors in (b). Rolling around different axes produces (c) an "armchair" nanotube, (d) a "zigzag" nanotube, or (e) one possible example of a "chiral" nanotube, which is neither armchair nor zigzag.

Since the two SWNTs that make up a double-walled nanotube are not commensurate in general, low friction can be expected. Furthermore, in a MWNT with many layers, even if some adjacent pairs are commensurate, it is likely that many are not. When used as a bearing, those layers with higher friction will be held in place while layers with lower friction begin to move. Thus, the MWNT has the opportunity to "self-select" [28] the optimal (lowest friction) pair of component shells to be the sliding interface.

Altogether, the ideal atomic level structure of MWNTs is well suited for use as a rotary bearing. The planar covalent bonding within the tube wall provides a strong, stable material, while the weak van der Waals forces holding the walls together allow relatively unimpeded movement between layers. The atom-sized spacing between layers also precludes performance and reliability issues that might arise from particulate contamination between the bearing surfaces. Finally, the likely presence of low-friction incommensurate shell pairs within a many-layered MWNT suggests that interlocking between shells is unlikely to be an issue in the bearing.

2.1.2 Defects in Carbon Nanotubes

Real nanotubes typically do not form "perfectly." In other words, although the ideal theoretical structure of a nanotube should be characterized by un-bonded, nested, circular-cylinder-shaped hexagonal lattice sheets, in practice the structure can deviate from this locally or globally to varying degrees [49]. The level of "graphitization," or the degree to which the nanotube resembles concentric rolled graphene SWNTs, can vary from perfect to poor, as in Figure 2-9. Many types of discrete, well-defined defects can be present in any given CNT. Some defects are local, involving only a few atoms, while others cover a larger region of the tube. Some defects are constrained to a single layer, and hence may not affect inter-layer friction substantially, while others may span multiple sheets and make relative motion impossible. Since the low friction character of CNTs depends on the molecular structure, defects in the structure can be critical to bearing performance.

2.1.2.1 Types of Defects

Probably the simplest type of defect in the structure of a nanotube would be when polygons other than hexagons are formed within a graphene layer. The ideal nanotube is composed entirely of hexagons, other than the end-caps, but in a real nanotube there are likely to be pentagons and heptagons scattered throughout the layer [50]. Other polygons, such as triangles, rectangles, octagons, *etc.*, are also possible, but such higher-order polygons are more unstable, and quickly rearrange themselves into pentagons, hexagons, and heptagons [29]. It can be shown from group theory [51] that to have a closed fullerene, exactly 12 pentagons are required in a lattice where the rest of the structure is hexagonal. Each pentagon creates a topological change in the graphene sheet – a 60° disclination, preventing it from being flat (Figure 2-3). Any extra pentagons beyond the requirement would further alter the topology, making a closed structure impossible. However, heptagons in the lattice produce an opposite disclination from pentagons. Each heptagon effectively "cancels" one pentagon, so that a pentagon-heptagon pair (sometimes called a 5/7 defect [49, 51]) causes no net disclination, and hence does not prevent the formation of a fullerene (closed graphene structure).

However, even though these pentagon-heptagon pairs (Figure 2-4) are compatible with a single-graphene-sheet structure, they still create a topological change in the graphene, altering the alignment of the surrounding hexagonal lattice. Put another way, a single tube with a pentagon-hexagon pair must have two different chiralities on either side of the defect, and hence two different diameters. The farther apart the pentagon and hexagon are, the more severe the change in chirality. A kink in the tube is also likely, as the two different chiralities will not in general have collinear axes. A tube with a single pentagon-hexagon pair is likely to resist rotation or linear sliding, effectively exhibiting high friction, due to the presence of the kink.

If there are two 5-7 defects present (two pentagons and two heptagons) the structural alteration caused by the defect could be lessened. The two defects could have opposite orientations. One defect changes the chirality of the tuzbe, but a defect of the opposite orientation and same size changes it back. In effect, there is no chirality change except for the area between the two 5-7 pairs. In the limiting case, the two pairs are adjacent, and there is only a very small local region where the tube deviates from cylindrical. Such a case is called a Stone-Wales [52] defect, and is the most energetically stable defect possible in CNTs. It has been proposed [29] that these defects are responsible for the small friction measured experimentally in MWNT systems where there are no defects large enough for observation.

Although these defects are expected to be common, due to their stability and lack of impact on the long-range tube structure, they also should not significantly influence friction, because the geometry change is both small and local, and no inter-shell bonding is introduced.

Some other classes of defects are more likely to increase friction significantly in MWNTs than such local defects. For example, defects that involve covalent bonding between adjacent SWNTs within the MWNT directly worsen the concentric-tube structure of the nanotube. Since the normally weak interaction between adjacent shells is responsible for the low friction within perfect MWNTs, inter-shell defects directly increase the resistance to rotation by strengthening the interaction. Relative motion in the presence of such defects requires that the bonds be broken. Inter-layer defects can be local,

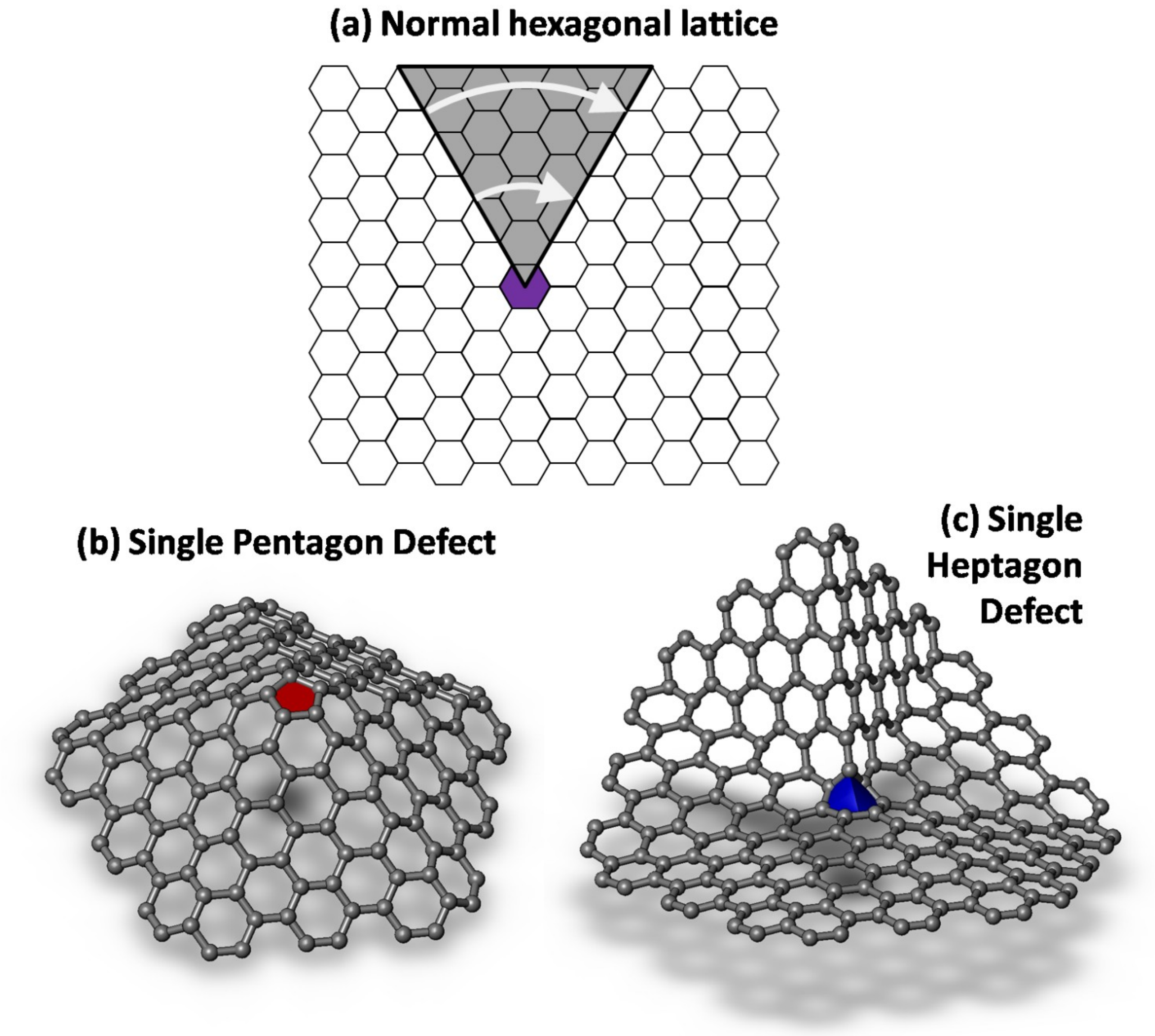

Figure 2-3: A single pentagon or heptagon causes a disclination, introducing curvature into the flat sheet. (a) The effect can be visualized by imagining the original flat sheet. (b) To turn the central purple hexagon into a pentagon, the shaded wedge is removed, and joining the two sides results in a dome-like surface. (c) To form a heptagon, an additional shaded wedge is added, creating a saddle-like surface.

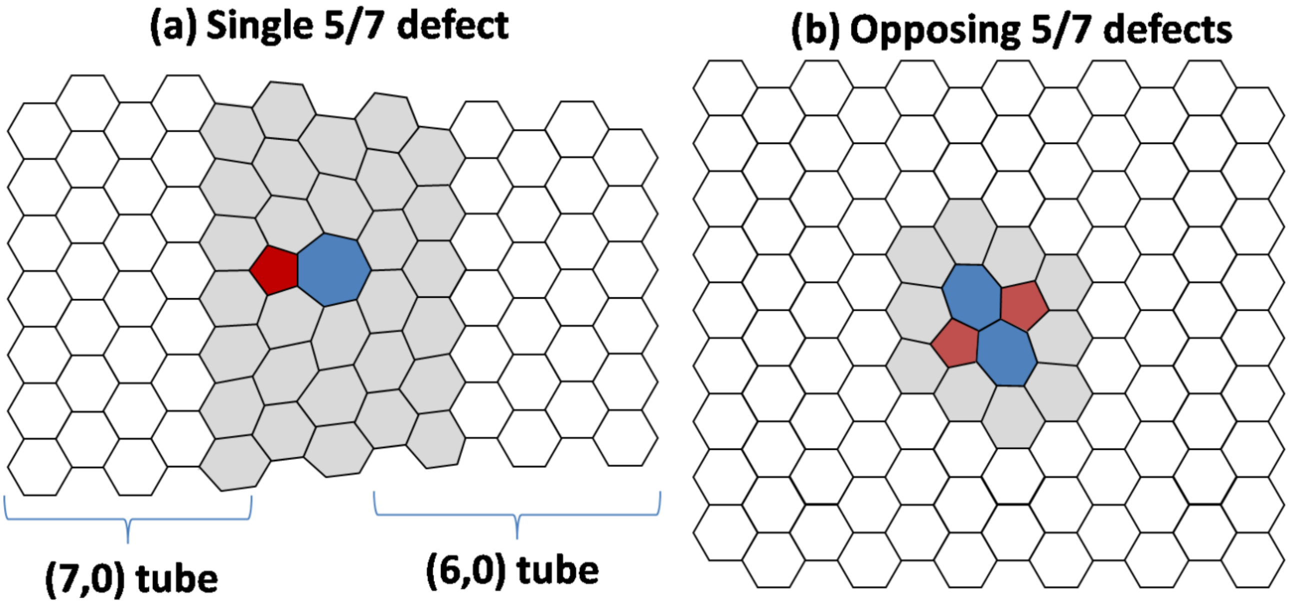

Figure 2-4: Pentagon-heptagon defects. Wrapping up these graphene sheets, and joining the top and bottom edges would illustrate how (a) a single pentagon-heptagon pair causes a chirality change, while (b) two opposing pairs (making one Stone-Wales defect) cause only local changes.

involving only one or a few carbon-carbon covalent bonds. In these cases, rotation can still be possible by breaking the individual bonds. However, multiple isolated inter-shell bonds worsen the situation, and larger scale inter-layer defects can exist.

It is also possible for the carbon to re-hybridize, changing from *sp*^{2} to *sp*^{3} hybridization. A carbon atom in *sp*^{3} hybridization has four bonds, instead of the three bonds of an atom in *sp*^{3} hybridization. While the sp^2 bonds lend themselves to the 2-D structure of graphene, *sp*^{3} bonding tends to produce 3-D structures (diamond is composed of entirely *sp*^{3}-bonded carbon.) A single extra bond might become an isolated inter-shell defect. As the abundance of *sp*^{3} hybridization increases, the structure approaches a state similar to that shown in Figure 2-5d and Figure 2-9d, where there is no discernable crystalline order – an allotrope called amorphous carbon. Amorphous carbon, in which *sp*^{2} and *sp*^{3} hybridization are present in similar quantities, lacks all the structural characteristics of CNTs, and thus does not exhibit the unique mechanical properties that CNTs demonstrate, including low friction. (In fact, there are no defined shells within the structure to allow relative motion.) Amorphous carbon is often present on the exterior of the tubes, deposited as a by-product during the growth process, but when amorphous carbon is the sole component, relative motion is completely impossible.

Besides the disarray of completely un-graphitized (amorphous) carbon nanotubes, some other large scale, but structured, defects are especially adverse for rotation. If a graphene sheet is wrapped up into a nanotube, but its edges are not joined together, and overlap instead, a scroll structure would be formed, as in Figure 2-5b. While the scroll structure is not as stable as a nanotube, simulations [53] and observations [54-57] indicate that such structures frequently coexist with the ideal tube structures within single MWNTs, especially in large MWNTs with many layers. The presence of a scroll defect could be catastrophic for CNT bearings: such a formation would either unravel (if the entire structure were a scroll) or fail to rotate at all (if tubes exist, but are partially joined together by scroll formations).

While these large-scale defects would be detrimental to bearing performance, some common large-scale defects may not necessarily prevent or hinder inter-shell rotation. For example, MWNTs can comprise SWNTs that are closed or terminated at different lengths. Generally, the inner tubes will be shorter than the outer tubes. In other words, inside the outer layers of the tube, instead of inner layers of the same length, several complete fullerenes adding up to the total length will be present. This type of defect, often referred to as "bamboo," does not introduce any bonding between the layers, and therefore might not hamper relative rotation or linear sliding between the inner fullerenes and outer tube. However, no experimental work has yet been done (to the author's knowledge) on friction in these systems, and it is possible that some other unforeseen effects could arise from the presence of bamboo defects.

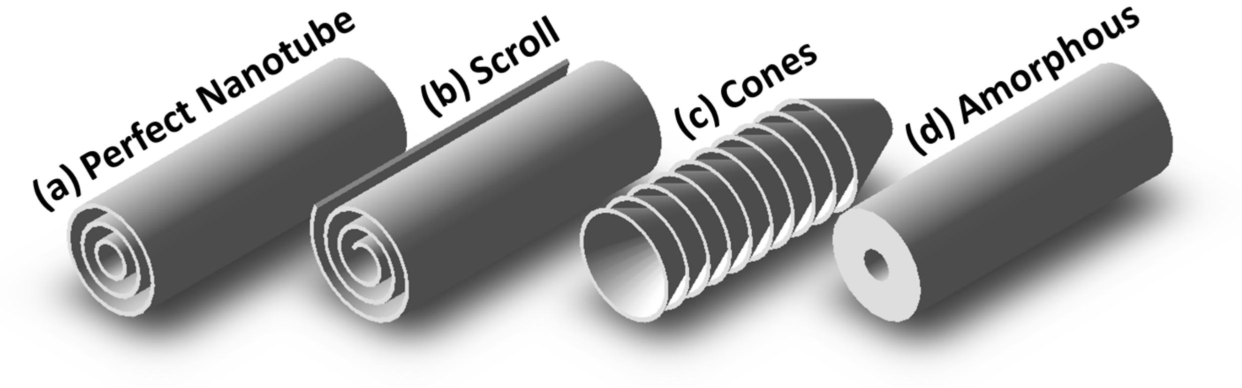

Figure 2-5: Large-scale defects in carbon nanotubes, with an ideal tube for comparison.

Another large-scale defect that might be acceptable for rotary (but not linear) bearings is the presence of conical (instead of cylindrical) graphene structures, shown in Figure 2-5c. Carbon structures composed entirely of stacked cones are also known as carbon nanofibers [58], and can result from the same basic PECVD growth methods as true carbon nanotubes. These defects might still allow rotation, as there is no bonding between adjacent stacked cones (they experience the same van der Waals interaction as the concentric tubes of a perfect nanotube structure). However, because the graphene sheets terminate at the circumference of the tube, there may be some bonding between adjacent sheets, or between the sheets on the outside of the tube and the rotor or support, which would interfere with rotation. Additionally, there would be no strong structures running the entire length of the tube (as there would for the ideal structure) and the bearing could separate or break easily.

The diversity in structure, stability, ubiquity, and frictional influence among the many types of possible defects makes incorporation of real MWNTs into mechanical bearings challenging. It is important to be able to identify and quantify the defects that are present in nanotubes used for fabrication, so that good tubes can be selected, and the performance of tubes with varying types and degrees of defects can be compared to elucidate the relationship between defect density and friction. Furthermore, techniques must be developed which mitigate the defects, in order to improve device performance.

2.1.2.2 Identifying Defects

Carbon nanotubes were first discovered using transmission electron microscopy (TEM) [47], and TEM continues to be used to characterize the structure and evaluate the quality of CNTs. TEM allows inspection of nanotubes at the atomic level. Individual defects, as well as the overall disorder of the tube can be observed. Although smaller, single- or few-atom defects such as Stone-Wales defects cannot often be identified with this technique, larger defects such as non-parallel (Figure 2-6) or non-closed, crossed, curved, and split graphitic planes (Figure 2-8), as well as bamboo structures (Figure 2-7), and general lack of graphitization (Figure 2-9) are readily apparent. These defects are likely to severely impact or even inhibit rotation, so their identification is important.

TEM also allows inspection and comparison of different regions of individual nanotubes (Figure 2-10). We have found that quality can vary along the tube length, typically decreasing towards the root. This is due to the longer time that the root region has been exposed to the plasma environment, and hence the more ion bombardment and amorphous carbon deposition it has experienced. Additionally, inspections have been performed at varying focal depths for thick multi-wall nanotubes, allowing detection of the presence of defects in the out of plane direction that may not have been visible otherwise.

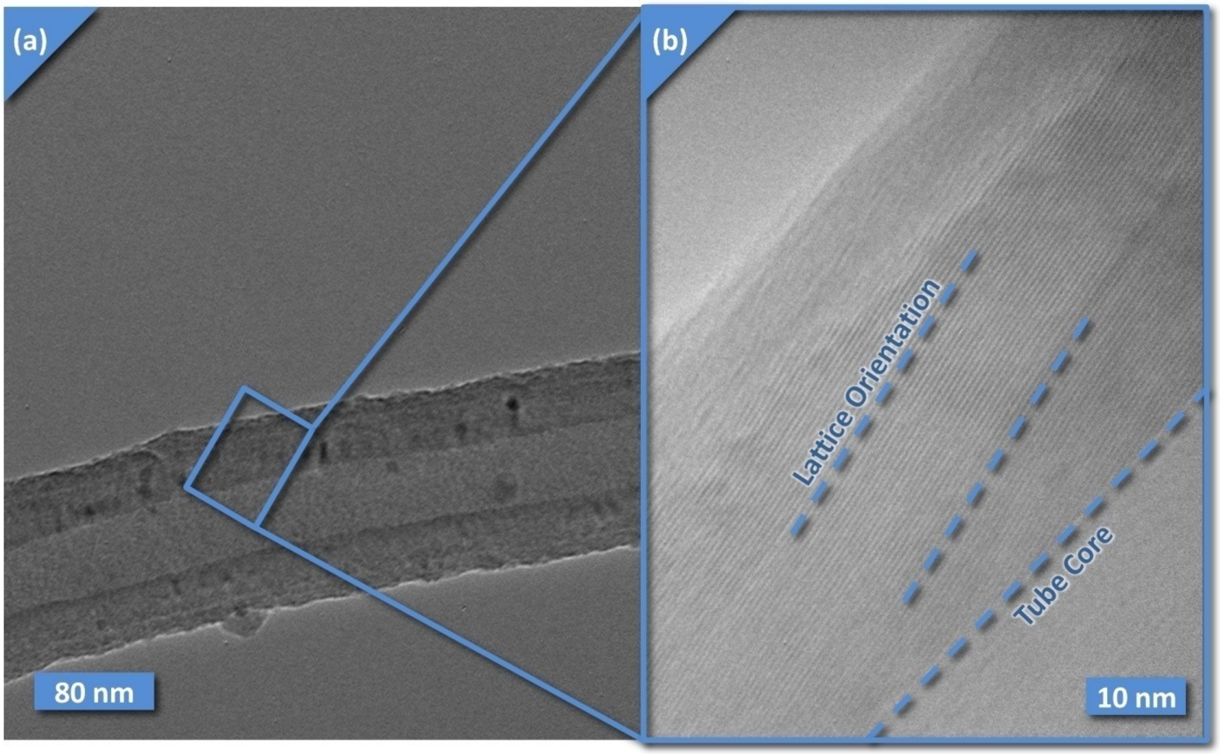

Figure 2-6: Graphene sheets can be wrapped conically, instead of parallel to the tube axis.

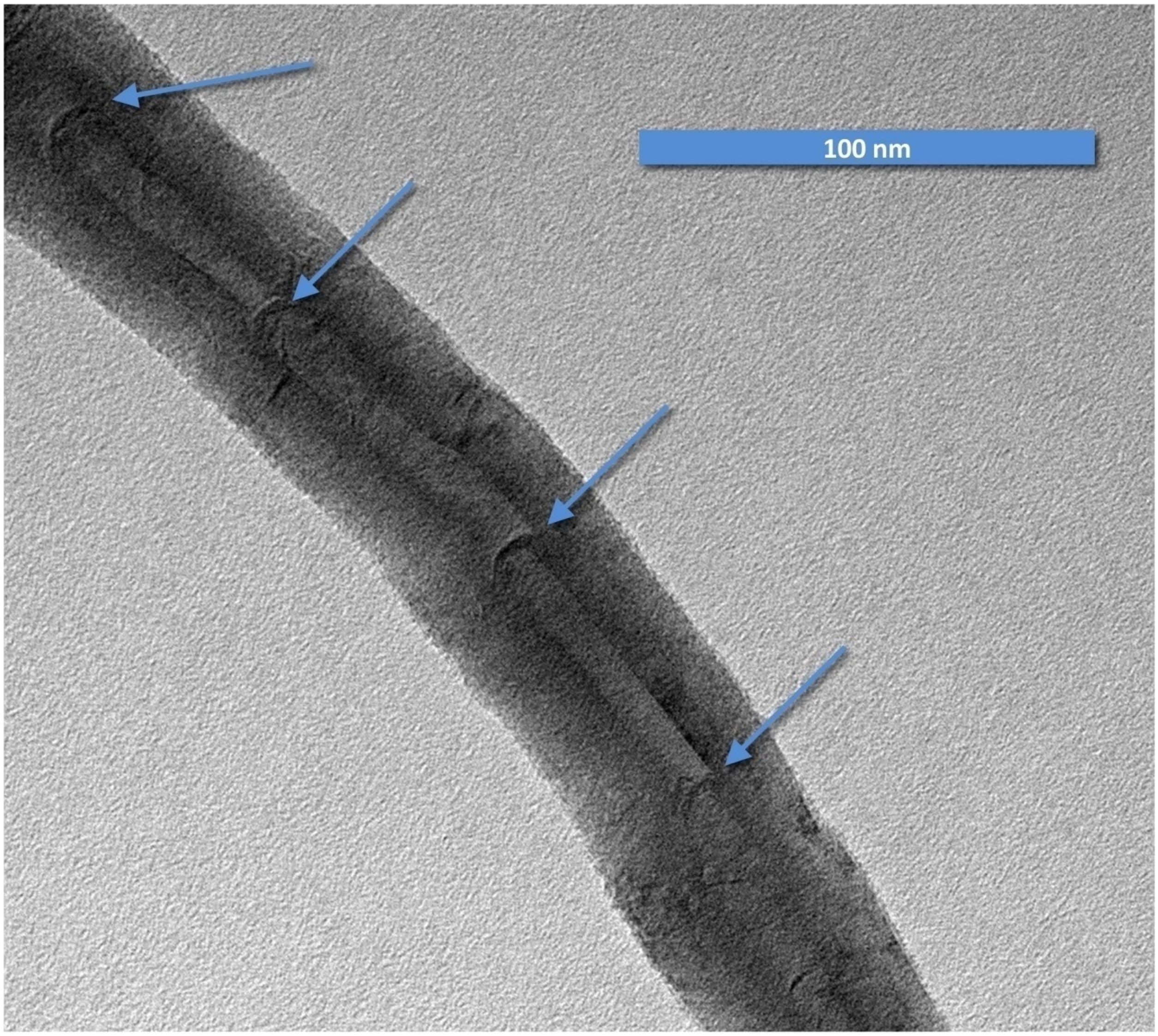

Figure 2-7: Bamboo defects in a carbon nanotube.

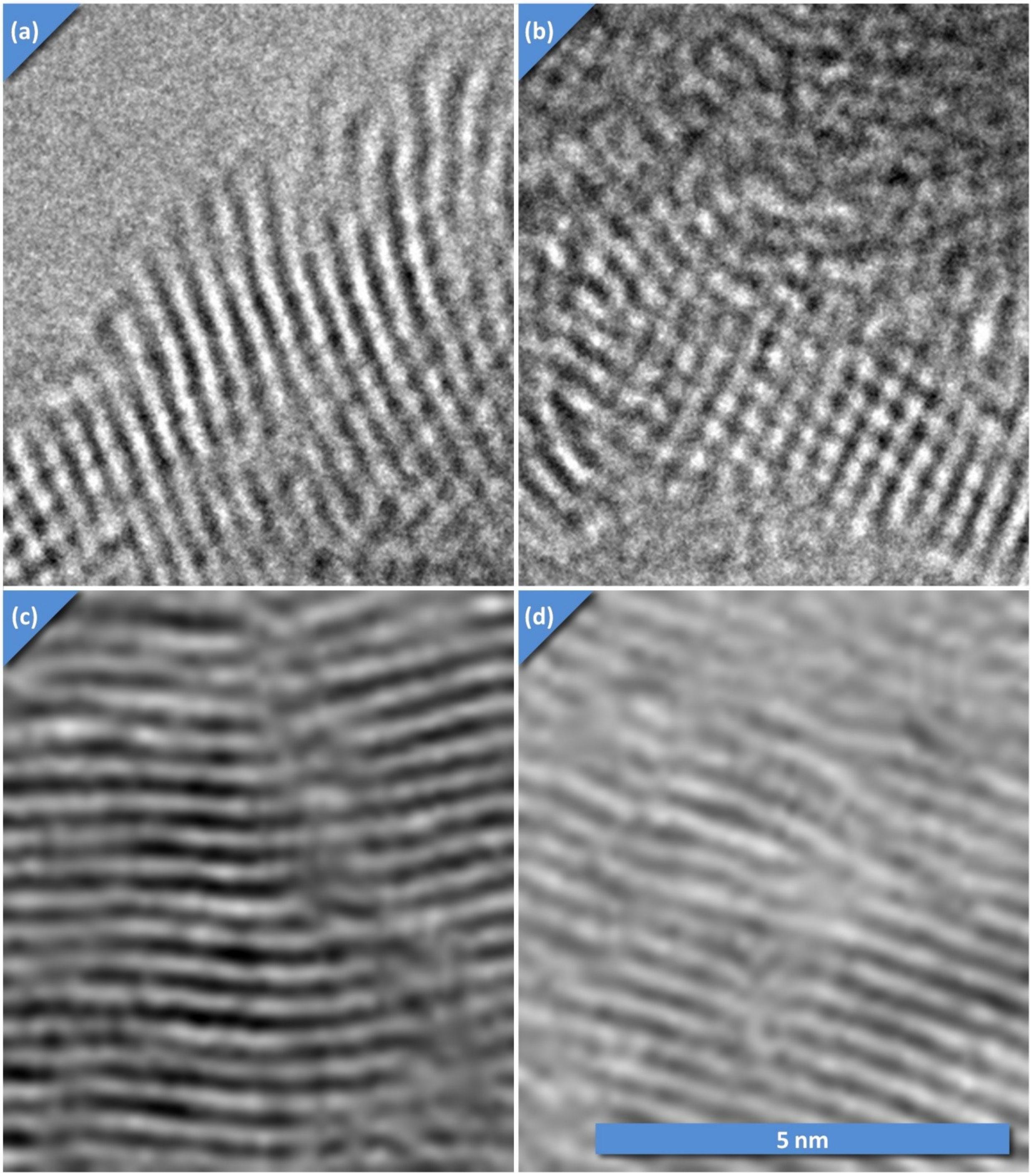

Figure 2-8: TEM can be used to identify (a) edge-terminated sheets, (b) crossed sheets at different depths, (c) curved sheets, and (d) split sheets.

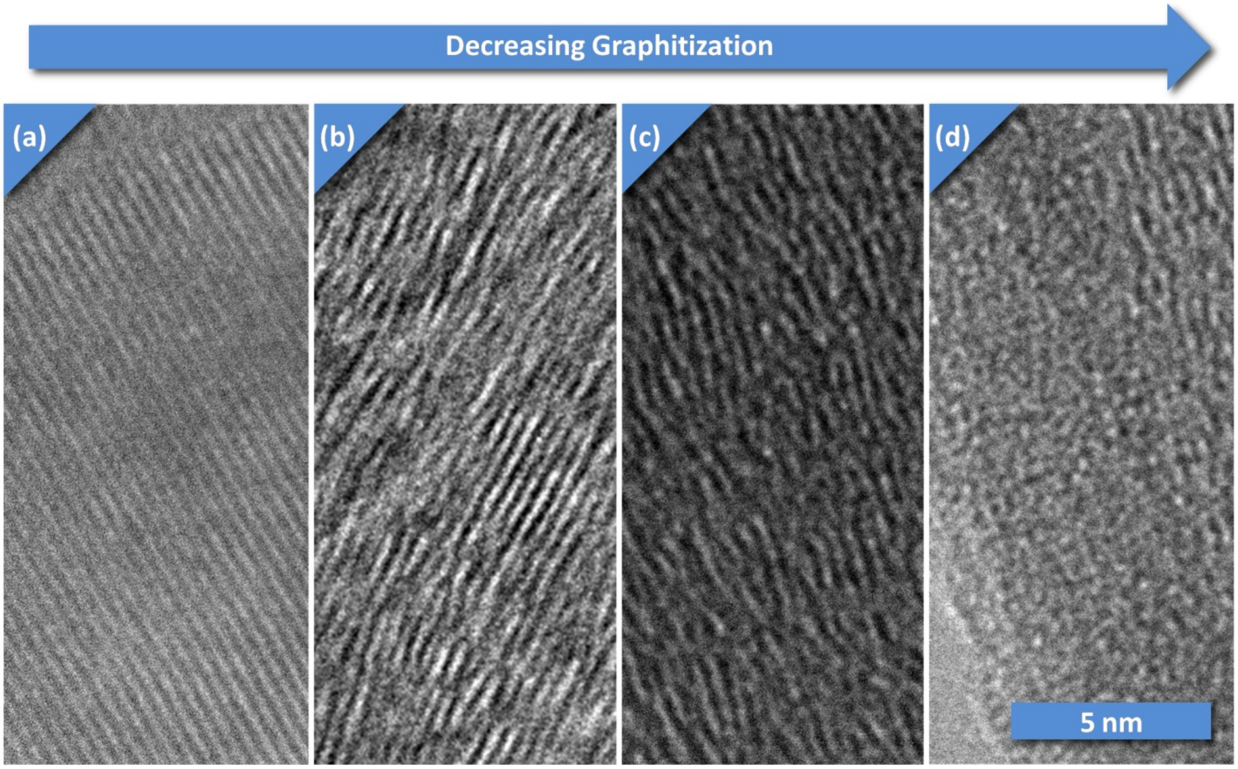

Figure 2-9: Varying degrees of graphitization in carbon nanotubes: (a) defect free, crystalline (b) crystal structure visible, with defects (c) difficult to identify crystal structure (d) completely amorphous.

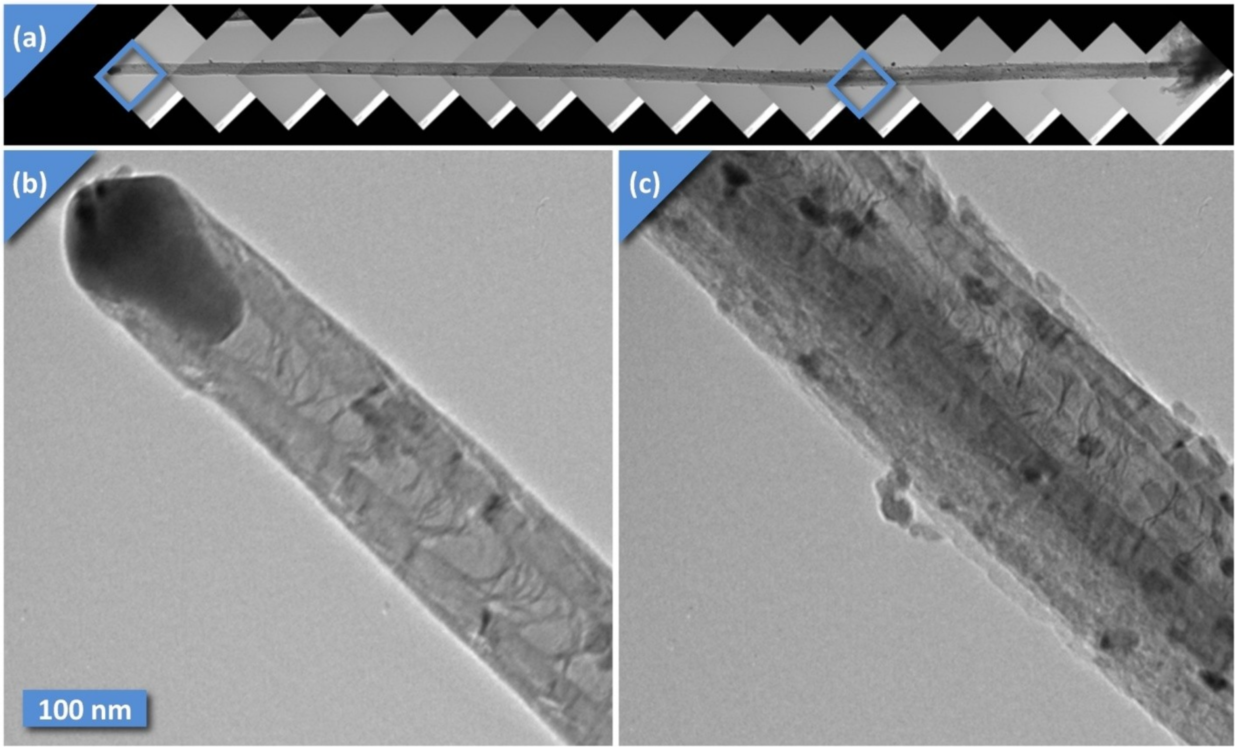

Figure 2-10: We have developed techniques to observe the entirety of tubes up to 20 micrometers in length, and compare structure and defects between regions.

The ability to detect and classify defects in CNTs is especially important for the scientific objective of this work. Since defects are likely to an important factor in determining the value and behavior of friction in MWNT systems, it is critical to correlate the friction measurements taken using the proposed friction test stand with knowledge of the defect density and type in the particular nanotubes used for each test. The ability to make such correlations could be a robust way to qualify and quantify the relationship between defects in CNTs and friction performance.

2.1.2.3 Effects of Defects

It is well known that defects affect all the properties of carbon nanotubes, including elastic modulus [59, 60], tensile strength [61], thermal conductivity [62] and electrical conductivity [51, 63]. It is not surprising then that defects should play a major role in determining the inter-shell friction. For the successful demonstration of the CNT bearing, and to be able to comment intelligently on the effects of defects on friction in these devices, it is important to understand precisely how defects affect friction.

Unfortunately the literature to date has not yet thoroughly established expectations about the relationship between defects and friction. Although many molecular dynamics simulations of friction in nanotube bearings have been conducted [18-21, 23-26], generally they have not included defects. There is one study, by Guo *et al.* [22], which did simulate the presence of a Stone-Wales defect, but did not address larger scale defects. The results of these studies may not capture the frictional effects present in real CNTs, because experiments on actual nanotube bearings indicate that defects are in fact the dominant cause of friction in practice [3, 29, 30]. This gap between experimental knowledge that defects are important, and the lack of a model to describe how, is the basic motivation for pursuing a friction test stand for CNTs – if the test stand is successful, in conjunction with defect identification techniques, some light could be shed on this question.

For the bearing, certain defects would probably be more critical in dictating operability and performance. Isolated defects involving small regions of a single shell such as Stone-Wales defects [52] or other pentagon or hexagon formations change the local shape, but do not directly increase the bonding between layers. Such defects may be responsible for variations in the reaction force around a single rotation, but if they are stable, should not generally cause dissipation [29].

Even larger defects such as bamboo structures [59] and chevron- or cone-shaped graphene layers may not significantly alter bonding between concentric shells. Dangling bonds at the edges of these structures will likely try to interact with adjacent structures, resisting relative motion, but the large surfaces between edges are stable and should exhibit the low friction characteristics of layered graphene sheets. If the axes of the cones or bamboo are close to being aligned with the tube axis, and if the structures do not deviate significantly from circular, rotation could still be possible.

However, defects that involve bonding between shells are expected to dramatically increase resistance to rotation. Vacancies and interstitials can evolve into single-point bonds between adjacent shells, transferring load and increasing friction across the gap [64-67]. Even more disruptive to rotation would be larger cross-shell defects such as scrolls [53]. In these cases portions of the tube would be a single graphene sheet rolled up over itself, not concentric sheets joined only to themselves [54]. In order to achieve rotation many bonds would need to be broken or relocated in this case, leading to a high initial static friction.

Even with defects, friction can still be vanishingly low. Stable defects that create a potential barrier to movement will provide a conservative force, that is, the force vs. displacement will be repeated if the displacement is returned to the original position. Over a complete cycle back to the starting position, the net work is still zero, even though locally the forces fluctuate. Hysteresis is required to generate dissipation, or in other words, friction requires changes in the potential barriers with displacement, and thus “permanent” modification of defects in the tube [29].

While these ideas about how defects affect the friction in MWNT systems provide a starting point, there is still a lot of work do to understand the precise mechanisms whereby the defects influence friction, and the quantitative behavior of those mechanisms. Lack of prior knowledge is a challenge in producing CNT bearings with low enough friction to work, but if the challenge can be overcome, the friction test stand developed could be a powerful tool in generating that knowledge.

2.1.2.4 Mitigating Defects

The method used to produce CNTs strongly influences the quality of the tubes. Arc discharge and laser ablation techniques heat graphite to its melting point (3000-4000 °C), and nanotubes are formed from the condensation of evaporated carbon. Arc discharge tubes are usually straight and highly crystalline, with few defects [35]. The high temperature of these processes enhances surface diffusion of carbon atoms, so they are more likely to transit to low-energy sites before bonding. The result is a reduction of defects in the as-grown tubes.

Carbon nanotubes can also be produced by Chemical Vapor Deposition [35]. In this technique, transition metal catalysts (often Iron, Nickel, or Cobalt) are exposed to hydrocarbon gas (such as acetylene, ethylene, or methane) in a furnace at elevated temperatures (500-1000 °C). The gases decompose, and carbon is dissolved into the catalyst until saturation, when it precipitates out in sp^2-bonded structures such as nanotubes and nanofibers. PECVD includes a plasma in the growth chamber, which provides additional kinetic energy in the form of ion bombardment to promote dissociation of reactants. Use of PECVD allows control of the alignment of the tubes by the electric field present in the plasma [68]. However, PECVD also has the tendency to produce more defects than purely thermal CVD, for two reasons. First, the temperature in PECVD processes is often lower, reducing the ability of defects to diffuse out of the structure by annealing. Second, the tubes are exposed to the plasma for the duration, which can cause sputtering and dislocation of carbon atoms, as well as deposition of amorphous carbon in areas away from the catalyst [58].

While CVD nanotubes are not ideal for low-defect applications, they are required in this case because they can be vertically aligned effectively. Since CVD tubes must be used, collaborators at Boston College have been working to improve the as-grown quality of tubes for use in the CNT bearing device. These researchers have experience growing CVD CNTs [69-71] with controlled location and size, and with the required vertical alignment. However, tube defect density had not previously been a driving requirement for these experiments, and work must now be done to increase the tube quality. The primary method with which they intend to improve the tube quality is raising the temperature during the deposition process, allowing better diffusion of carbon atoms into the energetically favorable defect free structure prior to bonding. This can be accomplished by changing the chemistry of the deposition process (replacing acetylene with methane and ammonia with nitrogen) to allow higher decomposition temperatures of the reactants, and hence higher overall temperature.

After the growth of nanotubes, additional steps can be taken to further reduce the defect density. Simple annealing to high temperatures has proved effective in improving tube quality [72], but such high temperatures are not usable for the present device because the substrate would not survive. Other local annealing techniques are more promising. Passing electrical current through nanotubes can cause sufficient joule heating for local annealing and improvement of graphitization in nanotubes [73-75]. This procedure can be accomplished by fabricating electrical contacts into the device, or by making contact with a micro-scale probe, while observing the results with SEM, TEM, or Atomic Force Microscopy (AFM) . If catalyst material remains, it can further improve the effect of annealing the tube by encouraging diffusion of defects [76].

Since friction is likely to be strongly affected by defects, it is important to reduce the density of defects wherever possible. Defect mitigation techniques will undoubtedly be required to obtain optimized (lowest) friction in MWNT systems, and they could even be necessary to create a device that is capable of rotation at all. Hopefully these methods will prove capable of overcoming the disadvantages of CVD grown CNTs with adequate defect reduction.

2.1.2.5 Self-Repair

Because of the low edge and surface energy present in graphene sheets, bonds in a flawless sheet are difficult to dislodge. In other words, if defects are not present in a given CNT, they are unlikely to form without a substantially forceful stimulus, such as irradiation [77] or extreme mechanical stress [61, 78, 79]. Additionally, any structures and bonds that are not in the ideal configuration (*i.e.* defects) will tend to diffuse into such a configuration when given the opportunity (such as during growth, when thermal energy is provided by annealing, or when other events such as irradiation or inter-shell sliding cause atoms to be dislodged). Together, these two qualities lead to a nanotube that repairs itself: atoms that are in the right place stay where they are, and atoms that are in the wrong place tend to be knocked into the right place.

This self-healing character is particularly encouraging for MWNT bearing systems. If a bearing is able to move at all, it indicates that even in the presence of defects no deterioration in performance should be expected over time. In fact, improvement is likely, and has been demonstrated experimentally in linear MWNT bearing systems [29]. Therefore, unlike familiar macro-scale systems, where wear, contamination, and fatigue can lead to failure over time, MWNT bearings could actually experience "anti-wear," using operation over time as an additional defect-reduction mechanism.

2.2 Friction in Carbon Nanotube Bearings

The similarities between CNTs and graphite were noted immediately upon their discovery [47], including the weak bonding between concentric atomic layers that gives graphite its well-known [80] lubricating properties. It was not long before MWNTs were proposed [81] as a low-friction bearing for nano-engineering. This project represents the latest step towards realization of practical MWNT bearings, suggested by the low expected friction.

However, while all sources agree that the friction should be "low," (some have even gone so far as to use the term "super-lubricating," [19, 29, 30] comparing with such phenomena as superconductivity) exactly how low the friction is remains a point of contention. Copious theoretical simulations and calculations have been performed [18-26], and recently a few experimental investigations have been conducted [3, 18, 28-30], with the goal of establishing a qualitative and quantitative understanding of friction in MWNT systems, yet the results range by as much as ten orders of magnitude. Figure 2-11 shows the breadth of this range, along with the sliding speed at which these simulations or measurements were taken. If nanotube bearings are to be used in practical applications, it will be critical that reliable, accurate, and consistent methods for predicting the friction will be necessary. One of the goals of this project is to aid in establishing such methods, by providing many experimental data points on nanotube friction, building confidence in the quantitative value of friction.

There is an even more significant problem with the state of knowledge about friction in MWNTs: Qualitative disagreements persist about what factors are important in influencing the value of friction.

The classical macroscopic model of friction consists of constant static and kinetic coefficients that multiply the normal force, or the force with which the two surfaces are pressed together. The model assumes that the area in contact, the sliding speed, and the orientation of the surfaces have no influence on the friction. As the ability to perform friction experiments on micro-scale objects has become a reality, it has also become clear that the classical model is not complete [82]. Micro- and nano-scale friction tends to be proportional to contact area, and not dependent on the normal force. The apparent contradiction is resolved [83] by realizing that a macroscopically "smooth" surface actually has substantial surface topography at the micro- and nano-scales. Increasing normal force causes deformations in these features, allowing more area to be in true contact. Conversely, at the micro- and nano-scales, samples can be "perfect," or without topography even down to the atomic scale. Therefore these small samples will have the same contact area and friction regardless of the normal force.

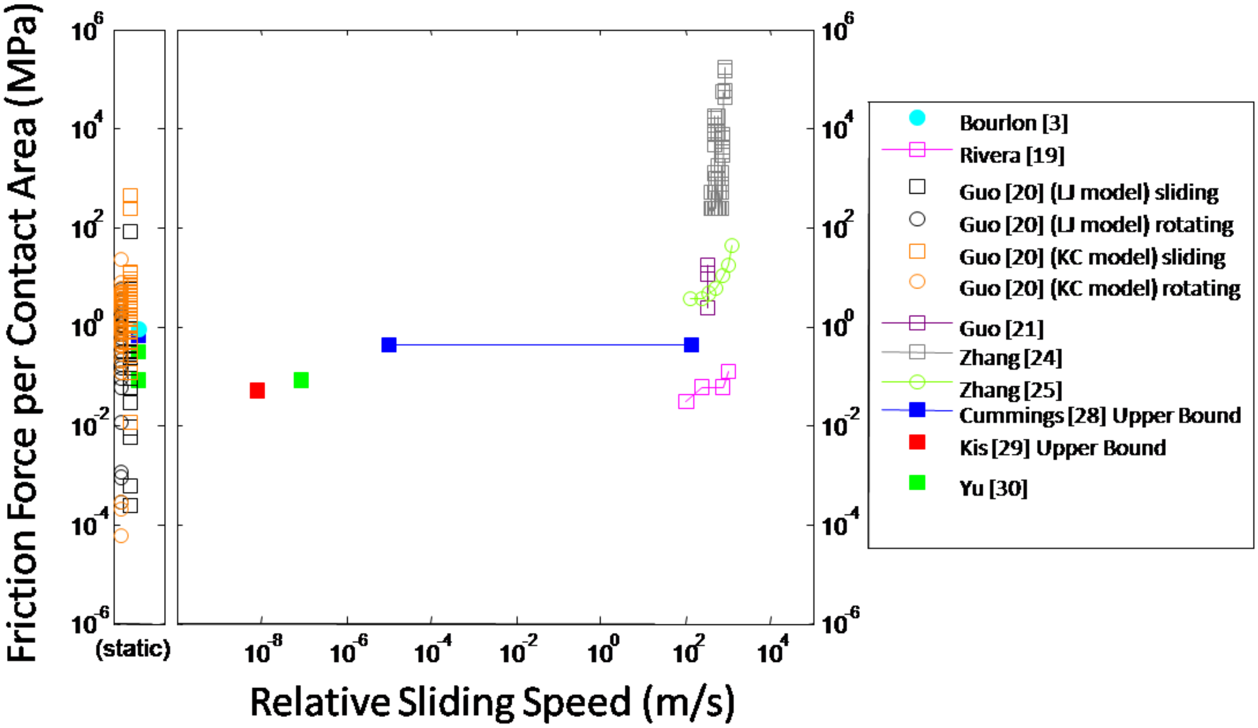

Figure 2-11: Simulated (open markers) and Experimental (closed makers) values from the literature on linear sliding (squares) and rotating (circles) friction in MWNTs. Wide disagreement remains, spanning almost ten orders of magnitude. These data wer converted from the references, and speed computed from various available data, including times, frequencies, and distances given in the references.

The more interesting friction effects that become important for micro- and nano-objects are also the effects that are more vigorously debated. One factor under debate is the speed of the relative motion between the surfaces. The classical convention is to distinguish only between zero (static) and non-zero (kinetic) speeds, and some have continued to use that assumption. Others quote friction data over a speed range, explicitly acknowledging the influence of speed. Another factor that is alien to macro-scale friction is commensurability. At the micro-scale, the possibility for entire components to have a single coherently ordered structure leads to friction that depends on the relative orientation of the objects (see also section 2.1.1). While it is difficult to determine the commensurability in a MWNT system in experimental situations (a few studies [84, 85] have addressed commensurability between a single CNT and flat graphite), simulations have addressed this factor extensively. There yet other factors, including temperature, inter-wall spacing, and defect density that only a few have explored. Table 2-1 shows just how widely the qualitative and quantitative results of friction studies vary.

Table 2-1: Summary of friction data from the literature

Reference	Type	Factors Influencing Friction						Friction	
		Area	Speed	Temp.	Comm.	Defects	Normal		
Yu [30]	EL	S	K	-	S	S	-	0.08 — 0.3	MPa
Akita [18, 86]	ETL	-	-	-	S	-	-	Below Measurement Threshold	
Cummings [28]	EL	S	K	-	-	S	X	$< 2.3 \times 10^{-14}$	N per atom
Kis [29]	EL	S	K	-	-	S	-	$< 1.4 \times 10^{-15}$	N per atom
Bourlon [3]	ER	S	K	-	S	S	-	0.85 +/- 0.15	MPa
Guo [20]	TLR	S/N	-	S	S	-	-	10^{-18} —10^{-11}	N per atom
Rivera [19, 87]	TL	-	S	S	S	-	S	0.3—0.12	MPa
Guo [21]	TL	S/N	-	S	S	-	-	0.85—6.12 $\times 10^{-13}$	N per atom
Zhang [25]	TR	-	S	-	S	-	S	~10^{-13}	N per atom
Omata [26]	TR							9.7×10^{-4}	N·m per m^2

Legend: "Type" is Experimental, Theoretical, Linear, or Rotating. For "Factors Influencing Friction," the entry designates whether, according to the reference, the factor has a Strong effect, a Negligible effect, No effect (X), or the factor was not addressed (-). For "Speed," (K) indicates that a distinction was made only between static and kinetic cases.

To have a coherent understanding of the mechanisms governing friction, it must be determined if and how strongly these factors influence the friction in MWNTs. This project could contribute data covering many of these factors, establishing the trends of friction over a wide range of each parameter. With a large enough sample, and sufficient confidence in its accuracy, the true nature of CNT friction might be easier to find. Experiments on Friction in Carbon Nanotubes

Experimental studies in CNT friction have been extremely challenging. Fabrication, observation, and testing of CNT devices requires techniques that are very advanced, even in most MEMS contexts. These experiments have generally required e-beam lithography, transmission electron microscopy, and nano-manipulation, instead of the more familiar and easier photolithography, scanning electron microscopy, and probe stations inherited from integrated circuit technology. Because of the difficulty of interfacing with these truly molecular devices, experiments have been relatively limited. Nevertheless, a few intrepid groups have gathered some useful data, and success for this project could contribute substantially to the existing data base.

2.2.1.1 Linear Sliding Friction Experiments

One obvious mode of motion between adjacent walls is the linear sliding mode. In this mode, shells slide parallel to the axis of the tube, relative to each other. This mode can include short outer tubes sliding along a longer inner "rail," or inner tubes extending ("telescoping") and retracting from an outer casing. The latter case has so far been the only MWNT bearing system explored experimentally.

The first study on friction in linear CNT sliding, by Yu *et al.* [30], was performed in a SEM with manipulators capable of measuring force and displacement [88]. Yu's group was originally conducting tensile strength tests on CNTs [89] and discovered that the specimens tended to fail in the outer shells ("sword-in-sheath" mechanism), occasionally leaving some portion of the inner and outer tubes overlapping. In these cases, force and extraction length vs. time data were collected as the remainder of the inner tube was extracted, allowing examination of the forces involved in relative motion between shells.

Several types of forces were considered in this study. First, the "capillary" force was computed from the tube geometry. This force is caused by the van der Waals interaction between the adjacent sliding shells. As the tube is extracted, the surface energy is increased because the contact area between the inner and outer tubes decreases. The van der Waals attractive force, which tends to restore the contact area, is the derivative of the energy with respect to extraction distance [28]. Because the energy is directly proportional to the contact area (and hence inversely proportional to extraction distance), the result is a constant force acting to retract the inner tube into the outer tube. In addition to this force, both static and dynamic friction forces, proportional to contact area, were assumed to be acting. Finally, it was noted that they could not distinguish between these surface friction forces and any additional forces arising from the interaction of the edges of the nanotubes.

One of the tubes Yu *et al.* [30] tested displayed a "stick-slip" behavior, stopping at several discrete locations until the force was increased back up (it was relaxed when motion began). They found that the force required to continue motion decreased proportionately with the length of overlapping contact area, to some constant at zero overlapping area. This is consistent with the assumption of area-dependent friction forces plus a constant van der Waals restoring force. A linear fit allowed estimation of the value of this constant force. Subtracting off this known force, they assumed the remainder of the force would be the frictional interface force, noting that they could not distinguish between surface-to-surface contact effects and any additional forces due to the interactions of the tube edge. This provided an estimate of static friction. The behavior of intermittent sticking may not seem promising for MWNT bearings, but it is important to recognize that the same static friction applied at several different points. If the force to overcome the static friction had been continuously applied, sticking might not have occurred.

On the second tube, a more smooth motion was observed. By correcting again for the capillary force, the remaining friction could be found in the same way. However, this time, the friction represented a continuous resistance to the continuous motion, rather than a barrier to initiating motion at discrete locations. It was therefore considered to be an estimate for the dynamic friction. Interestingly, the force required to initiate motion in this tube was the same, indicating that the static and dynamic friction for the second tube are the same. However, the static friction was much less for the first tube. Yu *et al.* attributed the difference to commensurability differences, or possibly geometrical variations between the tubes.

While this experiment was able to establish some estimates for friction, Akita *et al.* took the research a step further [18, 86]. They performed a very similar experiment in a similar apparatus, except for additional care taken with preparing the specimens. The mechanical breaking used previously to create specimens might have left extra dangling bonds and defects on the tube, resulting in unexpected additional friction from the interactions of the edge. In order to eliminate these effects, Akita *et al.* carefully burned off some portions of the outer tube using electrically induced local joule heating [90].

The force-displacement curve obtained by this group differed markedly from the previous attempt. The constant van der Waals attraction is readily apparent, but no variation with contact area is detectable. Since the contact-area-dependent portion of the force is assumed to be the friction, the friction was assumed to be so small that it could not be detected by the apparatus. This encouraging result indicates that if careful means are used to engineer the CNT to the desired configuration, superior friction performance can be obtained, compared with the more damaging specimen preparation methods used previously.

A different kind of experiment [28, 91, 92] was also conducted by Zettl *et al.* inside a transmission electron microscope (TEM) equipped with a nano-manipulator. This rare apparatus allows the nanotube to be mechanically and electrically probed while observing the atomic structure *in situ*. In order to extract inner nanotubes from the outer shells, the tip of the tube was burned off using similar local electrically-induced joule heating [93]. Then the manipulator was attached to the inner tubes by using a short, controlled electrical current pulse to induce deposition of organic materials present in the TEM, forming a "spot weld." This allowed the inner tubes to be mechanically extracted and reinserted.

Two types of forces involved in the system were investigated. The first is the van der Waals attraction, a constant restoring (spring) force. The restoring force is not of interest for rotational bearings, since rotation does not change the contact area, and hence the surface energy. However, the other force investigated was friction. By detaching the tubes from the manipulator, and allowing them to retract, two friction estimates were made. First, the van der Waals force (which was calculated from the measured tube geometry) must have been greater than the static friction to cause retraction, allowing an upper bound estimate on that static friction. With knowledge of the time taken for the tube to retract (it was less than one 33 ms video frame,) an upper bound on the dynamic friction could also estimated from the known van der Waals-induced acceleration.

Although a precise measure of friction was not possible, Zettl *et al.* established some important concepts. Since this was the first experiment capable of repeatably extracting and reinserting a single nanotube, it revealed the astounding reliability of the MWNT bearing system. Multiple different tubes were cycled approximately 20 times, with no behavioral change observed. Furthermore, no atomic damage was detected even at the highest TEM resolutions, indicating that such a system could actually be immune to wear over long periods of time. This result is believable when considering that nanotubes can have truly perfect, atomically stable and smooth surfaces for the majority of their extent, and such a small inter-layer spacing that debris cannot accumulate and accelerate wear. Zettl *et al.* also noted that only one pair of tubes experienced relative motion in each system, which tends to confirm the idea that the optimal sliding interface is self-selected in a many-walled system. Both of these qualities are encouraging for the present work. Long-term reliability can be expected, and interface self-selection should allow even less-than-perfect tubes to achieve rotation, provided they have even one "good" pair of tubes within their structure.

Yet probably the most important point raised by Zettl *et al.* is the distinction between the conservative van der Waals spring force and the dissipative friction force. It is easy to confuse the two, since both resist motion for the telescoping case. In fact, some of the other studies have not made the distinction, or are not clear about what is friction and what is a conservative force. However, the spring force is ***only*** present for the telescoping configuration – rotating systems and sliding systems with a short tube on or in a large tube do not experience a change in contact area over their movement range, and hence are immune to this spring force.

Zettl *et al.* went on to examine this exact problem more rigorously in a new experiment [29]. The same basic setup was used, except the addition of a manipulator with a known spring constant allowed force measurement by observing its deflections in the TEM. This time the tube was cyclically actuated, and the forced-displacement curve used to extract data. In this manner, friction can be distinguished from conservative spring forces, as friction will cause a non-zero integral of force vs. displacement over one cycle, indicating net work input was required.

The results showed a generally constant force over the displacement cycle, corresponding to the spring force as expected. Superimposed on that average was a highly irregular, non-periodic fluctuation with a much smaller amplitude. The irregularity probably indicates the presence of defects in the tube, which is expected for a real-world situation. Remarkably, however, the irregularity was highly repeatable – over many cycles, in both extraction and retraction, the force-displacement curve was essentially unchanged, including the irregular variation. Two important conclusions were drawn from that fact: first, stable defects are present, creating a unique force-displacement profile for each tube. Second, since the curve retraces itself without hysteresis, there is no detectable dissipation (the net integral of Fdx over a cycle is zero), or friction. In a few cases, temporary hysteresis was observed, however, generally within a few cycles it disappeared, restoring the original force profile. The sudden appearance of dissipation was attributed to the introduction of defects, which can be caused by the electron irradiation inherent in TEM. That means the restoration of the original force trace indicates that the defect was eliminated as suddenly as it was introduced. While it may seem remarkable that the MWNT is able to rapidly repair damage it sustains in the form of introduced defects, it makes sense in the context of the nanotube structure. A perfectly bonded graphene sheet is very stable, while defects are not, particularly severe defects such as vacancies and inter-shell bonding which resist inter-shell sliding. The mechanical energy provided by the continual motion could be enough to break these defects, allowing them to re-form in the more stable, defect-free configuration.

These studies are very promising for the idea of a carbon nanotube bearing. They show that motion between shells in a MWNT is possible, and friction is low, as expected. Furthermore, the evidence that stable defects do not necessarily lead to dissipation, and unstable defects can be self-repaired, indicates that even an imperfect tube (such as those produced by CVD as required for this project) may be able to serve as a bearing.

2.2.1.2 Rotating Friction Experiments

Unlike linear sliding friction, experimental data on rotating friction in CNTs remains scarce. Two experiments [2, 3] have demonstrated that the general concept of a rotating CNT bearing is feasible. In both cases, a MWNT was placed horizontally on a substrate, and anchored in place with metal electrodes patterned by e-beam lift-off. In the first study, by Zettl *et al.* [2], a seesaw-like paddle was build onto the outside of the nanotube in the same step as the electrodes. Two additional electrodes were also patterned near the ends of the paddle, and a third electrode was buried under the device. At the end of the process the paddle was released by undercutting the electrodes with a wet etch.

The paddle was then actuated by applying appropriate voltages to the electrodes, causing electrostatic attractions and repulsions. Initially, the actuator was torqued and released, returning to its initial position. This gave some interesting data on the torsional properties of the nanotube, but the device was not a true rotor at that point. However, Zettl *et al.* proceeded to remove or sever the outer shells of the nanotube to allow free rotation of the paddle around an intact inner axle. Several methods were attempted, but the one finally used was simply the application of sufficient torque to shear the outer tubes mechanically. Once the tube was free, complete revolutions at consistent speeds, as well as positioning to specific angles were demonstrated with appropriate voltage signals. Additionally, continuous operation for thousands of cycles revealed no apparent wear, as the group had shown for linear bearings [28]. The experiment proved beyond doubt that a rotational bearing made from an MWNT is possible, and may serve as a reliable component for rotary NEMS.

While the experiment was a remarkable proof of concept, Bourlon *et al.* went on to improve on the design [3]. Instead of simply torquing the nanotube until failure, they used the electrical breakdown technique (as used for some of the linear bearing experiments) to selectively vaporize some of the outer walls of the tube before the paddle was constructed. The rationale was that in this way a cleaner interface between the rotor (consisting of the long inner tube and attached paddle) and the stator (the outer shells remaining embedded in the electrodes on the ends) could be obtained than from mechanical fatigue-induced failure.

When actuating the device, Bourlon *et al.* first noted that the paddle did not return to the original position when released, indicating that the electrical breakdown technique was successful in defining a clear slipping interface, preventing the tube from torquing. However, they did observed a “stick-slip” behavior similar to what one of the linear experiments found [30]. They attributed the behavior to the same cause, namely the presence of defects at specific locations. While it is troubling that smooth behavior was not obtained, the friction at these sticking points was low enough that the electrostatic actuation system could overcome it.

In fact, Bourlon *et al.* was able to estimate the friction quantitatively. To date this is the only data point on rotational friction in MWNTs in the literature, to the author’s knowledge. To determine the static friction, the group estimated the electrostatic torque required to initiate rotation of the device (which would be equal to the static frictional torque) based on a finite-element electrical capacitance model for the system. The result is the highest experimental estimate for friction yet reported. However, the friction was still well within the capabilities of the actuation system to overcome. In addition, the previous rotational experiment might be expected to have higher friction (though it was not measured) due to the rough edges left by the mechanical fatigue-induced failure, and even so the friction was sufficiently low to allow actuation and continuous rotation. Together the two demonstrations provide confidence that rotational bearings are feasible and realizable.

These two demonstrations are just the starting point; the specific area of experimental measurement of rotating friction in CNTs is ripe for work. A great deal more data on both static and dynamic friction remains to be gathered, across a wide variety of tube types, speeds, defect densities, and other parameters.

The new approach investigated in the present work could provide advantages in furthering rotational friction research. Most importantly, the vertically oriented tube used here could enable substantial geometric improvements. Rather than the two or three actuator electrodes available in the previous studies, which resulted in asymmetric driving forces [94] and lack of coverage around the entire revolution [3], the new design suggests the possibility of arbitrarily many evenly spaced symmetric electrodes, with multiple phases and complete, fine-grained coverage for the entire 360 degrees. Furthermore, the vertical alignment might improve the rotor placement accuracy, improving balance and enabling high-speed rotation. Finally, the opportunity for a manufacturable, patterning-based process, instead of the single-shot hand-selection approach previously required, suggests that rapid production of many test devices could be used to examine the friction data across a wide space of nanotube geometry and quality. Eventually experimental rotating MWNT bearings may become a critical instrument for furthering the state of knowledge about CNT inter-shell friction.

2.2.2 Theoretical Studies of Friction in Carbon Nanotubes

The theoretical investigation and simulation of friction in MWNTs has been a popular topic for several reasons. First, the theory is what originally inspired the notion of using MWNTs as bearings. Long before direct experiments were possible at this scale, it was noted by Charlier and Michenaud [81] that the intrinsic lack of bonds between concentric layers in carbon nanotubes could present a unique opportunity for extremely low friction. Theory was the only available way to address the problem at first.

In addition, an MWNT is a particularly interesting system to study using the available atomic and molecular scale models. In some sense, models capable of addressing the dynamics of the system were created without a specific problem in mind, and the MWNT bearing was a good fit. Most of these models have been developed *ab initio,* building up from knowledge of atomic physics and dynamics rather than working from existing data. One popular approach is the numerical solution of the equations governing inter-atomic forces, called molecular dynamics (MD). While that approach is fitting, especially since the behavior of nano-scale systems often differs substantially from macro analogues, the lack of validation for the models from experimental evidence is apparent from the wide range of results. In fact, the theoretical friction predictions are spread over almost ten orders of magnitude, while the experiments all lie within three. It is important to realize that some models may not capture all the important concepts, and to not be lulled into false security by the preponderance of data they can generate.

Nevertheless, theory is critically important in understanding the true nature of friction in MWNTs. Only with knowledge of the underlying principles behind friction can intelligent designs for practical systems be pursued.

2.2.2.1 Linear Friction Simulations

The simulation of friction in linear MWNT has covered a range of different motions, including infinitely long tubes in relative motion, and small tube sections moving inside and outside of longer tubes. Because of the high computational cost, MD simulations are typically limited to a double-walled nanotube (DWNT), the smallest MWNT capable of relative sliding. The simplest simulation involves tubes moving relative to each other at a prescribed speed or extraction force, similar to the tension-testing experiments.

In fact, one of the groups that was able to perform an experiment on linear friction, Akita *et al.* [18, 86], also conducted a molecular mechanics simulation. They computed the potential energy of a tube as it was extracted from another tube based on an empirical model [95]. The resistance force was then taken to be the derivative of that potential with respect to the spatial coordinate. Like the experiment, the tensile force resisting tube extraction was constant at all overlapping areas, with only a variation of about 0.05%, periodic in the period of the carbon lattice. While the experiments have displayed a non-periodic variation [29], they were attributed to the likely presence of defects in the real case. In the theoretical case, there is no disorder, so any variation would have to be from the regular carbon lattice. The model matches the experimental data well. Since the model considers only potential (conservative) forces, and not dissipative forces, the fact that the experiment agrees serves to reinforce the notion that only the spring forces due the van der Waals interaction are being measured in the experiment. The friction must be so much less that it is essentially undetectable.

Rivera *et al.* [19, 87] also examined the telescoping mode using molecular dynamics. A single infinite DWNT was simulated using MD with an established numerical potential model [96]. Different constant relative velocities were imposed on the tubes, and the force resisting the motion was recorded. This force should represent the friction, since in an infinite tube there is no contact area change and hence no van der Waals restoring force. They found the friction to depend strongly on the sliding velocity, but not in a regular way. A monotonic increase in friction with velocity was observed between 100 and 250 m/s, and between 750 and 1000 m/s, but friction appeared independent of velocity between 250 and 750 m/s. No mechanism explaining the trend was proposed. Further study of exactly how friction depends on velocity is needed, and experimental data from the present work could be useful in that regard.

Another sliding mode has been popular in these simulations: If a tube is extracted from its outer shell, and released, as in one of the experiments by Zettl *et al.* [28], the van der Waals restoring force will pull it back in. If both ends of the tube are uncapped, the inner tube will continue going through and out the opposite end, until the spring force reverses its direction. The result is a simple linear oscillator. It is not a true harmonic oscillator, because the force is constant, not proportional to the "spring extension," or the separation of the inner and outer tubes' centers of mass. Friction is an important factor in these oscillators, as it controls the damping and the rate at which the oscillations decay. This system has been the subject of several theoretical studies and simulations.

Rivera *et al.* [19, 87] also examined DWNT oscillators. First, several systems of different sizes and commensurabilities were simulated the same MD with an established numerical potential model [96]. The inner tube was extracted and released, and the simulations showed decaying oscillations as expected. The velocity (computed as a numerical derivative of the position vs. time) showed a saw-tooth profile with constant positive and negative slopes, indicating the axial accelerations and forces were roughly constant in magnitude, only changing in sign as the tube crossed the midpoint. This is consistent with a constant van der Waals restoring force.

While over one or two cycles the axial force appeared constant, over many oscillations the amplitude of motion clearly decayed, indicating the presence of friction. In order to determine the friction, a simple model was fit to the simulated result. Assuming that the restoring force is constant and always acts towards the center, while friction is constant but always acts against the velocity, each period can be divided into four sections based on the combination of the two force signs. The motion is a simple quadratic, and fitting each quarter-period to that quadratic gave the value of the two forces. Examining the resulting forces over time as the oscillations decayed yielded two interesting notes. First, River *et al.* noted that the van der Waals force is constant for most of the duration, as expected. It only changes when the oscillations damp down to approximately the same magnitude as random thermal fluctuations, where the simple model breaks down. That is not of interest for the present work, as the restoring force is absent in rotating systems. Second, the friction force is at least two orders of magnitude smaller than the restoring (van der Waals) force. That is encouraging for bearing designs.

Rivera *et al.* examined a few parameters briefly to determine their effects on friction. Temperature is always a consideration for MD simulations, so it was an obvious choice for variation. They found that elevated temperatures cause the oscillations to damp out more quickly. They hypothesize that the higher temperatures lead to greater fluctuations in the geometry due to random motion, leading to more interaction between adjacent walls. They also reported that the oscillations damped out very quickly for a perfectly commensurate system, in agreement with expectations that the aligned ridges would interlock easily.

However, there was also a strange assertion in this study by Rivera *et al*. The normal force between tubes was also recorded over the length of the oscillations, and the report mentioned that the friction force could be considered some fraction of it. This is not in agreement with the prevailing view that micro-scale friction is not dependent on the normal force. Furthermore, the friction force was assumed constant for the model, while the recorded normal force fluctuated wildly, with an amplitude more than 5 times the friction force. In addition, the time scale of the normal force fluctuations is significantly shorter than the oscillation period, and hence if the friction really does depend on it, could not be treated as constant for each quarter-period. It is not clear what effect, if any, the normal force has, which warrants further investigation.

Guo *et al.* [21] attempted to quantify friction in DWNT oscillator simulations by a different method. Rather than working with position vs. time data directly, they observed the energy dissipation rate as the oscillations damped out. Specifically, they monitored the decay in the amplitude of the potential energy present due to the axial displacement of the inner tube. Friction was taken to be the time derivative of the energy divided by the average sliding velocity. This procedure yielded friction measurements for several systems.

Guo *et al.* also checked for the influence of additional parameters on the friction. For temperature, they found the same trend of increased dissipation at high temperature. However, they reported a more severe impact of this trend than the previous group. Their simulations were performed at 8K and 150K, and they reported oscillations dying off as fast as 3 ns for the higher temperature. Extrapolating to 300K, they expect that even a few cycles may be difficult, while the previous group's simulations persisted oscillating for hundreds of cycles. Some experimental data on friction vs. temperature may help clarify the exact dependence. Guo *et al.* also reported much stronger damping in commensurate systems, as expected.

Guo *et al.* also calculated forces in a different way. Rather than simulating the entire motion, they evaluated the potential energy from the model at many different possible displacements, independent of time. The force was then computed as the derivative of the potential with respect to position. They observed a constant mean force (the restoring van der Waals force) with a smaller periodic variation superimposed on it. They noted that for different systems, when the friction increased, so did the amplitude of this variation. It is not clear why the two should correlate, because the friction is a dissipative force, while the amplitude variations in the restoring force are conservative (they were computed as the gradient of a potential). A quantitative relationship between the two, established by more data points, might help elucidate the mechanism responsible for this perceived trend.

2.2.2.2 Rotational Friction Simulations

While rotation has not been simulated as extensively as linear sliding, a few studies have been conducted. Zhang *et al.* [25] examined two DWNT systems of the same size but different commensurabilities. They first computed the potential energy from an established model [97] at several angular positions. They noted that for armchair or zigzag tubes, which have high rotational symmetry, the potential varies much less than chiral tubes, which indicates that no particular relative angular displacement is preferred strongly. For the chiral case, certain discreet locations, with a period determined by the chirality of the tubes, would be more energetically favorable. These systems might therefore tend to "lock" in place in the absence of actuation. This is not truly friction, however, because the forces involved are conservative – tracing a complete revolution (or a period of symmetry) returns the potential to its original value, and the net work done is zero. The group also noted that these potential energy barriers are about an order of magnitude smaller than those reported for linear sliding, indicating that rotational bearings should be even less "lossy" than linear bearings.

Since these time-independent computations do not capture the dynamic effects leading to friction, MD simulations were also performed. The edge of one tube was held still while the edge of the other was forced to rotate. The rest of the tubes were dragged along by the bonding dynamics with their neighbors, until the whole tube was rotating. The whole assembly was allowed to dissipate heat to a constant temperature reservoir. The potential energy was observed to fluctuate with a magnitude approximately an order of magnitude higher than for the steady case, indicating that it did not in fact capture the main causes of friction. Like some of the linear sliding simulations, Zhang *et al.* determined the friction by observing the energy dissipation rate, in the form of heat leaving the system. Friction is the energy dissipation rate divided by the frictional sliding speed. Once the simulations reached a steady state, the energy dissipation rate (and friction) was constant.

Zhang *et al.* examined the effect of speed by adjusting the applied rotational speed at the edge. It was found that the friction increased more than linearly with rotational speed. The speeds simulated were limited by the mechanical strength of the tube – above 250 rotations per femtosecond (which is well beyond the expectations of any practically attainable speed), the bonds between the atoms were not strong enough to accelerate the free atoms in the tube to the enforced edge speed before the tube disintegrated. Such a problem could be corrected by simulating a slow acceleration to the desired speed, but even without that a few good data points on rotational friction vs. speed were found. Experimental data on dynamic friction at different speeds could be provided by the project, which would help to validate the trend.

One troubling aspect of the study by Zhang *et al.* was the use of a friction coefficient, a proportionality constant between friction and the normal force. As noted previously, the notion that friction scales with normal force is not necessarily true for atomic scale systems. While it was possible to compute the coefficient by averaging the friction force and the normal force extracted from the simulation, it is not clear whether this is a relevant parameter. There was no direct evidence given that the normal force causes the friction force, and the two tubes simulated had similar normal forces and friction forces, so it is difficult to make a comparison. Further study would be needed to truly understand the effect of normal forces.

Omata *et al.* [26] tried a simpler MD simulation, in which the inner tube was given an initial angular velocity, and as time progressed the inner tube slowed down while the outer tube sped up, presumably under the influence of friction. Observing the angular momentum of the inner tube revealed a gradual decrease, as momentum was transferred to the outer tube. There were also two oscillations superimposed on the trace. A short period, small amplitude variation matched the frequency of the radial breathing mode, a mechanical mode in which the nanotube expands and contracts. This variation was not significant compared to the overall trend, and was ignored. However, there was a much larger and slower variation, which was reported to stem from a flaw in the simulation. Unlike other similar simulations, this one was conducted adiabatically, with no way for the frictionally-generated heat to escape. As a result, the researchers supposed that the heat energy was injected back into the tube as kinetic or potential energy, leading to the variations in angular velocity. While that might not be the actual cause of the variation, it would be an important flaw to correct for future simulations. Despite the large, unexpected and probably erroneous fluctuations, an average frictional torque estimate was made by dividing the total angular momentum transferred by the total time. While the alternate method of a coast-down simulation (compared with enforced constant velocity) could provide friction predictions, it must be refined before the results can be considered accurate.

These simulations do give a starting point for estimating the friction in rotating MWNT bearings, but more work is needed to establish the relationship between friction and the possible governing parameters. Experimental data could help validate or invalidate the models, and provide more points on curves matching friction to these parameters.

2.2.2.3 Simulations of Combined Rotation and Linear Sliding

Guo *et al.*, who had studied oscillators [20], also performed simulations of combined sliding and rotation, focusing on the effects of commensurability in nanotube friction. They considered linear sliding and rotating in two configurations: a short outer nanotube sliding along an infinite inner tube, and a long inner tube telescoping out of the outer tube. In each case they examined the variation of potential energy (computed by two different methods, [98] and [97]) with distance as the nanotubes are displaced relative to each other. They then compute the forces simply as the spatial gradient of the potential energy. The tubes are assumed completely rigid, and the effects of deformation of the tubes is demonstrated to be negligible by comparison of a few cases with full MD simulations.

Guo *et al.* found that the rotational friction was significantly lower than the linear sliding friction. This is expected, as there is no overall displacement during a complete rotation of the tube. However, in contrast with the prevailing view, they found that certain commensurate systems (in which both tubes are either zigzag or armchair) experience a very low resistance compared with incommensurate systems. This could be explained by the fact that for these special cases, the ridges align with a circumference of the tube, so that their interlocking would prevent linear sliding motion rather than rotary motion. Indeed, these systems experienced the maximum linear sliding resistance, with any other tubes (commensurate or incommensurate) having about two to five orders of magnitude lower friction.

One puzzling result from the work of Guo *et al.* is the assertion that the dependence of resistive force on tube size is opposite for different systems. For some systems, the force increases with either length or radius, while for others it remains constant. The former is indicative of a contact area dependence, while the latter would suggest there is no such dependence. It is not clear ***why*** the difference is observed, and it would be important to establish what is responsible for the perceived qualitative difference.

A more concerning facet of the study by Guo *et al.*is the way that the resistance forces are equated to friction. The paper states that fluctuations in the forces are directly linked to energy dissipation, so that a tube which experiences a large amplitude in resistance force over a given motion will dissipate energy quickly. This is based on their own prior MD calculations [21]. However, it is not clear why this correlation should hold, especially since the forces are computed as the gradient of a potential, and are therefore conservative by definition. A complete rotation of a bearing would result in zero net frictional work if the resistance forces were in fact truly potential. However, the MD simulations they use for comparison show a clear decrease in the amplitude of the fluctuation over time, indicating that the time-independent potential model is not capturing some important dynamics. It could be true that the amplitude with which the resistance force varies correlates in some way to the conversion of rotational motion into phonons, leading to the eventual loss of energy as heat, but the precise manner of such a relationship was not given, and in any case such a mechanism cannot be detected by a method which begins with the use of explicitly conservative forces.

Combined sliding and rotation is not expected to occur in the initial device, but it could be a topic of interest for future CNT bearing devices. More work is needed to clarify the true nature of the underlying phenomena.

2.2.3 Remaining Work on Carbon Nanotube Friction

While the community has invested substantially in understanding the problem of carbon nanotube friction, a clear, general theory is still lacking. Experiments have been extremely challenging, yielding few data points. Simulations have provided a great deal of data, but it is not consistently generated, and sometimes potential factors of influence have not been completely controlled or understood. There is a schism between theory and experiment, which needs to be bridged.

Experimental studies are conducted on real tubes, which generally have defects, whereas theoretical simulations have the capability to examine perfect structures. The lack of defects in these simulations is not representative of real tubes, and such simulations do not address the additional friction due to these defects. In fact, experiments tend to show that defect density has so significant an influence on friction [29] that other effects cannot be detected. Without capturing such a strong factor in friction performance, the simulations are not applicable to the current real situation. As tube quality improves, approaching the perfection in the simulations, experiment and theory can be more readily compared.

Additionally, simulations are limited to extremely small systems, for computational practicality. Even though CNT bearings are at the molecular scale, the tubes used for real bearings thus far comprise millions to billions of atoms, whereas simulations have been limited to a few thousand. As computational power increases, or as smaller bearings are developed, the two approaches will converge, and meaningful comparisons will become easier to make.

Finally, experimental data has thus far varied within a much smaller range than theoretical simulations. Experimental friction estimates have been within three orders of magnitude, while theoretical simulated estimates range by as much as ten orders. The simulations are based on a wide range of different models and interpretations, with different boundary conditions and data extraction techniques, and it remains to be seen which are accurate and representative of the true physics. In order to validate the models, more experimental data is needed, covering a wider data space that can eventually cover more of the cases explored by the models. Hopefully the CNT based Stodola friction test stand some of the data required to bridge the gap can begin to be collected.

3 DEVICE MODEL

In order to have an understanding of how the device will operate, which can guide the design, it is necessary to develop a model describes the behavior of the device. Before the device is built, the model is needed to set guidelines for what ranges of geometry and scale would be likely to yield a functional device. To that end, thirteen possible failure modes were analyzed based on the model, describing a design space in which the device must lie. Within the design space, the rotor thickness and diameter, as well as the nanotube length were optimized to provide the best performance (maximum coast-down time) while remaining manufacturable. After construction of the device, the model could also inform testing and operation of the device, by providing expected performance estimates.

The device is nano-scale, and molecular dynamics or other similarly small-scale models may be the most accurate. These approaches numerically solve the equations governing the motion of individual atoms, taking into account all the interaction forces. However, the computation of these models would be prohibitively expensive, requiring careful set-up of the numerical domain and boundary conditions, as well as substantial processing time. Furthermore, this particular problem contains components substantially larger than nano-scale. The silicon rotor disk is 20 micrometers in diameter – well outside the few to tens of nanometers typical for a true atomistic simulation. The rotor comprises approximately 10^{13} atoms, compared with the few thousand atoms described in a typical atomistic simulation. This device is currently beyond the practical capability of such numerical simulations.

Besides the impracticality of a numerical simulation, there is also inherent benefit in the use of an analytical model. Describing the system in analytical terms makes the concepts that govern the operation of the system more readily apparent. At such an early stage in development, the insight into what influences the device behavior strongly and what trends can be expected is much more useful than a detailed, accurate description of the behavior with no knowledge of the "why." For these reasons, a relatively simple analytical model, based on classical continuum mechanics, has been used here.

The assumption that continuum mechanics are applicable at this scale is based on the (relatively) large size of the device, as mentioned above. As more and more atoms are required to make up the device, the non-uniformities in material properties become less significant, because the length scales of the non-uniformities are smaller relative to the scale of the problem. It is therefore important to recognize that the model would be less applicable to smaller devices.

Some researchers, including Yakobson and Avouris [61], have not been satisfied with continuum mechanics as an adequate description for the mechanical behavior of CNTs. They rightly point out that molecular scale structures possess substantial anisotropy and local variation in properties corresponding to the actual atoms and bonds, and that material properties across the nanotube are therefore not truly uniform. Furthermore, it is difficult to define geometric features such as cross-sectional area for atoms and molecules, leading to a variation in quantities such as density and Young's modulus depending on the somewhat arbitrary choice of dimension on which the measurements are based. However, the CNTs used in this device are relatively large (50 or more walls,) thus closer to a true classical continuum than the single- or few-walled tubes favored for study by the theoreticians. The ambiguities associated with defining the geometry are less important, since the variation in any given dimension is smaller relative to the dimension itself. Furthermore, experimental investigations [99] have indicated that for large tubes, mechanical properties that do not vary from tube to tube can be established with some degree of accuracy and repeatability. Since the only mechanical property used in the analytical model (the Young's modulus) is used to describe beam bending, which was exactly the phenomenon used to determine the Young's modulus in the study [99], it is expected that the continuum model will be a good starting point for describing the mechanical behavior of the nanotube in this device.

The model treats the deflections of the device, under static and dynamic conditions, based on classical structural analysis. From the deflections, stresses in the device are also monitored. The approach used to determine which designs are viable is based on constraints; the deflections and stresses are compared to geometric and physical conditions that would cause the device to fail. Based on the deflection and stress information generated by the model, each constraint can be checked for different configurations. In that way, the constraints determine the boundaries of the design space. The design chosen by the model, based on a 100 nm diameter MWNT, is a 20 µm diameter, 2 µm thick rotor, supported on a 2 µm long nanotube.

3.1 Summary of Constraints on Device

Between the static and dynamic analyses of the device, there are 13 constraints which must be met for a potential design to be viable. Table 3-1 contains a complete list of all of the constraints.

Table 3-1: Summary of constraints on the device

Constraint	Symbol	Limit	Design Value		Section	Equation
Static Constraints						
Beam Tip Deflection	δ_{beam}	$< 0.1L$	6.9	pm	3.2.1	(3.1)
Beam Stress	σ_{beam}	$< \sigma_{f,\text{CNT}}$	310	kPa	3.2.1	(3.6)
Column Tip Deflection	δ_{column}	$< 0.1L$	5.2	pm	3.2.3	(3.11)
Column Stress	σ_{column}	$< \sigma_{f,\text{CNT}}$	156	kPa	3.2.3	(3.15)
Weight - Euler Buckling	W	$< P_{\text{crit, Euler}}$	14	pN	3.2.2.1	(3.7)
Weight - Shell Buckling	W	$< P_{\text{crit, shell}}$	14	pN	3.2.2.2	(3.8)
Dynamic Constraints						
Speed	Ω	$< 0.8\,\Omega_{\text{crit}}$	3.2	MRPM	3.3.2	(3.42)
Dynamic Rotor Deflection	δ_{dynamic}	$< 0.1L$	70	nm	3.3.3.2	(3.72)
Rotor Angle Deflection	β_{dynamic}	$< 5^\circ$	3.4	°	3.3.3.3	(3.84)
Rotor Substrate Clearance	h	$> 0.1L$	540	nm	3.3.3.5	(3.92)
Beam Dynamic Stress	σ_{dynamic}	$< 0.5\,\sigma_{f,\text{CNT}}$	10	GPa	3.3.3.4	(3.90)
Shaft Telescoping	F_{vdW}	$> F_{cent}\,\sin(\beta_{worst})$	180	nN	3.3.3.6	(3.96)
Rotor Centrifugal Stress	σ_{cent}	$< 0.5\,\sigma_{f,\text{Si}}$	10	kPa	3.3.4	(3.97)

3.2 Statics

Before considering the dynamics of the device, the behavior of the device in the absence of motion is considered. Even without moving, the device must satisfy several conditions in order to avoid failing. The nanotube will defect under the influence of any forces applied to the disk. The deflections under these loads are computed and constrained. Additionally, the forces on the disk can may cause the tube to buckle in one of two possible modes. The design must size the disk to avoid buckling the tube. Finally, the stresses in the deformed tube must be constrained below the failure strength of the tube to prevent permanent deformation. All of the deflections and forces can be computed from classical continuum mechanics, allowing boundaries for the device dimensions to be set such that the deflections and forces are constrained within acceptable limits.

3.2.1 Euler Beam Bending Theory

The nanotube shaft, which provides the only support for the rotor disk, is modeled using Euler simple beam theory. There are several assumptions that are required for simple beam theory to be valid. First, continuum mechanics must be applicable. The applicability of continuum mechanics to this nano-scale problem was already justified, based on prior experimental work [99]. This work further demonstrated that the assumption of isotropic behavior, which does not seem realistic for structures as highly ordered as nanotubes, nevertheless can yield consistent, repeatable results. We have further assumed that the beam mass is negligible, since the diameter is roughly 100 times smaller than the silicon rotor it supports. Additionally, loads are assumed to be applied at and perpendicular to the neutral axis (which is the axis of the tube), resulting in pure bending with no torsion or tension. Also, since the nanotube is axisymmetric, the product moments of area are zero, and there is no coupling between bending in the xz- and yz-planes. All those assumptions together enable the use of classical Euler beam bending theory.

The tip deflection of the cantilevered nanotube shaft results from two loads. The weight of the rotor applies a transverse tip load (in the case that the device is held with the tube horizontally), and there is also a moment applied, due to the additional lever arm provided by the z-separation between the beam tip and the rotor center of mass. The deflection under these loads is (as derived in Appendix 6.1):

$$\begin{aligned}\delta_{beam} &= v(L) \\ &= \frac{F_{y,\,\text{applied}}}{6EI}\left(-L^3+3L(L)^2\right)-\frac{M_{x,\,\text{applied}}}{2EI}L^2 \\ &= \frac{WL^3}{3EI}+\frac{WL^2a_z}{2EI}\end{aligned} \tag{3.1}$$

The Young's modulus was taken to be 1.2 TPa, based on the literature [99], and the second moment of area was based on a 100-nm diameter CNT. Note that the deflection could equivalently be $u(L)$ or $\sqrt{u(L)^2+v(L)^2}$, depending on the orientation of the transverse load. For simplicity, the yz-plane bending case is used. For the device, this static beam tip deflection was constrained to be less than 10% of the total beam length. The static angular displacements were not constrained, because an angular constraint that takes dynamic factors into account was included. This is one of the constraints a design must satisfy in order to be viable. This limit ensures that the nanotube deflection while the device is held sideways will remain within the region described well by the simple beam model. This constraint only tends to be important for large rotors on long nanotubes, as one might expect.

The Euler Beam model also allows the computation of stresses in the beam due to the bending. In the model the axial stress in the beam varies linearly from compressive to tensile across the cross section of the beam. At any point in the beam the stresses due to bending in the yz-plane can be found from

$$\sigma_{zz} = -\frac{M(z)y}{I_{xx}} \tag{3.2}$$

Where $M(z)$ is the internal moment at axial position z along the beam. For a single load at the tip, which is the case for the heavy rotor on the end of the narrow nanotube beam, the internal moment is greatest at the root of the beam where it attaches to the substrate. The value of the moment can be found by recalling the formula for the internal moment from (6.5):

$$\begin{aligned}(M_x)_{z=0} &= EI\left(\frac{\partial^2 v}{\partial z^2}\right)_{z=0} \\ &= 2EIB \\ &= -M_{x,\text{ applied}} + LF_{y,\text{ applied}}\end{aligned} \tag{3.3}$$

In other words, for no moment applied at the tip ($M_{x,\text{ applied}} = 0$), and a transverse load equal to the weight of the rotor applied at the tip $F_{y,\text{ applied}} = W$, the internal moment at the root is:

$$(M_x)_{z=0} = W(L + a_z) \tag{3.4}$$

Leading to a stress of

$$\sigma_{\text{beam}} = \sigma_{zz} = -\frac{W(L + a_z)y}{I_{xx}} \tag{3.5}$$

The worst stresses clearly occur for maximum and minimum values of y, corresponding to positive and negative values of the tube outer radius. Therefore the maximum stress in the entire nanotube due to a transverse load equal to the weight of the rotor applied at the tip of the shaft is

$$\sigma_{\text{beam}} = \sigma_{zz} = \frac{W(L + a_z)r_o}{I} \tag{3.6}$$

Note that the negative sign has been dropped, because both positive and negative (tensile and compressive) stresses are present on opposite sides of the tube. Also, the “xx” subscript was dropped from the second moment of area, because the tube is completely axisymmetric and the same stress relation holds regardless of the orientation of the bending plane, so long as it contains the z-axis.

In order for the device to survive being held sideways, this stress was constrained to below 10 GPa, a conservative estimate for the failure strength of carbon nanotubes from the literature [61]. This constraint ensures that the nanotube will not break if held with the nanotube horizontal. Like the static deflection constraint, this limit only becomes important for heavy rotors on long nanotubes, as would be expected.

3.2.2 Carbon Nanotube Buckling

It is also important to consider forces acting along the axis of the nanotube. These forces could lead to buckling of the nanotube, especially since it is a high aspect ratio structure. There are two possible modes of buckling. The first is the classical beam buckling case, which is also described by Euler beam theory. The second is a more complicated mode, in which individual shells of the nanotube buckle radially. Both modes are treated here.

3.2.2.1 Euler Buckling

Given a general beam-column subjected to an external compressive force, the column has the potential to buckle. The load at which the carbon nanotube will buckle is (as derived in Appendix 6.3):

$$P_{\text{crit, Euler}} = \frac{\pi^2 EI}{4L^2} \tag{3.7}$$

Here the subscript "Euler" indicates that this is the maximum safe load to avoid buckling in the classical Euler mode. For a device design to be viable, it must not fail in the Euler buckling mode, so the rotor weight was constrained to be below the Euler critical buckling load. Once again, this constraint becomes important for heavy rotors on long shafts. This constraint provides assurance that the device will not fail without even being moved.

3.2.2.2 Shell Buckling

The nanotube can fail in another buckling mode. Since a MWNT is composed of many thin graphene shells, it is possible for some of these shells to buckle independently. This situation has been addressed specifically for carbon nanotubes [100]. The basic equation governing the buckling of a shell is

$$\sigma_{\text{crit, shell}} = \frac{E_w h}{r\sqrt{3(1-\nu^2)}} \tag{3.8}$$

where $\sigma_{\text{crit, shell}}$ is the compressive stress required to cause buckling, r is the radius of the SWNT or single layer of a MWNT, and h is the thickness of the graphene layer. The thickness is difficult to define, because it is essentially the thickness of a carbon atom. However, when using a set of mechanical properties defined consistently with the somewhat arbitrary choice of h, repeatable results that agree with fully atomistic simulations have been demonstrated [78]. Because for this model the tube is analyzed as a single structure, the values of the Young's modulus E_w and Poisson's ratio ν used are based on this defined wall thickness, and not on multiple walls including the regular spacing between them. The result is a significantly different value for the modulus than that used for the pure continuum model of Euler buckling. The difference does not signify an inconsistency in material property, but a difference in definition of the model parameters.

Assuming that the compressive load is evenly distributed across the cross-section of the nanotube, the critical load can be found from the critical stress via the cross sectional area:

$$A_{cs} = \sum_{i=1}^{n} 2\pi r_i h \tag{3.9}$$

where n is the number of shells in the tube, r_i is the radius of each shell, and h is the thickness of each of the shells. Then the critical load is:

$$\begin{aligned} P_{\text{crit, shell}} &= \sigma_{\text{crit, shell}} A_{cs} \\ &= \frac{E_w h A_{cs}}{r\sqrt{3(1-\nu^2)}} \end{aligned} \tag{3.10}$$

For a multi-walled tube, the critical load is thus lowest for the largest radius, indicating that the outer-most wall of a MWNT should be the first to fail in shell buckling.

The tube must not buckle in either mode for the device to be successful. Therefore the compressive force on the nanotube shaft due the weight of the rotor disk must be kept below the critical loads for both of the two buckling modes at all times, independent of any rotor rotation.

3.2.3 Eccentric Column Loading

The buckling formulae describe what critical load will cause catastrophic deflection (buckling) of the column. Strictly interpreted, the Euler buckling models state that there is no deflection until the critical load is reached, at which point the deflection goes to infinity. For a real column finite deflections are observed prior to buckling, caused by imperfections in the column. One such imperfection could be an "eccentric" load, or a compressive load applied not at the column center. The moment created by the off-center load causes deflections that are well described by Euler beam theory. The maximum deflection occurs at the beam tip (as derived in Appendix 6.2):

$$\delta_{\text{column}} = v(L) = e\left[\sec\left(L\sqrt{\frac{P}{EI}}\right) - 1\right] \tag{3.11}$$

As before, although the yz-plane bending case has been used, the xz-plane bending case is the same due to the symmetry of the beam. The eccentricity is most likely to arise from lateral misalignment of the rotor during patterning, leading to a separation of the center of mass from the nominal center at the tip of the nanotube. An estimate of 1 micrometer was used for this misalignment, representing a conservative estimate of the capabilities to align e-beam lithographic features. For the device to be deemed acceptable, the tip deflection due to the rotor weight under this column loading was constrained to less than 10% of the beam length. Note also that when the critical load for the non-eccentrically loaded column (from equation (3.7)) is reached, the secant term becomes unbounded, indicating infinite deflection, or buckling. The critical buckling load is thus the same for the eccentric and non-eccentric cases.

The stress in the nanotube shaft when subjected to column loading is computed in the same way as for transverse (beam) loading:

$$\sigma_{zz} = -\frac{M(z)y}{I_{xx}} \tag{3.12}$$

Where $M(z)$ is the internal moment at axial position z along the beam. For a single load at the tip, which is the case for the heavy rotor on the end of the narrow nanotube column, the internal moment is greatest at the root of the beam where it attaches to the substrate. The value of the moment can be found by recalling the formula for the internal moment from (6.5):

$$\begin{aligned}(M_x)_{z=0} &= EI\left(\frac{\partial^2 v}{\partial z^2}\right)_{z=0} \\ &= e\sec\left(L\sqrt{\frac{P}{EI}}\right)EI\end{aligned} \tag{3.13}$$

Leading to a stress of

$$\sigma_{\text{column}} = \sigma_{zz} = -e\sec\left(L\sqrt{\frac{P}{EI}}\right)EI\,\frac{y}{I_{xx}} \tag{3.14}$$

The worst stresses clearly occur for maximum and minimum values of y, corresponding to positive and negative values of the tube outer radius. Therefore the maximum stress in the entire nanotube due to a transverse load equal to the weight of the rotor applied at the tip of the shaft is

$$\sigma_{\text{column}} = \sigma_{zz} = e\sec\left(L\sqrt{\frac{P}{EI}}\right)EI\,\frac{r_o}{I} \tag{3.15}$$

The same stress limit of 10 GPa used for the stress caused by beam loading was held on the stress caused by column loading. This limit ensures that the weight of the rotor, combined with the misalignment of the rotor center of mass with the beam tip, will not provide a moment strong enough to break the nanotube.

3.3 Dynamics – The Stodola Rotor Model

The dynamics of the device are well understood from the Stodola rotordynamic model, developed originally for turbomachinery, and depicted in Figure 3-1. The formulation of the model given here follows Childs [101]. The equations of motion are derived by determining the degrees of freedom, expressing the kinetic and potential energies of the system in terms of these degrees of freedom, and then applying the Lagrangian method. Details of the derivation can be found in the first Appendix – Derivation of Static Constraints.

The assumption of a thin rigid disk used in the Stodola is not a perfect representation of the proposed device, mainly because the shaft length is comparable to the disk thickness. Therefore the center of mass of the disk is separated from the nanotube tip in the direction parallel to the tube axis (z-direction) by a significant fraction of the tube length. However, the aspect ratio of the tube is still very high (on the order of 20) as is the ratio of the disk diameter to thickness. These ratios support the notion that the disk is rigid compared to the shaft, and that the shaft can be adequately treated by beam bending theory. The separation of the rotor center of mass from the beam tip (which would be neglected if the disk were truly thin) has been accounted for. While a more accurate model could be developed, this model is sufficient to give a first order behavior estimate needed to begin designing CNT based rotary devices.

The dynamic model is used to for two main purposes. First, it can describe the natural frequencies of the system. The operating speed must avoid these frequencies, as large displacements can occur due to resonance. The natural frequencies and modes make up the free response. On the other hand, the model can also be used to predict deflections of a given device excited by imbalance in the rotor. These deflections, if allowed to become large, can cause the device to fail. By predicting the natural frequencies and forced response of the device, the dynamic model shows what designs can avoid these failure modes.

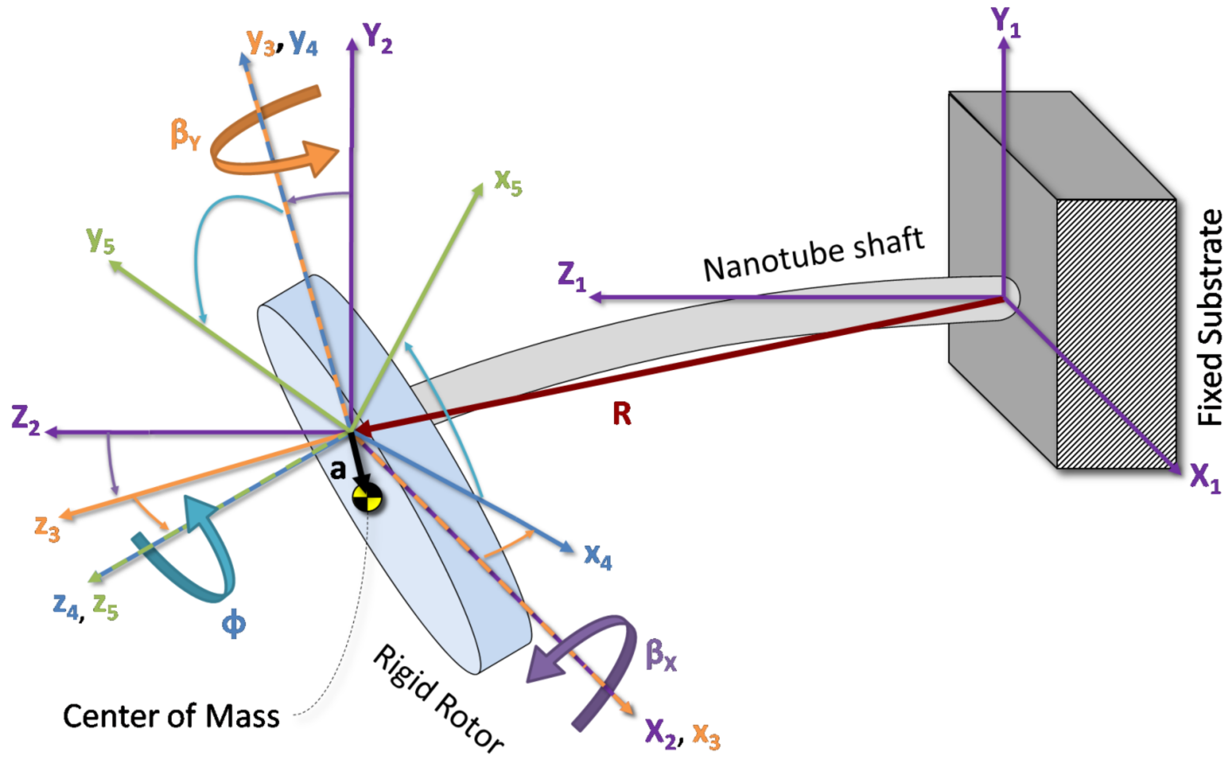

Figure 3-1: The Stodola rotordynamic model consists of a thin rigid disk on a cantilevered shaft. It includes two translational degrees of freedom (R_X, R_Y) and three translational degrees of freedom (β_X, β_Y, and ϕ).

3.3.1 Equations of Motion

The five equations of motion which govern the behavior of the five degrees of freedom are :

$$\begin{aligned} &m\ddot{R}_X - ma_x c\phi\dot{\phi}^2 + ma_y s\phi\dot{\phi}^2 - ma_x s\phi\ddot{\phi} - ma_y s\phi\ddot{\phi} + ma_z\ddot{\beta}_Y \\ &\qquad = -EI\left[-\frac{6\beta_Y}{L^2} + \frac{12R_X}{L^3}\right] \end{aligned} \tag{3.16}$$

$$\begin{aligned} &m\ddot{R}_Y - ma_x s\phi\dot{\phi}^2 - ma_y c\phi\dot{\phi}^2 + ma_x c\phi\ddot{\phi} - ma_y s\phi\ddot{\phi} - ma_z\ddot{\beta}_X \\ &\qquad = -EI\left[\frac{6\beta_X}{L^2} + \frac{12R_Y}{L^3}\right] \end{aligned} \tag{3.17}$$

$$\begin{aligned} &(J + ma_z^2)\ddot{\beta}_X + J_{zz}\dot{\phi}\dot{\beta}_Y + \ddot{\phi}\left[(J_{xz} - ma_x a_z)c\phi - (J_{yz} - ma_y a_z)s\phi\right] \\ &\qquad - \dot{\phi}^2\left[(J_{yz} - ma_y a_z)c\phi + (J_{xz} - ma_x a_Z)s\phi\right] - ma_z\ddot{R}_Y \\ &\qquad = -EI\left[\frac{4\beta_X}{L} + \frac{6R_Y}{L^2}\right] \end{aligned} \tag{3.18}$$

$$\begin{aligned} &(J + ma_z^2)\ddot{\beta}_Y - J_{zz}\dot{\phi}\dot{\beta}_X + \ddot{\phi}\left[(J_{xz} - ma_x a_z)s\phi + (J_{yz} - ma_y a_z)c\phi\right] \\ &\qquad + \dot{\phi}^2\left[(J_{xz} - ma_x a_z)c\phi - (J_{yz} - ma_y a_z)s\phi\right] + ma_z\ddot{R}_X \\ &\qquad = -EI\left[\frac{4\beta_Y}{L} - \frac{6R_X}{L^2}\right] \end{aligned} \tag{3.19}$$

$$\begin{aligned} &\ddot{\phi}\left[J_{zz} + m(a_x^2 + a_y^2)\right] + m(\ddot{R}_Y - a_z\ddot{\beta}_X)(a_x c\phi - a_y s\phi) \\ &\qquad - m(\ddot{R}_X - a_z\ddot{\beta}_Y)(a_x s\phi + a_y c\phi) + \ddot{\beta}_Y\left[J_{xz}s\phi + J_{yz}c\phi\right] \\ &\qquad + \ddot{\beta}_X\left[J_{xz}c\phi - J_{yz}s\phi\right] = 0 \end{aligned} \tag{3.20}$$

The detailed derivation of these equations is achieved by the Lagrangian method, and is presented in full in Appendix 7. These equations are essentially the standard Stodola rotor model as presented in [101], with one important difference: the term a_z, representing the axial distance separating the rotor center of mass from the tip of the beam is usually ignored, because the disk is treated as thin. In this case, however, while the disk diameter is very large compared to the thickness, rendering the thin disk assumption reasonable for determining the inertias, the disk thickness is comparable to the shaft length. The offset between the center of mass and the beam tip is the source of substantial coupling between the tilting and translating motions of the rotor, and is not ignored for the present model.

A little rearrangement yields:

$$
\left\{
\begin{array}{lr}
m\ddot{R}_X + ma_z\ddot{\beta}_Y = -m\dot{\phi}^2\left(a_x c\phi - a_y s\phi\right) - m\ddot{\phi}\left(a_x s\phi + a_y s\phi\right) - EI\left[\frac{6\beta_Y}{L^2} - \frac{12R_X}{L^3}\right] & \textbf{(3.21)} \\[2ex]
m\ddot{R}_Y - ma_z\ddot{\beta}_X = -m\dot{\phi}^2\left(a_x s\phi + a_y c\phi\right) + m\ddot{\phi}\left(a_x c\phi - a_y s\phi\right) - EI\left[\frac{6\beta_X}{L^2} + \frac{12R_Y}{L^3}\right] & \textbf{(3.22)} \\[2ex]
\begin{aligned}
&(J + ma_z^2)\ddot{\beta}_X - ma_z\ddot{R}_Y \\
&\qquad = -\ddot{\phi}\left[\left(J_{xz}c\phi - J_{yz}s\phi\right) - ma_z\left(a_x c\phi - a_y s\phi\right)\right] - J_{zz}\dot{\phi}\dot{\beta}_Y \\
&\qquad + \dot{\phi}^2\left[\left(J_{xz}s\phi + J_{yz}c\phi\right) - ma_z\left(a_x s\phi + a_y c\phi\right)\right] - EI\left[\frac{4\beta_X}{L} + \frac{6R_Y}{L^2}\right]
\end{aligned} & \textbf{(3.23)} \\[2ex]
\begin{aligned}
&(J + ma_z^2)\ddot{\beta}_Y + ma_z\ddot{R}_X \\
&\qquad = -\ddot{\phi}\left[\left(J_{xz}s\phi + J_{yz}c\phi\right) - ma_z\left(a_x s\phi + a_y c\phi\right)\right] + J_{zz}\dot{\phi}\dot{\beta}_X \\
&\qquad - \dot{\phi}^2\left[\left(J_{xz}c\phi - J_{yz}s\phi\right) - ma_z\left(a_x c\phi - a_y s\phi\right)\right] - EI\left[\frac{4\beta_Y}{L} - \frac{6R_X}{L^2}\right]
\end{aligned} & \textbf{(3.24)} \\[2ex]
\begin{aligned}
&\ddot{\phi}\left[J_{zz} + m\left(a_x^2 + a_y^2\right)\right] \\
&\qquad = -m\left(\ddot{R}_Y - a_z\ddot{\beta}_X\right)\left(a_x c\phi - a_y s\phi\right) \\
&\qquad + m\left(\ddot{R}_X - a_z\ddot{\beta}_Y\right)\left(a_x s\phi + a_y c\phi\right) - \ddot{\beta}_Y\left[J_{xz}s\phi + J_{yz}c\phi\right] \\
&\qquad - \ddot{\beta}_X\left[J_{xz}c\phi - J_{yz}s\phi\right]
\end{aligned} & \textbf{(3.25)}
\end{array}
\right.
$$

3.3.2 Eigensolution – Free Response

Having found the equations of motion, the first behavior of interest is the free response of the system. The free response is composed of the natural modes of the system. The operational speed will be kept well below the first critical speed, determined from the free response analysis, to avoid large deflections due to resonance. For this case, the imbalances in the rotor are not important – they will contribute the forcing functions to drive the forced response, which is treated in section 3.3.3. For now, imbalances due to misalignment of rotor with respect to the shaft (a_x a_y, and a_z) and imbalances due to angular misalignment between the disk axis and the actual nanotube (which gives rise to the products of inertia J_{xz} and J_{yz}) are neglected. Note that the axial distance between the center of mass and the beam tip a_z is not neglected, because this can be a significant fraction of the beam length L for the designs considered. Additionally, the rotation of the rotor is constrained to a constant speed, $\Omega = \dot{\phi}$, yielding the following form of the four equations of motion (the fifth equation is extraneous since $\dot{\phi}$ is constant):

$$\begin{cases} m\ddot{R}_X = -(12EI/L^3)R_X + (6EI/L^2)\beta_Y \\ m\ddot{R}_Y = -(12EI/L^3)R_Y - (6EI/L^2)\beta_X \\ J\ddot{\beta}_X = -\Omega J_{zz}\dot{\beta}_Y - (6EI/L^2)R_Y - (4EI/L)\beta_X \\ J\ddot{\beta}_Y = \Omega J_{zz}\dot{\beta}_X + (6EI/L^2)R_X - (4EI/L)\beta_Y \end{cases} \tag{3.26}$$

The four equations are separated into two sets of equations, one in R_X and β_Y:

$$\begin{cases} m\ddot{R}_X = -(12EI/L^3)R_X + (6EI/L^2)\beta_Y \\ J\ddot{\beta}_Y = \Omega J_{zz}\dot{\beta}_X + (6EI/L^2)R_X - (2EI/L)\beta_Y \end{cases} \tag{3.27}$$

And one in R_Y and β_X:

$$\begin{cases} m\ddot{R}_Y = -(12EI/L^3)R_Y - (6EI/L^2)\beta_X \\ J\ddot{\beta}_X = -\Omega J_{zz}\dot{\beta}_Y - (6EI/L^2)R_Y - (4EI/L)\beta_X \end{cases} \tag{3.28}$$

Note that the equations are not decoupled – the angles β_X and β_Y appear in each others' governing equations. Working with equation (3.27), it is helpful to rewrite the equation in matrix form:

$$\begin{bmatrix} m & 0 \\ 0 & J \end{bmatrix}\begin{bmatrix} \ddot{R}_X \\ \ddot{\beta}_Y \end{bmatrix} + \Omega J_{zz}\begin{bmatrix} 0 & 0 \\ 0 & -1 \end{bmatrix}\begin{bmatrix} \dot{R}_Y \\ \dot{\beta}_X \end{bmatrix} + \frac{EI}{L^3}\begin{bmatrix} 12 & -6L \\ -6L & 4L^2 \end{bmatrix}\begin{bmatrix} R_X \\ \beta_Y \end{bmatrix} = \begin{bmatrix} 0 \\ 0 \end{bmatrix} \tag{3.29}$$

It is now clear that the equation is homogenous. The matrices are assigned names:

$$[M_{X2}]\begin{bmatrix} \ddot{R}_X \\ \ddot{\beta}_Y \end{bmatrix} + [C_{X2}]\begin{bmatrix} \dot{R}_X \\ \dot{\beta}_Y \end{bmatrix} + [K_{X2}]\begin{bmatrix} R_X \\ \beta_Y \end{bmatrix} = \begin{bmatrix} 0 \\ 0 \end{bmatrix} \tag{3.30}$$

The subscripts "$X2$" indicates that these matrices are for the 2 equations relating to lateral x-deflections. Because the equations are coupled, a solution describing all four degrees of freedom is needed. A solution from the rotordynamic literature [101] for this coupled second order system consists of movements in the xz- and yz-planes being 90° out of phase. Since both planes experience identical behavior due to the axial symmetry of the system, the mode shapes are the same as well (with the exception of the sign change on the angle, stemming from the right-handed definition of the angle.) The solution is then:

$$\begin{bmatrix} R_X \\ \beta_Y \end{bmatrix} = \begin{bmatrix} c_1 \\ c_2 \end{bmatrix}\cos\lambda t = \Phi_X \cos\lambda t \tag{3.31}$$

$$\begin{bmatrix} R_Y \\ \beta_X \end{bmatrix} = \begin{bmatrix} c_1 \\ -c_2 \end{bmatrix} \sin\lambda t = \Phi_Y \sin\lambda t \tag{3.32}$$

where Φ are the eigenvectors and λ are the eigenvalues. This solution is periodic, with the eigenvalues corresponding to the frequency. The frequencies (imaginary parts of the eigenvalues) that solve the equation are called the natural frequencies. One way to find the eigenvalues is to substitute the solution back into equation (3.30):

$$[M_{X2}]\frac{d^2}{dt}\left(\begin{bmatrix} c_1 \\ c_2 \end{bmatrix}\cos\lambda t\right) + [C_{X2}]\frac{d}{dt}\left(\begin{bmatrix} c_1 \\ -c_2 \end{bmatrix}\sin\lambda t\right) + [K_{X2}]\left(\begin{bmatrix} c_1 \\ c_2 \end{bmatrix}\cos\lambda t\right) = \begin{bmatrix} 0 \\ 0 \end{bmatrix} \tag{3.33}$$

$$\left(-\lambda^2[M_{X2}]\begin{bmatrix} c_1 \\ c_2 \end{bmatrix} + \lambda[C_{X2}]\begin{bmatrix} c_1 \\ -c_2 \end{bmatrix} + [K_{X2}]\begin{bmatrix} c_1 \\ c_2 \end{bmatrix}\right)\cos\lambda t = 0 \tag{3.34}$$

$$\left(-\lambda^2[M_{X2}]\begin{bmatrix} c_1 \\ c_2 \end{bmatrix} + \lambda\begin{bmatrix} 0 & 0 \\ 0 & -\Omega J_{zz} \end{bmatrix}\begin{bmatrix} c_1 \\ -c_2 \end{bmatrix} + [K_{X2}]\begin{bmatrix} c_1 \\ c_2 \end{bmatrix}\right)\cos\lambda t = 0 \tag{3.35}$$

$$\left(-\lambda^2[M_{X2}]\begin{bmatrix} c_1 \\ c_2 \end{bmatrix} + \lambda\begin{bmatrix} 0 & 0 \\ 0 & \Omega J_{zz} \end{bmatrix}\begin{bmatrix} c_1 \\ c_2 \end{bmatrix} + [K_{X2}]\begin{bmatrix} c_1 \\ c_2 \end{bmatrix}\right)\cos\lambda t = 0 \tag{3.36}$$

$$(-\lambda^2[M_{X2}] - \lambda[C_{X2}] + [K_{X2}])\begin{bmatrix} c_1 \\ c_2 \end{bmatrix}\cos\lambda t = 0 \tag{3.37}$$

This equation is solved when:

$$\det(\lambda^2[M_{X2}] + \lambda[C_{X2}] - [K_{X2}]) = 0 \tag{3.38}$$

The determinant of the 2x2 matrix is expanded out, yielding a 4th order characteristic equation in λ:

$$\det\left(\lambda^2\begin{bmatrix} m & 0 \\ 0 & J \end{bmatrix} + \lambda\begin{bmatrix} 0 & 0 \\ 0 & -\Omega J_{zz} \end{bmatrix} - \frac{EI}{L^3}\begin{bmatrix} 12 & -6L \\ -6L & 4L^2 \end{bmatrix}\right) = 0 \tag{3.39}$$

$$\det\left(\begin{bmatrix} m\lambda^2 - 12\dfrac{EI}{L^3} & 6\dfrac{EI}{L^2} \\ 6\dfrac{EI}{L^2} & J\lambda^2 - \Omega J_{zz}\lambda - 4\dfrac{EI}{L} \end{bmatrix}\right) = 0 \tag{3.40}$$

$$\left(m\lambda^2 - 12\frac{EI}{L^3}\right)\left(J\lambda^2 - \Omega J_{zz}\lambda - 4\frac{EI}{L}\right) - \left(6\frac{EI}{L^2}\right)^2 = 0 \tag{3.41}$$

$$[mJ]\lambda^4 - [m\Omega J_{zz}]\lambda^3 - \left[\frac{EI(12J + 4mL^2)}{L^3}\right]\lambda^2 + \left[12J_{zz}\Omega\frac{EI}{L^3}\right]\lambda + \left[12\left(\frac{EI}{L^2}\right)^2\right] \tag{3.42}$$

The exact same characteristic equation would have been obtained had equation (3.28) been used as the starting point, instead of equation (3.27). The four roots of the equation, which are the natural frequencies of the device, depend on Ω. In other words, for a given device, the natural frequencies change as the device is operated at different speeds. Figure 3-2 shows the variation of natural frequencies with operating speed.

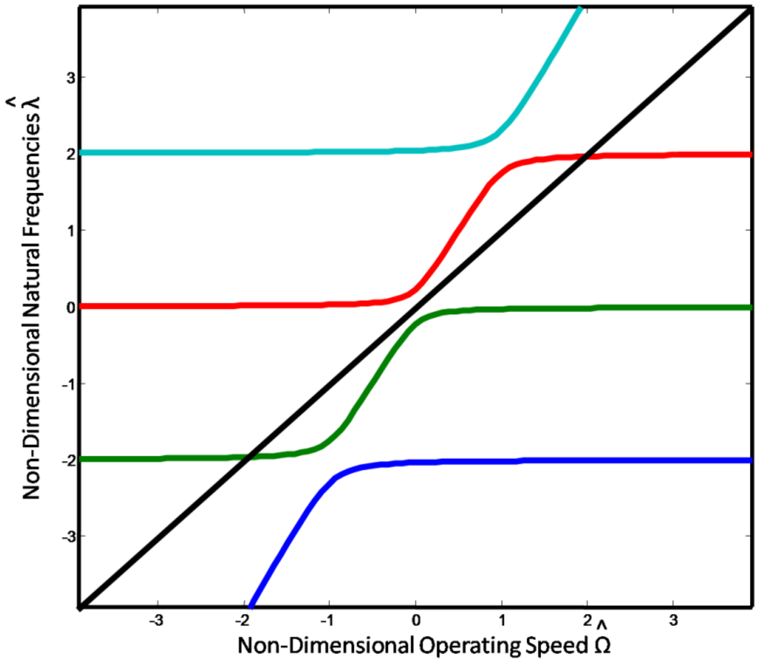

Figure 3-2: Natural frequencies of the Stodola rotor vs. operating speed. The operating speed Ω and natural frequencies λ are normalized by $\sqrt{3EI/mL^3}$. This particular plot is for a rotor whose non-dimensional "disk parameter" $d = 3J/mL^2$ is 18.75, the value for the final design of the device in this research.

The diagonal line in Figure 3-2 is a line of $\lambda = \Omega$. Where the diagonal line intersects one of the four curves corresponding to the natural frequencies, the natural frequency and operating frequency are equal at that operating speed. These speeds are called critical speeds Ω_{crit}, and when the operating speed approaches the critical speed, large deflections in the four degrees of freedom are likely due to the resonance between operating and natural frequencies. For that reason, the critical speeds should be avoided when practical. For this device, the critical speeds are on the order of hundreds of thousands to millions of revolutions per minute, so staying well below the lowest critical speed (or within the "subcritical" regime) is possible. In order to avoid the resonance effects, the device built for this study should stay well below the critical speed. Operation will be constrained to below 80% of the critical speed, to provide a margin of safety.

3.3.3 Forced Response

The critical speed can be found without considering the imbalance. However, in order to know what the deflections of the structure under steady state operation are, the forced response must be considered. With no external forces, the equations of motion are homogenous, as shown in equation (3.29). In other words, besides any transient response associated with the natural modes of the system, the steady state response would be zero. Put another way, without any forcing functions, there would be no deflections. In the real situation, there are forcing functions arising from the imbalance of the rotor. These functions, which were neglected in section 3.3.2, must be reintroduced to get a notion of the steady state behavior of the rotor.

3.3.3.1 Solution

The equations of motion with all the required terms included for the steady state forced response excited by imbalance are:

$$\left\{\begin{aligned}
& m\ddot{R}_X + ma_z\ddot{\beta}_Y = -m\dot{\phi}^2(a_x c\phi - a_y s\phi) - m\ddot{\phi}(a_x s\phi + a_y s\phi) - EI\left[\frac{6\beta_Y}{L^2} - \frac{12R_X}{L^3}\right] && \textbf{(3.43)} \\
& m\ddot{R}_Y - ma_z\ddot{\beta}_X = -m\dot{\phi}^2(a_x s\phi + a_y c\phi) + m\ddot{\phi}(a_x c\phi - a_y s\phi) - EI\left[\frac{6\beta_X}{L^2} + \frac{12R_Y}{L^3}\right] && \textbf{(3.44)} \\
& (J + ma_z^2)\ddot{\beta}_X - ma_z\ddot{R}_Y \\
& \qquad = -\ddot{\phi}\left[(J_{xz}c\phi - J_{yz}s\phi) - ma_z(a_x c\phi - a_y s\phi)\right] - J_{zz}\dot{\phi}\dot{\beta}_Y && \textbf{(3.45)} \\
& \qquad + \dot{\phi}^2\left[(J_{xz}s\phi + J_{yz}c\phi) - ma_z(a_x s\phi + a_y c\phi)\right] - EI\left[\frac{4\beta_X}{L} + \frac{6R_Y}{L^2}\right] \\
& (J + ma_z^2)\ddot{\beta}_Y + ma_z\ddot{R}_X \\
& \qquad = -\ddot{\phi}\left[(J_{xz}s\phi + J_{yz}c\phi) - ma_z(a_x s\phi + a_y c\phi)\right] + J_{zz}\dot{\phi}\dot{\beta}_X && \textbf{(3.46)} \\
& \qquad - \dot{\phi}^2\left[(J_{xz}c\phi - J_{yz}s\phi) - ma_z(a_x c\phi - a_y s\phi)\right] - EI\left[\frac{4\beta_Y}{L} - \frac{6R_X}{L^2}\right]
\end{aligned}\right.$$

We are interested in the steady state case, where the rotor is spinning at a constant rate:

$$\dot{\phi} = \Omega \tag{3.47}$$

Which means that

$$\ddot{\phi} = 0 \tag{3.48}$$

Furthermore, if ϕ is assigned the value zero at the initial time $t = 0$, then:

$$\phi = \Omega t \qquad \textbf{(3.49)}$$

Making these substitutions and considering the equations in matrix form gives:

$$\begin{bmatrix} m & 0 & 0 & ma_z \\ 0 & m & ma_z & 0 \\ 0 & -ma_z & J + ma_z^2 & 0 \\ ma_z & 0 & 0 & J + ma_Z^2 \end{bmatrix} \begin{bmatrix} \ddot{R}_X \\ \ddot{R}_Y \\ \ddot{\beta}_X \\ \ddot{\beta}_Y \end{bmatrix} + \Omega J_{zz} \begin{bmatrix} 0 & 0 & 0 & 0 \\ 0 & 0 & 0 & 0 \\ 0 & 0 & 0 & 1 \\ 0 & 0 & -1 & 0 \end{bmatrix} \begin{bmatrix} \dot{R}_X \\ \dot{R}_Y \\ \dot{\beta}_X \\ \dot{\beta}_Y \end{bmatrix}$$

$$+ \frac{EI}{L^3} \begin{bmatrix} 12 & 0 & 0 & -6L \\ 0 & 12 & 6L & 0 \\ 0 & 6L & 4L^2 & 0 \\ -6L & 0 & 0 & 4L^2 \end{bmatrix} \begin{bmatrix} R_X \\ R_Y \\ \beta_X \\ \beta_Y \end{bmatrix} \qquad \textbf{(3.50)}$$

$$= \Omega^2 \begin{bmatrix} -ma_x \\ -ma_y \\ J_{yz} - ma_y a_z \\ -J_{xz} + ma_y a_z \end{bmatrix} \cos(\Omega t) + \Omega^2 \begin{bmatrix} ma_y \\ -ma_x \\ J_{xz} - ma_x a_z \\ J_{yz} - ma_y a_z \end{bmatrix} \sin(\Omega t)$$

The matrices are assigned names:

$$[M_4] \begin{bmatrix} \ddot{R}_X \\ \ddot{R}_Y \\ \ddot{\beta}_X \\ \ddot{\beta}_Y \end{bmatrix} + [C_4] \begin{bmatrix} \dot{R}_X \\ \dot{R}_Y \\ \dot{\beta}_X \\ \dot{\beta}_Y \end{bmatrix} + [K_4] \begin{bmatrix} R_X \\ R_Y \\ \beta_X \\ \beta_Y \end{bmatrix} \qquad \textbf{(3.51)}$$

$$= \Omega^2 \begin{bmatrix} -ma_x \\ -ma_y \\ J_{yz} - ma_y a_z \\ -J_{xz} + ma_y a_z \end{bmatrix} \cos(\Omega t) + \Omega^2 \begin{bmatrix} ma_y \\ -ma_x \\ J_{xz} - ma_x a_z \\ J_{yz} - ma_y a_z \end{bmatrix} \sin(\Omega t)$$

as are the vectors:

$$[M_4][\ddot{RB}] + [C_4][\dot{RB}] + [K_4][RB] = \Omega^2 [CS]\cos(\Omega t) + \Omega^2 [SN]\sin(\Omega t) \qquad \textbf{(3.52)}$$

where the subscript “4” indicates that these are the matrices for the set of four equations. The solution to such a non-homogenous second order system must be of the same periodicity:

$$\begin{bmatrix} R_X \\ R_Y \\ \beta_X \\ \beta_Y \end{bmatrix} = \begin{bmatrix} A_1 \\ A_2 \\ A_3 \\ A_4 \end{bmatrix} \cos(\Omega t) + \begin{bmatrix} B_1 \\ B_2 \\ B_3 \\ B_4 \end{bmatrix} \sin(\Omega t) = [A]\cos(\Omega t) + [B]\sin(\Omega t) \tag{3.53}$$

The temporal derivatives are:

$$[\dot{RB}] = -\Omega[A]\sin(\Omega t) + \Omega[B]\cos(\Omega t) \tag{3.54}$$

and

$$[\ddot{RB}] = -\Omega^2[A]\cos(\Omega t) - \Omega^2[B]\sin(\Omega t) \tag{3.55}$$

Substituting these solutions back into the equation yields:

$$\begin{aligned} -\Omega^2[M_4][A]\cos(\Omega t) - \Omega^2[M_4][B]\sin(\Omega t) - \Omega[C_4][A]\sin(\Omega t) \\ + \Omega[C_4][B]\cos(\Omega t) + [K_4][A]\cos(\Omega t) + [K_4][B]\sin(\Omega t) \\ = \Omega^2[CS]\cos(\Omega t) + \Omega^2[SN]\sin(\Omega t) \end{aligned} \tag{3.56}$$

Grouping the sine and cosine terms gives:

$$\Omega^2[M_4][A] - \Omega[C_4][B] - [K_4][A] = \Omega^2[CS] \tag{3.57}$$

$$\Omega^2[M_4][B] + \Omega[C_4][A] - [K_4][B] = \Omega^2[SN] \tag{3.58}$$

These two sets of four equations can be combined into a single set of eight equations in all eight A's and B's:

$$\Omega^2 \begin{bmatrix} [M_4] & [0] \\ [0] & [M_4] \end{bmatrix} \begin{bmatrix} [A] \\ [B] \end{bmatrix} + \Omega \begin{bmatrix} [0] & -[C_4] \\ [C_4] & [0] \end{bmatrix} \begin{bmatrix} [A] \\ [B] \end{bmatrix} - \begin{bmatrix} [K_4] & [0] \\ [0] & [K_4] \end{bmatrix} \begin{bmatrix} [A] \\ [B] \end{bmatrix} = \begin{bmatrix} [CS] \\ [SN] \end{bmatrix} \tag{3.59}$$

The terms on in the right hand side contain only the known mass and operating speed of the rotor, as well as the offset of the center of mass from the axle and the products of inertia, computed from equations (7.34) through (7.36) for an angular misalignment. The terms in the matrices are also known. Therefore this set of eight algebraic equations can be solved, giving the values of the A's and B's, which when substituted back into equation (3.53) form the exact description of the rotor's movement at a given operating speed.

The motion of the rotor under a given operating speed also provides the basis for several design constraints based on the deflections caused by the imbalance. Each of these constraints describes a speed above which the deflections and stresses caused by them approach unacceptable levels. The lateral displacement of the beam tip and the angular displacement of the rotor disk are not allowed to exceed 10% of L or 5°, respectively, to avoid violating the small angle assumptions of the model. The stress in the beam must also be kept below the CNT fracture strength. Additionally, the rotor will not be allowed to crash into the substrate during operation. Finally the van der Waals attraction between the tubes must be able to supply the centripetal force required to keep the rotor on its circular path. All these constraints can be assessed based on the results of the forced response analysis.

3.3.3.2 Dynamic Lateral Deflection Constraint

Just as a limiting constraint on the tip deflection of the nanotube beam-axle is defined under static conditions, the deflections the nanotube experiences due to dynamic conditions are also constrained. The position of the beam tip in the inertial frame is described by the vector of lateral displacements:

$$\vec{R} = \begin{bmatrix} R_X \\ R_Y \\ 0 \end{bmatrix} \tag{3.60}$$

The magnitude of the deflection is simply the magnitude of the vector:

$$\delta_{\text{dynamic}} = \sqrt{R_X^2 + R_Y^2} \tag{3.61}$$

The components R_X and R_Y are known for a given operating speed from the computed forced response in equation (3.53):

$$R_X = A_1 \cos(\Omega t) + B_1 \sin(\Omega t) \tag{3.62}$$

$$R_Y = A_2 \cos(\Omega t) + B_2 \sin(\Omega t) \tag{3.63}$$

Because of the axial symmetry of the problem, the x- and y-deflections behave exactly the same way, except 90° out of phase. The result is that the constant magnitudes of these deflections always satisfy the following equations:

$$R_X(t) = R_Y\left(t + \frac{\pi}{2\Omega}\right) \tag{3.64}$$

$$A_1 \cos(\Omega t) + B_1 \sin(\Omega t) = A_2 \cos\left(\Omega t + \frac{\pi}{2}\right) + B_2 \sin\left(\Omega t + \frac{\pi}{2}\right) \tag{3.65}$$

$$A_1\cos(\Omega t) + B_1\sin(\Omega t) = -A_2\sin(\Omega t) + B_2\cos(\Omega t) \tag{3.66}$$

Equating the sine and cosine terms yields:

$$A_1 = B_2 \tag{3.67}$$

$$A_2 = -B_1 \tag{3.68}$$

which will lead to a compact expression for the tip deflection:

$$\delta_{\text{dynamic}} = \sqrt{R_X^2 + R_Y^2} \tag{3.69}$$

$$\delta_{\text{dynamic}} = \sqrt{[A_1\cos(\Omega t) + B_1\sin(\Omega t)]^2 + [-B_1\cos(\Omega t) + A_1\sin(\Omega t)]^2} \tag{3.70}$$

$$\delta_{\text{dynamic}} = \sqrt{A_1^2\cos^2(\Omega t) + B_1^2\sin^2(\Omega t) + B_1^2\cos^2(\Omega t) + A_1^2\sin^2(\Omega t)} \tag{3.71}$$

$$\delta_{\text{dynamic}} = \sqrt{A_1^2 + B_1^2} \tag{3.72}$$

Where A_1 and B_1 are found by solving equation (3.59). The magnitude of this deflection was held under 10% of the nanotube shaft length L, the same limit set for the deflection under static conditions.

3.3.3.3 Dynamic Angular Deflection Constraint

The angular deflections excited by the rotor imbalance must also meet a similar imposed constraint. Like the lateral deflections, the angular deflections β_X and β_Y are equal in magnitude and 90° out of phase. Therefore the angle of deflection at any given time can be found from

$$\beta_{\text{dynamic}} = \sqrt{\beta_X^2 + \beta_Y^2} \tag{3.73}$$

As before, the known relationship between the two makes the expression for the overall angular deflection come out to be compact. Beginning with the forced-response solution describing the instantaneous values of the angles:

$$\beta_X = A_3 \cos(\Omega t) + B_3 \sin(\Omega t) \tag{3.74}$$

$$\beta_Y = A_4 \cos(\Omega t) + B_4 \sin(\Omega t) \tag{3.75}$$

The phase relationship is:

$$\beta_X(t) = \beta_Y\left(t - \frac{\pi}{2\Omega}\right) \tag{3.76}$$

$$A_3 \cos(\Omega t) + B_3 \sin(\Omega t) = A_4 \cos\left(\Omega t - \frac{\pi}{2}\right) + B_4 \sin\left(\Omega t - \frac{\pi}{2}\right) \tag{3.77}$$

$$A_3 \cos(\Omega t) + B_3 \sin(\Omega t) = A_4 \sin(\Omega t) - B_4 \cos(\Omega t) \tag{3.78}$$

Equating the sine and cosine terms yields:

$$A_3 = -B_4 \tag{3.79}$$

$$A_4 = B_3 \tag{3.80}$$

The overall angular deflection is thus

$$\beta_{\text{dynamic}} = \sqrt{[A_3 \cos(\Omega t) + B_3 \sin(\Omega t)]^2 + [A_4 \cos(\Omega t) + B_4 \sin(\Omega t)]^2} \tag{3.81}$$

$$\beta_{\text{dynamic}} = \sqrt{[A_3 \cos(\Omega t) + B_3 \sin(\Omega t)]^2 + [A_3 \cos(\Omega t) - B_3 \sin(\Omega t)]^2} \tag{3.82}$$

$$\beta_{\text{dynamic}} = \sqrt{A_3^2 \cos^2(\Omega t) + B_3^2 \sin^2(\Omega t) + A_3^2 \cos^2(\Omega t) + B_3^2 \sin^2(\Omega t)} \tag{3.83}$$

$$\beta_{\text{dynamic}} = \sqrt{A_3^2 + B_3^2} \tag{3.84}$$

Where A_3 and B_3 are found by solving equation (3.59).The magnitude of this deflection was held under five degrees.

3.3.3.4 Dynamic Beam Stress Constraint

Just as the static beam deflection of the nanotube causes stresses within the nanotube, so do dynamic deflections. A good starting point for determining the stress is to find the reaction forces and moments applied by the nanotube beam onto the rotor. (The forces and moments acting on the beam to generate the stresses are of equal magnitude and opposite sense.) The expression for these forces and moments has already been found during the process of determining the equations of motion. Consider first bending in the yz-plane. The potential energy stored in the beam was found in equation (7.72):

$$PE_{\text{elastic},\, y} = EI\left[\frac{2\beta_X^2}{L} + \frac{6R_Y\beta_X}{L^2} + \frac{6R_Y^2}{L^3}\right] \tag{3.85}$$

The forces and moments can be calculated simply by taking the derivatives of the elastic potential energy with respect to the deflections (this concept is known as Castigliano's Theorem). These derivatives were taken as a part of the Lagrangian process to obtain the equations of motion (described in Appendix 7.2) in equation (7.106) and equation (7.155):

$$F_y = \frac{\partial}{\partial R_Y}\left(PE_{\text{elastic},\, y}\right) = EI\left[\frac{6\beta_X}{L^2} + \frac{12R_Y}{L^3}\right] \tag{3.86}$$

$$\frac{\partial}{\partial \beta_X}\left(PE_{\text{elastic},\, y}\right) = \frac{\partial}{\partial \beta_X}\left(EI_{xx}\left[\frac{2\beta_X^2}{L} + \frac{6R_Y\beta_X}{L^2} + \frac{6R_Y^2}{L^3}\right]\right) = EI_{xx}\left[\frac{4\beta_X}{L} + \frac{6R_Y}{L^2}\right] \tag{3.87}$$

Now the forces and moments applied at the beam tip are known. The maximum axial stresses, which are proportional to the internal moment, are always at the root for a tip-loaded cantilever beam. The internal moment at the root must counteract the tip moment and the lateral force times the lever arm of the nanotube length:

$$(M_x)_{z=0} = |(M_x)_{z=L}| + \left|\left(F_y\right)_{z=L} L\right| \tag{3.88}$$

The stress is found from the internal moment in the same way as for the static case:

$$\sigma_{\text{dynamic}} = \sigma_{zz} = -\frac{\left[|(M_x)_{z=L}| + \left|\left(F_y\right)_{z=L} L\right|\right] y}{I_{xx}} \tag{3.89}$$

The worst stress clearly occur for maximum and minimum values of y, corresponding to positive and negative values of the tube outer radius. Therefore the maximum stress in the entire nanotube due to a transverse load equal to the weight of the rotor applied at the tip of the shaft is

$$\sigma_{\text{dynamic}} = \sigma_{zz} = \frac{\left[\left|(M_x)_{z=L}\right| + \left|(F_y)_{z=L} L\right|\right] r_o}{I} \tag{3.90}$$

Note that the negative sign has been dropped, because both positive and negative (tensile and compressive) stresses are present on opposite sides of the tube. Also, the “xx” subscript was dropped from the second moment of area, because the tube is completely axisymmetric and the same stress relation holds regardless of the orientation of the bending plane, so long as it contains the z-axis.

In order for the device to survive at a given speed, this stress was constrained to below 10 GPa, the same limit chosen for the static case.

3.3.3.5 Substrate Clearance Constraint

Another important condition that operation of the rotor must meet is clearance of the substrate at all times. In other words, the rim of the disk cannot crash into the substrate as the rotor tilts about the x- and y-axes. Two separate effects contribute to the lack of clearance. The first is the dynamic angular deflections induced by the imbalance of the rotor. This was computed in section 3.3.3.3. The other contribution is the misalignment of the disk to the nanotube shaft during construction. This is the original reason that the products of inertia are non-zero, and hence angular deflections are excited. However, in this case, it also directly contributes to reducing the ground clearance.

The dynamic angular deflections are periodic, following the rotor around at its operational speed. The worst case is when the dynamic deflections tilt the rotor in the same direction as the static misalignment. In this case, the angles add:

$$\beta_{\text{worst}} = \beta_{\text{dynamic}} + \alpha \tag{3.91}$$

where α is the static misalignment. From geometry, the smallest clearance between rotor and substrate is

$$h = L - \frac{D}{2}\sin(\beta_{\text{worst}}) \tag{3.92}$$

For a device to be considered acceptable, it was deemed that the clearance should exceed 10% of the nanotube shaft length L. Note that it is possible for α alone to cause an unacceptably low clearance. In such a case, the constraint does not provide a limiting speed above which the clearance limit is violated, but instead, rules out operation at any speed. In this way the substrate clearance constraint can behave like a static constraint, ruling out certain designs altogether.

3.3.3.6 Beam Telescoping Constraint

There is an additional constraint which concerns a completely different failure mechanism of the device. In the ideal CNT bearing, the outer tubes are completely free from bonds to the inner tubes on which they rotate. If the bearing were subjected to axial tension, the outer tubes might slide off the end of the inner tubes, in a telescoping motion. The only forces holding the two parts together would be the van der Waals interaction and the friction between them.

The van der Waals interaction was discussed in section 2.2, where it was contrasted with the friction force between the layers. As discussed there, the friction force is neither well understood nor well quantified. Therefore, it cannot be relied on to hold the two parts of the bearing together, leaving only the van der Waals interaction. Because of the lack of bonds, this interaction cannot support as much tension as a solid, connected nanotube layer. It is therefore important to ensure that the device will not fail due to bearing telescoping before the tube strength limits are reached.

Fortunately, the only expected tensile load to which the tube is subjected during operation is a small component of the centripetal force required to hold the rotor in its circular path. The radius of the circle travelled by the center of mass of the rotor is at most the sum of the beam tip deflection magnitude (computed in section 3.3.3.2) and the magnitude of the imbalance (distance between the center of mass and the beam tip):

$$r_{\mathrm{CM}} = \delta_{\mathrm{dynamic}} + |\vec{a}| = \sqrt{A_1^2 + B_1^2} + \sqrt{a_x^2 + a_y^2} \tag{3.93}$$

The centrifugal force is then simply:

$$F_{\mathrm{cent}} = m\Omega^2 r_{\mathrm{CM}} \tag{3.94}$$

The van der Waals attractive spring force is taken from the literature [28]. The potential energy associated with the van der Waals force is:

$$PE_{\mathrm{vdW}} = C_{\mathrm{vdW}}\pi d_c l \tag{3.95}$$

where d_c is the diameter of the interface between inner and outer tubes, l is the length of the contact, and C_{vdW} is a constant with a value of -0.16 J/m^2. The force associated with this potential is then:

$$F_{\mathrm{vdW}} = -\frac{\partial PE_{\mathrm{vdW}}}{\partial l} = C_{\mathrm{vdW}}\,\pi d_c \tag{3.96}$$

Realistically, only the component of the centrifugal force aligned with the tube axis at the tip, that is, the product of the centrifugal force with the sine of the angle made between the tube and the plane of motion of the center of mass, would need to be resisted by the van der Waals force. In order to have a conservative constraint, the device was required to have sufficient van der Waals force to overcome the centrifugal force component multiplied by the sine of the maximum possible angle, described in equation (3.84).

3.3.4 Rotor Material Fracture Constraint

Another dynamic constraint is unrelated to the beam bending dynamics of the nanotube shaft. The rotor disk is subjected to centrifugal stress from the rotation of its own mass. The centrifugal stress in a thin rotating disk is:

$$\sigma_{\text{cent}} = \frac{\Omega^2 R^2 \rho (3+\nu)}{4} \tag{3.97}$$

Where Ω is the operating speed, r_o is the outer radius of the disk, ρ is the material density, and ν is the material Poisson's ratio. In order to ensure that the rotor, which is made of silicon, would not fracture, this stress was kept below 800 MPa, or half the fracture strength of silicon.

3.4 Optimal Device Design

The constraints define limits within which the device design must lie. That leaves a large space in which the three free design parameters (rotor diameter D, rotor thickness t, nanotube shaft length L) can be varied, producing many designs. In order to pick the best design it is necessary to choose a performance parameter that expresses the "goodness" of a given design. Then the best design can be chosen as the maximum of the performance parameters within the design space bounded by the constraints. Figure 3-3 shows how the constraints restrict the choice of the diameter and shaft length, with a rotor thickness chosen to be 2 µm.

Since the long term goal of the project is to measure friction of carbon nanotubes, a design that allows accurate measurement of friction is desired. The easiest way to measure the friction would be to allow the rotor to spin down from a constant speed, and record speed vs. time data, as discussed in section 1.4.1. In this case, better accuracy can be obtained with a device that takes longer to coast to a stop. Therefore a device with a long coast down time should be selected.

To compute the expected coast down time, the expected friction must be estimated. As discussed in section 2.2, the friction is not well quantified, and its dependence on speed is not well established. In order to account for the uncertainty, the worst (highest) value of friction from literature on experimental studies of CNT friction [3] was used, and it was assumed to be independent of speed. Friction was quoted there as a force per contact area, or in other words a stress. The torque caused on the rotor by friction is then:

$$\tau_{\text{fric}} = \sigma_{\text{fric}} \pi d_c L \left(\frac{d_c}{2}\right) \tag{3.98}$$

Taking equation (7.260)

$$\begin{aligned} \ddot{\phi}\left[J_{zz} + m\left(a_x^2 + a_y^2\right)\right] + m\left(\ddot{R}_Y - a_z \ddot{\beta}_X\right)\left(a_x c\phi - a_y s\phi\right) \\ - m\left(\ddot{R}_X - a_z \ddot{\beta}_Y\right)\left(a_x s\phi + a_y c\phi\right) + \ddot{\beta}_Y\left[J_{xz} s\phi + J_{yz} c\phi\right] \\ + \ddot{\beta}_X\left[J_{xz} c\phi - J_{yz} s\phi\right] = 0 \end{aligned} \tag{3.99}$$

and neglecting the coupling terms, but adding in the dissipative friction term gives:

$$\ddot{\phi}[J_{zz} + m(a_x^2 + a_y^2)] = -\tau_{\text{fric}} = -\sigma_{\text{fric}}\pi d_c L\left(\frac{d_c}{2}\right) \tag{3.100}$$

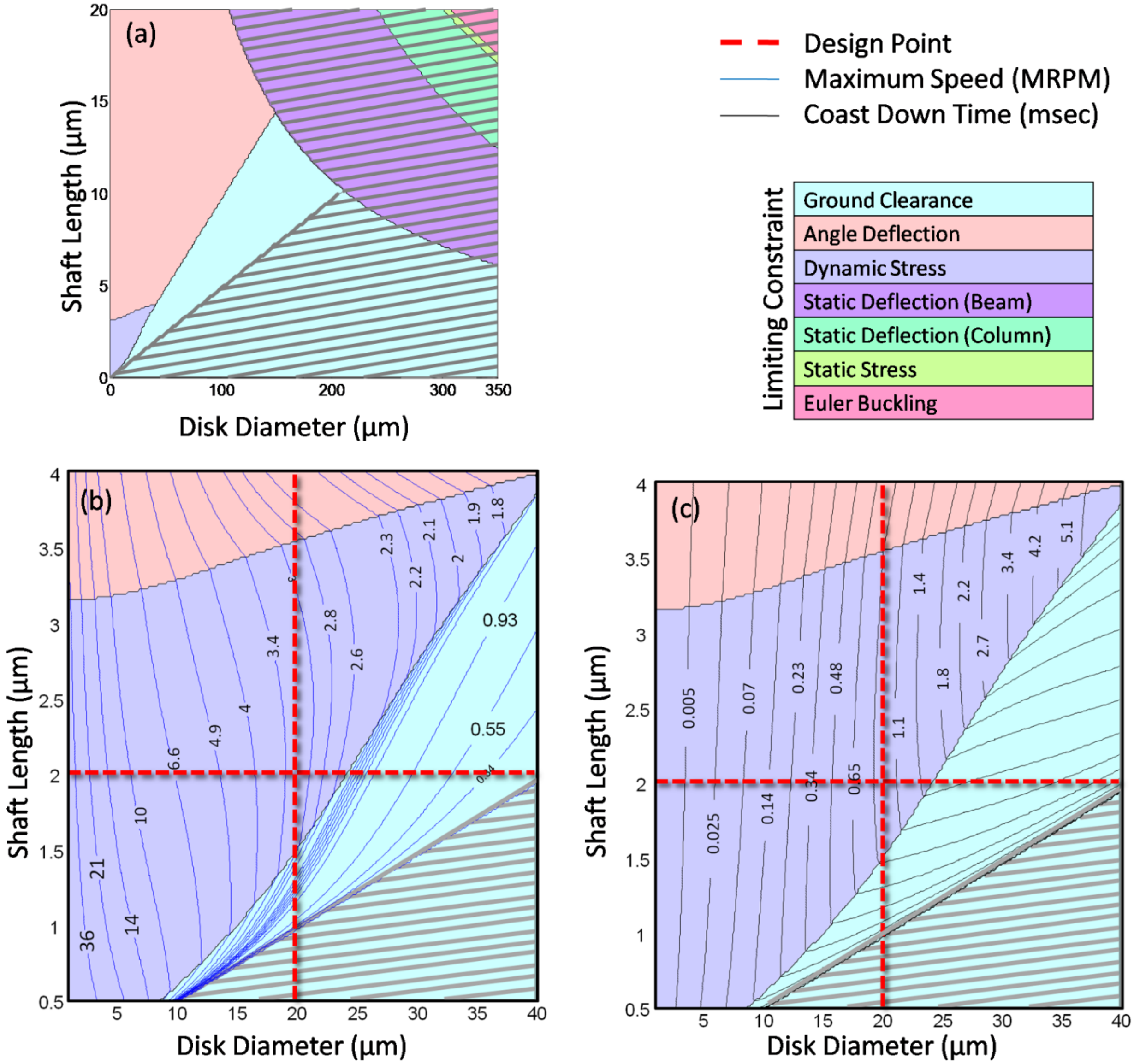

Figure 3-3: The device design space. The color codes indicate which constraint is the limit at each point. The thick grey bars indicate regions that fail to meet the constraints even at zero speed. (a) A large design space showing where the static constraints come into play. In practice, it would be difficult to construct devices at the larger edges of the space. Furthermore, the optimally performing devices are located towards the bottom left. (b) A close up of the region of interest, where fabrication is more realistic. The blue contours show the maximum acceptable rotational speed (in millions of revolutions per minute) at each location. (c) The same region, with black contours indicating coast down time (in milliseconds).

Integrating once, and noting the initial condition:

$$\left(\dot{\phi}\right)_{t=0} = \Omega \tag{3.101}$$

Yields:

$$\left[J_{zz} + m\left(a_x^2 + a_y^2\right)\right]\left[\dot{\phi}(t) - \Omega\right] = -\sigma_{\text{fric}}\pi d_c L\left(\frac{d_c}{2}\right)t \tag{3.102}$$

Therefore the coast down time, which is the time it takes for $\dot{\phi}$ to reach zero, is:

$$t_{\text{coast}} = \frac{\left[J_{zz} + m\left(a_x^2 + a_y^2\right)\right]\Omega}{-\sigma_{\text{fric}}\pi d_c L\left(\frac{d_c}{2}\right)} \tag{3.103}$$

As shown in Figure 3-3c, the coast down time essentially increases with disk diameter, provided that the design lies outside of the region where the ground clearance is the limiting constraint. Therefore the diameter should be maximized. A larger diameter also eases the actuation requirements, by requiring less force on the disk edge to get the same level of force.

While an essentially arbitrarily large diameter is possible to fabricate, other concerns restrict the diameter. In order to maintain a ten to one ratio between the disk diameter and thickness (to keep the rotor essentially rigid relative to the nanotube shaft), the thickness must be increased with the diameter. The thickness is set by the deposition time for the rotor layer, so thicker rotors could take inconveniently long to fabricate. For example, a 2 µm layer takes an entire day to deposit. Additionally, the length of the nanotube must be increased in order to avoid the ground clearance limited region, in which sudden failure is possible due to rotor crashes, and in which the coast down time quickly drops because the initial speed must be dropped to avoid crashes. While CNTs can be fabricated as long as 20 µm, tubes this long tend to be rife with defects, based on TEM observations made for this research. As discussed in section 2.1.2, defects are expected to be highly detrimental to friction performance. A shorter tube length of 4 µm (2µm shaft length + 2µm on which to attach the 2µm rotor) could have much better crystalline quality, producing a superior device. A tube of this length restricts the diameter to about 20 µm.

Based on these reasons, the parameters chosen for the initial device design were a 20 µm diameter, 2 µm thick rotor on a 2 µm long shaft (4 µm total CNT length). The point corresponding to this parameter set lies in the center of Figure 3-3b,c. This design should be capable of attaining a maximum speed of 3.2 MRPM, and 1 ms coast-down time. (Note that while 1 ms coast down time may be difficult to measure, it is based on the worst case experimental friction, and could be longer for lower friction. Even so, the choice of parameters is still the optimum, regardless of the actual performance achieved by that optimum.) The design is feasible and manufacturable, while providing optimal coast down time for optimal friction measurement, within the limits of fabrication capability, and avoiding failure in one of the thirteen failure modes addressed.

4 EXPERIMENTAL APPROACH

Having determined the optimal geometry for the device, construction was pursued. Fabrication and testing of micro- and nano-systems can be challenging. Typically, MEMS devices are constructed in a cleanroom, using techniques inherited from the integrated circuit industry. Although a wide range of techniques for making shapes and features small enough to make up a micro- or nano-system exist, these techniques can work together or interfere with each other in ways that can be difficult to predict. The fabrication of the device for this research, like most other MEMS devices, posed significant challenges. First, knowledge about the compatibility of CNTs with traditional MEMS fabrication techniques is somewhat limited, so these processes required testing on the CNTs to try to find any problems that had not previously been observed. Second, the interactions between the separate steps caused unforeseen problems that did not appear for the steps individually. Finally, in order to test the device, a method of applying torque to an object roughly 1/20 the diameter of a human hair while observing the motion needed to be developed. Together, these challenges made fabrication and testing of the experiment quite difficult.

4.1 A Fundamental Orientation Change

While two prior works have used CNTs as bearings for rotating MEMS devices [2, 3], there is a significant difference between those efforts and the present work: those devices were built on a nanotube oriented horizontally (with respect to the plane of the substrate), while this work uses a vertically oriented nanotube. This change in orientation of the device profoundly affects many aspects of device fabrication, since different techniques are required to produce the components that make up the device. Most notably, CVD is required to make the nanotubes, instead of the arc-discharge method used previously. The choice to use a vertically aligned nanotube was based on the substantial advantages afforded by the vertical orientation, but as with any choice, there are disadvantages.

4.1.1 Advantages of the Orientation Change

The most significant advantage afforded by a vertically aligned tube is the impact it has on the lithographic processes. MEMS fabrication techniques rely on three basic processes: deposition, etching, and lithography. When material is added to a device, a (generally uniform) layer of the material is deposited onto a (generally flat) substrate. These deposition methods can therefore only create planar features by themselves. Etching works in the opposite way: material is removed either by chemical reaction or by physical bombardment with ions, but generally at a uniform rate across the exposed surface. Etching too, therefore, is only capable of making planar features unaided. Lithography is the key process that enables features other than flat layers to be produced, and is hence probably the most important technique in any MEMS fabrication.

Lithography works by using a specific chemical (called resist) which is sensitive to irradiation, typically ultraviolet or electron beam. Resist is deposited on the surface of the device in a (typically uniform thickness) layer. Some such chemicals (positive resists) become soluble in the developer (another chemical) when exposed to radiation, while others (negative resists) become insoluble. If the irradiation is performed through a mask, the pattern on the mask is transferred to the resist, and when the developer is applied the specific parts of the resist exposed (or unexposed, for a negative resist) are dissolved, leaving a two-dimensional pattern.

When combined with etching and deposition, three-dimensional structures are possible. For example, if an etch is applied to an object with resist protecting portions of it, only the exposed portions will be etched. Alternatively, if material is deposited on top of patterned resist, and then the resist is dissolved, the material which had resist under it will be “lifted-off,” leaving a two-dimensional structure made of the material. By composing successive two-dimensional layers, certain three-dimensional structures can be created.

The problem, and the reason a vertically oriented tube is attractive, is that only ***certain*** three-dimensional shapes are possible, not arbitrary shapes. For example, a circular disk in the plane parallel to the substrate is relatively straightforward to produce – a mask with a circle on it is needed. On the other hand, producing a circular disk, or a cylinder, or even a sphere, which is round in any other plane, is next to impossible. The layers that produce dimensions out of the lithographic plane are limited to flat shapes. For a rotating bearing, circular shapes for the rotor and surrounding stationary parts (stator) are obviously desirable.

If the nanotube is oriented vertically, the axis of the bearing is vertical. That means that circular or axisymmetric geometry can be relatively easily created around the bearing axis, simply by using a circular mask. Figure 1-2 shows what kinds of devices are possible with the vertical orientation compared with the horizontal orientation. As described in section 1.2,this capability to produce circular geometry should provide numerous advantages for the current and future rotating devices based on CNT bearings. Axisymmetry should provide superior balance, enabling high speed operation. allowing high speed rotation to be pursued with minimum imbalance excitation. Additionally, exterior devices such as drive or sense electrodes, fluidic components, or optical components can be readily arranged in precise locations and sizes around the rotor. These advantages hold great promise for all kinds of CNT based rotating micro- and nano-devices.

4.1.2 Consequences of the Orientation Change

The requirement for a vertically oriented nanotube in a precise location has serious implications for the choice of method whereby the nanotube is produced. Both of the prior works involved nanotubes produced by arc-discharge methods, which results in loose nanotubes. In order to incorporate these tubes into devices, they must be placed on a substrate, meaning that they generally have a horizontal orientation. While it may be possible to pick up an individual nanotube and move it to a vertical position using manipulators with nano precision, and one could even conceive of attaching it to the substrate with a deposition process, this technique has not been tried, and would likely require substantial development to perfect. Furthermore, it would likely be time consuming, requiring an operator to locate and attach each individual nanotube. Finally, it is far from clear that the tubes could be placed accurately and consistently at right angles to the substrate plane. Since manually manipulating nanotubes into the appropriate position seems so difficult, an alternative method of producing the nanotubes, Catalytic Chemical Vapor Deposition (C-CVD), is required to produce the precisely placed, vertically aligned nanotubes that form the basis of the device.

The precise mechanism whereby CVD works is not completely understood [102]. However, there is a general idea of how the process works. Growth begins with a catalyst, which is usually iron, nickel, or cobalt. When the catalyst is heated (to between 500 and 1000°) in a furnace, it softens. When a hydrocarbon gas, such as methane or acetylene is supplied to the furnace, the gas dissociates and carbon atoms are dissolved into the semi-molten catalyst. As the concentration of carbon within the catalyst increases, it approaches saturation, and carbon precipitates back out. However, when the carbon exits the catalyst, it is bonded in low energy structures such as CNTs.

This technique has been proven highly effective for producing CNTs with a vertical orientation [69-71, 103-107]. The verticality and straightness of the nanotubes can be enhanced by using PECVD instead of plain thermal CVD [69], because besides providing extra energy to encourage dissociation of the hydrocarbon, the plasma also provides a vertical electric field, along which the tubes tend to align themselves during growth. In addition, the location of the nanotubes can be controlled precisely by controlling the location of the catalyst [70, 104, 106, 107], *i.e.* catalyst patterned with lithography results in CNTs grown in the same pattern. Besides controlling the location, the diameter and length of the tubes can be controlled via the diameter of the catalyst and growth time, respectively [104].

However, there is a drawback to the use of CVD as a nanotube growth tool. CVD tubes are usually of much lower crystalline quality than arc-discharge tubes [35], meaning that they have more defects and less graphitization. The primary reason for the low quality is the low temperature used in the growth process, and increased temperature has been shown to improve graphitization [70, 103, 105]. Whereas in the arc-discharge method, high temperatures (3000-4000 °C) provide substantial thermal energy to encourage carbon atoms to diffuse to ideal, low-energy, graphitized locations, the CVD method uses lower temperatures (300-1000°C) and hence produces less diffusion.

The defects may impede rotation, as discussed in section 2.1.2.3. However, with sufficient use of techniques to improve the crystalline quality of the CNTs, like those mentioned in section 2.1.2.4, the challenge of low quality tubes might hopefully be overcome.

4.2 Fabrication

Having decided to use vertically oriented CNTs for the device, the rest of the fabrication process had to be designed to work with these CNTs. First, the individual processes that must be compatible with the CNTs were tested on them to identify potential problems. Some data on MEMS processing techniques applied to CNTs exists, but not enough to cover the range of processes used here completely. Then, each step in the overall fabrication process was isolated and optimized. Finally, the steps were combined to produce the complete device. Unfortunately, there are still some problems in the sequence that prevented a functional device from being produced, but work is ongoing to resolve these issues.

4.2.1 Carbon Nanotube Process Compatibility

Before fabricating the test device, additional data on how CNTs react to MEMS processing was required. Electron microscopy was the primary tool used to observe the effects these processes had on the nanotubes. Three different TEMs of varying capabilities were used, along with one SEM. Three types of C-CVD grown CNTs, depicted in Figure 4-1, were used for these studies. Loose CNTs were obtained from two commercial vendors[2,3] and arrays of vertically aligned tubes on a substrate were also obtained[2]. The loose tubes are easier to observe in a TEM, because they can be simply dispersed on a support grid designed for TEM use. The arrays of tubes, sometimes called “Vertically Aligned Carbon nanotube Forests” (VACNF), are more similar to the isolated vertically aligned tube intended for use in the device, and hence were desirable for use as test specimens.

In order to observe the VACNFs in a TEM, a technique to mount small pieces of the VACNF substrate into the TEM was developed. TEM works by transmitting electrons through the sample, so very thin (a few hundreds of nanometers) samples are required. An entire array of tubes is too thick, so a way to look at a single tube was needed. The substrate was diced into parallelograms with a base of 850 μm and a height of 100 μm, with an interior angle of 30°. The angle helps to reduce the probability of tubes

---

[2] Cheap Tubes Inc., www.cheaptubes.com

[3] NanoLab, www.nano-lab.com

obscuring each other by reducing the density of tubes near the point. Mounting these parallelograms with the nanotubes perpendicular to the electron beam, individual tubes could be precisely identified, and imaged for their entire length, while remaining attached to the substrate and maintaining their orientation.

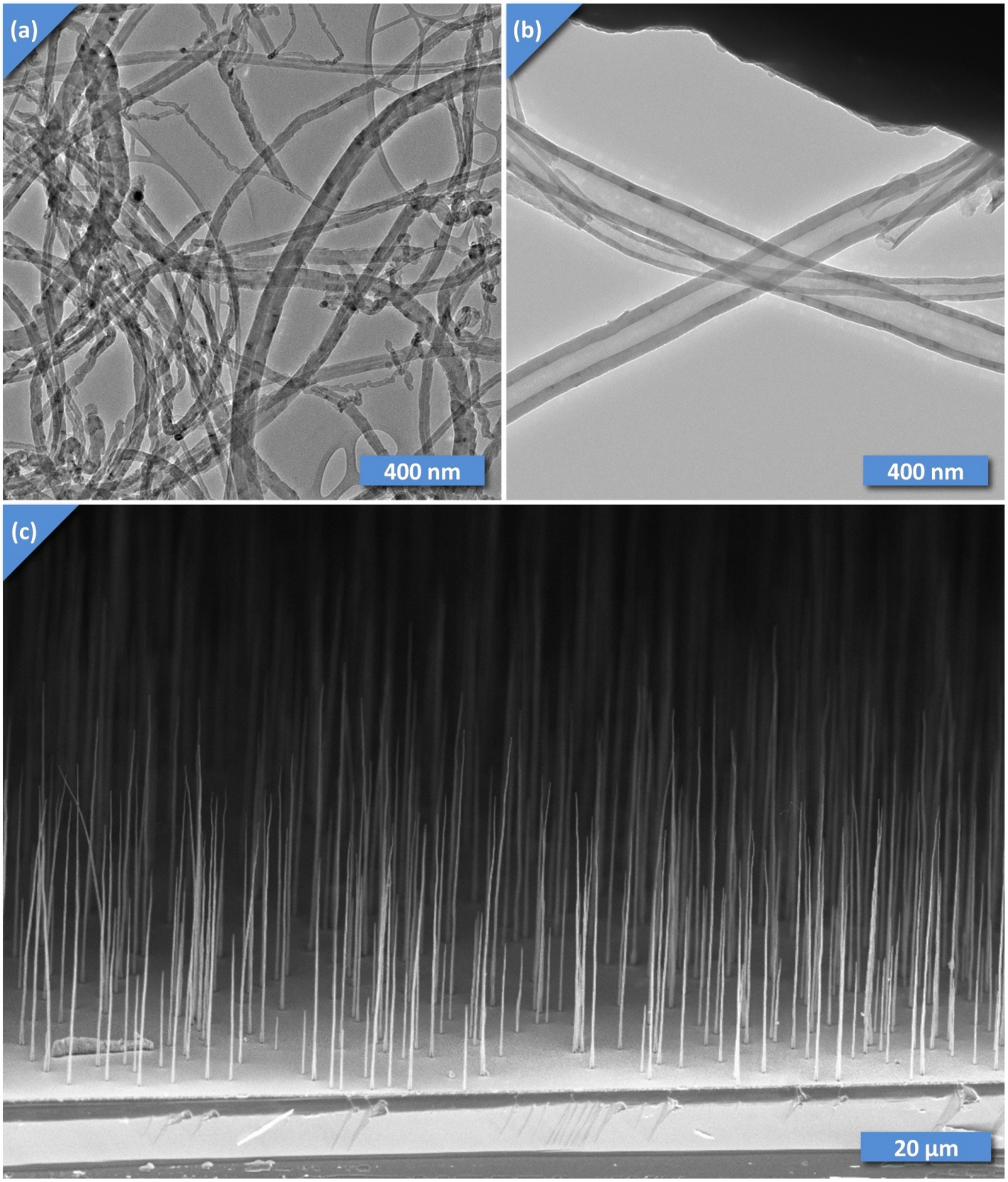

Figure 4-1: Types of nanotubes used for MEMS processing compatibility experiments. (a): Cheap Tubes, Inc. (b) NanoLab Loose tubes. (c) NanoLab vertically aligned carbon nanotube forest.

One of the first processing methods tested on the nanotubes was Silicon Dioxide (SiO_2) deposition. SiO_2 was used as the sacrificial layer to support the rotor during fabrication, so it had to come into direct contact with the nanotube. The oxide used here was deposited by PECVD at a temperature of 380°C. To observe the effects of the deposition, several thicknesses were put down on nanotube samples.

A thick coating (300 nm) applied to the nanotube forest (see Figure 4-2a) reveals that the oxide deposition is highly conformal, and appears to have a very uniform thickness. There were no uncoated or heavily coated patches, indicating that the oxide growth was consistent and repeatable across the entire tube surface area. Observed in SEM, the oxide showed a very smooth surface.

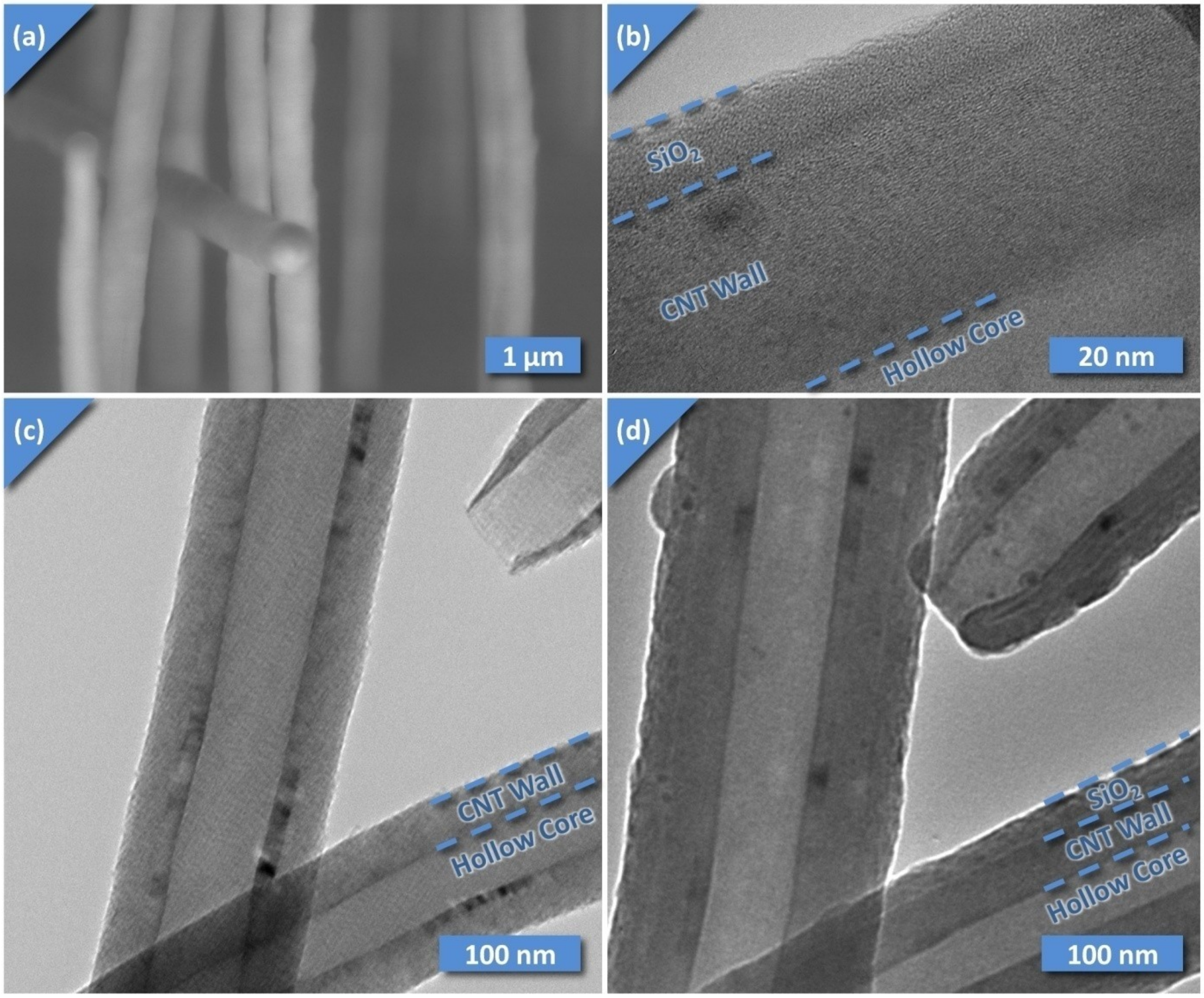

Figure 4-2: Silicon dioxide coatings on carbon nanotubes. (a) A 300 nm coating applied to a VACNF. (b) A 5 nm coating applied to a loose nanotube. Bottom: loose tubes before (c) and after (d) a 20 nm layer was deposited.

The oxide deposition process was also repeated on the loose tubes. When observed in the TEM, the 300 nm oxide coating was too thick to allow transmission of the electrons, preventing viewing of the inner tube structure. Much thinner coatings of 5-25 nm were performed on the loose tubes (Figure 4-2b,c,d). These coatings showed the same uniform thickness, and good adhesion to all surface areas of the tube. (There is one exception – for open ended tubes, the coating was not uniform on the ***inside*** of the tube – the coating only penetrated one or two diameters into the interior, gradually falling off in thickness.) Additionally, observing specific nanotubes before and after the deposition revealed that no damage on the tens of nanometer scale was apparent, since the TEM was able to view through the coating to the interior of the tube.

SiO_2 coating was also applied to the parallelograms, to obtain TEM images of a single isolated tube under the oxide coating. The same uniform adhesion and consistent film thickness were observed as for the loose tubes. In addition, no clear signs of damage to the underlying tube were detected. Although atomic resolution imaging was attempted before and after the deposition, the tubes from the VACNFs used had very high levels of disorder, making identification of atomic scale defects impossible. However, while it is possible that the oxide induced unobservable atomic scale defects in the tube, the fact that no larger scale manifestation of them was produced indicates that the tubes are generally resilient to the deposition process, and should be unharmed, especially in deeper portions away from the surface.

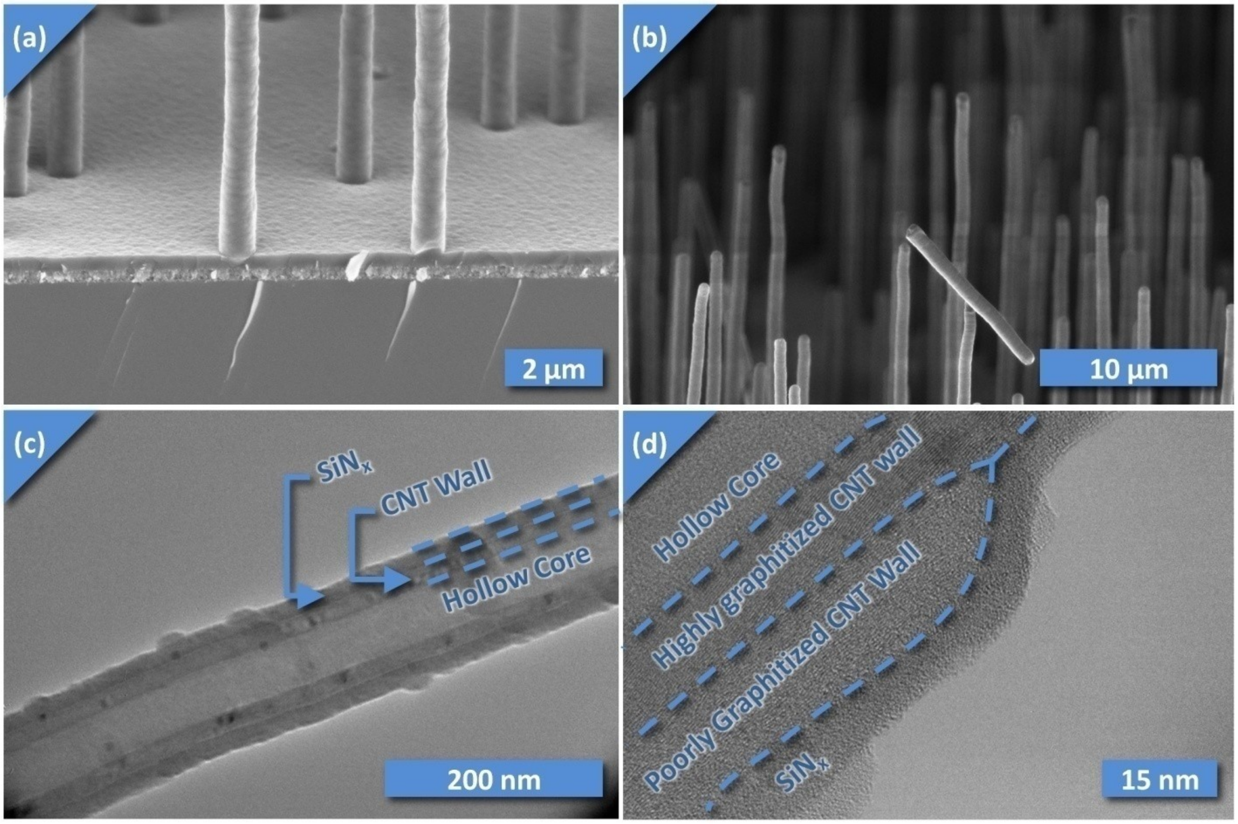

Figure 4-3: Silicon nitride coatings on CNTs. (a) A 300 nm coating applied to a VACNF. (b) The fact that the coating and inner nanotube consistently fail at the distance from the substrate on a particular tube indicates that the adhesion is likely strong. (c) A 20 nm coating applied to a loose tube. (d) High resolution TEM imagery shows how the crystalline nanotube structure differs from the amorphous silicon nitride coating.

In addition to SiO_2, Silicon Nitride (SiN_x) was deposited by a similar PECVD process on loose and substrate-attached tubes. Although nitride is not a part of the specific fabrication process for the present device, knowledge about its interaction with CNTs could prove useful for future AFM based NEMS fabrication efforts.

The nitride showed very similar results to the oxide. Thicker coatings (300 nm) on the VACNFs (Figure 4-3a) showed the same uniform thickness and adhesion. In addition, several broken SiN_x-coated tubes were observed (as in Figure 4-3b), probably broken during sample handling. All of the broken tubes had a break that continued straight through the nitride coating and underlying CNT. That could be an indication that the adhesion between the two is very good. Poor adhesion might result in the outer coating breaking, and then sliding relative to the inner tube before breaking, producing a discontinuous break. Furthermore, the tubes did not seem to break from the substrate surface, but at some distance from it. That could indicate that the bonding between the tubes and the substrate is of similar strength to the bonding within the tubes themselves. Also like the oxide, the nitride continued to be uniform at thinner (5-25 nm) thicknesses. No damage was observable after the nitride deposition (shown in Figure 4-3c,d), further indicating the resilience of the nanotubes to plasma deposition processes.

The loose tubes subjected to PECVD deposition processes did show one anomaly. Dense particles, approximately 5 nm in diameter, appeared at the interface between the tube and the coating. Energy dispersive X-ray Spectroscopy (EDX) was used to identify the particles as copper. Since the TEM support grids on which the loose tubes were processed were made of copper, it is proposed that these small particles are pieces of the grid that were dislodged by the high electric fields present at the beginning of the plasma process. This theory is corroborated by the fact that the particles did not show up after the grids were switched with molybdenum grids, or in the VACNF parallelograms in which there was never copper present.

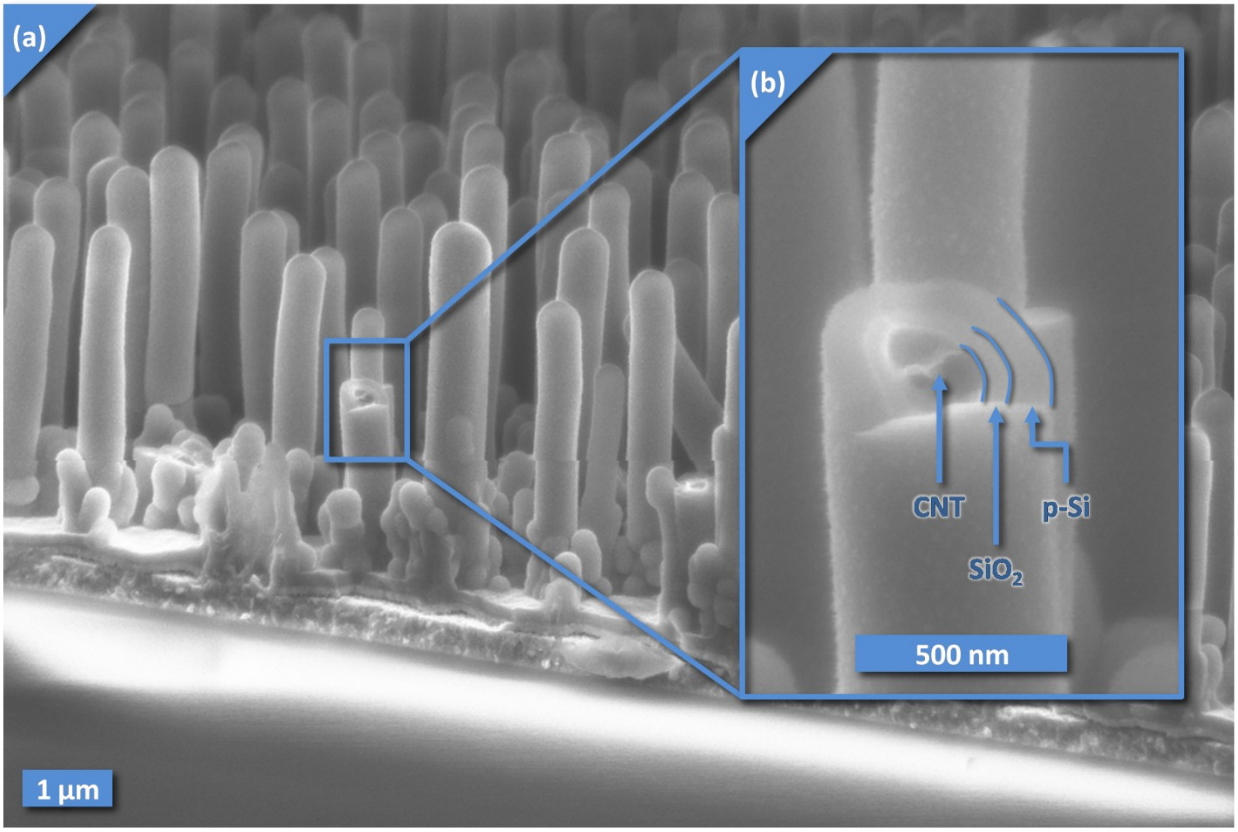

Figure 4-4: Polysilicon and silicon dioxide coatings on a VACNF. The polysilicon shows similar uniformity and adhesion to as the oxide and nitride layers. The two layers can be seen clearly in the inset (b).

Pure silicon posed more of an issue for observation, primarily because of the temperature of deposition. While the PECVD system used for the oxide and nitride (operating at 380°C) is capable of producing amorphous silicon (AFM) layers, this material has extremely high residual stress, and poses substantial fabrication challenges even without CNTs involved. It was decided to us a low-pressure chemical vapor deposition furnace to produce poly-crystalline silicon (p-Si). This process uses a higher temperature (600° C), which is too high for the copper support grids to survive. Since the direct deposition of p-Si onto nanotubes is not a requirement of the device fabrication process, it was decided not to pursue TEM imagery of p-Si samples. SEM was conducted on a sample that was coated with oxide and then silicon (shown in Figure 4-4), as in the device fabrication process. Similar conformality and uniformity to the oxide and nitride was observed.

Photoresist coatings are also not required for fabrication of the device, but they were examined for compatibility, since such knowledge could be useful for future CNT fabrication. Resists are not typically applied by CVD, like inorganic materials such as Silicon and its oxide and nitride. Instead, a large wafer or chip is spun to a high speed (several thousand rpm), and liquid resist is dropped onto it. The centrifugal force produces an even coating on the surface. However, since this technique requires a sample large enough to mount on the spinning chuck, testing was only possible for large pieces of the VACNF samples.

The resist caused problems for the CNTs. After the resist was dissolved in acetone and rinsed with de-ionized water, the sample was observed in SEM (Figure 4-5c). The tubes were all bent over and clustered together. Presumably, as the solvent dried, the surface tension pulled the tubes together, where they stayed due to the van der Waals interactions between each other. This phenomenon, were thin objects bend and stick to each other, is common enough in MEMS to have a name: "stiction."

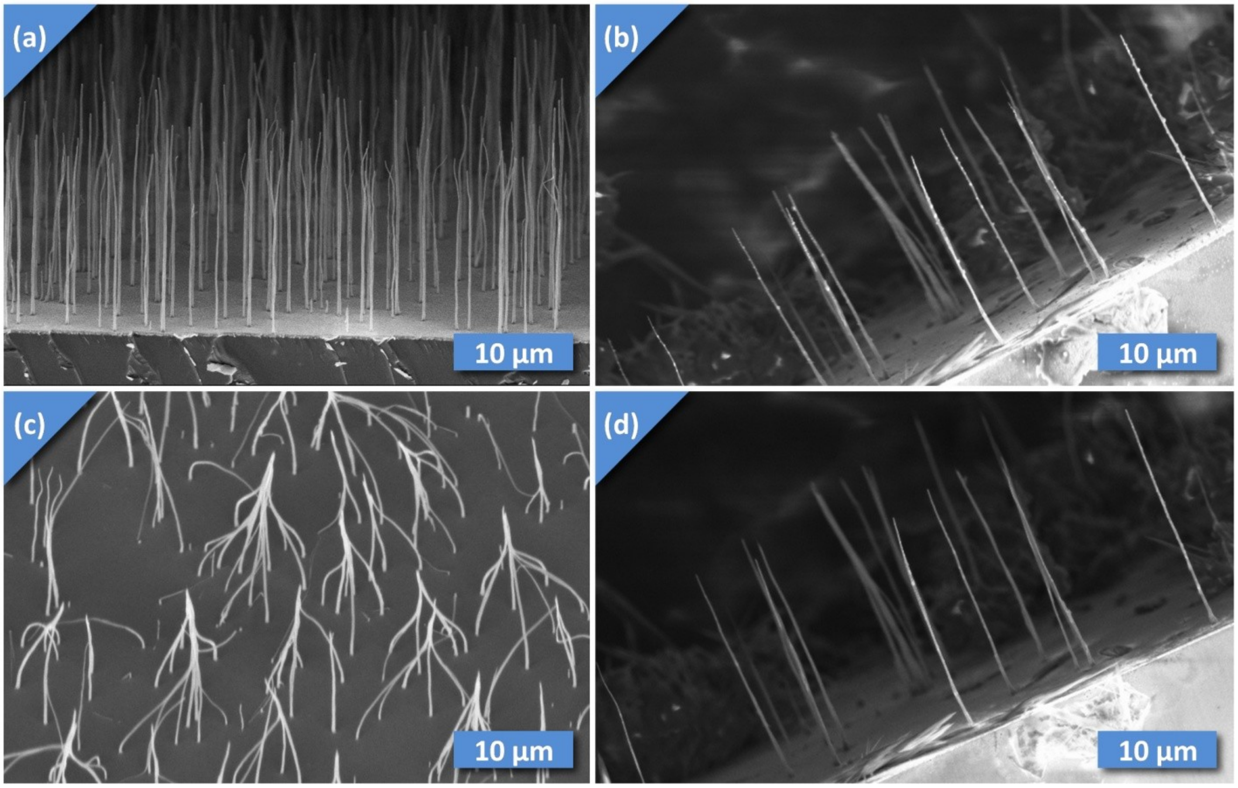

Figure 4-5: The critical point dryer is effective at preventing stiction. Two samples are shown before (a,b) and after(c,d) submersion in isopropyl alcohol. On the right, the critical point dryer removed isopropyl alcohol from the sample with out the adverse effects of surface tension, such as the stiction at left, where no critical point dryer was used.

One way to combat stiction is with the use of a critical point dryer. This apparatus takes a submerged sample through the critical point of the liquid (in this case carbon dioxide), where the liquid and gas phases are indistinguishable and the surface tension between them is zero. Going from there into the gas phase allows the sample to dry without experiencing any surface tension effects, effectively preventing stiction. A critical point dryer was tested on carbon nanotubes after they were submerged in acetone (the chemical used to dissolve the resist coating from the other sample), and then isopropyl alcohol (shown in Figure 4-5b). The critical point dryer was successful in preventing stiction (Figure 4-5d), and the tubes remained separated and vertical.

It is important to note that the sample that failed due to stiction contained a higher density of CNTs. It may be tempting to attribute the lack of stiction in the second sample to the density alone, however, even the tubes on the denser sample which were as far from their neighbors as those on the sparser sample experienced stiction. Therefore it is likely the critical point dryer that made the difference.

In addition to the deposition processes examined, several etching processes were also tested on CNTs. The first etch is critical to the device fabrication process. The sacrificial layer of SiO_2 must be removed at the end of the process, to allow the rotor to rotate freely. Hydrofluoric Acid (HF) is known to dissolve SiO_2, while leaving pure silicon and most other materials unharmed. HF was therefore used to remove the SiO_2 layer, by exposing the entire device to it.

To test the compatibility of HF with CNTs, several experiments were conducted. First, vapor phase HF was applied to substrate-attached CNT samples. These tubes showed no apparent damage even at high magnifications in the TEM. That is not surprising, since HF tends to be selective to SiO_2, and carbon nanotubes should be a very stable substance.

However, it was also necessary to try the vapor phase HF etch on a CNT coated with SiO_2. This is most similar to the actual device fabrication procedure, where oxide will need to be removed from the silicon rotor and the nanotube. However, an issue was encountered with this experiment: The vapor phase HF consistently left a thin (~5nm) layer of oxide untouched on the nanotube (see Figure 4-6). It is possible that this layer is caused by transient behavior in the PECVD start-up process. The plasma may take a few seconds to stabilize, and since the entire layer only takes 20 seconds to form, a substantial fraction of it may be deposited under different conditions, leading to a different chemistry in the layer. A different chemistry would explain resistance to HF, as HF only selectively etches SiO_2. More study is needed to verify this possibility.

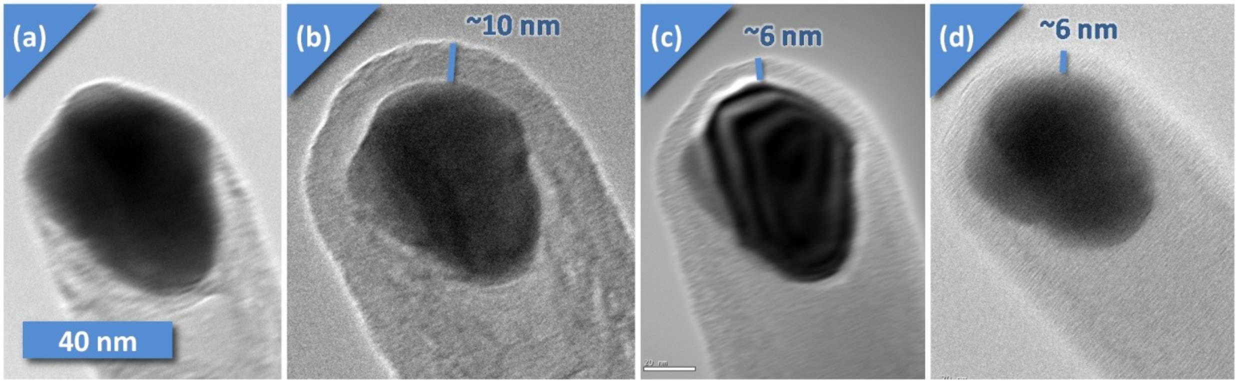

Figure 4-6: A tube was subjected to HF vapor before oxide (a), and after an oxide coating (b) was applied, for 20 minutes (c) and then an additional 120 minutes (d).The vapor HF etch was did not harm the nanotubes (a), but also was unable to remove a thin layer of the silicon dioxide (c,d). This could be a result of transient conditions at the beginning of the plasma deposition process, which may cause chemical composition variation within the silicon dioxide layer.

While a layer of oxide only 5 nm thick may be able to be sheared (since the tube itself is more than 100 nm in diameter), resulting in an operational device, that is less desirable than an etch that can completely remove the residue. In an attempt to resolve the issue, liquid HF etching was also used on oxide-coated CNT samples. Unfortunately, the liquid HF did not resolve the problem, and in fact produced an additional concern. The surface of the oxide was markedly roughened by the liquid HF treatment, while remaining intact. The liquid HF option was not pursued any further, and additional investigation is warranted to determine the cause of the unexpected behavior.

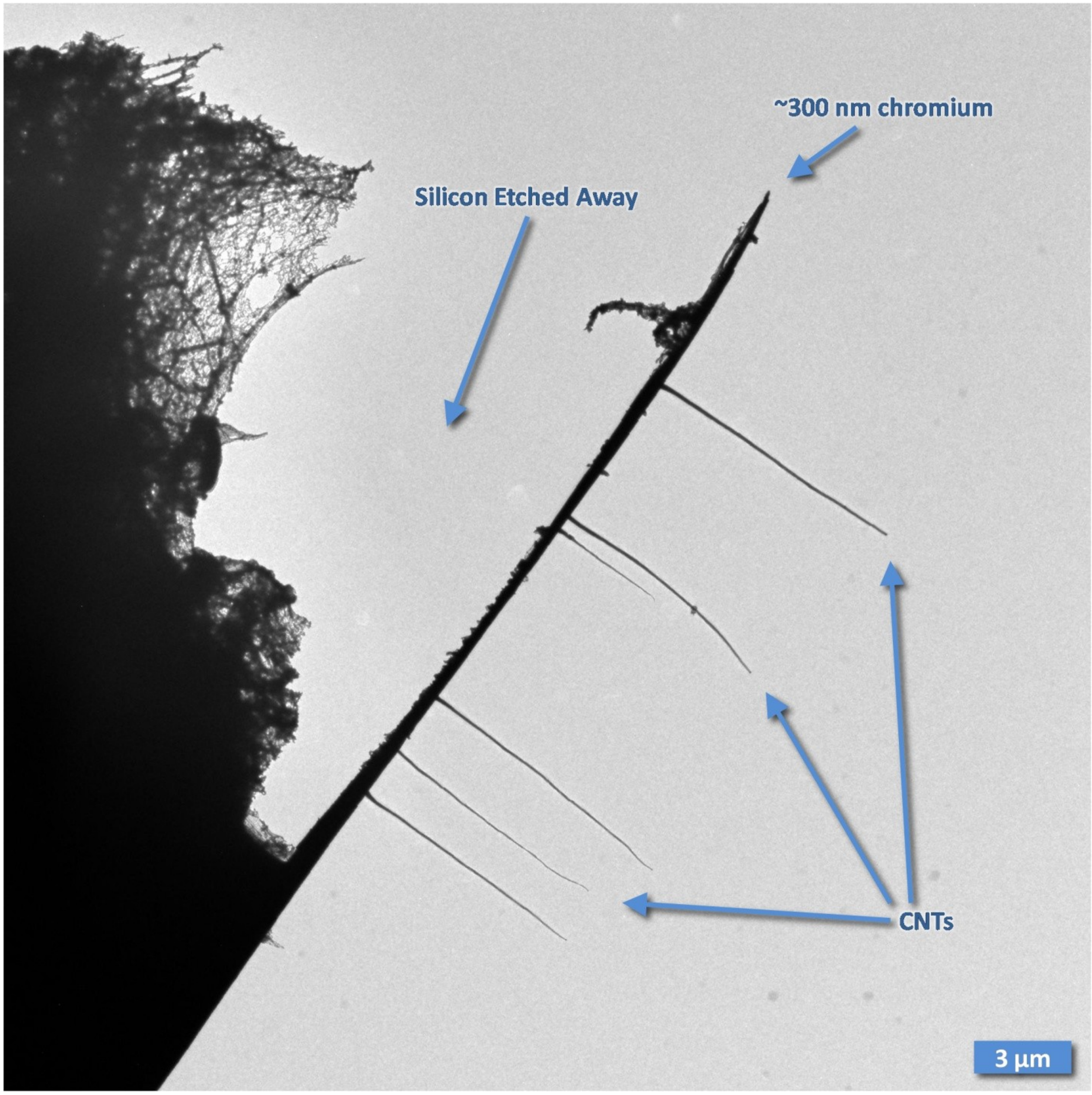

Figure 4-7: Xenon difluoride etching vigorously attacks silicon, while leaving the CNTs and chrome adhesion layer untouched.

Xenon difluoride (XeF_2) vapor phase etching was also tried on the CNTs. XeF_2 is not required for fabricating the device, but was available to test. XeF_2 selectively etches silicon, without attacking silicon oxides or nitrides, requiring no external energy source. As a vapor phase etch, it also doesn't suffer from the problem of stiction. XeF_2 was used on VACNFs, which were then observed in the TEM, and recorded in Figure 4-7. Interestingly, the etch did not seem to attack the tubes themselves to any measurable extent, however, the catalyst particles left at the tips of the tubes after growth became very roughened and somewhat enlarged. The mechanism behind this behavior is not known, but it was not pursued, since the process is not essential to the present work.

As a result of these tests, all the processes that are required to interact with the nanotube, and a few that are not, were evaluated. The only issue that provides the potential to interfere with the device construction and operation is the residual thin oxide layer left by the vapor HF release etch.

4.2.2 Device Fabrication Process

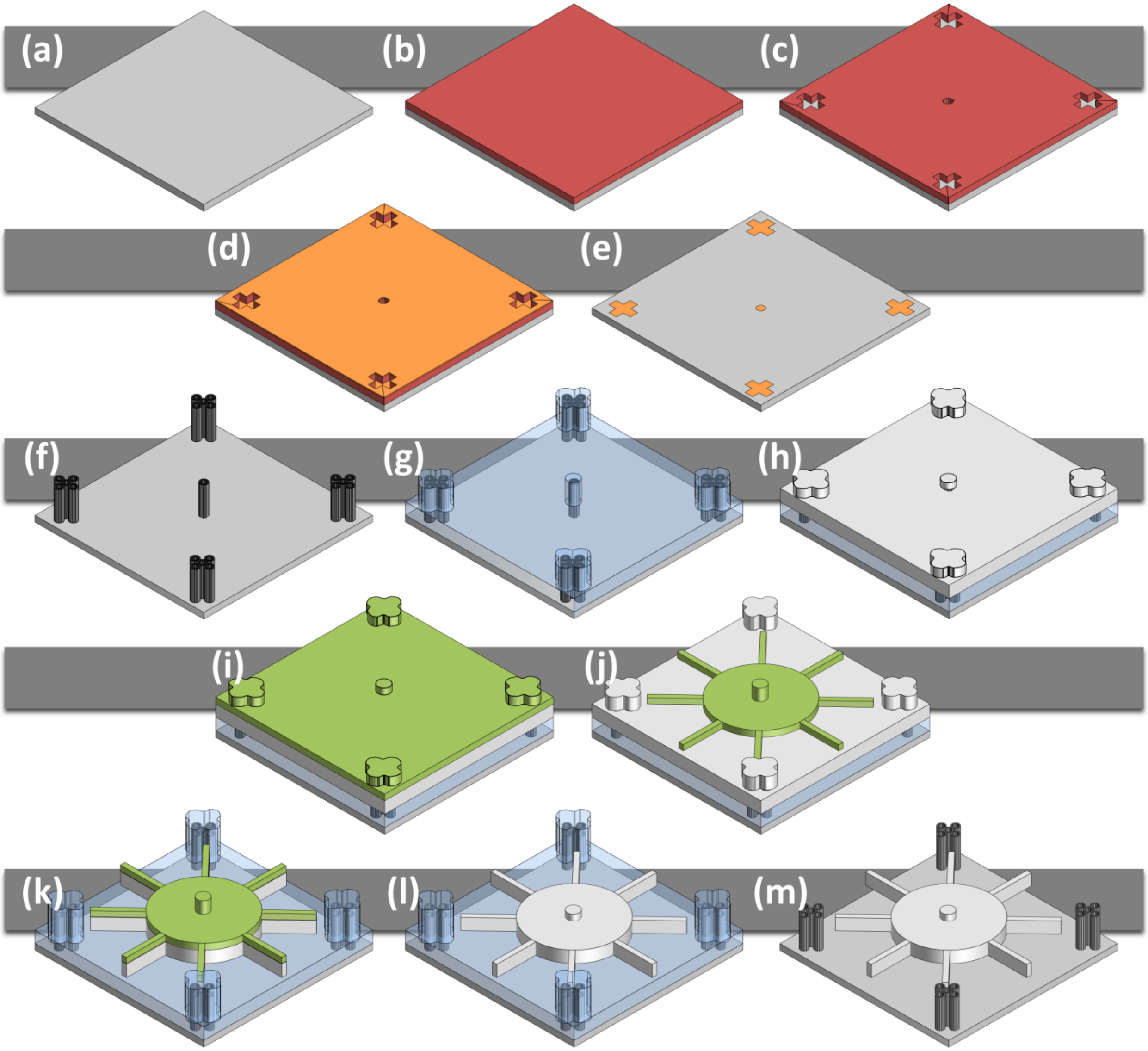

Figure 4-8: The entire device fabrication process. (a) Bare substrate is coated with Chromium adhesion layer. (b) PMMA positive e-beam resist is spun on. (c) e-beam exposure and development. (d) Nickel catalyst evaporated onto sample. (e) Lift off leaves patterned catalyst. (f) C-CVD CNT growth. (g) PECVD SiO_2 sacrificial layer deposited. (h) LPCVD p-Si layer for the rotor deposited. (i) maN-2403 negative e-beam resist is spun on. (j) e-beam exposure and development. (k) Cryogenic RIE of the polysilicon layer. (l) resist stripped. (m) HF vapor removes sacrificial layer, releasing device.

The device constructed for this research, and which could eventually be used to conduct experiments on friction in carbon nanotubes, was constructed using both well-established methods for MEMS fabrication, and techniques that are still under active research. Each step in the fabrication process, shown in Figure 4-8, presented its own unique challenges, some of which were overcome, and some of which are still under investigation. The processes were demonstrated individually first, but when combined new problems arose. The overall fabrication process has proved quite difficult to complete from start to finish, and although it has been undergone completely, the issues have not yet been resolved to the point where a functional device can be produced. The steps in the fabrication procedure are described in order, and the parameters used in each process are found in Table 4-1

The fabrication began by depositing a nickel catalyst dot in the location where the nanotube was desired using e-beam lithography and lift-off on top of a chromium adhesion layer. Then nanotubes were then grown using a DC PECVD process. A silicon dioxide layer was deposited with PECVD, to support the polycrystalline silicon rotor layer, which was applied by LPCVD. The rotor was cut out of the polycrystalline silicon layer using e-beam lithography with a cryogenic reactive ion etch. The rotor was then relased by etching away the silicon dioxide with hydrofluoric acid vapor.

Table 4-1: Parameters used in fabrication processes.

Process	Ni Liftoff	CNT Growth	PECVD SiO2	LPCVD p-Si	Cryo Si Etch	HF Release
Rate (nm/min)	6	100	85	5	100	500
Temperature (°C)	40	625	380	585	-10	40
Pressure (mTorr)	0.002	6000	1000	150	10	7.6×10^5
Gas 1	-	C_2H_2	SiH_4	SiH_4	SF_6	HF vapor
Flow rate (sccm)	-	80	22	80	85	-
Gas 2	-	-	N_2O	-	O_2	-
Flow rate (sccm)	-	-	750	-	6	-
Carrier Gas	-	NH_3	N_2	-	-	-
Flow rate (sccm)	-	160	430	-	-	-
Power (W)	-	100	20	-	10	-
Power source	e-beam	DC	RF (13.56MHz)	furnace	RF (13.56MHz)	-
ICP Power (W)	-	-	-	-	1000	-
Lithography	e-beam	-	-	-	e-beam	-
Resist	PMMA	-	-	-	maN-2403	-
Discussed in sec.	4.2.2.1	4.2.2.2	4.2.2.3	4.2.2.4	4.2.2.6	4.2.2.7

4.2.2.1 Catalyst Patterning

The first step in constructing a CNT based rotor is to prepare for the growth of a CNT, depicted in Figure 4-8a-e. The device requires a vertically oriented CNT placed in a precisely specified location, so that the following steps can construct the rotor onto the nanotube axle with as high accuracy as possible. As discussed in section 4.1.2, C-CVD growth of tubes provides the capability to grow tubes exactly where desired, and to well-controlled sizes, so long as particle of catalyst of the right size can be placed in the right place. For this research, the target nanotube size is 100 nm, which is structurally robust without being too large to make reliably. The catalyst dots were deposited using evaporation on top of an e-beam patterned layer of resist. The resist was then dissolved, "lifting off" the nickel that was on top of resist, while leaving nickel that was on the bare substrate.

Originally, two methods were used in an attempt to produce the required catalyst "dots." The lift-off method, which would eventually be chosen, has been demonstrated by the collaborators Ren *et al.*, of Boston College, who are doing the CVD CNT growth [70, 104]. The technique uses electron beam (e-beam) lithography to define small dots of nickel in the precise locations where nanotubes are desired. First, a positive resist sensitive to e-beam (polymethylmethacylate, or PMMA) is applied to a flat substrate, and exposed in the shape of the dot, along with a few other markings to help align subsequent steps to the dot. In e-beam lithography, a mask is not used; instead, the beam is electrically scanned over the substrate in the shape desired. While time consuming, this process allows the desired shape to be changed without making a new mask. Additionally, better resolution is possible compared with conventional photolithography. Applying the developer removes the exposed resist, leaving a bare spot on the substrate. Nickel is then deposited onto the sample using evaporation (the nickel is heated to high temperatures in an ultrahigh vacuum, and evaporates, re-depositing on the sample). When the resist is dissolved, the nickel that is on top of the resist is lifted-off, leaving only the small dot.

Because this technique has already been used successfully, it was believed that it would be relatively straightforward to implement again. However, some unforeseen problems emerged. First, the nickel dots appear to be diffusing around on the surface of the substrate during the next step, the nanotube growth, as shown in Figure 4-9a,c. Around areas where nickel was deposited there are many extra nickel dots, which seem to be denser near the areas where the nickel originally was. Additionally, individual nickel dots have been observed to move a few hundred nanometers from their original location (as in Figure 4-10c,d). This proliferation of extraneous nickel could be caused to sputtering of the nickel in the plasma environment of the nanotube growth chamber. Extra energy provided by the plasma could also explain nickel dots diffusing or "traveling" across the substrate.

In any event, this result was quite unexpected. The process followed previously successful catalyst patterning methods fairly closely. Those studies did not observe this behavior. In order to combat the problem, an adhesion layer was added underneath the nickel. Chromium has been used successfully in such a role, so it was chosen as the material for the adhesion layer. However, the chromium also had difficulty adhering to the bare silicon substrate. Several attempts at producing a well-attached chromium layer were attempted, but the layer continued to peel or flake off during the resist development, nickel lift-off, or CNT growth.

The first attempt to secure the chromium to the substrate was to raise the temperature of deposition. While the evaporation system applies high heat at the nickel source, the sample remains at room temperature. Having a higher sample temperature could help the chromium to bond with the silicon better during its formation. To that end, the collaborators were able to deposit the chromium in their system which has a substrate heating capability. The result was unchanged.

An additional step taken to promote chromium adhesion was thorough cleaning of the sample prior to chromium deposition. Any particulate contamination on the surface could create islands of poor adhesion, at which delamination could nucleate and the propagate over the sample. While cleaning did improve the adhesion of the chromium, it still was not sufficient to withstand the CNT growth process.

As a final option, substrates with chromium already applied were obtained from the collaborators. These substrates, made of glass, were used for an alternative catalyst patterning strategy the collaborators are pursuing. They also experienced significant delamination problems, but had high enough yield of samples that CNT growth was possible (shown in Figure 4-9b,d). When using e-beam patterning on these samples, the diffusion problem was dramatically reduced, but still present. Growth of individual, isolated nanotubes in the designed location was achieved with these substrates.

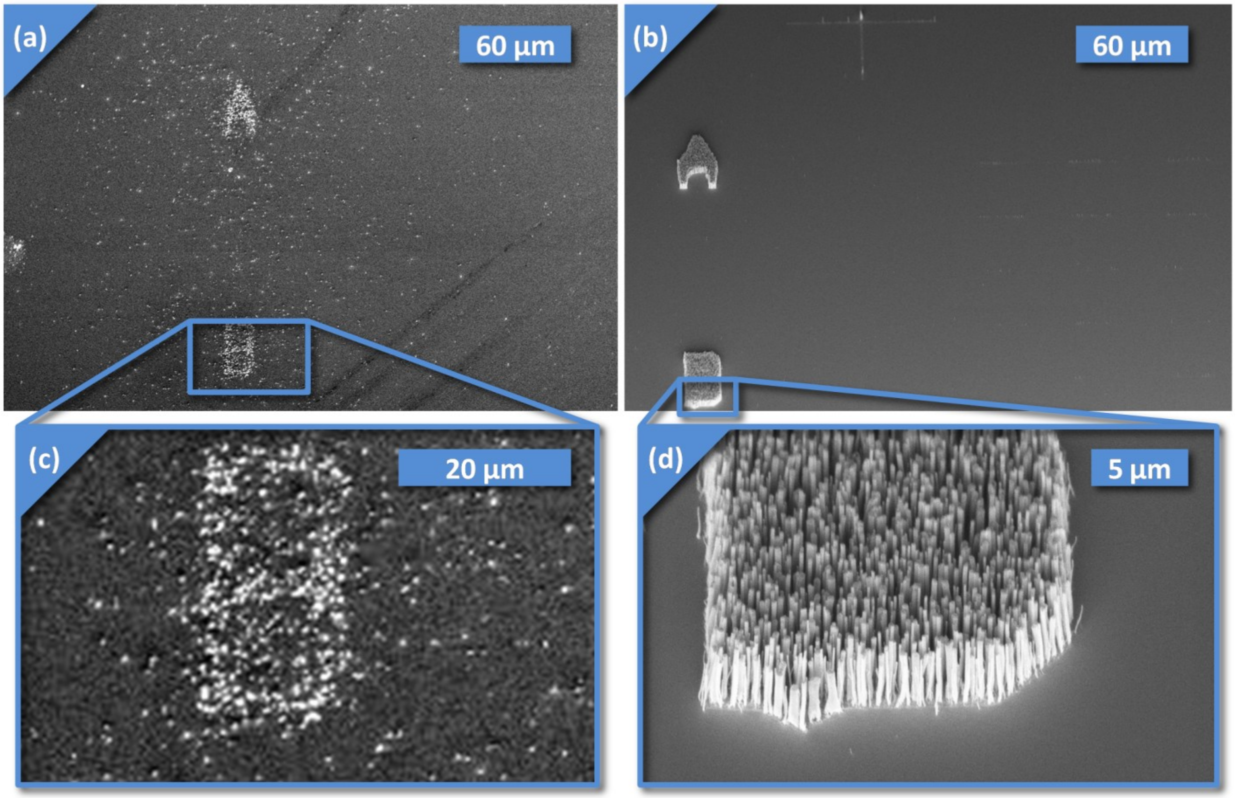

Figure 4-9: Nickel catalyst diffusing on the substrate surface, resulting in scattered nanotubes. On the original silicon substrate (a,c) diffusion was a serious problem. The glass and chromium substrates (b,d) have shown better results.

When the e-beam patterning approach to generating a single, isolated nickel dot for the single, isolated CNT bearing began to show signs of difficulty, another approach was devised. The alternative patterning approach developed by the collaborators at Boston College [106, 107] was producing significantly better yield than the primary, e-beam based approach. Their approach used a technique called micro-sphere lithography. Polystyrene spheres between one and two micrometers in diameter are floated on water, and the substrate is lifted up through the surface. The result is a one-sphere thick layer (monolayer) on the substrate surface. Nickel is then evaporated onto the substrate in the same way as for the e-beam process. Here, the exposed triangular-like areas between adjacent spheres are where the nickel lands. When the spheres are lifted off, a hexagonal array of nickel triangles is left. Annealing causes the triangles to ball up into dots.

The micro-sphere approach provides a dense, regular array of catalyst, rather than the single catalyst dot required for an isolated tube. In order to use this approach for the present device, it was planned to protect a single dot with an e-beam patterned patch, and remove the others with an etch step that targets nickel. While the protective patch was successfully made, two different commercially available liquid nickel etchants failed to remove the extra dots. The etchants worked successfully on a few other nickel samples, but agitation and temperature adjustment did not help with the micro-sphere sample, nor did removing the anneal step. It is currently hypothesized that galvanic effects between the chromium adhesion layer and the nickel catalyst may be responsible for the etch resistance of the nickel. Since the primary approach ended up producing results that were more useful, this approach was not pursued any further.

It should be noted that while the current technique makes use of costly and slow e-beam lithography to define catalyst particles for tube nucleation, other techniques could be substituted (such as deep ultraviolet stepper-based photolithography), provided they can produce small enough, precisely located catalyst dots. Additionally, the other components of the device can be aligned to the tubes with standard MEMS alignment techniques, rather than requiring a hand-selection of each bearing candidate tube, and careful adjustment of device patterns to match to it, as has been required for previous rotary CNT devices. In short, while the current procedure uses e-beam lithography, there is a clear path toward a more manufacturable approach for future incarnations of the device.

4.2.2.2 Carbon Nanotube Growth

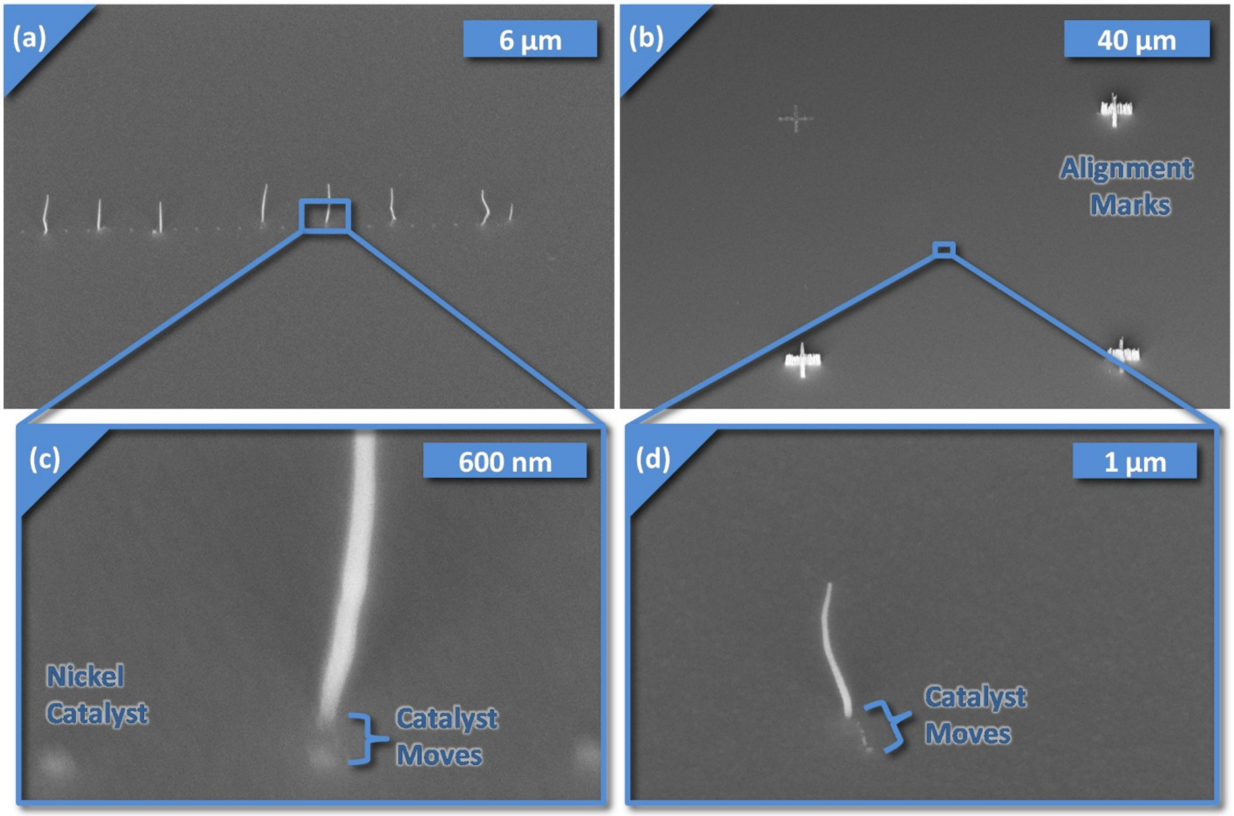

Figure 4-10: Nanotubes growng from catalysts. (a) Yield is not 100%. (b) The alignment marks grow nanotube as well, allowing them to be detected through the subsequent layers. (c,d) Nickel catalyst migrates up to a few hundred nanometers.

With the catalyst in place, nanotube growth was performed (Figure 4-8f) by the collaborators at Boston College. Their direct current (DC) plasma enhanced C-CVD system, described in [69, 70], uses acetylene (C_2H_2) as the carbon source, with ammonia (NH_3) as the diluent and plasma medium. While this current system produces tubes with defect densities typical of CVD tubes, the collaborator has plans to improve the as-grown crystalline quality of the tubes. One option is to add gold to the nickel catalyst. Gold and nickel have a eutectic point with a low melting temperature, so adding an appropriate proportion of gold could make the catalyst more liquid, allowing easier diffusion of the dissolved carbon atoms to ideal non-defect locations. Another option is to replace acetylene with methane, which dissociates at higher temperatures, allowing the reactor temperature to be increased, also improving carbon diffusion.

4.2.2.3 Silicon Dioxide Sacrificial Layer

After the CNT that is to perform as the bearing has been produced, a sacrificial layer of SiO_2 is deposited (Figure 4-8g). The purpose of this layer is to support the rotor temporarily, so that when it is etched away there will be space between the rotor and the ground. For this layer, a PECVD reactor was used to deposit two micrometers of SiO_2. This reactor applies a high power radio frequency (RF) electric field to a mixture of silane (SiH_4) and nitrous oxide (N_2O) gases, with an argon diluent, under high vacuum. The gasses flow from small holes in one electrode, while the sample lies on the other electrode. The configuration produces a vertical electric field and plasma in the gap between the electrodes.

The deposition process for the SiO_2 was developed extensively before the nanotube was introduced. The growth parameters were adjusted to provide a very uniform deposition rate (and hence a uniform thickness), allowing fine control over the gap spacing. Another potential issue that was optimized was the residual stress. When these films are deposited, they can have a substantial internal stress due to various factors such as a mismatch of their thermal expansion coefficient with the substrate or damage caused by ion bombardment in the plasma. The deposition for this oxide layer was tuned to provide under 50 MPa of stress, as measured by an adaptation of Stoney's formula.

The oxide layer was tested on VACNFs, as mentioned in section 4.2.1, and showed good uniformity and good adhesion even on the nanotubes, without damaging them visibly. The thick layer (2 µm) required for the rotor spacing came out as well as the thinner layers used for process compatibility checking.

4.2.2.4 Poly-Silicon Rotor Layer

For the silicon material used to make the rotor (Figure 4-8h), two approaches were considered. The PECVD reactor used to deposit the SiO_2 is also capable of producing an amorphous silicon material by removing the nitrous oxide from the feed gases, and adjusting the reaction parameters to compensate. This capability was considered and rejected for a number of reasons. First, the a-Si is fairly impure, containing substantial hydrogen mixed in with it. This alters the properties of the silicon, which could pose a problem for subsequent etching steps. Furthermore, amorphous silicon lacks the order and structure of crystalline silicon, consisting of atoms almost haphazardly arranged, bonding where they can. The result is a weaker material. Finally, the deposition procedure produces extremely high residual stresses, which for films thicker than a few hundred nanometers proved unmanageable. While it may be possible to adjust the deposition parameters to achieve a better a-Si product, another option was readily available.

The other approach deposited polycrystalline silicon in an LPCVD tube furnace. The LPCVD process does not rely on plasma to provide the energy necessary to dissociate the reactants, but uses only temperature. A low pressure is used because low pressure enables the deposition rate to depend strongly on the inherent chemical reaction rate, rather than the rate at which gas arrives at the surface. The reaction rate is strongly temperature controlled, while the gas flow rate can be quite unpredictable. Low pressure thus enables precise control of the deposition rate, and hence the final film thickness.

The p-Si is also a structurally superior material to a-Si. While it is not as strong as silicon in a single crystal (such as silicon wafers available commercially), p-Si is made up of “grains,” or domains in which a crystal lattice extends for a substantial portion of the silicon piece. The presence of order in the bonding structure gives p-Si a higher fracture strength. Furthermore, the p-Si process can be used to produce silicon with relatively low residual stress. The stress measured by using Stoney’s formula was below 50 MPa. Additionally, when releasing disks as part of the testing for the final step in the fabrication process, bowing of less than 0.1% of the diameter was observed in the disks as measured by optical interferometry and AFM. This indicates that any stress gradient within the p-Si layer to be low enough not to cause large deflections that could prevent an otherwise normal device from operating.

As mentioned in section 4.2.1, the p-Si deposition process was tested on an oxide coated nanotube. The results for the thicker (2 µm) layer required to produce the rotor worked as well as the thinner (few hundred nanometer) coating used for compatibility assessment. Figure 4-11 shows the bumps made by nanotubes underneath the two layers.

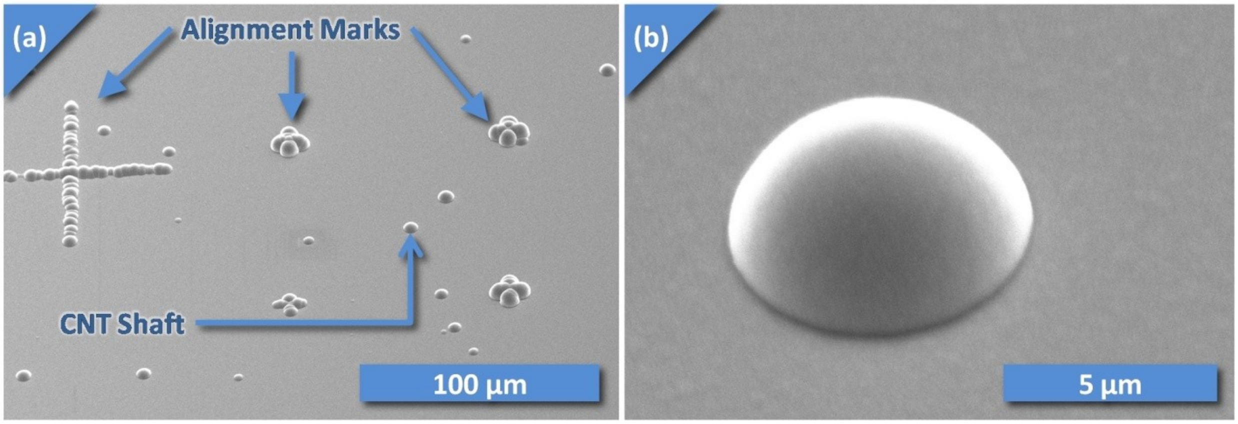

Figure 4-11: The nanotubes all show up through the silicon dioxide and polysilicon layers, including the nanotubes that grew on the alignment marks and the intentionally patterned central dot, as well as the unintended nanotubes resulting from catalyst migration.

4.2.2.5 Rotor Lithography

While the p-Si deposition provides the material that will form the rotor, it still needs to be shaped into a disk, with blades for the actuation mechanism (see section 4.3.1). This is accomplished by lithography (Figure 4-8I,j). For this research, e-beam lithography was used, because it doesn’t require a mask, and the pattern can be changed easily. Because only a few devices are needed, and the first design may prove to have flaws, e-beam lithography is a good option. It should be stressed that in a production setting, where the time required for e-beam lithography is impractical, standard photolithography could be substituted, as the resolution required is obtainable and the design would not be subject to change.

To perform the e-beam lithography, a negative resist (maN-2403, from Micro Resist Technology, GmbH) was first spun onto the chip with the nanotube and oxide and polysilicon layers. The alignment markers that were originally placed with the nickel dot for the axle were visible through the 4 µm of material because nanotubes grew on them as well. The resist was exposed in the shape of the rotor, using the alignment marks to match the rotor center to the nanotube shaft. The results are shown in Figure 4-12). Some difficulty was encountered with the alignment. The first attempt missed the tube altogether, probably due to a calibration error in the equipment. The second attempt was off by about

5 µm. This distance is well above the 1 µm estimate that should be achievable on the e-beam lithography system and which is used for the dynamic model of the device, but low enough that a device which rotates is still possible. Further use of the lithography is expected to enable improvement in the alignment, as familiarity with use of the buried-nanotube alignment markers is gained. If that doesn't provide sufficient improvement, in the future the alignment markers could be exposed by etching the silicon and oxide in an additional step, while protecting the rotor with a larger resist patch. Another possible cause of the misalignment is the diffusion or movement of nickel catalysts observed during the fabrication process. Nanotubes were observed growing a few hundred nanometers from the catalyst's original location. Motion of the catalyst would cause the tube not to be at the expected location, contributing to misalignment.

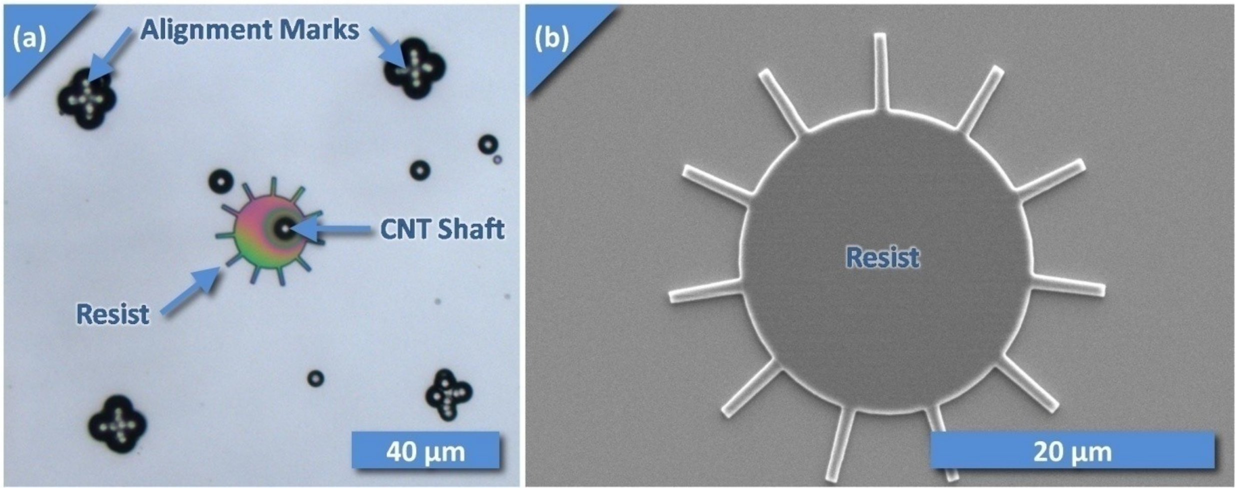

Figure 4-12: The e-beam pattern defining the rotor, after development. (b) It is clear that the tool can create a crisp pattern of the appropriate scale. (a) The alignment based on the buried nanotubes requires further work.

4.2.2.6 Silicon Rotor Etch

After the exposed resist was developed, resist was left only in the shape of the rotor. The rotor must then be cut out of the silicon layer, using the resist as a mask (Figure 4-8k). In order to get a rotor that has the same shape for its entire thickness, an anisotropic etch was required. Whereas an isotropic etch, such as most liquid chemical etchants, removes material in all directions evenly, an anisotropic etch etches straight down without etching sideways. The technique usually used to achieve anisotropic etches is Reactive Ion Etching (RIE). This technique uses a plasma similar to PECVD, but generally with higher power. In addition, instead of gases that tend to react and deposit on the substrate, gases that chemically attack the sample are used. While the energetic bombardment of the plasma forcefully displaces some material from the sample physically, the chemicals react with specific target materials. The two effects combine synergistically to generate high etching rates, as well as the ability to etch very anisotropically while retaining some selectivity to certain materials. It was decided to use a cryogenic RIE method for the silicon rotor etch, after considering two particular types of RIE.

The first approach considered is Deep Reactive Ion Etching (DRIE), which is capable of extremely anisotropic etching of silicon. It operates by alternating brief periods of etching with passivation, a step where a protective coating is applied. Because of the anisotropy already present due to the plasma, the protective coating is removed from the horizontal surface but left on the sidewalls, enabling vertical etching. However, DRIE is designed for very high rate etching through deep (several hundred micrometers) features, and could be difficult to control for the relatively thin silicon layer employed in this device. Although a DRIE system was successfully used to cut out circles in a test p-Si layer of the appropriate thickness, another option was selected based on its superior controllability.

The other way to etch silicon anisotropically is with a cryogenic RIE process. Keeping the sample at low (-5°C) temperatures works in a similar way to the protective coating. The horizontal surfaces are exposed to the plasma bombardment, and tend to heat up despite the cooling. The vertical surfaces, on the other hand, remain colder, discouraging the chemical etching reactions. The result is that the etch proceeds mainly downwards and not sideways.

The cryogenic silicon etch process used in this work was developed before the nanotube was introduced. The process parameters were adjusted to get nearly vertical etching at a reasonable rate. The etch was tested on silicon, but one important factor was overlooked. The rotor itself is made of polysilicon, not crystalline silicon on which the etch was tested. As a result, the etch rate can differ, and in fact turned out to be substantially slower for the polysilicon. The unfortunate consequence is that in order to cut through the silicon to the underlying oxide, longer etch times must be used. That is not a problem of itself, but the resist is also exposed to the etch longer. In this case, the resist could not hold up, and was etched away before the bottom was reached. The result is that some of the rotor was eroded as well, having lost the protection of the resist (shown in Figure 4-13). Another test was performed with a different, thicker resist that used photolithography instead of e-beam lithography, shown in Figure 4-14). This resist was able to hold up for the etch duration, resulting in good crisp patterns, although not patterns of the desired rotor.

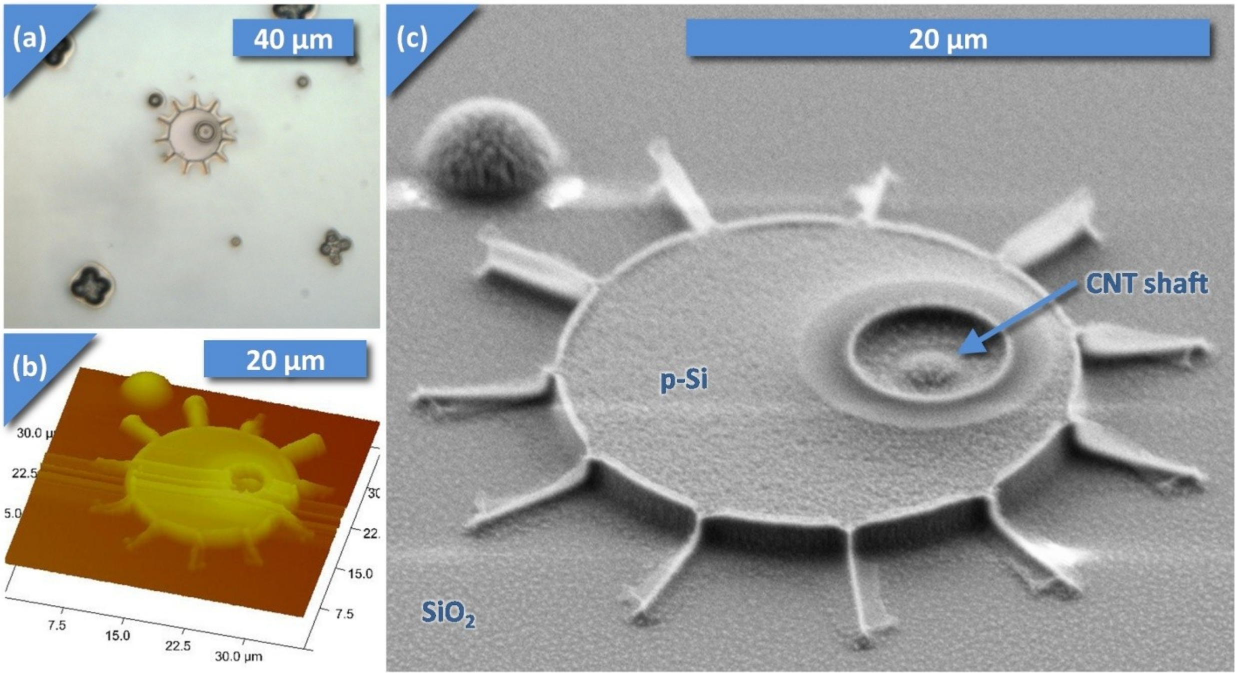

Figure 4-13: The rotor after the cryogenic silicon etch. The resist was not able to last for the entire duration, resulting in significant erosion of the thin fins, and visible roughening of the silicon surface. At left, an optical microscope image and AFM three-dimensional data show alternative views of the rotor.

For future attempts at fabricating a device, the issue will need to be corrected so that the rotor geometry comes out as designed. One possible way is to re-adjust the etch parameters to increase the etch rate of polysilicon, hopefully without increasing the speed at which the resist is destroyed. Alternatively, a thicker resist could be used, providing longer protection. That could pose problems for the lithography step, however. A third option is to decrease the rotor thickness. That would require adjustment of the rest of the geometry to compensate.

4.2.2.7 Silicon Dioxide Release

Although both the lithographic alignment and rotor etch encountered problems, the final release step (Figure 4-8m) was also attempted on the device. In this step, the device is exposed to HF vapor to remove the sacrificial SiO_2 layer, freeing the rotor from the substrate and allowing it to turn. There are several important considerations for this etch. First, an etch that selectively dissolves only silicon without harming the other components is required – HF fits that bill. Secondly, the timing of the etch is important. Because the SiO_2 layer is conformal, it continues up along the nanotube shaft all the way to the tip. The etch must be allowed to proceed long enough that all the SiO_2 is cleared from under the rotor, but it must be stopped before it reaches the tip. Otherwise, it would remove all the oxide, leaving the rotor completely unconnected to the nanotube. HF in the vapor phase was used for the release etch.

In order to determine the time required for the etch to proceed, a test was conducted using disks of various known diameters. The disks were fabricated on a polysilicon and oxide layer stack identical to the one used for the device. Instead of e-beam lithography, conventional photolithography was used, and the corresponding thicker resist was able to stand up to the silicon etch step, producing clean features. The result was silicon disks 2 µm thick and 10-300µm diameter on a continuous oxide sheet.

The HF vapor release etch was applied to the disk arrays in measured time intervals of five minutes, and after each interval the disks were examined (Figure 4-14). Those disks which were missing were assumed to have been released, i.e. the SiO_2 supporting them had been completely dissolved. In this way, the etch time required to release the various diameters of disk was measured. For the 20 µm disks corresponding to the device design, 35 minutes were required.

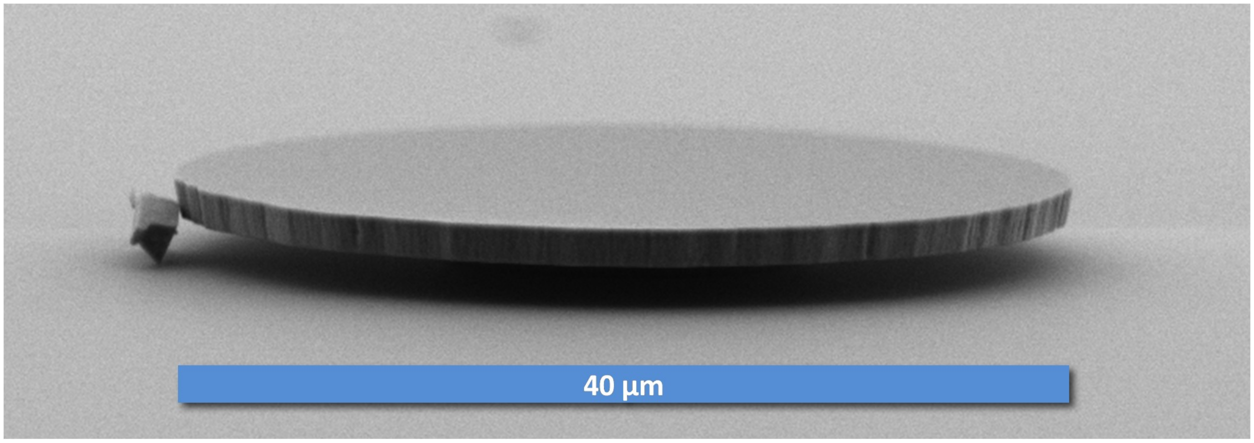

Figure 4-14: The anisotropic silicon etch and the release etch worked very well in tests. The silicon dioxide was partially undercut from this 40 micrometer diameter polysilicon disk after 35 minutes of etching, with no damage to the disk or substrate. The particle on the left is a stray piece of debris, which provides grounding to the otherwise insulated disk, promoting superior SEM imagery by preventing charge accumulation on the disk.

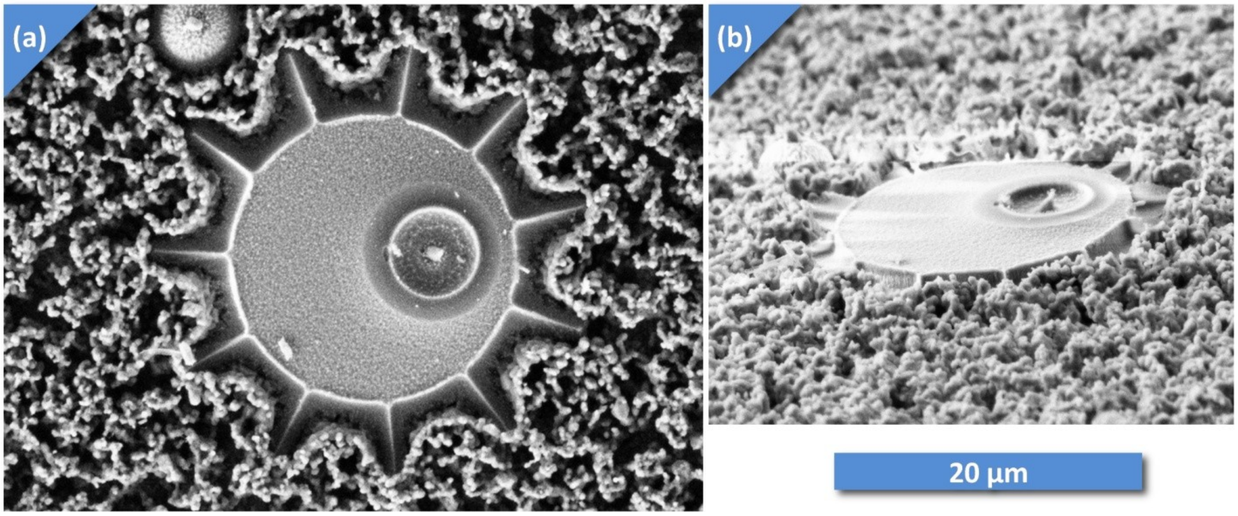

Figure 4-15: Bizarre results from the release etch. While the etch performed perfectly in prior tests, on the actual device it failed. Instead of undercutting the rotor, leaving it free to rotate, the rotor became buried in a highly porous material of unknown composition. Further investigation is required to determine the reason for this result.

No problems were encountered with the release etch test on the various circles, so it was believed that it should work well for the actual device release. Unfortunately when the device was run through an identical release test, a completely unexpected outcome occurred. The HF did not etch the SiO_2 as expected. Instead, an extremely rough and porous material appeared on the surface, burying the rotor, and rendering the device inoperable (Figure 4-15). The cause of this strange appearance is unknown. One possible explanation could be related to the substrate material. Instead of placing the SiO_2 on pure silicon as originally planned, and as used in the test shown in Figure 4-14, glass substrates had been used to address the chromium adhesion problem discussed in section 4.2.2.1. The result was a glass and chromium substrate under the SiO_2. Glass is also composed of mostly silicon dioxide, and is therefore susceptible to HF etching. Since the HF vapor etch is performed with the sample upside down (i.e. with the nanotubes pointing down), it is conceivable that the HF partially dissolved glass that was thought to be protected by the chromium layer. This glass could have been drawn down by gravity, and then re-hardened into the porous structure observed. Only one device has so far made it to the release step, so this issue may not necessarily be repeatable. In order to try to resolve it, the catalyst patterning step will be adapted to work on silicon substrates, as was the original plan.

While the entire fabrication process has not yet yielded a functional device, only one compete run through the process has been completed. It is not unusual for MEMS devices to have significant problems on their first fabrication attempt. With perseverance the present difficulties should be resolved, eventually leading to successful fabrication of the proposed CNT based Stodola rotor.

4.3 Actuation Mechanisms

If an operational device can be successfully fabricated, a method of rotating the rotor will be required. Applying torque to a device only 20 µm in diameter is a challenge in itself. Several schemes to actuate the disk were considered. Electrostatic and electromagnetic actuation, laser and ion beam radiation pressure actuation, and physical actuation with a probe were all considered. Air jet actuation was selected, because it poses the least risk to implement, requiring only blades to be added to the circular rotor disk.

4.3.1 Air Jet Drive

The most straightforward method to actuate the disk would be to use jets of air impinging on vanes or blades on the rotor, as shown in Figure 4-16. In essence, this would be a nano-scale turbomachine. Like the laser actuation scheme discussed in section 4.3.3, the only fabrication change required would be the addition of blades on the rotor, which could ease the potential for unforeseen fabrication problems to arise. However, unlike the laser, this approach does not suffer the problem of heat dissipation. For these reasons, this is the approach that was chosen to first attempt actuation of the nano Stodola rotor.

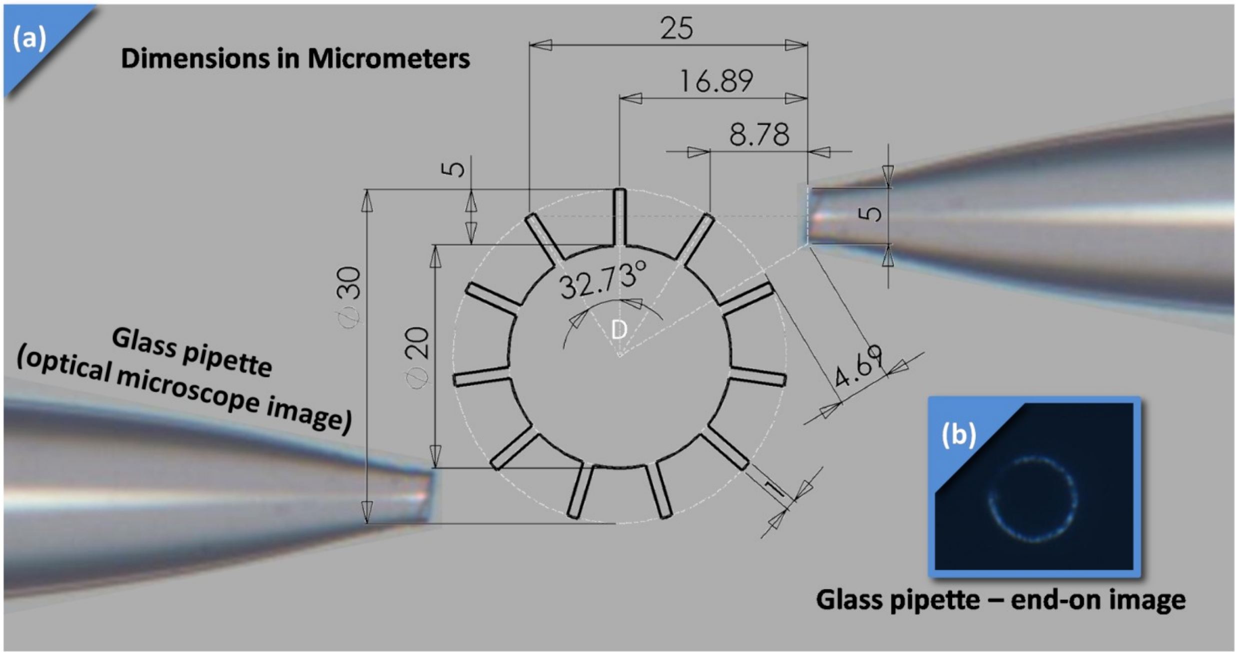

Figure 4-16: Air drive actuation scheme. The drawing is given in dimensions of micrometers. The glass needles are optical micrographs, scaled so the drawing dimensions accurately represent the image dimensions as well. The inset (b) shows a micrograph of the tip of the pipette, displaying the thin walls.

In order to direct jets of air onto the device, extremely small jet orifices are required. Such orifices area available, in the form of glass micro pipettes (shown in Figure 4-16a, and end-on in Figure 4-16b) available from a medical equipment supplier. These pipettes have orifices as small as half a micrometer in diameter, and feature tube walls as thin as a micrometer near the tip. (A 5 micrometer diameter was selected for testing, which is similar in size to the blades on the rotor). With those dimensions the orifice can be placed within a diameter of the blades on the rotor, providing a well defined jet impinging on the blades. Two needles in opposing directions are used to provide torque about the nanotube axis while reducing torque about the x- and y-diameters of the rotor. In order to control the positioning of the needles, a probe station is used. This station includes a microscope for observation, and micro-positioners capable of 1 cm of travel at sub-micrometer resolution. Attaching the needles to these allows the tip to be brought within a micrometer of the rotor without bumping it, which could damage it. The other ends of the needles are connected to a syringe pump, capable of supply flow rates of under a microliter per minute, by means of polyetheretherketone (PEEK) tubing. The complete apparatus is illustrated in Figure 4-20.

The major drawback of the air jet actuation scheme is the difficulty in computing the torque supplied. The aerodynamics of the system are complex. One issue is the geometry: a circular jet is impinging on an angular plate of comparable size. This situation would most likely be approached with computational fluid dynamics if any accuracy were desired. Besides the geometry, the flow is in an transitional regime. If operated in standard sea level conditions, the Knudsen number (ratio of the mean free path in the gas to a characteristic dimension of the device) is close to one, indicating that the device is on the boundary between continuum fluid dynamics and free molecular flow.

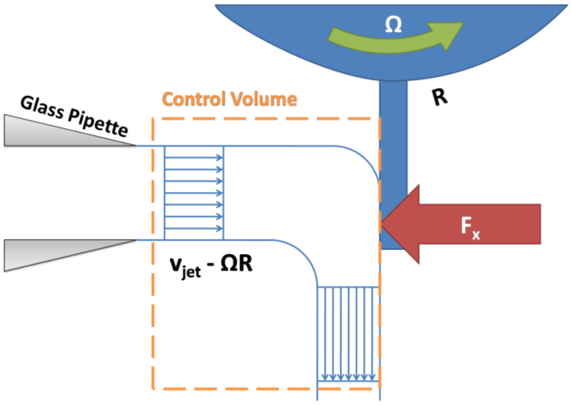

Figure 4-17: Control volume used for momentum equation

Despite all the difficulties, a very rough estimate of the torque is desired, to know what flow rates should be demanded of the syringe pump. To that end, a control volume analysis (depicted in Figure 4-17) was used to estimate roughly the torque an impinging jet could provide. The jet is assumed to impinge on a flat blade which is perpendicular to the jet direction. The jet is assumed to be deflected such that it leaves tangent to the flat blade – in other words, its momentum in the jet direction has been completely removed. Working in a control volume fixed on the blade, the incompressible momentum equation in the jet direction (called the x-direction), ignoring viscous forces, is:

$$\frac{d}{dt}\iiint_{\mathcal{V}} \rho\, v_x d\mathcal{V} + (\dot{m}v_x)_{\text{in}} - (\dot{m}v_x)_{\text{out}} = \iint_{\mathcal{A}} (-p\hat{n}\cdot\hat{x})d\mathcal{A} - F_x \tag{4.1}$$

where ρ is the density of the fluid (in this case air at standard sea level conditions), v_x is the x-component of the velocity (measured in the blade-fixed frame), $\dot{m}$ is the jet mass flow rate (also in the blade-fixed frame), p is the pressure, $\hat{n}$ is the unit normal to the control volume, $\hat{x}$ is the unit vector in the x-direction, $\mathcal{V}$ and $\mathcal{A}$ denote the control volume and its bounding area, respectively, and F_x is the external force, in this case supplied by the turbine blade.

The flow is assumed to be steady so the first term is neglected. The pressure integral also drops out, because the pressure is uniform across the entire boundary surface (all the mass streams entering and exiting have straight streamlines, which cannot support a pressure gradient. The remaining terms are:

$$\dot{m}\left(v_{\text{jet}} - \frac{\Omega D}{2}\right) = F_x \tag{4.2}$$

If the velocity provide within the jet is assumed uniform, and the diameter of the jet is the diameter of the glass needle orifice d_{jet} , then

$$F_x = \frac{\rho \pi d_{\text{jet}}^2}{4}\left[v_{\text{jet}} - \left(\frac{\Omega D}{2}\right)\right]^2 \tag{4.3}$$

And the torque is:

$$\tau_{\text{air}} = \frac{\rho \pi d_{\text{jet}}^2 D}{8}\left[v_{\text{jet}} - \left(\frac{\Omega D}{2}\right)\right]^2 \tag{4.4}$$

With a 5 µm needle orifice, at standard sea level conditions (ρ=1.23 kg/m^3), the jet velocity must exceed the rotor blade linear velocity by about 10 m/s to supply adequate torque to overcome the friction estimate. For an angular speed of one million revolutions per minute, that rotor blade linear velocity is only 1 m/s, so this margin should be easy to achieve.

While this very simple calculation is only a rudimentary estimate, for the initial testing of the device, it is important first to simply move the rotor at all. The problem of computing the torque accurately is secondary, and can be set aside for the first set of tests. Once successful operation has been demonstrated, issues about accurately measuring the torque applied can be considered, and potentially a different actuation mechanism can be implemented.

4.3.2 Capacitive Electrostatic Motor

Electrostatic actuation is a well-established staple of MEMS. Whereas electrostatic actuation is rare at the macro-scale, where electromagnetic actuation is commonly favored, electrostatic actuation is preferred at the micro- and nano-scales, where the scaling laws work in favor of the electrostatic force. While the voltages can remain essentially the same, the distances are much smaller, resulting in a stronger electric field. Electrostatic motors have been used for various linear MEMS actuation needs [108-111], including commercially available products [112, 113]. Rotational electrostatic motors have also been studied [114-116], and several successful devices constructed. (The main issue with these motors was high friction and wear in the bearing, which this work hopes to address.) It is therefore reasonable to expect that an electro static motor could be successful in actuating the CNT based Stodola rotor. However, the electrostatic motor is complicated to fabricate, so it was not chosen as the initial actuation mechanism. It might be a good candidate for use later, when more accurate measurements of the supplied torque are required.

The basic principle is that an electric potential applied between two electrodes will generate a force that tends to move the electrodes into alignment. For a rotary motor, like the one depicted schematically in Figure 4-18, the electrodes are arranged on two concentric circles. The oppositely charged electrodes are attracted by the electrostatic force (here the stator electrodes induce local charges in the rotor electrodes). Another way to consider the phenomenon is to look at the energy stored in the capacitance between the two electrodes. Just like for the elastic energy in a bent beam, the force can be computed as the derivative of the energy with respect to the relative position of the electrodes in the direction of the force. The energy in a capacitor is:

$$PE_{\text{cap}} = \frac{1}{2} C V^2 \tag{4.5}$$

Where V is the voltage across the gap and C is the capacitance, given by:

$$C = \frac{\varepsilon A_{\mathrm{cap}}}{g} \tag{4.6}$$

Where ε is the permittivity, A_{cap} is the overlapping area of the electrodes, and g is the gap spacing between the electrodes. This formula is based on the assumption that the gap is very much smaller than the overlapping length of the electrodes, allowing the fringing fields at the electrode edges to be ignored. If it is further assumed that the gap is very small compared to the motor radius, the electrodes can be "unwrapped," that is, treated like flat plates moving linearly instead of curved plates rotating.

The overlapping area between the electrodes is

$$\frac{Dt\phi}{2} \tag{4.7}$$

Where D is the rotor diameter, t is the rotor thickness, and ϕ is the angle over which the electrodes overlap. The torque in the ϕ- direction is then found as the derivative of the energy with respect to ϕ:

$$\tau_{\mathrm{cap}} = \frac{\partial PE_{\mathrm{cap}}}{\partial \phi} = \frac{1}{2}V^2 \frac{\partial}{\partial \phi}\left(\frac{\varepsilon D t \phi}{2g}\right) = \frac{1}{4}\frac{Dt}{g}\varepsilon V^2 \tag{4.8}$$

This is the torque for each electrode pair, so multiple electrode pairs can be used to increase the torque (so long as the assumption that the electrode length is large compared to the gap holds.)

The frictional torque which the electrostatic torque must overcome, assuming a constant frictional force per contact area (*i.e.* a frictional stress), is:

$$\tau_{\mathrm{fric}} = \sigma_{\mathrm{fric}}(\pi r_c^2 L) \tag{4.9}$$

with r_c being the radius of the contact interface between tubes, and L the bearing length. Based on the worst case experimental estimate for rotational friction in MWNTs from the literature [3], the frictional stress is 0.85 MPa. Assuming a 4-electrode rotor with a 2 µm thickness and 20 µm diameter, with stators that can be placed with a 500 nm clearance of the rotor, and bearing thickness of 2 µm, approximately 6 Volts would be required to overcome the frictional torque, well within the capability of any drive electronics.

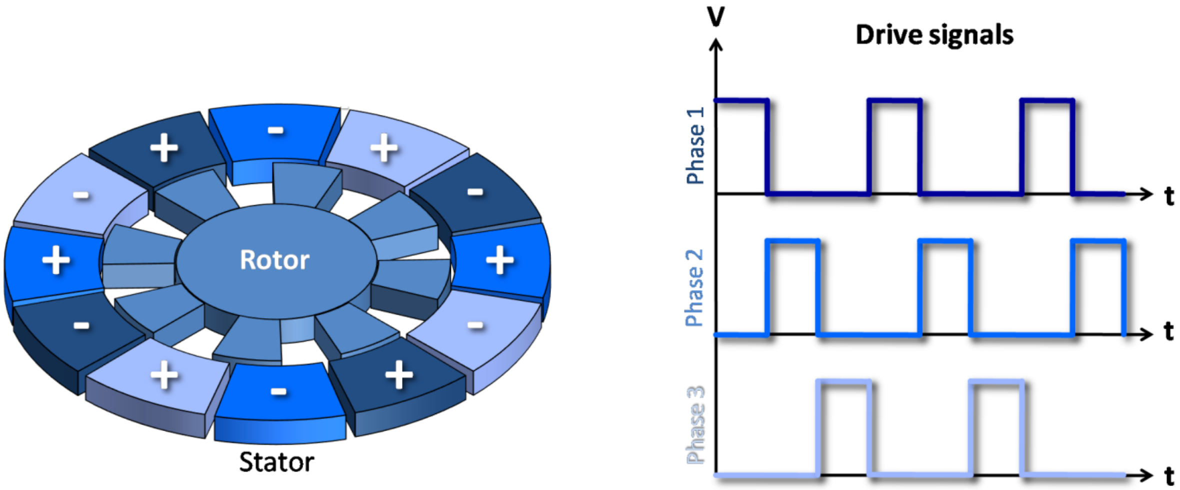

Figure 4-18: Schematic representation of a capacitive electrostatic motor. There are three phases, allowing bi-directional actuation. The staggering of the electrodes also provides full torque coverage.

The straightforward calculability of the torques provided by an electrostatic motor is an advantage for them. In addition to the simple capacitive model described above, more complicated (and more accurate) models can be developed relatively easily with the use of finite element numerical analysis.

Besides predictable performance, electrostatic actuation also provides substantial robustness. Unlike the other proposed mechanisms, the motor would be built right onto the device, providing precise control over the geometry. This would eliminate the possibility of damage by over-zealous or imprecise use of external, manually operated actuators.

Furthermore, electrostatic motors offer the promise of highly controllable operation. Step actuation is possible by simply energizing electrodes at a constant bias. With appropriate positioning of the electrodes, complete coverage of the rotation can be guaranteed, so that no matter where the rotor is it can be moved by the electrodes. Additionally, smooth operation at a precisely controlled speed is possible with application of continuously varying periodic potentials to the electrodes. All these advantages point to electrostatic actuation as the best choice for high performance rotary devices. In the long term, electrostatic actuation will likely be the most reasonable choice for all such devices.

In the short term, however, one substantial disadvantage discourages the use of electrostatic actuation for the initial testing of the device. Adding an electrostatic motor adds fabrication complexity, increasing the number of steps in the process. Rotor and stator electrodes must be added to the device, with their associated contacts and supports. With each additional step comes an additional opportunity for something to go awry. Therefore, in order to get to the point where the first device is produced, it is desirable to minimize avoidable complexity, even at the cost of device performance. An actuation scheme which is easy to fabricate will be the first one to use.

Use of an electromagnetic motor, instead of an electrostatic motor, was also considered. While successful MEMS devices utilizing electromagnetic components have been constructed [34, 117], the added complexity involved would not provide a foreseeable advantage over electrostatic drive. Incorporation of magnets requires careful conventional machining and placement of the magnets. In addition, the curie temperature of the magnets must be avoided to prevent demagnetization, which is a difficult temperature constraint for the rest of the fabrication processes. Magnetic actuation does not currently appear to be a good option.

4.3.3 Laser Radiation Pressure Drive

An actuation technique that would require less fabrication would be to use a laser to drive the device, as illustrated in Figure 4-19. By simply adding fins or paddles onto the rotor, radiation pressure (transfer of momentum from photons to the rotor) from the laser can be harnessed to drive the rotor. While radiation pressure is normally negligible at the macro-scale, it could be sufficient to provide the requisite torque, considering the small inertia of the rotor, and the (hopefully) small friction in the bearing. Laser drive is an elegant solution, requiring only a laser and the rotor itself.

Radiation pressure is computed based on the momentum of light, carried by the momentum of individual photons. The rate at which momentum is incident on a surface exposed to a laser beam is

$$\frac{dp}{dt} = \frac{P_{\text{laser}}}{c} \tag{4.10}$$

Where p is the total momentum, P_{laser} is the laser power, and c is the speed of light. If all the light is absorbed, its momentum is removed. From Newton's second law, the force required is equal to the rate of momentum change, or in other words, the laser exerts a force of

$$F_{\text{laser}} = \frac{dp}{dt} = \frac{P_{\text{laser}}}{c} \tag{4.11}$$

Some photons may be reflected, in which case their momentum is not reduced to zero, but the direction is reversed, so they impart twice as much force. If the fraction of photons reflected is denoted R, then the total force is:

$$F_{\text{laser}} = (1 + R)\frac{P_{\text{laser}}}{c} \tag{4.12}$$

If the force can be focused onto a blade protruding from the rotor, it can provide torque to overcome the friction. The torque is:

$$\tau_{\text{laser}} = F_{\text{laser}}\frac{\mathrm{D}}{2} = (1 + R)\frac{\mathrm{D}}{2}\frac{P_{\text{laser}}}{c} \tag{4.13}$$

If the rotor diameter, rotor thickness, bearing length remain the same (from equation (4.9)), and the reflectivity of the substrate is taken to be 0.4, then a laser power of 570 mW is required to overcome the friction. Lasers with this power capability are rare, but obtainable, so this method could be a conceivable way to attain actuation.

The main problem with laser radiation pressure actuation comes from the absorbed energy. The high power of the laser focused onto the tiny spot of the rotor results in a huge power density. Whatever power is not reflected by the rotor must be absorbed, and then lost as heat. Unless the reflectivity of the rotor is very high, the rotor likely reach unacceptably high temperatures before it can dissipate sufficient heat power to maintain a steady state.

Quantitatively, the problem can be understood by examining the ratio of work accomplished by the laser to the input power. This metric is a kind of efficiency, describing how much of the supplied power is used effectively to overcome the friction. The rate at which work is supplied towards overcoming friction is the product of the force and the speed:

$$\dot{W} = F_{\mathrm{laser}} \Omega \frac{D}{2} \tag{4.14}$$

The "efficiency" is then

$$\eta_{\mathrm{laser}} = \frac{\dot{W}}{P_{\mathrm{laser}}} = \frac{(1+R)}{2} \frac{\Omega D}{c} \tag{4.15}$$

Clearly, the ratio of the device speed to the speed of light is working against this scheme, and even perfect reflectivity (close to 1) would not be able to obtain any reasonable efficiency. The excess input power must be dumped as heat, and if that excess power is most of the 570 mW input power, a 20 µm device could be hard pressed to dissipate it without melting. This actuation scheme thus appears implausible for rotors moving at less-than-relativistic speeds.

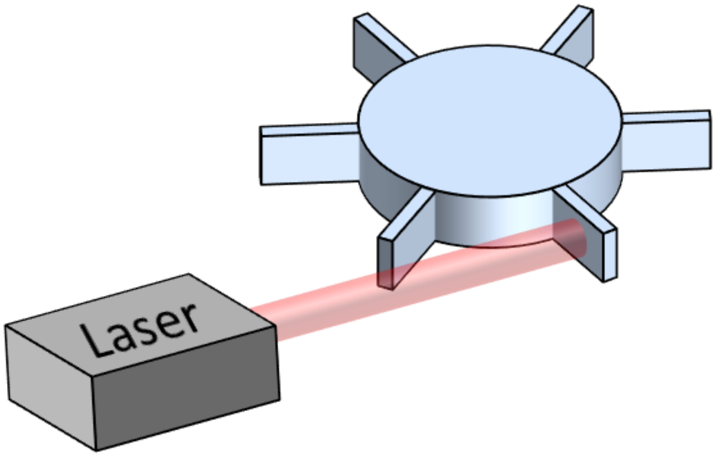

Figure 4-19: Schematic representation of laser radiation pressure drive.

Another alternative considered was the use of an ion beam instead of a laser for radiation pressure actuation. This would eliminate the heat dissipation concern, as ions are not absorbed like photons. Additionally, each ions provides substantially more momentum than a photon, so fewer ions would be required to get the requisite torque.

Two approaches to ion beam drive are possible. Micro-sized ion beam generators have been demonstrated for propulsion applications. Such a generator could conceivably be integrated onto the rotor device substrate, providing an ion beam directly at the correct position. However, such fabrication would be extremely complex and require a great deal of development, as these beam generators are still a topic of current research. Alternatively, macro-scale ion beam systems are available as machining tools for micro-fabrication. The beam from such a tool could be directed onto vanes on the rotor, transferring momentum to it. However, it might be difficult to observe actuation in progress. In both cases, ions have the capability to sputter or etch the rotor material, depending on operating parameters. Such a nanoscale device might be quickly destroyed by any etching activity, as it does not contain a great deal of mass. Even if the power could be turned down sufficiently to prevent etching, the resulting beam might not provide the thrust power needed to drive the rotor.

4.3.4 Manual Manipulation

One simple way to turn the device could be to physically push on it with a manipulator, such as those used to probe microelectronic devices. Manipulators with sub-micrometer resolution are readily available, which is precise enough to interface with the rotor. The main problem is the fear of damaging the rotor. The forces such a manipulator can exert on the rotor could be well in excess of the material strengths, not to mention any forces that would arise during operation due to imbalances in the rotor. Without any feedback on the amount of force being exerted, the operator of the manipulator could easily destroy or cripple the device accidentally.

More subtle physical manipulators might be less harmful. One possibility is to use an atomic force microscope (AFM). These devices contain a vibrating cantilever. They can sense when they are in contact with an object by observing a decrease in the vibration amplitude, caused by the cantilever bumping into the target. The problem is that AFMs are usually set up to probe in the vertical direction (perpendicular to the substrate), and wouldn't be able to provide the horizontal forces necessary to drive the device.

Another problem with manipulator-based actuation is that it is incapable of providing continuous actuation. Once the manipulator stops moving, so does the rotor. Observation of the rotor in continuous motion is desired to prove the bearing feasible, which this mechanism cannot provide. Further down the road, if friction measurements are attempted, it would be difficult to make these measurements without a high initial speed, which would likely not be achievable by a single push from a manipulator.

4.4 Testing and Data Collection

While fabrication is still in development, testing plans have been conceived, and as progress is made on fabrication, data could be gathered from functional devices. A test apparatus, depicted in Figure 4-20, has been designed and assembled.

The initial method for collecting data on rotation would be to monitor the device in the probe station's optical microscope. As air jet actuation is applied, video of the device could be recorded, capturing any successful rotation, or other motion such as torsion of the nanotube shaft, or even failure of the device. If continuous rotation of the device is achieved, video could also be used to take speed measurements up to about a hundred revolutions per minute, limited by the frame rate of the camera. While capturing video is not the most precise way to measure the device performance, it would provide a compelling demonstration of the initial successful rotation, if and when successful rotation is achieved.

In the long term, more accurate measurement could be required to take precise friction measurements that could contribute to the debate about the value and behavior of carbon nanotube friction. A simple yet effective solution would be the uses of an optical sensor such as those available from Philtec, Inc.. These sensors are capable of recording the speed of rotating devices by bouncing a light off of them, and observing the intensity change as blades or bumps pass by the light. Speeds as high as millions of revolutions per minute are directly measurable with these systems. In addition, the sensor can measure the displacement of the rotor in the direction of the light beam, by observing the reflected signal intensity variation. Such information could be used to deduce the lateral and angular displacements of the rotor due to imbalances. These calculations could then be used to confirm or adjust the dynamic model of the rotor, and measure the imbalances in the rotor.

While successful demonstration of a CNT bearing and Stodola Rotor has yet to be achieved, substantial progress has been made. Besides evaluating various MEMS processing techniques, the complete fabrication process for the device was executed, and some problems in the sequence resolved. A testing capability including actuation and measurement has been established, and is ready for the first successful rotor fabrication.

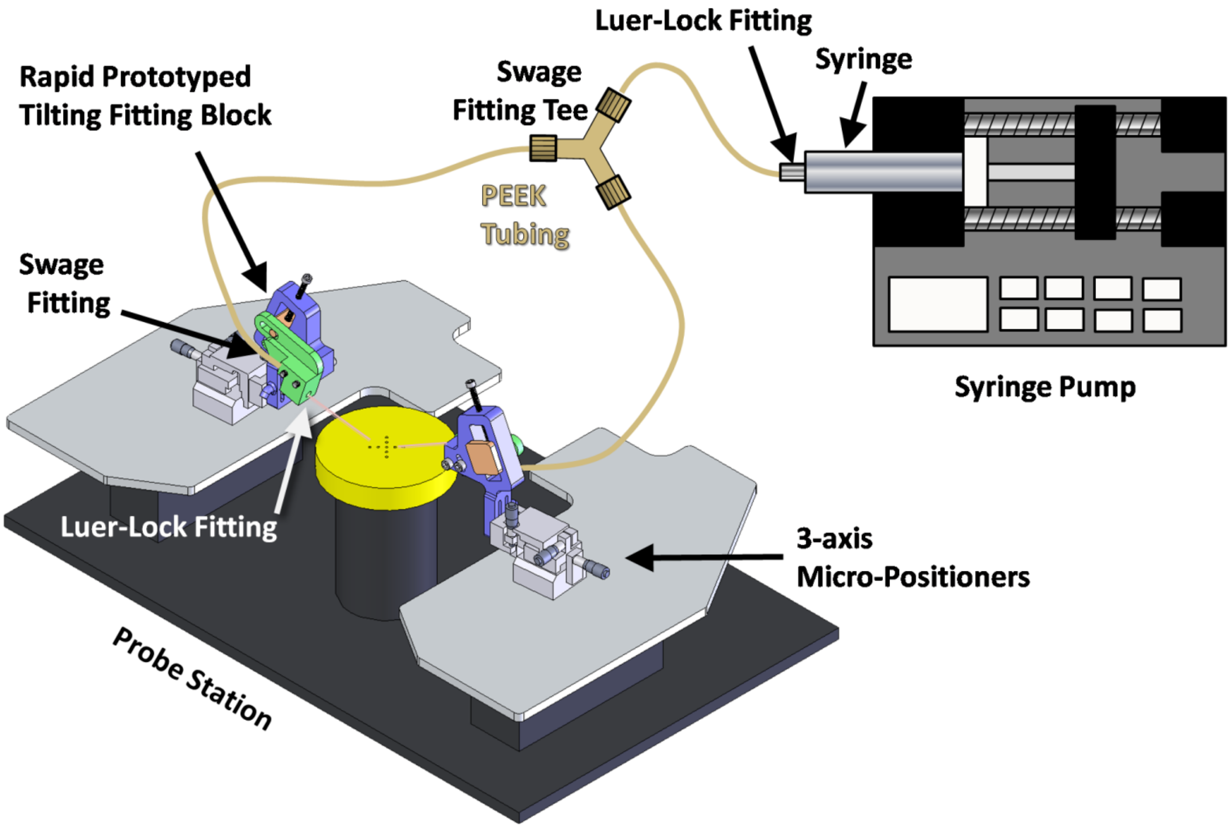

Figure 4-20: Schematic representation of the testing apparatus that would be used to initially demonstrate rotation of the CNT based Stodola rotor. The probe station includes positioning devices with one micrometer resolution, as well as an overhead optical microscope with video recording capability. The glass pipettes, secured to the positioners for precise location, are connected to a syringe pump by tubing and fittings. While a working device has yet to be produced, the test apparatus has been assembled and works as designed.

5 CONCLUSIONS

5.1 Contributions of the Project

The project has been successful in developing the concept for a nano Stodola rotor supported by a vertically aligned, CVD grown carbon nanotube. The concept should enable a wide range of novel geometries for nanotube-bearing based rotary micro-devices. The use of the bearing as a friction test stand has been conceived. The large (ten orders of magnitude) range of friction data reported in the literature invites further study, and in particular dynamic rotary friction has yet to be measured experimentally. Furthermore, the test stand concept could be used to gather data on different nanotubes, establishing correlations between friction and other governing parameters including sliding speed, nanotube size, and defect density.

A dynamic model based on classical mechanics was developed, which provides guidelines for device design. The model indicates that rotational speeds as high as millions of revolutions per minute should be achievable without violating any of the thirteen failure modes analyzed. The model estimates deflections and stresses within the device at a given operating condition, and could be useful for future device design efforts.

A fabrication process for the proposed rotor device has been developed, and the first iteration completed. The critical steps which present the most significant challenges to device fabrication have been identified, including adhesion of the catalyst for nanotube growth to the substrate, and the sacrificial layer release etch. Work is ongoing to refine the fabrication process, pushing towards a functional device. An actuation mechanism and test apparatus have been created, and are ready to be used to gather data from the first working device.

5.2 Follow On Work

There is a great deal of additional work to be done on CNT bearings and rotors based on them. While a fabrication process has been developed, there are still issues that need resolution within it. Efforts to correct the process, so that a functional device can be produced, will continue. If successful demonstration of a simple CNT based Stodola Rotor can be achieved, the next step would be to pursue the original scientific goals of the project, namely, investigation of the nature and value of friction in rotating MWNT systems. Finally, a working device could pave the way for numerous applications, which will take additional development effort to bring to fruition.

5.2.1 Development and Improvement of the Fabrication Process

It is not unusual for a micro-fabrication process to be unsuccessful on its first attempt. Because of the difficulty in developing the individual techniques and predicting their interactions, it takes iteration to establish a complete process that provides repeatable, functional devices. More time will be spend on this device's fabrication method, potentially resulting in a robust, complete fabrication process.

The first issue that needs to be addressed is the difficulty in placing catalyst dots for CNT growth, discussed in section 4.2.2.1. Because the e-beam patterning technique had already been demonstrated, this step in the process was not expected to pose a problem. Thorough investigation will be required to determine, if possible, what difference between the demonstrated successful process and the present method leads to the diffusion of the catalyst particles, and the delamination of the chromium adhesion layer.

In order to isolate the cause of the problem, many experiments will need to be conducted, with careful control of all possible influencing factor. One potential cause of the problem could be related to the specific e-beam patterning tool used for this work. To eliminate that possibility, a separate e-beam tool is becoming available that will be tested against each experiment conducted on the first tool. This will also allow faster turn-around time on each experiment, increasing the speed with which potential causes of the diffusion problem can be eliminated.

Another possible influencing factor is the method of depositing the adhesion layer. Two different evaporators have been used, but other methods such as sputtering could also be tried. The cleaning process employed was also rudimentary, involving only a dip in solvent. More thorough cleaning methods, such as brief exposure to oxygen plasma (which removes organic material) may help prevent contaminant particles from interfering with the bond between the adhesion layer and the substrate.

The problem with the resist being destroyed during the silicon etching step (from section 4.2.2.6) is not as troublesome, as there is a clear path to resolution. Between using a thicker resist, possibly a thinner silicon layer, and adjusting the etch parameters, a complete silicon etch should be possible without completely destroying the resist. After all, a different resist (designed for photolithography) was able to protect the silicon for a suitable time. Even if the problem cannot be resolved through changes to the resist and etch parameters, the other option for the silicon etch (DRIE) is available as a fallback.

The other serious issue is the unexplained behavior of the final HF release step, described in section 4.2.2.7. This is most problematic because the etch produced completely unexpected and counterintuitive results: when SiO_2 was supposed to be removed, instead an unidentified, rough, porous material appears to have been added to the structure.

The first course of action to correct this problem should be to eliminate all the unnecessary complications in the process. For example, glass substrates were used in the process for the sole reason that they were available, and working occasionally for another nanotube growth experiment. The fact that the substrate was glass could well be a significant factor in the unexplained behavior, as HF specifically targets silicon oxides such as glass. It would be desirable to resolve the nanotube growth issues on a plain silicon substrate as originally planned, so that this potential problem could be eliminated.

Another step to determine the cause of the problem would be to conduct material analysis on the unknown porous material. If the material turns out to be glass, then it would be likely to have formed out of the glass substrate. If it was silicon, it might indicate that there was an undetected problem with the silicon etch, leaving material behind in that somehow catalyzed the strange, porous formations. If it was discovered to be another material, it might lead to discovery of other potential causes.

The work in the immediate future will focus on resolving these problems in the fabrication process. If these issues can be resolved, a device may be completed, leading to the first demonstration of a vertically-aligned CNT based device. Once that is accomplished, the further scientific and engineering goals can be addressed.

5.2.2 Science

The main scientific goal of the program is to gather data on the friction performance of MWNT bearings. This data is needed, as disagreement abounds about the quantitative and qualitative nature of MWNT friction (discussed in section 2.2). Data collected from thorough experiments could help to bridge the gaps between current experimental and theoretical investigations of MWNT friction.

One important facet of friction that might be pursued with a CNT bearing and Stodola Rotor is the behavior of friction under continuous, constant motion. All experimental measurements of MWNT friction thus far have either used linear bearing systems, which have a limited travel, or only studied partial rotation of rotary bearing systems. A friction test stand that is capable of running the bearing at a consistent speed over a substantial period of time could provide knowledge of how the friction performance holds up in the long run. Additionally, much higher speeds might be attainable if the direction of motion did not need to be reversed after a few micrometers of travel. Initial efforts could focus on obtaining the first experimental measurement of such high speed, continuous friction.

If the rotor device fabrication process can be established to repeatably produce functional devices, it would likely be useful to pursue the electrostatic actuation option discussed in section 4.3.2. Rather than the air drive actuation scheme, which is less complicated to implement, but whose torque capability is difficult to predict , the electrostatic option should provide the opportunity for more precise measurements, as well as greatly enhanced predictability and reliability. If many friction tests are to be performed, it would most likely be worth the additional effort to work the electrostatic motor into the fabrication process in order to obtain the substantial performance enhancement.

The next step beyond establishing the capability to measure friction accurately would be to begin using the device as a measurement tool across a wide variety of nanotubes. Most importantly, the way friction depends on the type and density of defects could be examined. If the device construction becomes reliable, and its measurements are repeatable, building identical rotors onto nanotubes of varying defect densities would provide a method to gain comparable friction data across a wide range of nanotubes. Additional parameters, such as the effects of temperature could also be studied. In generally, the ability to produce nanotube friction testers quickly and reliably would open the door to investigating all manner of influences that might or might not play a role in nanotube friction.

5.2.3 Applications

Besides the scientific objective of contributing significant knowledge in the field of nanotube friction, a working CNT based Stodola rotor would also be a starting point for many applications. Essentially any rotating machine might take advantage of the bearing technology if it can provide the low friction, high durability operation that is expected. Even if the friction turns out to be higher than expected, because the nanotube is structurally robust, it can support large rotors on a small diameter shaft, resulting in a small lever arm and low frictional torque. Besides the promise of excellent performance, CNT bearings have a number of special properties that could be useful for devices. For example, CNT bearings should not cease to operate at vacuum conditions. They also exhibit high conductivity, which could be used to establish an electrical path to the rotor in a spinning device. All these properties make CNT bearings an exciting technology to pursue for use in micro- and nano-machines.

One application in particular seems well-matched to the CNT bearing: vacuum pumping. There is very high demand for pumping capabilities in a small package. Chemical and biological sensors including spectrometers [38, 41-43] and chromatographs [39, 40] have been developed using MEMS technology for portability and inexpensive operation. However, all these devices have a common issue – they require a pump, either to push analyte through the system, or to pull a vacuum that the system requires for operation. The requirements of these systems can comfortably be met by current macro-scale pumping systems, but that defeats the purpose of miniaturization in the first place. A chemistry-lab-on-a-chip is not any better than a chemistry-lab-on-a-tabletop if it requires a tabletop-sized pump to operate.

In order to address this problem, there have been efforts to develop MEMS pumping systems. Many different approaches have been taken, including diaphragm pumps [118, 119], scroll pumps [120], thermal transpiration pumps [121], and Knudsen pumps [122], as well as other novel designs [123-125]. However, these systems have fallen short of the requirements of the MEMS sensors for which they are needed. In particular, the vacuum performance of these pumps can at best reach pressures of approximately 2 kPa, whereas some for the sensors call for high vacuum in the range of tenths or hundredths of a Pascal.

One reason for the failure of MEMS pumps to approach the capabilities of macro-scale vacuum pumps is the fact that the most common pump design for attaining pressures in this range and lower, called a turbomolecular pump, has not been practical thus far, because it requires extraordinarily high speed rotating components (with tip speeds of hundreds of meters per second). No previous MEMS bearings could achieve such speeds in vacuum.

While a turbomolecular pump seems at first to resemble turbomachinery such as compressors from aircraft turbine engines, with staged axial (or radial) rotors and stators with many blades, the principle of operation is quite different. While compressors operate well in the continuum regime, where the laws of fluid dynamics apply, ultra-high vacuum conditions are not governed by the same laws.

Under high vacuum, molecules of air travel in essentially straight lines, and are not influenced by “information” transmitted from nearby particles via pressure. There are no such phenomena as streamlines or flow separation. The blades of the pump are completely flat, and are used to strike individual molecules of gas, rather than smoothly add work to a flow. By angling the blades and moving them at as high a speed as possible, the probability that impacted molecules are pushed to one side is increased. For an effective turbomolecular pump, then, the primary performance parameter is the linear speed of the blades through the gas, which should be as high as possible.

Typical macro turbomolecular pumps may have a diameter of about 10 cm, and operate at 50,000 rpm in order to be effective, corresponding to a blade speed of 260 m/s. To achieve similar performance, a MEMS pump with a diameter of 100 µm would have to spin much faster, at 50 million rpm. This is an extremely demanding speed for any bearing, but if the expected low friction and low wear properties of the MWNT bearing system are demonstrated as effective, the dynamic model predicts that such speeds would be close to attainable. With the use of a doubly supported shaft (instead of the cantilevered Stodola configuration), the stiffness could be dramatically improved, potentially bringing such designs in reach. In other words, CNT bearings might be able to make MEMS turbomolecular pumps possible, enabling much stronger vacuum performance.

The first steps towards designing and fabricating a turbomolecular pump based on the CNT bearing would likely be to stiffen the system by adding the other support to the shaft and reducing clearance. A system of arranging multiple stages would also need to be devised, as the axial arrangement common in macro pumps would be nearly impossible to fabricate at the micro-scale.

Another application that is particularly attractive for the CNT bearing would be a spinning-mass gyroscope. MEMS gyroscopes based on the tuning-fork principle are well established, but have so far been less accurate than traditional macro systems, which are bulky, power-hungry, and expensive. A bearing with the capability for high-speed rotation could make the conventional spinning-mass gyroscope design available at the micro scale, combining the best of performance and size.

One of the reasons nanotubes show such promise for high-accuracy gyroscopes is their expected low amount of "wobble," or play in the bearing. Because the tubes are separated by a few angstroms, there is not much room for the shaft to move. Since wobble is a strong contributor to error in spinning gyroscopes, its elimination or reduction would be desirable.

The expected low friction in MWNT bearings also lends itself to spinning gyroscope performance. The less power dissipation is caused by friction, the less power is needed to operate the gyro, leading to ultra-portable systems. Even if the friction turns out to be high, the lever arm of the friction torque, which is based on the nanotube diameter, might be thousandths of the rotor diameter or less, so that the input torque (which could make use of the larger lever arm of the rotor) has substantial mechanical advantage.

A final reason that MWNT bearings are attractive for gyroscopes is the expectation of reliability. Self repair of the bearings was noted over time by prior works (see section 2.1.2.5), indicating that a system built on these bearings may be able to operate for extremely long times quite reliably. That capability, along with the very low weight inherent in anything micro-sized, makes such gyroscopes seem attractive for all kinds of air- and space navigation needs.

As with the vacuum pump, the first steps toward building a CNT based gyroscope would be to stiffen the system, to allow higher speeds to be attained without fear of large displacements or failure. Additionally, all of the sensors, gimbals, and other parts that are required for a functional rotating gyroscope would need to be designed for incorporation into the motor.

Both the vacuum pump and gyroscope application concepts indicate that there is a great deal of promise in MWNT bearings. While these particular applications jump out as particularly appetizing, there is no end to the types of micro-scale rotating devices that could be envisioned with CNT bearings. If the initial demonstration and friction measurements can be accomplished, future work on these and other applications would be exciting to pursue.

6 APPENDIX –DERIVATION OF STATIC CONSTRAINTS

6.1 Euler Beam Deflections

The basic equation governing a beam in transverse loading, if deflections are taken to be small, is

$$EI_{xx}\frac{\partial^4 v}{\partial z^4} = p \tag{6.1}$$

where v is the transverse deflection in the y-direction, and p is the transverse loading force per unit length, both functions of z, the coordinate along the beam length. E is the Young's modulus, and I_{xx} is the second moment of area of the tube's cross-section, both constant for the length of the tube. Additionally, the subscript "xx" is dropped because the tube is axisymmetric about the z-axis, and all its second moments of area in the cross sectional plane are equal. The equation can equivalently refer to transverse deflections in the x-direction, by substituting u for v. For the device described here, the only loads on the beam occur at the base and the tip, so $p = 0$, leading to the homogeneous form of equation (6.1):

$$EI\frac{\partial^4 v}{\partial z^4} = 0 \tag{6.2}$$

The solution is a polynomial:

$$v(z) = Az^3 + Bz^2 + Cz + D \tag{6.3}$$

The boundary conditions for the device must be specified to determine the constants. At the base of the tube, where it is attached to the substrate, the beam is fixed, allowing no deflection or slope at this coordinate:

$$v|_{z=0} = \left.\frac{\partial v}{\partial z}\right|_{z=0} = 0 \tag{6.4}$$

The other end of the tube is free, with unconstrained position and slope. However, we are interested in the deflections due to a particular load. Therefore, the internal shear and moment at the end of the tube must be equal and opposite to the applied force and moment in that plane.

$$(M_x)_{z=L} = EI\left(\frac{\partial^2 v}{\partial z^2}\right)_{z=L} = -M_{x,\,\mathrm{applied}} \tag{6.5}$$

$$\left(V_y\right)_{z=L} = \left(\frac{\partial M_x}{\partial z}\right)_{z=L} = \frac{\partial}{\partial z}\left[EI\left(\frac{\partial^2 v}{\partial z^2}\right)\right]_{z=L} = -F_{y,\,\text{applied}} \tag{6.6}$$

Constants C and D can be found immediately from boundary condition (6.4)):

$$\begin{aligned} v|_{\mathrm{z}=0} &= A(0)^3 + B(0)^2 + C(0) + D \\ &= D = 0 \end{aligned} \tag{6.7}$$

$$\begin{aligned} \left.\frac{\partial v}{\partial z}\right|_{z=0} &= 3A(0)^2 + 2B(0) + C \\ &= C = 0 \end{aligned} \tag{6.8}$$

The other two boundary conditions (6.5) and (6.6) lead to the values of constants A and B:

$$\frac{\partial}{\partial z}\left[EI\left(\frac{\partial^2 v}{\partial z^2}\right)\right]_{z=L} = EI(6A) = -F_{y,\ \text{applied}} \tag{6.9}$$

$$A = -\frac{F_{y,\,\text{applied}}}{6EI} \tag{6.10}$$

$$EI\left(\frac{\partial^2 v}{\partial z^2}\right)_{z=L} = EI(6AL + 2B) = -M_{x,\,\text{applied}} \tag{6.11}$$

$$B = \frac{-M_{x,\ \text{applied}} + LF_{y,\,\text{applied}}}{2EI} \tag{6.12}$$

Substituting the values for the constants back into Equation (6.3) gives the y-displacement of the nanotube in terms of the known applied forces and torques to the disk:

$$v(z) = \frac{F_{y,\,\text{applied}}}{6EI}\left(-z^3 + 3Lz^2\right) - \frac{M_{x,\,\text{applied}}}{2EI}z^2 \tag{6.13}$$

The deflections in the other plane can be found in the same way:

$$u(z) = \frac{F_{x,\,\text{applied}}}{6EI}(-z^3 + 3Lz^2) - \frac{M_{y,\,\text{applied}}}{2EI}z^2 \tag{6.14}$$

In addition to the linear deflections, the angular deflections due to these loads can be computed. The angle that the beam makes with the z-axis can be found from the slope:

$$\theta_x = \tan^{-1}\frac{\partial v}{\partial z} \tag{6.15}$$

$$\theta_y = \tan^{-1}\frac{\partial u}{\partial z} \tag{6.16}$$

Where θ_x and θ_y are the angles about the x- and y-axes, respectively. Since angles are assumed to be small, these can be approximated by:

$$\begin{aligned}\theta_x &= \frac{\partial v}{\partial z} \\ &= \frac{F_{y,\,\text{applied}}}{2EI}(-z^2 + 4Lz) - \frac{M_{x,\,\text{applied}}}{EI}z\end{aligned} \tag{6.17}$$

$$\begin{aligned}\theta_y &= \frac{\partial u}{\partial z} \\ &= \frac{F_{x,\,\text{applied}}}{2EI}(-z^2 + 4Lz) - \frac{M_{y,\,\text{applied}}}{EI}z\end{aligned} \tag{6.18}$$

These results allow the computation of the static deflection of the nanotube shaft in response to external moments and forces applied in the nominal plane of rotation of the disk. The forces might arise from gravitational or other accelerations acting on the rotor disk. For this device, the only load assumed applied was the weight of the rotor disk acting transversely to the tube axis at the tip of the tube ($F_{y,\,\text{applied}} = W$) However, because this load is separated from the beam tip by half of the rotor thickness (which may be a significant fraction of L), there is also an external moment applied:

$$M_{x,\,\text{applied}} = -Wa_z \tag{6.19}$$

where $a_z = t/2$ is the axial displacement between the rotor center of mass and the beam tip. The maximum deflection is at the beam tip for this tip-loaded case, and is given the symbol

$$\delta_{beam} = v(L). \tag{6.20}$$

Note that the deflection could equivalently be $u(L)$ or $\sqrt{u(L)^2 + v(L)^2}$, depending on the orientation of the transverse load. For simplicity, the yz-plane bending case is used. The resulting static lateral tip deflection from this load is:

$$\begin{aligned} \delta_{beam} &= v(L) \\ &= \frac{F_{y,\text{ applied}}}{6EI}\left(-L^3 + 3L(L)^2\right) - \frac{M_{x,\text{ applied}}}{2EI}L^2 \\ &= \frac{WL^3}{3EI} + \frac{WL^2 a_z}{2EI} \end{aligned} \tag{6.21}$$

For the device, this static beam tip deflection was constrained to be less than 10% of the total beam length. The static angular displacements were not constrained, because an angular constraint that takes dynamic factors into account was included.

6.2 Euler Column Deflections

Euler column deflections occur when a compressive load is applied at an offset from the centroid of the column cross section (eccentrically). The starting point is once again Euler's equation for beam theory:

$$EI\frac{\partial^4 v}{\partial z^4} + P\frac{\partial^2 v}{\partial z^2} = 0 \tag{6.22}$$

For which the solution remains

$$v(z) = A\sin\left(z\sqrt{\frac{P}{EI}}\right) + B\cos\left(z\sqrt{\frac{P}{EI}}\right) + Cz + D \tag{6.23}$$

The boundary conditions at the fixed end are the same as for the buckling analysis:

$$v|_{z=0} = \left.\frac{\partial v}{\partial z}\right|_{z=0} = 0 \tag{6.24}$$

as is the shear boundary condition:

$$\left(V_y\right)_{z=L} = -F_{y,\text{ applied}} = -P\left.\frac{\partial v}{\partial z}\right|_{z=L} \tag{6.25}$$

The moment boundary condition on the beam tip has changed, however. Because the axial load P is not applied at the centroid of the beam tip, it causes a moment of Pe, where e is the eccentricity, or distance between the centroid and the point at which P acts. This moment is the internal moment at the tip:

$$(M_x)_{z=L} = M_{x,\,\text{applied}} = Pe \tag{6.26}$$

Starting with the shear boundary condition C can be found:

$$\begin{aligned}(V_y)_{z=L} &= EI\left(\frac{\partial^3 v}{\partial z^3}\right)_{z=L} \\ &= EI\left(\frac{P}{EI}\right)^{\frac{3}{2}}\left[-A\cos\left(L\sqrt{\frac{P}{EI}}\right) + B\sin\left(L\sqrt{\frac{P}{EI}}\right)\right]\end{aligned} \tag{6.27}$$

$$\begin{aligned}-F_{y,\,\text{applied}} &= -P\left.\frac{\partial v}{\partial z}\right|_{z=L} \\ &= -P\left[A\sqrt{\frac{P}{EI}}\cos\left(L\sqrt{\frac{P}{EI}}\right) - B\sqrt{\frac{P}{EI}}\sin\left(\sqrt{\frac{P}{EI}}\right) + C\right]\end{aligned} \tag{6.28}$$

$$(V_y)_{z=L} = -F_{y,\,\text{applied}} \tag{6.29}$$

$$\begin{aligned}&EI\left(\frac{P}{EI}\right)^{\frac{3}{2}}\left[-A\cos\left(L\sqrt{\frac{P}{EI}}\right) + B\sin\left(L\sqrt{\frac{P}{EI}}\right)\right] \\ &\qquad = -P\left[A\sqrt{\frac{P}{EI}}\cos\left(L\sqrt{\frac{P}{EI}}\right) - B\sqrt{\frac{P}{EI}}\sin\left(\sqrt{\frac{P}{EI}}\right) + C\right]\end{aligned} \tag{6.30}$$

$$-A\cos\left(L\sqrt{\frac{P}{EI}}\right) + B\sin\left(L\sqrt{\frac{P}{EI}}\right) = -A\cos\left(L\sqrt{\frac{P}{EI}}\right) + B\sin\left(L\sqrt{\frac{P}{EI}}\right) + C \tag{6.31}$$

$$C = 0 \tag{6.32}$$

Then from the slope boundary condition at the root, A is found:

$$\begin{aligned}\left.\frac{\partial v}{\partial z}\right|_{z=0} &= A\sqrt{\frac{P}{EI}}\cos\left(0\sqrt{\frac{P}{EI}}\right) - B\sqrt{\frac{P}{EI}}\sin\left(0\sqrt{\frac{P}{EI}}\right) + C \\ &= A\sqrt{\frac{P}{EI}} - B(0) + C = 0\end{aligned} \quad \textbf{(6.33)}$$

$$A = -C\sqrt{\frac{EI}{P}} = 0 \quad \textbf{(6.34)}$$

The moment boundary condition at the tip allows B to be found:

$$\begin{aligned}(M_x)_{z=L} &= EI\left(\frac{\partial^2 v}{\partial z^2}\right)_{z=L} \\ &= -AP\sin\left(L\sqrt{\frac{P}{EI}}\right) - BP\cos\left(L\sqrt{\frac{P}{EI}}\right) \\ &= -BP\cos\left(L\sqrt{\frac{P}{EI}}\right) \\ &= M_{x,\,\text{applied}} = Pe\end{aligned} \quad \textbf{(6.35)}$$

$$-BP\cos\left(L\sqrt{\frac{P}{EI}}\right) = Pe \quad \textbf{(6.36)}$$

$$B = -e\sec\left(L\sqrt{\frac{P}{EI}}\right) \quad \textbf{(6.37)}$$

D can finally be found from the displacement boundary condition at the beam root:

$$\begin{aligned} v|_{z=0} &= A\sin\left(z\sqrt{\frac{P}{EI}}\right) + B\cos\left(z\sqrt{\frac{P}{EI}}\right) + Cz + D \\ &= A\sin\left(0\sqrt{\frac{P}{EI}}\right) + B\cos\left(0\sqrt{\frac{P}{EI}}\right) + C(0) + D \\ &= -e\sec\left(L\sqrt{\frac{P}{EI}}\right) + D = 0 \end{aligned} \tag{6.38}$$

$$D = e\sec\left(L\sqrt{\frac{P}{EI}}\right) \tag{6.39}$$

Now that all the constants have been found, the deflection of the entire beam is known from the compressive tip load:

$$\begin{aligned} v(z) &= A\sin\left(z\sqrt{\frac{P}{EI}}\right) + B\cos\left(z\sqrt{\frac{P}{EI}}\right) + Cz + D \\ &= e\sec\left(L\sqrt{\frac{P}{EI}}\right)\left[1 - \cos\left(z\sqrt{\frac{P}{EI}}\right)\right] \end{aligned} \tag{6.40}$$

The maximum deflection occurs at the beam tip:

$$\delta_{\text{column}} = v(L) = e\left[\sec\left(L\sqrt{\frac{P}{EI}}\right) - 1\right] \tag{6.41}$$

6.3 Euler Buckling

Given a general beam-column subjected to an external compressive force in addition to the transverse force, the governing equation is more complicated than for the transverse load case:

$$EI\frac{\partial^4 v}{\partial z^4} + P\frac{\partial^2 v}{\partial z^2} = p \tag{6.42}$$

Here P denotes a compressive load on the end of the beam. As before, the only loads applied to the beam are at the end, so the equation becomes homogeneous:

$$EI\frac{\partial^4 v}{\partial z^4} + P\frac{\partial^2 v}{\partial z^2} = 0 \tag{6.43}$$

The general solution to the differential equation is:

$$v(z) = A\sin\left(z\sqrt{\frac{P}{EI}}\right) + B\cos\left(z\sqrt{\frac{P}{EI}}\right) + Cz + D \tag{6.44}$$

The boundary conditions at the fixed end of the tube are the same as before, as in equation (6.4). Also, there is no applied moment, so the boundary condition in (6.5) is set to zero. For the final boundary condition in (6.6), there is an applied shear load resulting from the deflection of the beam: A component of the compressive load acts in the direction parallel to the beam axis. This component is found through the tangent of the angular deflection at the beam tip:

$$F_{y,\,\text{applied}} = P\tan\theta_x\,\Big|_{z=L} = P\frac{\partial v}{\partial z}\Big|_{z=L} \tag{6.45}$$

From the fixed end boundary conditions in (6.4), C can be found in terms of A:

$$\begin{aligned}\frac{\partial v}{\partial z}\Big|_{z=0} &= A\sqrt{\frac{P}{EI}}\cos\left(0\sqrt{\frac{P}{EI}}\right) - B\sqrt{\frac{P}{EI}}\sin\left(0\sqrt{\frac{P}{EI}}\right) + C \\ &= A\sqrt{\frac{P}{EI}} - B(0) + C = 0\end{aligned} \tag{6.46}$$

$$C = -A\sqrt{\frac{P}{EI}} \tag{6.47}$$

From the moment boundary condition, a relation can be established between B and A:

$$
\begin{aligned}
(M_x)_{z=L} &= EI\left(\frac{\partial^2 v}{\partial z^2}\right)_{z=L} \\
&= -AP\sin\left(L\sqrt{\frac{P}{EI}}\right) - BP\cos\left(L\sqrt{\frac{P}{EI}}\right) = 0
\end{aligned}
\tag{6.48}
$$

$$
A\sin\left(L\sqrt{\frac{P}{EI}}\right) + B\cos\left(L\sqrt{\frac{P}{EI}}\right) = 0
\tag{6.49}
$$

Then from the shear boundary condition in (6.6) along with (6.45):

$$
\begin{aligned}
\left(V_y\right)_{z=L} &= \left(\frac{\partial M}{\partial z}\right)_{z=L} = \frac{\partial}{\partial z}\left[EI\left(\frac{\partial^2 v}{\partial z^2}\right)\right]_{z=L} \\
&= -AP\sqrt{\frac{P}{EI}}\cos\left(L\sqrt{\frac{P}{EI}}\right) + BP\sqrt{\frac{P}{EI}}\sin\left(L\sqrt{\frac{P}{EI}}\right) \\
&= P\sqrt{\frac{P}{EI}}\left[B\sin\left(L\sqrt{\frac{P}{EI}}\right) - A\cos\left(L\sqrt{\frac{P}{EI}}\right)\right]
\end{aligned}
\tag{6.50}
$$

$$
\begin{aligned}
F_{y,\text{ applied}} &= P\left.\frac{\partial v}{\partial z}\right|_{z=L} \\
&= AP\sqrt{\frac{P}{EI}}\cos\left(L\sqrt{\frac{P}{EI}}\right) - BP\sqrt{\frac{P}{EI}}\sin\left(L\sqrt{\frac{P}{EI}}\right) + CP \\
&= P\sqrt{\frac{P}{EI}}\left[A\cos\left(L\sqrt{\frac{P}{EI}}\right) - B\sin\left(L\sqrt{\frac{P}{EI}}\right) - A\right]
\end{aligned}
\tag{6.51}
$$

$$
\left(V_y\right)_{z=L} = -F_{y,\text{ applied}}
\tag{6.52}
$$

$$\begin{aligned} P\sqrt{\frac{P}{EI}}\left[B\sin\left(L\sqrt{\frac{P}{EI}}\right)-A\cos\left(L\sqrt{\frac{P}{EI}}\right)\right] \\ = -P\sqrt{\frac{P}{EI}}\left[A\cos\left(L\sqrt{\frac{P}{EI}}\right)-B\sin\left(L\sqrt{\frac{P}{EI}}\right)-A\right] \end{aligned} \tag{6.53}$$

$$0 = A \tag{6.54}$$

And then finally the value of A can be substituted back into (6.44):

$$\begin{aligned} A\sin\left(L\sqrt{\frac{P}{EI}}\right)+B\cos\left(L\sqrt{\frac{P}{EI}}\right)=0 \\ B\cos\left(L\sqrt{\frac{P}{EI}}\right)=0 \end{aligned} \tag{6.55}$$

This equation has two solutions. Clearly $B = 0$ is a solution, but this solution is trivial and does not say anything about the buckling load. However, the equation is also solved for

$$\cos\left(L\sqrt{\frac{P}{EI}}\right)=0 \tag{6.56}$$

which is true for

$$L\sqrt{\frac{P}{EI}}=\pi\left(n+\frac{1}{2}\right) \tag{6.57}$$

$$P=\frac{\pi^2\left(n+\frac{1}{2}\right)^2 EI}{L^2} \tag{6.58}$$

Where n is any whole number. This result indicates that the equation is satisfied for this load, with arbitrarily large B, or in other words, infinite deflection. That means this value of the load P is the load at which the column will buckle. The smallest positive value of P is the limit, above which failure can occur, and is called the critical buckling load P_{critical}:

$$P_{\text{crit, Euler}} = \frac{\pi^2 EI}{4L^2} \tag{6.59}$$

Here the subscript “Euler” indicates that this is the maximum safe load to avoid buckling in the classical Euler mode. For a device design to be viable, it must not fail in the Euler buckling mode, so the rotor weight was constrained to be below the Euler critical buckling load.

7 APPENDIX - DERIVATION OF THE EQUATIONS OF MOTION

7.1 Degrees of Freedom

The Stodola rotordynamic model is illustrated in Figure 7-1. The model consists of a thin rigid disk mounted on the end of an elastic cantilever beam. As the beam deflects, the center of the disk translates. Additionally, the disk tilts with the bending of the beam, besides rotating about the nominal bearing axis. In order to describe the position and orientation of the disk, it is helpful to consider five coordinate systems, illustrated in Figure 7-1, and denoted by subscripts 1 through 5.

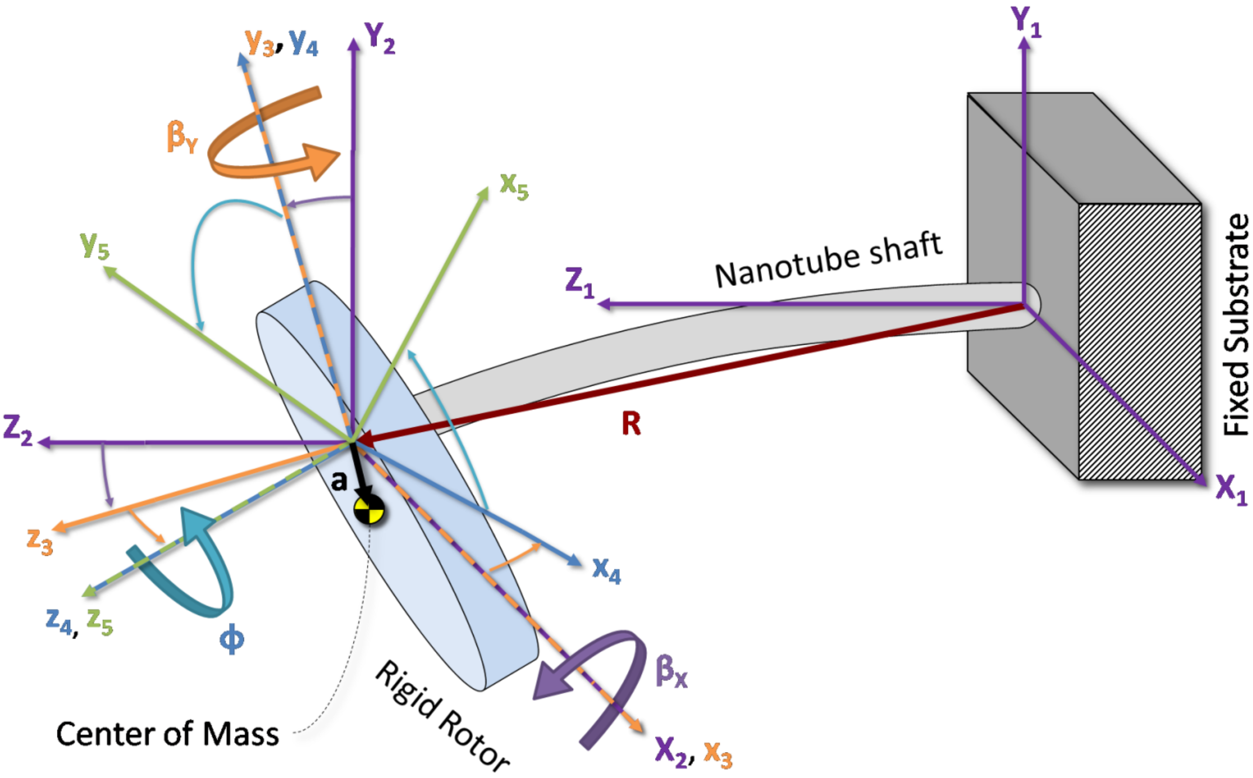

Figure 7-1: Stodola rotor coordinate systems. System 1 is inertial, fixed at support. System 2 has its origin at the disk center; position vector R describes its location. System 3 is tilted about x, and System 4 is tilted about x, then y. System 5 is fixed on the disk, i.e. tilted about x, then y, and then spun around the nominal axis of symmetry, z_5.

Coordinate system 1 (shown in purple) is fixed at the base of the device. This is an inertial frame, from which all the other frames are based. The axes names are capitalized here to indicate that it is not rotated. However, the disk itself is not inertial, but is allowed to deflect relative to the base as the nanotube axle bends. These deflections are represented by the position vector from the beam root to the disk center $\vec{R}_1$. Equivalently, $\vec{R}_1$ describes the location of the origin of the second coordinate system in the coordinates of the first (fixed inertial) system. Since the length of the beam is constant, the small angle assumption requires that the z-displacement is always equal to the beam length:

$$R_{1Z} \equiv L \tag{7.1}$$

The remaining two components of $\vec{R}_1$ are free, and describe the location of the second coordinate frame. However, the second coordinate frame does not rotate relative to the first frame.

Besides translating as described by $\vec{R}_1$ and coordinate frames 1 and 2, the disk also rotates, both with the spinning of the disk and with the beam deflections. The disk orientation is described by the three Euler angles β_{X_2}, β_{Y_3}, and ϕ_4, taken in that order. The disk is first tilted about the x_2 axis bringing it from frame 2 (purple) to frame 3 (orange). Then the disk is tilted about the y_3 axis bringing it from frame 3 (orange) to frame 4 (blue). Finally, the spin angle of the disk about its axis of symmetry z_4 brings it from frame 4 (blue) to frame 5 (green). This final fifth coordinate system is fixed on the disk.

It is important to note the rationale for keeping the Euler angles β_{X_2} and β_{Y_3} in the non-rotating frame, rather than the rotating frame. The important realization is that the nanotube beam shaft does not spin here. Unlike other rotating systems where the axle may be attached to the rotor and spin with it, here the axle is built into the substrate. The rotational bearing interface is between inner and outer shells of the nanotube away from the base, near the beam tip. Since the beam is fixed, the description of its bending reaction forces and moments should also be described in the fixed frame, to avoid having to work with time-varying elastic constants as the frame rotates. Therefore the Euler angles are also kept in the non-rotating frame.

The inertia tensor of the disk, however, is more easily determined in the rotating frame fixed to the disk. In the rotating frame, the inertia tensor is time-invariant. However, in order to keep the elastic constants for the beam time-invariant, the inertia tensor will end up being converted into the stationary frame as well, so that the entire equations of motion will be expressed in the inertial, non-rotating frame.

Rotation matrices can be defined which transform coordinates given in one frame to another. These matrices will be denoted with subscripts, i.e. A_{34} transforms from frame 4 to frame 3 when multiplied on the left of a column vector. The forms of the rotation matrices are well known:

$$A_{32} = \begin{bmatrix} 1 & 0 & 0 \\ 0 & \cos(\beta_X) & \sin(\beta_X) \\ 0 & -\sin(\beta_X) & \cos(\beta_X) \end{bmatrix} \tag{7.2}$$

$$A_{43} = \begin{bmatrix} \cos(\beta_Y) & 0 & -\sin(\beta_Y) \\ 0 & 1 & 0 \\ \sin(\beta_Y) & 0 & \cos(\beta_Y) \end{bmatrix} \tag{7.3}$$

$$A_{54} = \begin{bmatrix} \cos(\phi) & \sin(\phi) & 0 \\ -\sin(\phi) & \cos(\phi) & 0 \\ 0 & 0 & 1 \end{bmatrix} \tag{7.4}$$

The overall transformation matrix from frame 2 to frame 5 is then, using $c\phi$ to indicate $\cos(\phi)$, *etc.*:

$$
\begin{aligned}
A_{52} &= A_{54}A_{43}A_{32} \\
&= \begin{bmatrix} c\phi\, c\beta_Y & s\phi\, c\beta_X + c\phi\, s\beta_Y\, s\beta_X & s\phi\, s\beta_X - c\phi\, s\beta_Y\, c\beta_X \\ -s\phi\, c\beta_Y & c\phi\, c\beta_X - s\phi\, s\beta_Y\, s\beta_X & c\phi\, s\beta_X + s\phi\, s\beta_Y\, c\beta_X \\ s\beta_Y & -c\beta_Y\, s\beta_X & c\beta_Y\, c\beta_X \end{bmatrix}
\end{aligned}
\tag{7.5}
$$

An additional complication arises from the fact that the center of mass of the disk is not necessarily collocated with the tip of the nanotube beam, which is also the center of coordinate systems 2, 3, 4, and 5. While perfect alignment between these two would be ideal, it is impossible in practice. Therefore it is important to include such misalignment in the model, in order to compute the deflections that will be excited by it when the disk is rotating. The location of the center of mass is described by the vector $\vec{a}_5$, expressed in the rotor-fixed frame (frame 5). In the inertial frame (frame 1), the location of the center of mass is denoted

$$\vec{R}_{C1} = \vec{R}_1 + \vec{a}_2 \tag{7.6}$$

The accuracy with which the disk center of mass aligns to the beam tip is likely to depend most strongly on the capability of lateral alignment accuracy during the rotor patterning lithography step. Here it is assumed that the distance between the two points, *i.e.* the magnitude of $\vec{a}_5$, will be kept under one micrometer. This is a conservative estimate for e-beam alignment capability.

Having defined the coordinate systems, the notation can be simplified. Only the first and fifth frames will be of further interest, so instead of numeric subscripts, the frame in which quantities are referred will be denoted by the case of the subscript. Capital subscripts will indicate the fixed inertial frame (frame 1) while lower case will indicate the rotor-fixed frame (frame 5). The five degrees of freedom that define the state of the system are then R_X, R_Y, β_X, β_Y, and ϕ. Euler angles β_X and β_Y describe both the beam bending at the tip and the corresponding disk angular displacement, and are taken to be small, in keeping with the beam model of the nanotube shaft.

7.2 Lagrangian of the System

A straightforward way to determine the equations of motion for an arbitrary system is Lagrange's method. By taking the appropriate derivatives of the kinetic and potential energies in the system, the equations can be derived. The Lagrangian of the system is defined as the difference between the kinetic and potential energies. There are five sources of kinetic energy arising from the five degrees of freedom. The translation of the disk center of mass gives rise to the terms for linear kinetic energy:

$$KE_{\text{linear}} = \frac{1}{2}m(\dot{R}_{CX}^2 + \dot{R}_{CY}^2 + \dot{R}_{CZ}^2) \tag{7.7}$$

The center of mass has two parts to its motion. First, the rotor-fixed coordinate frame is translating in the XY-plane, described by $\dot{R}_X$ and $\dot{R}_Y$. However, since the center of mass of the disk is not at the origin of this frame, there are additional velocities due to the rotation of the frame:

$$\begin{aligned}\vec{R}_{C1} &= \vec{R}_1 + \vec{a}_2 \\ &= \vec{R}_1 + A_{25}\vec{a}_5 \\ &= \vec{R}_1 + A_{52}^T\vec{a}_5\end{aligned} \tag{7.8}$$

$$\begin{bmatrix} R_{CX} \\ R_{CY} \\ R_{CZ} \end{bmatrix} = \begin{bmatrix} R_X \\ R_Y \\ L \end{bmatrix} + \begin{bmatrix} c\phi\, c\beta_Y & -s\phi\, c\beta_Y & s\beta_Y \\ s\phi\, c\beta_X + c\phi\, s\beta_Y\, s\beta_X & c\phi\, c\beta_X - s\phi\, s\beta_Y\, s\beta_X & -c\beta_Y\, s\beta_X \\ s\phi\, s\beta_X - c\phi\, s\beta_Y\, c\beta_X & c\phi\, s\beta_X + s\phi\, s\beta_Y\, c\beta_X & c\beta_Y\, c\beta_X \end{bmatrix} \begin{bmatrix} a_x \\ a_y \\ a_z \end{bmatrix} \tag{7.9}$$

The z-component of the rotor misalignment is equal to half the thickness of the rotor, as the center of mass of the disk is at the z-midpoint of the disk, while the beam tip (and the center of the rotor-fixed coordinate system) is at the edge of the surface of the disk. The other two components of imbalance arise from misalignment of the rotor lithography. The second term in equation (7.8) then works out to be

$$\begin{aligned}\vec{a}_2 = \begin{bmatrix} a_X \\ a_Y \\ a_Z \end{bmatrix} &= \begin{bmatrix} c\phi\, c\beta_Y & -s\phi\, c\beta_Y & s\beta_Y \\ s\phi\, c\beta_X + c\phi\, s\beta_Y\, s\beta_X & c\phi\, c\beta_X - s\phi\, s\beta_Y\, s\beta_X & -c\beta_Y\, s\beta_X \\ s\phi\, s\beta_X - c\phi\, s\beta_Y\, c\beta_X & c\phi\, s\beta_X + s\phi\, s\beta_Y\, c\beta_X & c\beta_Y\, c\beta_X \end{bmatrix} \begin{bmatrix} a_x \\ a_y \\ a_z \end{bmatrix} \\ &= \begin{bmatrix} a_x c\phi\, c\beta_Y - a_y s\phi\, c\beta_Y + a_z s\beta_Y \\ a_x[s\phi\, c\beta_X + c\phi\, s\beta_Y\, s\beta_X] + a_y[c\phi\, c\beta_X - s\phi\, s\beta_Y\, s\beta_X] + a_z[-c\beta_Y s\beta_X] \\ a_x[s\phi\, s\beta_X - c\phi\, s\beta_Y\, c\beta_X] + a_y[c\phi\, s\beta_X + s\phi\, s\beta_Y\, c\beta_X] + a_z[c\beta_Y c\beta_X] \end{bmatrix}\end{aligned} \tag{7.10}$$

Applying the small angle assumption to the Euler angles β_X and β_Y and neglecting second order terms in these small angles allows considerable simplification:

$$\vec{a}_2 = \begin{bmatrix} a_X \\ a_Y \\ a_Z \end{bmatrix} \approx \begin{bmatrix} a_x c\phi - a_y s\phi + a_z\beta_Y \\ a_x s\phi + a_y c\phi - a_z\beta_X \\ a_x[s\phi\, \beta_X - c\phi\, \beta_Y] + a_y[c\phi\, \beta_X + s\phi\, \beta_Y] + a_z \end{bmatrix} \tag{7.11}$$

Substituting this into equation (7.8) yields

$$\begin{bmatrix} R_{CX} \\ R_{CY} \\ R_{CZ} \end{bmatrix} = \begin{bmatrix} R_X + a_x c\phi - a_y s\phi + a_z\beta_Y \\ R_Y + a_x s\phi + a_y c\phi - a_z\beta_X \\ R_Z + a_x[s\phi\, \beta_X - c\phi\, \beta_Y] + a_y[c\phi\, \beta_X + s\phi\, \beta_Y] + a_z \end{bmatrix} \tag{7.12}$$

Recall that this model only treats two linear degrees of freedom, x and y. The description of the z motion of the center of mass is not relevant, and is neglected. The velocities are then the temporal derivative of this position expressed in the fixed inertial frame:

$$\begin{bmatrix} \dot{R}_{CX} \\ \dot{R}_{CY} \\ \dot{R}_{CZ} \end{bmatrix} = \begin{bmatrix} \dot{R}_X - (a_x s\phi + a_y c\phi)\dot{\phi} + a_z \dot{\beta}_Y \\ \dot{R}_Y + (a_x c\phi - a_y s\phi)\dot{\phi} - a_z \dot{\beta}_X \\ 0 \end{bmatrix} \tag{7.13}$$

Substituting these into equation (7.7) for the linear kinetic energy of the rotor yields

$$\begin{aligned} KE_{\text{linear}} &= \frac{1}{2} m\left(\dot{R}_{CX}^2 + \dot{R}_{CY}^2 + \dot{R}_{CZ}^2\right) \\ &= \frac{1}{2} m\left[\dot{R}_X - (a_x s\phi \ + a_y c\phi\ )\dot{\phi} + a_z \dot{\beta}_Y\right]^2 \\ &\qquad + \frac{1}{2} m\left[\dot{R}_Y + (a_x c\phi - a_y s\phi)\dot{\phi} - a_z \dot{\beta}_X\right]^2 \\ &= KE_{\text{linear},\, x} + KE_{\text{linear},\, y} \end{aligned} \tag{7.14}$$

The rotation and tilting of the disk provide angular kinetic energy, which is more complex. The moments of inertia of the disk are represented by the inertia tensor, expressed in the rotor-fixed frame about the center of mass:

$$\tilde{J} = \begin{bmatrix} J_{xx} & J_{xy} & J_{xz} \\ J_{xy} & J_{yy} & J_{yz} \\ J_{xz} & J_{yz} & J_{zz} \end{bmatrix} \tag{7.15}$$

For a perfect disk, with its axis of symmetry aligned with the z-axis, the inertia tensor is already in the principal axes, and therefore the products of inertia J_{xy}, J_{xz}, and J_{yz} would be zero. However, this model will take into account deflections excited by imbalances in the disk. For example, if the nanotube (which is the axle of the disk) is not aligned with the true axis of symmetry, or in other words if the disk lies in a plane at some small angle to the xy-plane, as might be the case for a nanotube that is not perfectly vertical after growth, these products would be non-zero. Therefore the products of inertia are not immediately neglected. However, the inertia tensor can be simplified significantly by actually computing the terms for a thin disk. The disk will be tilted by a small angle α_x about the x-axis to account for the possible angular misalignment due to non-vertical nanotubes. (The disk is symmetric, so the same tilting around the y-axis, or any other axis in the xy-plane would be equivalent.)

The inertia tensor of a thin disk, expressed in the principal axes, is well known:

$$\tilde{J}_{\text{principal}} = \frac{mR^2}{4}\begin{bmatrix} 1 & 0 & 0 \\ 0 & 1 & 0 \\ 0 & 0 & 2 \end{bmatrix} \tag{7.16}$$

To find the inertia tensor in the rotor-fixed axes, given the rotation about the x-axis by α_x, the rotation matrix for this angle is used:

$$\begin{aligned}
\tilde{J} &= \begin{bmatrix} 1 & 0 & 0 \\ 0 & c\alpha_x & -s\alpha_x \\ 0 & s\alpha_x & c\alpha_x \end{bmatrix} \tilde{J}_{\text{principal}} \begin{bmatrix} 1 & 0 & 0 \\ 0 & c\alpha_x & -s\alpha_x \\ 0 & s\alpha_x & c\alpha_x \end{bmatrix}^{\mathrm{T}} \\
&= \frac{mR^2}{4}\begin{bmatrix} 1 & 0 & 0 \\ 0 & c\alpha_x & -s\alpha_x \\ 0 & s\alpha_x & c\alpha_x \end{bmatrix}\begin{bmatrix} 1 & 0 & 0 \\ 0 & 1 & 0 \\ 0 & 0 & 2 \end{bmatrix}\begin{bmatrix} 1 & 0 & 0 \\ 0 & c\alpha_x & s\alpha_x \\ 0 & -s\alpha_x & c\alpha_x \end{bmatrix} \\
&= \frac{mR^2}{4}\begin{bmatrix} 1 & 0 & 0 \\ 0 & c\alpha_x & -s\alpha_x \\ 0 & s\alpha_x & c\alpha_x \end{bmatrix}\begin{bmatrix} 1 & 0 & 0 \\ 0 & c\alpha_x & s\alpha_x \\ 0 & -2s\alpha_x & 2c\alpha_x \end{bmatrix} \\
&= \frac{mR^2}{4}\begin{bmatrix} 1 & 0 & 0 \\ 0 & c^2\alpha_x + 2s^2a_x & -c\alpha_x s\alpha_x \\ 0 & -c\alpha_x s\alpha_x & s^2\alpha_x + 2c^2\alpha_x \end{bmatrix}
\end{aligned} \tag{7.17}$$

$$\tilde{J} = \begin{bmatrix} J_{xx} & J_{xy} & J_{xz} \\ J_{xy} & J_{yy} & J_{yz} \\ J_{xz} & J_{yz} & J_{zz} \end{bmatrix} = \frac{mR^2}{4}\begin{bmatrix} 1 & 0 & 0 \\ 0 & (1+s^2)a_x & -c\alpha_x s\alpha_x \\ 0 & -c\alpha_x s\alpha_x & (1+c^2)\alpha_x \end{bmatrix} \tag{7.18}$$

An alternative method of computing the inertia tensor is to compute each term individually from the integral that defines it. The moments and products of inertia are defined by the following integrals:

$$J_{xx} = \iiint_{\text{disk}} (y^2 + z^2)dm \tag{7.19}$$

$$J_{yy} = \iiint_{\text{disk}} (x^2 + z^2)dm \tag{7.20}$$

$$J_{zz} = \iiint_{\text{disk}} (x^2 + y^2)dm \tag{7.21}$$

$$J_{xy} = -\iiint_{\text{disk}} (xy)dm \tag{7.22}$$

$$J_{xz} = -\iiint_{\text{disk}} (xz)dm \tag{7.23}$$

$$J_{yz} = -\iiint_{\text{disk}} (yz)dm \tag{7.24}$$

The disk is considered thin, so a differential mass within the disk can be represented by

$$dm = \rho t dA \tag{7.25}$$

Where ρ is the density of the disk material, t is the thickness of the disk, and dA is a differential area within the 2-dimensional disk. The whole disk area is expressed in polar coordinates $0 < \theta < 2\pi$ and $0 < r < R$ where R is the outer disk radius, making

$$dm = \rho t r dr d\theta \tag{7.26}$$

The Cartesian coordinates in the xyz-system for a point on the disk specified in rθ-coordiantes, remembering that the disk is tilted by α_X about the x-axis, are

$$x = r\cos\theta \tag{7.27}$$

$$y = r\sin\theta\cos\alpha_x \tag{7.28}$$

$$z = r\sin\theta\sin\alpha_x \tag{7.29}$$

Substituting these expressions into the definitions, the moments of inertia are found:

$$\begin{aligned} J_{xx} &= \iiint_{\text{disk}} (y^2 + z^2)dm \\ &= t \int_0^{2\pi} \int_0^R \llbracket[(r \sin\theta \cos\alpha_x)\rrbracket^2 + (r \sin\theta \sin\alpha_x)^2]r\rho dr\, d\theta \\ &= t\rho \left[\int_0^{2\pi} \sin^2\theta\, d\theta\right]\left[\int_0^R r^3 dr\right] = t\rho[\pi]\left[\frac{R^4}{4}\right] = \frac{\rho t \pi R^4}{4} = \frac{mR^2}{4} \end{aligned} \tag{7.30}$$

$$\begin{aligned} J_{yy} &= \iiint_{\text{disk}} (x^2 + z^2)dm = \mathrm{t} \int_0^{2\mathrm{\pi}} \int_0^{\mathrm{R}} [(r\cos\theta)^2 + (r \sin\theta \sin\alpha_x)^2]r\rho dr\, d\theta \\ &= t\rho \left[\int_0^{2\pi} \cos^2 \theta + \sin^2\theta \sin^2\alpha_x\, d\theta]\right]\left[\int_0^R r^3 dr\right] \\ &= t\rho[\pi(1 + \sin^2\alpha_x)]\left[\frac{R^4}{4}\right] = \frac{\rho t \pi R^4}{4}(1 + \sin^2\alpha_x) \\ &= \frac{mR^2}{4}(1 + \sin^2\alpha_x) \end{aligned} \tag{7.31}$$

$$\begin{aligned} J_{zz} &= \iiint_{\text{disk}} (x^2 + y^2)dm = \mathrm{t} \int_0^{2\mathrm{\pi}} \int_0^{\mathrm{R}} [(r\cos\theta)^2 + (r \sin\theta \cos\alpha_x)]r\rho dr\, d\theta \\ &= t\rho \left[\int_0^{2\pi} \cos^2\theta + \sin^2\theta \cos^2\alpha_x\, d\theta\right]\left[\int_0^R r^3 dr\right] \\ &= t\rho[\pi(1 + \cos^2\alpha_x)]\left[\frac{R^4}{4}\right] = \frac{\rho t \pi R^4}{4}(1 + \cos^2\alpha_x) \\ &= \frac{mR^2}{4}(1 + \cos^2\alpha_x) \end{aligned} \tag{7.32}$$

Since α_x is small, the small angle assumption is appropriate. The two “diametral” moments of inertia J_{xx} and J_{yy}, that is, those taken with respect to the x- and y- axes (which are nominally diameters) are equal within the assumption, and given a single name:

$$J_{xx} = J_{yy} = J \tag{7.33}$$

The products of inertia are found from their definitions:

$$\begin{aligned} J_{xy} &= -\iiint_{\text{disk}} (xy)dm = t\int_0^{2\pi}\int_0^R (r\cos\theta)(r\sin\theta\cos\alpha_x)r dr\, d\theta \\ &= -t\rho\left[\int_0^{2\pi}\cos\theta\sin\theta\cos\alpha_x\, d\theta\right]\left[\int_0^R r^3 dr\right] = 0 \end{aligned} \tag{7.34}$$

$$\begin{aligned} J_{xz} &= -\iiint_{\text{disk}} (xz)dm = -t\int_0^{2\pi}\int_0^R (r\cos\theta)(r\sin\theta\sin\alpha_x)r dr\, d\theta \\ &= -t\rho\left[\int_0^{2\pi}\cos\theta\sin\theta\sin\alpha_x\, d\theta\right]\left[\int_0^R r^3 dr\right] = 0 \end{aligned} \tag{7.35}$$

$$\begin{aligned} J_{yz} &= -\iiint_{\text{disk}} (yz)dm = -t\int_0^{2\pi}\int_0^R (r\sin\theta\cos\alpha_x)(r\sin\theta\sin\alpha_x)r dr\, d\theta \\ &= -t\rho\left[\int_0^{2\pi}\sin^2\theta\sin\alpha_x\cos^2\alpha_x\, d\theta\right]\left[\int_0^R r^3 dr\right] \\ &= -t\rho[\pi\sin\alpha_x\cos\alpha_x]\left[\frac{R^4}{4}\right] = -\frac{\rho t\pi R^4}{4}\sin\alpha_x\cos\alpha_x \\ &= -\frac{mR^2}{4}(1+\cos^2\alpha_x) \end{aligned} \tag{7.36}$$

Note that because the disk is misaligned by α_X about the x-axis, the corresponding products of inertia J_{xy} and J_{xz} are zero. If the misalignment had been α_y about the y-axis, then J_{xy} and J_{yz} would be zero. Therefore only the product J_{xy} can be safely neglected, and the product J_{xz} must be kept, for cases where the angular misalignment of the rotor disk is about an axis other than the x-axis. This results in a simplified inertia tensor:

$$\tilde{J} = \begin{bmatrix} J_{xx} & 0 & J_{xz} \\ 0 & J_{yy} & J_{yz} \\ J_{xz} & J_{yz} & J_{zz} \end{bmatrix} \tag{7.37}$$

The angular kinetic energy of the disk can be written:

$$KE_{\text{angular}} = \frac{1}{2}\vec{\omega}^T\tilde{J}\vec{\omega} \tag{7.38}$$

where $\vec{\omega}$ is the vector of angular velocities of the system, expressed also in the rotor-fixed frame. The angular velocity vector is the vector sum of the angular velocities described by the rate of change of the Euler angles. However, the Euler angles are not expressed in the rotor-fixed frame, so they must be rotated into that frame prior to addition:

$$\vec{\omega} = A_{54}\begin{bmatrix}0\\0\\\dot{\phi}\end{bmatrix} + A_{54}A_{43}\begin{bmatrix}0\\\dot{\beta}_Y\\0\end{bmatrix} + A_{54}A_{43}A_{32}\begin{bmatrix}\dot{\beta}_X\\0\\0\end{bmatrix} \tag{7.39}$$

However, any angular velocity remains unchanged when it is rotated about an axis containing the vector. For that reason, the last rotation matrix in each term drops out. (Alternatively, note that these matrices as quoted in equations (7.2), (7.3), and (7.4) do not change the vectors in the terms above when multiplied by them.) The result is:

$$\begin{aligned}
\vec{\omega} &= \begin{bmatrix}0\\0\\\dot{\phi}\end{bmatrix} + A_{54}\begin{bmatrix}0\\\dot{\beta}_Y\\0\end{bmatrix} + A_{54}A_{43}\begin{bmatrix}\dot{\beta}_X\\0\\0\end{bmatrix}\\
&= \begin{bmatrix}0\\0\\\dot{\phi}\end{bmatrix} + \begin{bmatrix}c\phi & s\phi & 0\\-s\phi & c\phi & 0\\0 & 0 & 1\end{bmatrix}\begin{bmatrix}0\\\dot{\beta}_Y\\0\end{bmatrix} + \begin{bmatrix}c\phi & s\phi & 0\\-s\phi & c\phi & 0\\0 & 0 & 1\end{bmatrix}\begin{bmatrix}c\beta_Y & 0 & -s\beta_Y\\0 & 1 & 0\\s\beta_Y & 0 & c\beta_Y\end{bmatrix}\begin{bmatrix}\dot{\beta}_X\\0\\0\end{bmatrix}\\
&= \begin{bmatrix}0\\0\\\dot{\phi}\end{bmatrix} + \begin{bmatrix}\dot{\beta}_Y s\phi\\\dot{\beta}_Y c\phi\\0\end{bmatrix} + \begin{bmatrix}\dot{\beta}_X c\beta_Y c\phi\\-\dot{\beta}_X c\beta_Y s\phi\\\dot{\beta}_X s\beta_y\end{bmatrix}\\
&= \begin{bmatrix}\dot{\beta}_Y s\phi + \dot{\beta}_X c\beta_Y c\phi\\\dot{\beta}_Y c\phi - \dot{\beta}_X c\beta_Y s\phi\\\dot{\phi} + \dot{\beta}_X s\beta_y\end{bmatrix} = \begin{bmatrix}\omega_x\\\omega_y\\\omega_z\end{bmatrix}
\end{aligned} \tag{7.40}$$

Rather than substituting these directly into equation (7.38), it is first useful to expand (7.38) and assign names to the terms. This will allow each term to be treated individually, alleviating confusion:

$$\begin{aligned}
KE_{\text{angular}} &= \frac{1}{2}\vec{\omega}^T\tilde{J}\vec{\omega}\\
&= \frac{1}{2}\begin{bmatrix}\omega_x & \omega_y & \omega_z\end{bmatrix}\begin{bmatrix}J_{xx} & 0 & J_{xz}\\0 & J_{yy} & J_{yz}\\J_{xz} & J_{yz} & J_{zz}\end{bmatrix}\begin{bmatrix}\omega_x\\\omega_y\\\omega_z\end{bmatrix}\\
&= \frac{1}{2}J_{xx}\omega_x^2 + \frac{1}{2}J_{yy}\omega_y^2 + \frac{1}{2}J_{zz}\omega_z^2 + 0 + J_{xz}\omega_x\omega_z + J_{yz}\omega_y\omega_z\\
&= KE_{\text{ang},\,xx} + KE_{\text{ang},\,yy} + KE_{\text{ang},\,zz} + KE_{\text{ang},\,xy} + KE_{\text{ang},\,xz} + KE_{\text{ang},\,yz}
\end{aligned} \tag{7.41}$$

Substituting the values of the angular velocity components from equation (7.40) gives each term in the angular kinetic energy in terms of the degrees of freedom:

$$KE_{\text{ang},\,xx} = \frac{1}{2}J_{xx}\left(\dot{\beta}_Y s\phi + \dot{\beta}_X c\beta_Y c\phi\right)^2 \tag{7.42}$$

$$KE_{\text{ang, } yy} = \frac{1}{2} J_{yy} \left(\dot{\beta}_Y c\phi - \dot{\beta}_X c\beta_Y s\phi\right)^2 \tag{7.43}$$

$$KE_{\text{ang, } zz} = \frac{1}{2} J_{zz} \left(\dot{\phi} + \dot{\beta}_X s\beta_y\right)^2 \tag{7.44}$$

$$KE_{\text{ang, } xy} = 0 \tag{7.45}$$

$$KE_{\text{ang, } xz} = J_{xz} \left(\dot{\beta}_Y s\phi + \dot{\beta}_X c\beta_Y c\phi\right)\left(\dot{\phi} + \dot{\beta}_X s\beta_y\right) \tag{7.46}$$

$$KE_{\text{ang, } yz} = J_{yz} \left(\dot{\beta}_Y c\phi - \dot{\beta}_X c\beta_Y s\phi\right)\left(\dot{\phi} + \dot{\beta}_X s\beta_y\right) \tag{7.47}$$

Having computed all the kinetic energy terms in the Lagrangian, the potential energy terms must now be computed. Gravity is ignored, since the mass of the structure is small. The only source of potential energy is then the elastic energy stored in the cantilever beam axle. To compute the elastic bending energy, the deflections of the beam must be known as a function of the degrees of freedom of the system. The solution to the beam equation (6.3) is repeated here:

$$u(z) = Az^3 + Bz^2 + Cz + D \tag{7.48}$$

$$v(z) = Ez^3 + Fz^2 + Gz + H \tag{7.49}$$

The boundary conditions at the root are the same as before, since the root remains fixed:

$$u(0) = v(0) = \frac{du}{dz}(0) = \frac{dv}{dz}(0) = 0 \tag{7.50}$$

However, for determining the elastic bending energy, the boundary conditions at the “free” end are different than those typically used for a loaded cantilever. The end is not free, but taken to be constrained at some known position and rotation. This allows the energy for any given displacement state to be computed. Hence instead of conditions on the moment and shear at the free end, we have conditions on the displacement and angle:

$$u(L) = R_X \tag{7.51}$$

$$v(L) = R_Y \tag{7.52}$$

$$\frac{du}{dz}(L) = \beta_Y \tag{7.53}$$

$$\frac{dv}{dz}(L) = -\beta_X \tag{7.54}$$

The fixed end boundary conditions require that constants C, D, G, and H are zero. Constants A and B are determined from boundary conditions (7.51) and (7.52):

$$R_X = AL^3 + BL^2 \tag{7.55}$$

$$B = \frac{R_X}{L^2} - AL \tag{7.56}$$

$$\beta_Y = 3AL^2 + 2BL = 3AL^2 + \frac{2R_X}{L} - 2AL^2 \tag{7.57}$$

$$A = \frac{\beta_Y}{L^2} - \frac{2R_X}{L^3} \tag{7.58}$$

$$B = \frac{3R_X}{L^2} - \frac{\beta_Y}{L} \tag{7.59}$$

$$u(z) = \left(\frac{\beta_Y}{L^2} - \frac{2R_X}{L^3}\right) z^3 + \left(\frac{3R_X}{L^2} - \frac{\beta_Y}{L}\right) z^2 \tag{7.60}$$

Similarly, applying boundary conditions (7.53) and (7.54) to the y-deflections $v(z)$ gives:

$$v(z) = \left(-\frac{\beta_X}{L^2} - \frac{2R_Y}{L^3}\right) z^3 + \left(\frac{3R_Y}{L^2} + \frac{\beta_X}{L}\right) z^2 \tag{7.61}$$

The elastic energy in a system (in this case the bent beam) can be found from

$$PE_{\text{elastic}} = \frac{1}{2}\int_V \tilde{\varepsilon}\tilde{\sigma}\, dV \tag{7.62}$$

For Euler simple beam theory, the only components of stress or strain that are considered are along the beam axis:

$$PE_{\text{elastic}} = \frac{1}{2}\int_V \varepsilon_{zz}\sigma_{zz}\, dV \tag{7.63}$$

The stresses and strains arising from bending in the x-z plane are

$$\varepsilon_{zz} = -x\frac{d^2u}{dz^2} \tag{7.64}$$

and

$$\sigma_{zz} = \varepsilon_{zz}E \tag{7.65}$$

Substituting these into (7.62) results in:

$$\begin{aligned} PE_{\text{elastic, x}} &= \frac{1}{2}E\iiint_V x^2\left(\frac{d^2u}{dz^2}\right)^2 dV \\ &= \frac{1}{2}E\int_0^L \frac{d^2u}{dz^2}\iint_A x^2\, dA\, dz \end{aligned} \tag{7.66}$$

and recognizing the definition of the second moment of area:

$$I_{yy} = \int_A x^2 dA \tag{7.67}$$

yields

$$PE_{\text{elastic, x}} = \frac{1}{2}EI_{yy}\int_0^L \left(\frac{d^2u}{dz^2}\right)^2 dz \tag{7.68}$$

The square of the partial derivative is evaluated:

$$
\begin{aligned}
\left(\frac{d^2u}{dz^2}\right)^2 &= \left[6\left(\frac{\beta_Y}{L^2}-\frac{2R_X}{L^3}\right)z+2\left(\frac{3R_X}{L^2}-\frac{\beta_Y}{L}\right)\right]^2 \\
&= 36\left(\frac{\beta_Y}{L^2}-\frac{2R_X}{L^3}\right)^2 z^2+24\left(\frac{\beta_Y}{L^2}-\frac{2R_X}{L^3}\right)\left(\frac{3R_X}{L^2}-\frac{\beta_Y}{L}\right)z+4\left(\frac{3R_X}{L^2}-\frac{\beta_Y}{L}\right)^2
\end{aligned}
\tag{7.69}
$$

Integrating over the tube length gives:

$$
\begin{aligned}
\int_0^L \left(\frac{d^2u}{dz^2}\right)^2 dz = {} & 12\left(\frac{\beta_Y}{L^2}-\frac{2R_X}{L^3}\right)^2 L^3+12\left(\frac{\beta_Y}{L^2}-\frac{2R_X}{L^3}\right)\left(\frac{3R_X}{L^2}-\frac{\beta_Y}{L}\right)L^2 \\
& +4\left(\frac{3R_X}{L^2}-\frac{\beta_Y}{L}\right)^2 L \\
& =\frac{12\beta_Y^2}{L}-\frac{48R_X\beta_Y}{L^2}+\frac{48R_X^2}{L^3}+\frac{36\beta_YR_X}{L^2}-\frac{72R_X^2}{L^3}-\frac{12\beta_Y^2}{L}+\frac{24R_X\beta_Y}{L^2} \\
& +\frac{36R_X^2}{L^3}-\frac{24R_X\beta_Y}{L^2}+\frac{4\beta_Y^2}{L} \\
& =\frac{4\beta_Y^2}{L}-\frac{12R_X\beta_Y}{L^2}+\frac{12R_X^2}{L^3}
\end{aligned}
\tag{7.70}
$$

which means the elastic energy is

$$
\begin{aligned}
PE_{\text{elastic, x}} &= \frac{1}{2}EI_{yy}\int_0^L \left(\frac{d^2u}{dz^2}\right)^2 dz \\
&= EI_{yy}\left[\frac{2\beta_Y^2}{L}-\frac{6R_X\beta_Y}{L^2}+\frac{6R_X^2}{L^3}\right]
\end{aligned}
\tag{7.71}
$$

Similarly for bending in the y-z plane:

$$
PE_{\text{elastic, y}} = EI_{xx}\left[\frac{2\beta_X^2}{L}+\frac{6R_Y\beta_X}{L^2}+\frac{6R_Y^2}{L^3}\right]
\tag{7.72}
$$

Since the tube is axisymmetric, the second moment of area is the same for the two directions in the cross sectional plane,, hence $I_{yy} = I_{zz} = I$.

Now all the terms in the Lagrangian for the system have been computed. The Lagrangian is defined as the difference between kinetic energy and potential energy, which when written out is:

$$\begin{aligned}\mathcal{L} &= KE_{\text{linear}} + KE_{\text{angular}} - PE_{\text{elastic}} \\ &= KE_{\text{linear},\,X} + KE_{\text{linear},\,Y} + KE_{\text{ang},\,xx} + KE_{\text{ang},\,yy} + KE_{\text{ang},\,zz} \\ &\quad + KE_{\text{ang},\,xy} + KE_{\text{ang},\,xz} + KE_{\text{ang},\,yz} - PE_{\text{elastic, x}} - PE_{\text{elastic, y}}\end{aligned} \tag{7.73}$$

$$\begin{aligned}\mathcal{L} = \frac{1}{2}m\left[\dot{R}_X - (a_x s\phi + a_y c\phi)\dot{\phi}\right]^2 + \frac{1}{2}m\left[\dot{R}_Y + (a_x c\phi - a_y s\phi)\dot{\phi}\right]^2 \\ + \frac{1}{2}J_{xx}\left(\dot{\beta}_Y s\phi + \dot{\beta}_X c\beta_Y c\phi\right)^2 + \frac{1}{2}J_{yy}\left(\dot{\beta}_Y c\phi - \dot{\beta}_X c\beta_Y s\phi\right)^2 \\ + \frac{1}{2}J_{zz}\left(\dot{\phi} + \dot{\beta}_X s\beta_y\right)^2 + 0 + J_{xz}\left(\dot{\beta}_Y s\phi + \dot{\beta}_X c\beta_Y c\phi\right)\left(\dot{\phi} + \dot{\beta}_X s\beta_y\right) \\ + J_{yz}\left(\dot{\beta}_Y c\phi - \dot{\beta}_X c\beta_Y s\phi\right)\left(\dot{\phi} + \dot{\beta}_X s\beta_y\right) \\ - EI_{yy}\left[\frac{2\beta_Y^2}{L} - \frac{6R_X\beta_Y}{L^2} + \frac{6R_X^2}{L^3}\right] - EI_{xx}\left[\frac{2\beta_X^2}{L} + \frac{6R_Y\beta_X}{L^2} + \frac{6R_Y^2}{L^3}\right]\end{aligned} \tag{7.74}$$

7.3 Equations of Motion

The equations of motion can be derived directly from the Lagrangian by way of Lagrange's equation:

$$\frac{d}{dt}\left(\frac{\partial\mathcal{L}}{\partial\dot{q}_j}\right) = \frac{\partial\mathcal{L}}{\partial q_j} \tag{7.75}$$

For the Stodola rotor, the generalized coordinates q_j are the translational and angular displacements R_X, R_Y, β_X, β_Y, and ϕ. The system of five equations of motion is:

$$\begin{cases}\dfrac{d}{dt}\left(\dfrac{\partial\mathcal{L}}{\partial\dot{R}_X}\right) = \dfrac{\partial\mathcal{L}}{\partial R_X} \\ \dfrac{d}{dt}\left(\dfrac{\partial\mathcal{L}}{\partial\dot{R}_Y}\right) = \dfrac{\partial\mathcal{L}}{\partial R_Y} \\ \dfrac{d}{dt}\left(\dfrac{\partial\mathcal{L}}{\partial\dot{\beta}_X}\right) = \dfrac{\partial\mathcal{L}}{\partial\beta_X} \\ \dfrac{d}{dt}\left(\dfrac{\partial\mathcal{L}}{\partial\dot{\beta}_Y}\right) = \dfrac{\partial\mathcal{L}}{\partial\beta_Y} \\ \dfrac{d}{dt}\left(\dfrac{\partial\mathcal{L}}{\partial\dot{\phi}}\right) = \dfrac{\partial\mathcal{L}}{\partial\phi}\end{cases} \tag{7.76}$$

Recall the Lagrangian for the Stodola rotor system:

$$\begin{aligned}\mathcal{L} = KE_{\text{linear}, X} + KE_{\text{linear}, Y} + KE_{\text{ang}, xx} + KE_{\text{ang}, yy} + KE_{\text{ang}, zz} + KE_{\text{ang}, xy} \\ + KE_{\text{ang}, xz} + KE_{\text{ang}, yz} - PE_{\text{elastic}, x} - PE_{\text{elastic}, y}\end{aligned} \tag{7.77}$$

It is helpful to consider each term separately for each of the five equations of motion, evaluating the derivatives and then combining terms.

7.3.1 Linear X Motion

The equation for linear motion in the x-direction is found from the Lagrangian as:

$$\frac{d}{dt}\left(\frac{\partial \mathcal{L}}{\partial \dot{R}_X}\right) = \frac{\partial \mathcal{L}}{\partial R_X} \tag{7.78}$$

$$\frac{d}{dt}\left(\frac{\partial [KE - PE]}{\partial \dot{R}_X}\right) = \frac{\partial [KE - PE]}{\partial R_X} \tag{7.79}$$

The derivatives for each term in the Lagrangian are evaluated. First the linear kinetic energy in the x-direction, from equation (7.14):

$$\begin{aligned}\frac{\partial}{\partial \dot{R}_X}\left(KE_{\text{linear}, x}\right) &= \frac{\partial}{\partial \dot{R}_X}\left(\frac{1}{2} m\left[\dot{R}_X - \left(a_x s\phi + a_y c\phi\right)\dot{\phi} + a_z \dot{\beta}_Y\right]^2\right) \\ &= m\dot{R}_X - m\left(a_x s\phi + a_y c\phi\right)\dot{\phi} + m a_z \dot{\beta}_Y\end{aligned} \tag{7.80}$$

$$\begin{aligned}\frac{d}{dt}\frac{\partial}{\partial \dot{R}_X}\left(KE_{\text{linear}, x}\right) &= \frac{\mathrm{d}}{\mathrm{dt}}\left[m\dot{R}_X - m\left(a_x s\phi + a_y c\phi\right)\dot{\phi} + a_z \dot{\beta}_Y\right] \\ &= m\left[\ddot{R}_X - a_x c\phi\dot{\phi}^2 + a_y s\phi\dot{\phi}^2 - a_x s\phi\ddot{\phi} - a_y c\phi\ddot{\phi} + a_z \ddot{\beta}_Y\right]\end{aligned} \tag{7.81}$$

The other derivative from equation (7.78) is

$$\frac{\partial}{\partial R_X}\left(KE_{\text{linear}, x}\right) = \frac{\partial}{\partial R_X}\left(\frac{1}{2} m\left[\dot{R}_X - \left(a_x s\phi + a_y c\phi\right)\dot{\phi} + a_z \dot{\beta}_Y\right]^2\right) = 0 \tag{7.82}$$

The derivatives of the other linear kinetic energy term, also from equation (7.14), vanish, because the terms do not contain any dependence on R_X and $\dot{R}_X$:

$$\frac{\partial}{\partial \dot{R}_X}\left(KE_{\text{linear}, y}\right) = \frac{\partial}{\partial \dot{R}_X}\left(\frac{1}{2}m\left[\dot{R}_Y + \left(a_x c\phi - a_y s\phi\right)\dot{\phi} - a_z\dot{\beta}_X\right]^2\right) = 0 \tag{7.83}$$

$$\frac{d}{dt}\frac{\partial}{\partial \dot{R}_X}\left(KE_{\text{linear}, y}\right) = 0 \tag{7.84}$$

$$\frac{\partial}{\partial R_X}\left(KE_{\text{linear}, y}\right) = \frac{\partial}{\partial R_X}\left(\frac{1}{2}m\left[\dot{R}_Y + \left(a_x c\phi - a_y s\phi\right)\dot{\phi} - a_z\dot{\beta}_X\right]^2\right) = 0 \tag{7.85}$$

The angular kinetic energy terms, given in equations (7.42) through (7.47), do not contribute to the equation of linear x-motion, because R_X and $\dot{R}_X$ do not appear in them, so all the derivatives are zero. Finally, the elastic energy terms, from equations (7.71) and (7.72) are evaluated:

$$\frac{\partial}{\partial \dot{R}_X}\left(PE_{\text{elastic, x}}\right) = \frac{\partial}{\partial \dot{R}_X}\left(EI_{yy}\left[\frac{2\beta_Y^2}{L} - \frac{6R_X\beta_Y}{L^2} + \frac{6R_X^2}{L^3}\right]\right) = 0 \tag{7.86}$$

$$\frac{d}{dt}\frac{\partial}{\partial \dot{R}_X}\left(PE_{\text{elastic}, x}\right) = 0 \tag{7.87}$$

$$\begin{aligned}\frac{\partial}{\partial R_X}\left(PE_{\text{elastic, x}}\right) &= \frac{\partial}{\partial R_X}\left(EI_{yy}\left[\frac{2\beta_Y^2}{L} - \frac{6R_X\beta_Y}{L^2} + \frac{6R_X^2}{L^3}\right]\right) \\ &= EI_{yy}\left[-\frac{6\beta_Y}{L^2} + \frac{12R_X}{L^3}\right]\end{aligned} \tag{7.88}$$

$$\frac{\partial}{\partial \dot{R}_X}\left(PE_{\text{elastic, y}}\right) = \frac{\partial}{\partial \dot{R}_X}\left(EI_{xx}\left[\frac{2\beta_X^2}{L} + \frac{6R_Y\beta_X}{L^2} + \frac{6R_Y^2}{L^3}\right]\right) = 0 \tag{7.89}$$

$$\frac{d}{dt}\frac{\partial}{\partial \dot{R}_X}\left(PE_{\text{elastic}, y}\right) = 0 \tag{7.90}$$

$$\frac{\partial}{\partial R_X}\left(PE_{\text{elastic, y}}\right) = \frac{\partial}{\partial R_X}\left(EI_{xx}\left[\frac{2\beta_X^2}{L} + \frac{6R_Y\beta_X}{L^2} + \frac{6R_Y^2}{L^3}\right]\right) = 0 \tag{7.91}$$

Having evaluated the appropriate derivatives of all the terms in the Lagrangian, they can be substituted back into equation (7.79), giving the equation of x-motion for the system:

$$\begin{aligned} &m\ddot{R}_X - ma_x c\phi\dot{\phi}^2 + ma_y s\phi\dot{\phi}^2 - ma_x s\phi\ddot{\phi} - ma_y s\phi\ddot{\phi} + ma_z\ddot{\beta}_Y \\ &\quad = -EI_{yy}\left[-\frac{6\beta_Y}{L^2} + \frac{12R_X}{L^3}\right] \end{aligned} \tag{7.92}$$

7.3.2 Linear Y Motion

The equation for linear motion in the y-direction is found from the Lagrangian as:

$$\frac{d}{dt}\left(\frac{\partial\mathcal{L}}{\partial\dot{R}_Y}\right) = \frac{\partial\mathcal{L}}{\partial R_Y} \tag{7.93}$$

$$\frac{d}{dt}\left(\frac{\partial[KE - PE]}{\partial\dot{R}_Y}\right) = \frac{\partial[KE - PE]}{\partial R_Y} \tag{7.94}$$

The derivatives for each term in the Lagrangian are evaluated. Here, the linear kinetic energy in the x-direction yields all zero derivatives:

$$\frac{\partial}{\partial\dot{R}_Y}\left(KE_{\text{linear},\,X}\right) = \frac{\partial}{\partial\dot{R}_Y}\left(\frac{1}{2}m\left[\dot{R}_X - \left(a_x s\phi\; + a_y c\phi\;\right)\dot{\phi} + a_z\dot{\beta}_Y\right]^2\right) = 0 \tag{7.95}$$

$$\frac{d}{dt}\frac{\partial}{\partial\dot{R}_Y}\left(KE_{\text{linear},\,x}\right) = 0 \tag{7.96}$$

$$\frac{\partial}{\partial R_Y}\left(KE_{\text{linear},\,x}\right) = \frac{\partial}{\partial R_Y}\left(\frac{1}{2}m\left[\dot{R}_X - \left(a_x s\phi\; + a_y c\phi\;\right)\dot{\phi} + a_z\dot{\beta}_Y\right]^2\right) = 0 \tag{7.97}$$

The derivatives of the y-direction linear kinetic energy, from equation (7.14), are

$$\begin{aligned} \frac{\partial}{\partial\dot{R}_Y}\left(KE_{\text{linear},\,y}\right) &= \frac{\partial}{\partial\dot{R}_Y}\left(\frac{1}{2}m\left[\dot{R}_Y + \left(a_x c\phi - a_y s\phi\right)\dot{\phi} - a_z\dot{\beta}_X\right]^2\right) \\ &= m\left[\dot{R}_Y + \left(a_x c\phi - a_y s\phi\right)\dot{\phi} - a_z\dot{\beta}_X\right] \end{aligned} \tag{7.98}$$

$$\frac{d}{dt}\frac{\partial}{\partial \dot{R}_Y}\left(KE_{\text{linear},\,y}\right) = m\frac{d}{dt}\left[\dot{R}_Y + m\left(a_x c\phi - a_y s\phi\right)\dot{\phi} - a_z\dot{\beta}_X\right]$$
$$= m\left[\ddot{R}_Y - a_x s\phi\dot{\phi}^2 - a_y c\phi\dot{\phi}^2 + a_x c\phi\ddot{\phi} - a_y s\phi\ddot{\phi} - a_Z\dot{\beta}_X\right] \tag{7.99}$$

The other derivative from equation (7.93) is

$$\frac{\partial}{\partial R_Y}\left(KE_{\text{linear},\,y}\right) = \frac{\partial}{\partial R_Y}\left(\frac{1}{2}m\left[\dot{R}_Y + \left(a_x c\phi - a_y s\phi\right)\dot{\phi} - a_Z\dot{\beta}_X\right]^2\right) = 0 \tag{7.100}$$

The angular kinetic energy terms, given in equations (7.42) through (7.47), do not contribute to the equations of linear y-motion, because R_Y and $\dot{R}_Y$ do not appear in them, so all the derivatives are zero. Finally the elastic energy terms, from equations (7.71) and (7.72) are evaluated:

$$\frac{\partial}{\partial \dot{R}_Y}\left(PE_{\text{elastic},\,x}\right) = \frac{\partial}{\partial \dot{R}_Y}\left(EI_{yy}\left[\frac{2\beta_Y^2}{L} - \frac{6R_X\beta_Y}{L^2} + \frac{6R_X^2}{L^3}\right]\right) = 0 \tag{7.101}$$

$$\frac{d}{dt}\frac{\partial}{\partial \dot{R}_Y}\left(PE_{\text{elastic},\,x}\right) = 0 \tag{7.102}$$

$$\frac{\partial}{\partial R_Y}\left(PE_{\text{elastic, x}}\right) = \frac{\partial}{\partial R_Y}\left(EI_{yy}\left[\frac{2\beta_Y^2}{L} - \frac{6R_X\beta_Y}{L^2} + \frac{6R_X^2}{L^3}\right]\right) = 0 \tag{7.103}$$

$$\frac{\partial}{\partial \dot{R}_Y}\left(PE_{\text{elastic, y}}\right) = \frac{\partial}{\partial \dot{R}_Y}\left(EI_{xx}\left[\frac{2\beta_X^2}{L} + \frac{6R_Y\beta_X}{L^2} + \frac{6R_Y^2}{L^3}\right]\right) = 0 \tag{7.104}$$

$$\frac{d}{dt}\frac{\partial}{\partial \dot{R}_Y}\left(PE_{\text{elastic},\,y}\right) = 0 \tag{7.105}$$

$$\frac{\partial}{\partial R_Y}\left(PE_{\text{elastic},\,y}\right) = \frac{\partial}{\partial R_Y}\left(EI_{xx}\left[\frac{2\beta_X^2}{L} + \frac{6R_Y\beta_X}{L^2} + \frac{6R_Y^2}{L^3}\right]\right)$$
$$= EI_{xx}\left[\frac{6\beta_X}{L^2} + \frac{12R_Y}{L^3}\right] \tag{7.106}$$

Having evaluated the appropriate derivatives of all the terms in the Lagrangian, they can be substituted back into (7.93), giving the equation of linear y-motion for the system.

$$m\ddot{R}_Y - ma_x s\phi\dot{\phi}^2 - ma_y c\phi\dot{\phi}^2 + ma_x c\phi\ddot{\phi} - ma_y s\phi\ddot{\phi} - ma_z\ddot{\beta}_X = -EI_{xx}\left[\frac{6\beta_X}{L^2} + \frac{12R_Y}{L^3}\right] \tag{7.107}$$

7.3.3 Angular X Motion

For angular motion about the x-axis, the governing equation is found from the Lagrangian as:

$$\frac{d}{dt}\left(\frac{\partial\mathcal{L}}{\partial\dot{\beta}_X}\right) = \frac{\partial\mathcal{L}}{\partial\dot{\beta}_X} \tag{7.108}$$

$$\frac{d}{dt}\left(\frac{\partial[KE - PE]}{\partial\dot{\beta}_X}\right) = \frac{\partial[KE - PE]}{\partial\dot{\beta}_X} \tag{7.109}$$

The derivatives of each term in the Lagrangian are taken one at a time. The derivatives of the linear kinetic energy terms, given in (7.14), are as follows.

$$\frac{\partial}{\partial\dot{\beta}_X}\left(KE_{\text{linear},\,x}\right) = \frac{\partial}{\partial\dot{\beta}_X}\left(\frac{1}{2}m\left[\dot{R}_X - \left(a_x s\phi\ + a_y c\phi\ \right)\dot{\phi} + a_z\dot{\beta}_Y\right]^2\right) = 0 \tag{7.110}$$

$$\frac{d}{dt}\frac{\partial}{\partial\dot{\beta}_X}\left(KE_{\text{linear},\,x}\right) = 0 \tag{7.111}$$

$$\frac{\partial}{\partial\beta_X}\left(KE_{\text{linear},\,x}\right) = \frac{\partial}{\partial\beta_X}\left(\frac{1}{2}m\left[\dot{R}_X - \left(a_x s\phi\ + a_y c\phi\ \right)\dot{\phi} + a_z\dot{\beta}_Y\right]^2\right) = 0 \tag{7.112}$$

$$\begin{aligned}\frac{\partial}{\partial\dot{\beta}_X}\left(KE_{\text{linear},\,y}\right) &= \frac{\partial}{\partial\dot{\beta}_X}\left(\frac{1}{2}m\left[\dot{R}_Y + \left(a_x c\phi - a_y s\phi\right)\dot{\phi} - a_z\dot{\beta}_X\right]^2\right)\\ &= -ma_z\left[\dot{R}_Y + \left(a_x c\phi - a_y s\phi\right)\dot{\phi} - a_z\dot{\beta}_X\right]\end{aligned} \tag{7.113}$$

$$\begin{aligned}\frac{\mathrm{d}}{\mathrm{dt}}\frac{\partial}{\partial\dot{\beta}_X}\left(KE_{\text{linear},\,y}\right) &= -ma_z\frac{\mathrm{d}}{\mathrm{dt}}\left[\dot{R}_Y + \left(a_x c\phi - a_y s\phi\right)\dot{\phi} - a_z\dot{\beta}_X\right]\\ &= -ma_z\left[\ddot{R}_Y + \left(-a_x s\phi - a_y c\phi\right)\dot{\phi}^2 + \left(a_x c\phi - a_y s\phi\right)\ddot{\phi} - a_z\ddot{\beta}_X\right]\end{aligned} \tag{7.114}$$

$$\frac{\partial}{\partial \beta_X}\left(KE_{\text{linear, }Y}\right)=\frac{\partial}{\partial \beta_X}\left(\frac{1}{2}m\left[\dot{R}_X-\left(a_x s\phi\ +a_y c\phi\ \right)\dot{\phi}+a_z\dot{\beta}_Y\right]^2\right)=0 \tag{7.115}$$

The derivatives of each term in the angular kinetic energy terms are found one at a time:

$$\begin{aligned}\frac{\partial}{\partial \dot{\beta}_X}\left(KE_{\text{ang, }xx}\right)&=\frac{\partial}{\partial \dot{\beta}_X}\left(\frac{1}{2}J_{xx}\left(\dot{\beta}_Y s\phi+\dot{\beta}_X c\beta_Y c\phi\right)^2\right)\\&=J_{xx}\left(\dot{\beta}_Y s\phi+\dot{\beta}_X c\beta_Y c\phi\right)\left(c\beta_Y c\phi\right)\\&=J_{xx}\left(\dot{\beta}_Y\ c\beta_Y s\phi c\phi+\dot{\beta}_X c^2\beta_Y c^2\phi\right)\end{aligned} \tag{7.116}$$

$$\begin{aligned}\frac{d}{dt}\frac{\partial}{\partial \dot{\beta}_X}\left(KE_{\text{ang, }xx}\right)&=J_{xx}\frac{d}{dt}\left(\dot{\beta}_Y\ c\beta_Y s\phi c\phi+\dot{\beta}_X c^2\beta_Y c^2\phi\right)\\&=J_{xx}\left[\ddot{\beta}_Y\ c\beta_Y s\phi c\phi-\dot{\beta}_Y^2\ s\beta_Y s\phi c\phi+\dot{\beta}_Y\dot{\phi}\ c\beta_Y c^2\phi\right.\\&\quad-\dot{\beta}_Y\dot{\phi}\ c\beta_Y s^2\phi+\ddot{\beta}_X c^2\beta_Y c^2\phi-2\dot{\beta}_X\dot{\beta}_Y c\beta_Y s\beta_Y c^2\phi\\&\quad\left.-2\dot{\beta}_X\dot{\phi}c^2\beta_Y c\phi s\phi\right]\end{aligned} \tag{7.117}$$

Since angles β_X and β_Y are assumed small, the trigonometric functions of these angles can be simplified:

$$\begin{aligned}&\frac{d}{dt}\frac{\partial}{\partial \dot{\beta}_X}\left(KE_{\text{ang, }xx}\right)\\&\quad=J_{xx}\left[\ddot{\beta}_Y\ s\phi c\phi-\dot{\beta}_Y^2\ \beta_Y s\phi c\phi+\dot{\beta}_Y\dot{\phi}\ c^2\phi-\dot{\beta}_Y\dot{\phi}\ s^2\phi+\ddot{\beta}_X c^2\phi\right.\\&\quad\left.-2\dot{\beta}_X\dot{\beta}_Y\beta_Y c^2\phi-2\dot{\beta}_X\dot{\phi}c\phi s\phi\right]\end{aligned} \tag{7.118}$$

All terms that are second or higher order in β_X, β_Y, and their temporal derivatives are neglected, since these angles are small. Note that second order terms containing $\dot{\phi}$ are specifically kept, since ϕ is not small, and $\dot{\phi}$ is the actual rotor operation speed, which factors strongly into the dynamics.

$$\begin{aligned}&\frac{d}{dt}\frac{\partial}{\partial \dot{\beta}_X}\left(KE_{\text{ang, }xx}\right)\\&\quad=J_{xx}\left[\ddot{\beta}_Y\ s\phi c\phi+\dot{\beta}_Y\dot{\phi}\ c^2\phi-\dot{\beta}_Y\dot{\phi}\ s^2\phi+\ddot{\beta}_X c^2\phi-2\dot{\beta}_X\dot{\phi}c\phi s\phi\right]\end{aligned} \tag{7.119}$$

The other derivative of this term vanishes:

$$\frac{\partial}{\partial \beta_X}\left(KE_{\text{ang, }xx}\right) = \frac{\partial}{\partial \beta_X}\left(\frac{1}{2}J_{xx}\left(\dot{\beta}_Y s\phi + \dot{\beta}_X c\beta_Y c\phi\right)^2\right) = 0 \tag{7.120}$$

The derivatives of the next angular kinetic energy term are found in the same way:

$$\begin{aligned}\frac{\partial}{\partial \dot{\beta}_X}\left(KE_{\text{ang, }yy}\right) &= \frac{\partial}{\partial \dot{\beta}_X}\left(\frac{1}{2}J_{yy}\left(\dot{\beta}_Y c\phi - \dot{\beta}_X c\beta_Y s\phi\right)^2\right)\\ &= -J_{yy}\left(\dot{\beta}_Y c\phi - \dot{\beta}_X c\beta_Y s\phi\right)c\beta_Y s\phi\\ &= J_{yy}\left(-\dot{\beta}_Y c\beta_Y c\phi s\phi + \dot{\beta}_X c^2\beta_Y s^2\phi\right)\end{aligned} \tag{7.121}$$

$$\begin{aligned}\frac{d}{dt}\frac{\partial}{\partial \dot{\beta}_X}\left(KE_{\text{ang, }yy}\right) &= J_{yy}\,\frac{d}{dt}\left(-\dot{\beta}_Y c\beta_Y c\phi s\phi + \dot{\beta}_X c^2\beta_Y s^2\phi\right)\\ &= J_{yy}\left[-\ddot{\beta}_Y c\beta_Y c\phi s\phi + \dot{\beta}_Y^2 s\beta_Y c\phi s\phi + \dot{\beta}_Y\dot{\phi} c\beta_Y s^2\phi\right.\\ &\quad - \dot{\beta}_Y\dot{\phi} c\beta_Y c^2\phi + \ddot{\beta}_X c^2\beta_Y s^2\phi - 2\dot{\beta}_X\dot{\beta}_Y c\beta_Y s\beta_Y s^2\phi\\ &\quad \left.+ 2\dot{\beta}_X\dot{\phi} c^2\beta_Y s\phi c\phi\right]\end{aligned} \tag{7.122}$$

Since angles β_X and β_Y are assumed small, the trigonometric functions of these angles can be simplified:

$$\begin{aligned}&\frac{d}{dt}\frac{\partial}{\partial \dot{\beta}_X}\left(KE_{\text{ang, }yy}\right)\\ &\quad = J_{yy}\left[-\ddot{\beta}_Y c\phi s\phi + \dot{\beta}_Y^2 \beta_Y c\phi s\phi + \dot{\beta}_Y\dot{\phi} s^2\phi - \dot{\beta}_Y\dot{\phi} c^2\phi + \ddot{\beta}_X s^2\phi\right.\\ &\quad \left.- 2\dot{\beta}_X\dot{\beta}_Y \beta_Y s^2\phi + 2\dot{\beta}_X\dot{\phi} s\phi c\phi\right]\end{aligned} \tag{7.123}$$

All terms that are second or higher order in β_X, β_Y, and their temporal derivatives are neglected, since these angles are small. Note that second order terms containing $\dot{\phi}$ are specifically kept, since ϕ is not small, and $\dot{\phi}$ is the actual rotor operation speed, which factors strongly into the dynamics.

$$\begin{aligned}&\frac{d}{dt}\frac{\partial}{\partial \dot{\beta}_X}\left(KE_{\text{ang, }yy}\right)\\ &\quad = J_{yy}\left[-\ddot{\beta}_Y c\phi s\phi + \dot{\beta}_Y\dot{\phi} s^2\phi - \dot{\beta}_Y\dot{\phi} c^2\phi + \ddot{\beta}_X s^2\phi + 2\dot{\beta}_X\dot{\phi} s\phi c\phi\right]\end{aligned} \tag{7.124}$$

The other derivative of this term vanishes:

$$\frac{\partial}{\partial \beta_X}\left(KE_{\text{ang, }yy}\right) = \frac{\partial}{\partial \beta_X}\left(\frac{1}{2}J_{yy}\left(\dot{\beta}_Y c\phi - \dot{\beta}_X c\beta_Y s\phi\right)^2\right) = 0 \quad \textbf{(7.125)}$$

The derivatives of the next angular kinetic energy term are found in the same way:

$$\begin{aligned}\frac{\partial}{\partial \dot{\beta}_X}\left(KE_{\text{ang, }zz}\right) &= \frac{\partial}{\partial \dot{\beta}_X}\left(\frac{1}{2}J_{zz}\left(\dot{\phi} + \dot{\beta}_X s\beta_y\right)^2\right) \\ &= J_{zz}\left(\dot{\phi} + \dot{\beta}_X s\beta_Y\right)s\beta_y \\ &= J_{zz}\left(\dot{\phi}s\beta_Y + \dot{\beta}_X s^2\beta_Y\right)\end{aligned} \quad \textbf{(7.126)}$$

$$\begin{aligned}\frac{d}{dt}\frac{\partial}{\partial \dot{\beta}_X}\left(KE_{\text{ang, }zz}\right) &= J_{zz}\frac{d}{dt}\left(\dot{\phi}s\beta_Y + \dot{\beta}_X s^2\beta_Y\right) \\ &= J_{zz}\left(\ddot{\phi}s\beta_Y + \dot{\phi}\dot{\beta}_Y c\beta_Y + \ddot{\beta}_X s^2\beta_Y + 2\dot{\beta}_X\dot{\beta}_Y c\beta_Y\right)\end{aligned} \quad \textbf{(7.127)}$$

Since angles β_X and β_Y are assumed small, the trigonometric functions of these angles can be simplified:

$$\frac{d}{dt}\frac{\partial}{\partial \dot{\beta}_X}\left(KE_{\text{ang, }zz}\right) = J_{zz}\left(\ddot{\phi}\beta_Y + \dot{\phi}\dot{\beta}_Y + \ddot{\beta}_X\beta_Y^2 + 2\dot{\beta}_X\dot{\beta}_Y\right) \quad \textbf{(7.128)}$$

All terms that are second or higher order in β_X, β_Y, and their temporal derivatives are neglected, since these angles are small. Note that second order terms containing $\dot{\phi}$ are specifically kept, since ϕ is not small, and $\dot{\phi}$ is the actual rotor operation speed, which factors strongly into the dynamics.

$$\frac{d}{dt}\frac{\partial}{\partial \dot{\beta}_X}\left(KE_{\text{ang, }zz}\right) = J_{zz}\left(\dot{\phi}\dot{\beta}_Y\right) \quad \textbf{(7.129)}$$

The other derivative of this term vanishes:

$$\frac{\partial}{\partial \beta_X}\left(KE_{\text{ang, }zz}\right) = \frac{\partial}{\partial \beta_X}\left(\frac{1}{2}J_{zz}\left(\dot{\phi} + \dot{\beta}_X s\beta_y\right)^2\right) = 0 \quad \textbf{(7.130)}$$

The next term, the xy-angular-kinetic-energy term, has no contribution to the Lagrangian. Recall that the product of inertia J_{xy} is negligible for this thin disk system. Therefore, since the xy-angular-kinetic-energy term would contain this product of inertia, it and all of its derivatives are zero:

$$\frac{\partial}{\partial \dot{\beta}_X}\left(KE_{\text{ang},\ xy}\right) = \frac{\partial}{\partial \dot{\beta}_X} 0 = 0 \tag{7.131}$$

$$\frac{d}{dt}\frac{\partial}{\partial \dot{\beta}_X}\left(KE_{\text{ang},\ xy}\right) = 0 \tag{7.132}$$

$$\frac{\partial}{\partial \beta_X}\left(KE_{\text{ang},\ xy}\right) = \frac{\partial}{\partial \beta_X}(0) = 0 \tag{7.133}$$

The derivatives of the next angular kinetic energy term are found in the same way:

$$\begin{aligned}\frac{\partial}{\partial \dot{\beta}_X}\left(KE_{\text{ang},\,xz}\right) &= \frac{\partial}{\partial \dot{\beta}_X}\left[J_{xz}\left(\dot{\beta}_Y s\phi + \dot{\beta}_X c\beta_Y c\phi\right)\left(\dot{\phi} + \dot{\beta}_X s\beta_Y\right)\right] \\ &= J_{xz}\frac{\partial}{\partial \dot{\beta}_X}\left[\dot{\beta}_Y\dot{\phi} s\phi + \dot{\beta}_X\dot{\phi} c\beta_Y c\phi + \dot{\beta}_X\dot{\beta}_Y s\beta_Y s\phi + \dot{\beta}_X^2 c\beta_Y s\beta_Y c\phi\right] \\ &= J_{xz}\left[\dot{\phi} c\beta_Y c\phi + \dot{\beta}_Y s\beta_Y s\phi + 2\dot{\beta}_X c\beta_Y s\beta_Y c\phi\right]\end{aligned} \tag{7.134}$$

$$\begin{aligned}\frac{d}{dt}\frac{\partial}{\partial \dot{\beta}_X}\left(KE_{\text{ang},\ xz}\right) &= J_{xz}\frac{d}{dt}\left[\dot{\phi} c\beta_Y c\phi + \dot{\beta}_Y s\beta_Y s\phi + 2\dot{\beta}_X c\beta_Y s\beta_Y c\phi\right] \\ &= J_{xz}\left[\ddot{\phi} c\beta_Y c\phi - \dot{\beta}_Y\dot{\phi} s\beta_Y c\phi - \dot{\phi}^2 c\beta_Y s\phi + \ddot{\beta}_Y s\beta_Y s\phi + \dot{\beta}_Y^2 c\beta_Y s\phi\right. \\ &\quad + \dot{\beta}_Y\dot{\phi} s\beta_Y c\phi + 2\ddot{\beta}_X c\beta_Y s\beta_Y c\phi - 2\dot{\beta}_X\dot{\beta}_Y s^2\beta_Y c\phi + 2\dot{\beta}_X\dot{\beta}_Y c^2\beta_Y c\phi \\ &\quad \left. - 2\dot{\beta}_X\dot{\phi} c\beta_Y s\beta_Y s\phi\right]\end{aligned} \tag{7.135}$$

Since angles β_X and β_Y are assumed small, the trigonometric functions of these angles can be simplified:

$$\begin{aligned}&\frac{d}{dt}\frac{\partial}{\partial \dot{\beta}_X}\left(KE_{\text{ang},\ xz}\right) \\ &\quad = J_{xz}\left[\ddot{\phi} c\phi - \dot{\beta}_Y\dot{\phi}\beta_Y c\phi - \dot{\phi}^2 s\phi + \ddot{\beta}_Y\beta_Y s\phi + \dot{\beta}_Y^2 s\phi + \dot{\beta}_Y\dot{\phi}\beta_Y c\phi\right. \\ &\quad \left. + 2\ddot{\beta}_X\beta_Y c\phi - 2\dot{\beta}_X\dot{\beta}_Y\beta_Y^2 c\phi + 2\dot{\beta}_X\dot{\beta}_Y c\phi - 2\dot{\beta}_X\dot{\phi}\beta_Y s\phi\right]\end{aligned} \tag{7.136}$$

All terms that are second or higher order in β_X, β_Y, and their temporal derivatives are neglected, since these angles are small. Note that second order terms containing $\dot{\phi}$ are specifically kept, since ϕ is not small, and $\dot{\phi}$ is the actual rotor operation speed, which factors strongly into the dynamics.

$$\frac{d}{dt}\frac{\partial}{\partial\dot{\beta}_X}\left(KE_{\text{ang, }xz}\right) = J_{xz}\left[\ddot{\phi}c\phi - \dot{\phi}^2 s\phi\right] \tag{7.137}$$

The other derivative of this term vanishes:

$$\frac{\partial}{\partial\beta_X}\left(KE_{\text{ang, }xz}\right) = \frac{\partial}{\partial\beta_X}\left[J_{xz}\left(\dot{\beta}_Y s\phi + \dot{\beta}_X c\beta_Y c\phi\right)\left(\dot{\phi} + \dot{\beta}_X s\beta_Y\right)\right] = 0 \tag{7.138}$$

The derivatives of the next angular kinetic energy term are found in the same way:

$$\begin{aligned}\frac{\partial}{\partial\dot{\beta}_X}\left(KE_{\text{ang, }yz}\right) &= \frac{\partial}{\partial\dot{\beta}_X}\left[J_{yz}\left(\dot{\beta}_Y c\phi - \dot{\beta}_X c\beta_Y s\phi\right)\left(\dot{\phi} + \dot{\beta}_X s\beta_Y\right)\right] \\ &= J_{yz}\frac{\partial}{\partial\dot{\beta}_X}\left[\dot{\beta}_Y\dot{\phi}c\phi - \dot{\beta}_X\dot{\phi}c\beta_Y s\phi + \dot{\beta}_X\dot{\beta}_Y s\beta_y c\phi - \dot{\beta}_X^2 c\beta_Y s\beta_Y s\phi\right] \\ &= J_{yz}\left[-\dot{\phi}c\beta_Y s\phi + \dot{\beta}_Y s\beta_Y c\phi - 2\dot{\beta}_X c\beta_Y s\beta_Y s\phi\right]\end{aligned} \tag{7.139}$$

$$\begin{aligned}\frac{d}{dt}\frac{\partial}{\partial\dot{\beta}_X}\left(KE_{\text{ang, }yz}\right) &= J_{yz}\frac{d}{dt}\left[\dot{\phi}c\beta_Y s\phi + \dot{\beta}_Y s\beta_Y c\phi - 2\dot{\beta}_X c\beta_Y s\beta_Y s\phi\right] \\ &= J_{yz}[-\ddot{\phi}c\beta_Y s\phi + \dot{\beta}_Y\dot{\phi}s\beta_Y s\phi - \dot{\phi}^2 c\beta_Y c\phi + \ddot{\beta}_Y s\beta_Y c\phi \\ &+ \dot{\beta}_Y^2 c\beta_Y c\phi - \dot{\beta}_Y\dot{\phi}s\beta_Y s\phi - 2\ddot{\beta}_X c\beta_Y s\beta_Y s\phi - 2\dot{\beta}_X\dot{\beta}_Y c^2\beta_Y s\phi \\ &+ 2\dot{\beta}_X\dot{\beta}_Y s^2\beta_Y s\phi - 2\dot{\beta}_X\dot{\phi}c\beta_Y s\beta_Y c\phi]\end{aligned} \tag{7.140}$$

Since angles β_X and β_Y are assumed small, the trigonometric functions of these angles can be simplified:

$$\begin{aligned}&\frac{d}{dt}\frac{\partial}{\partial\dot{\beta}_X}\left(KE_{\text{ang, }yz}\right) \\ &= J_{yz}[-\ddot{\phi}s\phi + \dot{\beta}_Y\dot{\phi}\beta_Y s\phi - \dot{\phi}^2 c\phi + \ddot{\beta}_Y\beta_Y c\phi + \dot{\beta}_Y^2 c\phi - \dot{\beta}_Y\dot{\phi}\beta_Y s\phi \\ &- 2\ddot{\beta}_X\beta_Y s\phi - 2\dot{\beta}_X\dot{\beta}_Y s\phi + 2\dot{\beta}_X\dot{\beta}_Y\beta_Y^2 s\phi - 2\dot{\beta}_X\dot{\phi}\beta_Y c\phi]\end{aligned} \tag{7.141}$$

All terms that are second or higher order in β_X, β_Y, and their temporal derivatives are neglected, since these angles are small. Note that second order terms containing $\dot{\phi}$ are specifically kept, since ϕ is not small, and $\dot{\phi}$ is the actual rotor operation speed, which factors strongly into the dynamics.

$$\frac{d}{dt}\frac{\partial}{\partial \dot{\beta}_X}\left(KE_{\text{ang, }yz}\right) = J_{yz}\left[-\ddot{\phi} s\phi - \dot{\phi}^2 c\phi\right] \tag{7.142}$$

The other derivative of this term vanishes:

$$\frac{\partial}{\partial \beta_X}\left(KE_{\text{ang, }yz}\right) = \frac{\partial}{\partial \beta_X}\left[J_{yz}\left(\dot{\beta}_Y c\phi - \dot{\beta}_X c\beta_Y s\phi\right)\left(\dot{\phi} + \dot{\beta}_X s\beta_Y\right)\right] = 0 \tag{7.143}$$

Combining the derivatives from (7.120), (7.125), (7.130), (7.133), (7.138), and (7.143) yields:

$$\begin{aligned}\frac{d}{dt}\frac{\partial}{\partial \dot{\beta}_X}\left(KE_{\text{angular}}\right)&\\ = \frac{d}{dt}\frac{\partial}{\partial \dot{\beta}_X}\left(KE_{\text{ang, }xx}\right) &+ \frac{d}{dt}\frac{\partial}{\partial \dot{\beta}_X}\left(KE_{\text{ang, }yy}\right) + \frac{d}{dt}\frac{\partial}{\partial \dot{\beta}_X}\left(KE_{\text{ang, }zz}\right)\\ + \frac{d}{dt}\frac{\partial}{\partial \dot{\beta}_X}\left(KE_{\text{ang, }xy}\right) &+ \frac{d}{dt}\frac{\partial}{\partial \dot{\beta}_X}\left(KE_{\text{ang, }xz}\right) + \frac{d}{dt}\frac{\partial}{\partial \dot{\beta}_X}\left(KE_{\text{ang, }yz}\right)\end{aligned} \tag{7.144}$$

$$\begin{aligned}\frac{d}{dt}\frac{\partial}{\partial \dot{\beta}_X}\left(KE_{\text{angular}}\right)&\\ = J_{xx}&\left[\ddot{\beta}_Y\, s\phi c\phi + \dot{\beta}_Y \dot{\phi}\, c^2\phi - \dot{\beta}_Y \dot{\phi}\, s^2\phi + \ddot{\beta}_X c^2\phi - 2\dot{\beta}_X \dot{\phi} c\phi s\phi\right]\\ + J_{yy}&\left[-\ddot{\beta}_Y c\phi s\phi + \dot{\beta}_Y \dot{\phi} s^2\phi - \dot{\beta}_Y \dot{\phi} c^2\phi + \ddot{\beta}_X s^2\phi + 2\dot{\beta}_X \dot{\phi} s\phi c\phi\right]\\ + J_{zz}&\left(\dot{\phi}\dot{\beta}_Y\right) + J_{xz}\left[\ddot{\phi} c\phi - \dot{\phi}^2 s\phi\right] + 0 + J_{yz}\left[-\ddot{\phi} s\phi - \dot{\phi}^2 c\phi\right]\end{aligned} \tag{7.145}$$

Recalling equation (7.33) allows the cancelation of several terms:

$$\begin{aligned}\frac{d}{dt}\frac{\partial}{\partial \dot{\beta}_X}\left(KE_{\text{angular}}\right)&\\ = J&\left[\ddot{\beta}_Y\, s\phi c\phi + \dot{\beta}_Y \dot{\phi}\, c^2\phi - \dot{\beta}_Y \dot{\phi}\, s^2\phi + \ddot{\beta}_X c^2\phi - 2\dot{\beta}_X \dot{\phi} c\phi s\phi\right]\\ + J&\left[-\ddot{\beta}_Y c\phi s\phi + \dot{\beta}_Y \dot{\phi} s^2\phi - \dot{\beta}_Y \dot{\phi} c^2\phi + \ddot{\beta}_X s^2\phi + 2\dot{\beta}_X \dot{\phi} s\phi c\phi\right]\\ + J_{zz}&\left(\dot{\phi}\dot{\beta}_Y\right) + J_{xz}\left[\ddot{\phi} c\phi - \dot{\phi}^2 s\phi\right] + 0 + J_{yz}\left[-\ddot{\phi} s\phi - \dot{\phi}^2 c\phi\right]\end{aligned} \tag{7.146}$$

$$\begin{aligned}\frac{d}{dt}\frac{\partial}{\partial\dot{\beta}_X}\left(KE_{\text{angular}}\right)\\ &= J\left[\ddot{\beta}_X\right] + J\left[\dot{\beta}_Y\dot{\phi}s^2\phi\right] + J_{zz}\left(\dot{\phi}\dot{\beta}_Y\right) + J_{xz}\left[\ddot{\phi}c\phi - \dot{\phi}^2 s\phi\right] + 0\\ &- J_{yz}\left[\ddot{\phi}s\phi + \dot{\phi}^2 c\phi\right]\end{aligned} \tag{7.147}$$

$$\frac{d}{dt}\frac{\partial}{\partial\dot{\beta}_X}\left(KE_{\text{angular}}\right) = J\ddot{\beta}_X + J_{zz}\dot{\phi}\dot{\beta}_Y + \ddot{\phi}\left[J_{xz}c\phi - J_{yz}s\phi\right] - \dot{\phi}^2\left[J_{yz}c\phi + J_{xz}s\phi\right] \tag{7.148}$$

The remaining derivatives from (7.172), (7.177), (7.180), (7.184), (7.189), and (7.195) form:

$$\begin{aligned}\frac{\partial}{\partial\beta_X}\left(KE_{\text{angular}}\right) &= \frac{\partial}{\partial\beta_X}\left(KE_{\text{ang, }xx}\right) + \frac{\partial}{\partial\beta_X}\left(KE_{\text{ang, }yy}\right) + \frac{\partial}{\partial\beta_X}\left(KE_{\text{ang, }zz}\right)\\ &+ \frac{\partial}{\partial\beta_X}\left(KE_{\text{ang, }xy}\right) + \frac{\partial}{\partial\beta_X}\left(KE_{\text{ang, }xz}\right) + \frac{\partial}{\partial\beta_X}\left(KE_{\text{ang, }yz}\right) = 0\end{aligned} \tag{7.149}$$

Next the derivatives of the potential energy terms representing the elastic energy in the beam deflection are evaluated:

$$\frac{\partial}{\partial\dot{\beta}_X}\left(PE_{\text{elastic, x}}\right) = \frac{\partial}{\partial\dot{\beta}_X}\left(EI_{yy}\left[\frac{2\beta_Y^2}{L} - \frac{6R_X\beta_Y}{L^2} + \frac{6R_X^2}{L^3}\right]\right) = 0 \tag{7.150}$$

$$\frac{d}{dt}\frac{\partial}{\partial\dot{\beta}_X}\left(PE_{\text{elastic, x}}\right) = 0 \tag{7.151}$$

$$\frac{\partial}{\partial\beta_X}\left(PE_{\text{elastic, x}}\right) = \frac{\partial}{\partial\beta_X}\left(EI_{yy}\left[\frac{2\beta_Y^2}{L} - \frac{6R_X\beta_Y}{L^2} + \frac{6R_X^2}{L^3}\right]\right) = 0 \tag{7.152}$$

$$\frac{\partial}{\partial\dot{\beta}_X}\left(PE_{\text{elastic, y}}\right) = \frac{\partial}{\partial\dot{\beta}_X}\left(EI_{xx}\left[\frac{2\beta_X^2}{L} + \frac{6R_Y\beta_X}{L^2} + \frac{6R_Y^2}{L^3}\right]\right) = 0 \tag{7.153}$$

$$\frac{d}{dt}\frac{\partial}{\partial\dot{\beta}_X}\left(PE_{\text{elastic, y}}\right) = 0 \tag{7.154}$$

$$\frac{\partial}{\partial \beta_X}\left(PE_{\text{elastic, y}}\right) = \frac{\partial}{\partial \beta_X}\left(EI_{xx}\left[\frac{2\beta_X^2}{L}+\frac{6R_Y\beta_X}{L^2}+\frac{6R_Y^2}{L^3}\right]\right) = EI_{xx}\left[\frac{4\beta_X}{L}+\frac{6R_Y}{L^2}\right] \tag{7.155}$$

Having completed all the derivatives, they can be substituted back into equation (7.109) to get the equation of motion for angular motion about the x-axis:

$$\frac{d}{dt}\left(\frac{\partial \mathcal{L}}{\partial \dot{\beta}_X}\right) = \frac{\partial \mathcal{L}}{\partial \beta_X} \tag{7.156}$$

$$\begin{aligned} &\frac{d}{dt}\frac{\partial}{\partial \dot{\beta}_X}\left(KE_{\text{linear}} + KE_{\text{angular}} - PE_{\text{elastic}}\right) \\ &\qquad = \frac{\partial}{\partial \beta_X}\left(KE_{\text{linear}} + KE_{\text{angular}} - PE_{\text{elastic}}\right) \end{aligned} \tag{7.157}$$

$$\begin{aligned} J\ddot{\beta}_X &+ J_{zz}\dot{\phi}\dot{\beta}_Y + \ddot{\phi}\left[J_{xz}c\phi - J_{yz}s\phi\right] - \dot{\phi}^2\left[J_{yz}c\phi + J_{xz}s\phi\right] \\ &- ma_z\left[\ddot{R}_Y + \left(-a_x s\phi - a_y c\phi\right)\dot{\phi}^2 + \left(a_x c\phi - a_y s\phi\right)\ddot{\phi} - a_z\ddot{\beta}_X\right] \\ &= -EI_{xx}\left[\frac{4\beta_X}{L}+\frac{6R_Y}{L^2}\right] \end{aligned} \tag{7.158}$$

Combining terms makes the expression cleaner:

$$\begin{aligned} (J + ma_z^2)\ddot{\beta}_X &+ J_{zz}\dot{\phi}\dot{\beta}_Y + \ddot{\phi}\left[(J_{xz} - ma_x a_z)c\phi - \left(J_{yz} - ma_y a_z\right)s\phi\right] \\ &- \dot{\phi}^2\left[\left(J_{yz} - ma_y a_z\right)c\phi + (J_{xz} - ma_x a_z)s\phi\right] - ma_z\ddot{R}_Y \\ &= -EI_{xx}\left[\frac{4\beta_X}{L}+\frac{6R_Y}{L^2}\right] \end{aligned} \tag{7.159}$$

7.3.4 Angular Y Motion

For angular motion about the y-axis, the governing equation is found from the Lagrangian as:

$$\frac{d}{dt}\left(\frac{\partial \mathcal{L}}{\partial \dot{\beta}_Y}\right) = \frac{\partial \mathcal{L}}{\partial \beta_Y} \tag{7.160}$$

$$\frac{d}{dt}\left(\frac{\partial[KE-PE]}{\partial\dot{\beta}_Y}\right)=\frac{\partial[KE-PE]}{\partial\beta_Y} \tag{7.161}$$

The derivatives of each term in the Lagrangian are taken one at a time. The derivatives of the linear kinetic energy terms, given in equation (7.14), are as follows:

$$\begin{aligned}\frac{\partial}{\partial\dot{\beta}_Y}\left(KE_{\text{linear},\,x}\right)&=\frac{\partial}{\partial\dot{\beta}_Y}\left(\frac{1}{2}m\left[\dot{R}_X-\left(a_x s\phi\ +a_y c\phi\ \right)\dot{\phi}+a_z\dot{\beta}_Y\right]^2\right)\\&=ma_z\left[\dot{R}_X-\left(a_x s\phi\ +a_y c\phi\ \right)\dot{\phi}+a_z\dot{\beta}_Y\right]\end{aligned} \tag{7.162}$$

$$\begin{aligned}\frac{d}{dt}\frac{\partial}{\partial\dot{\beta}_Y}\left(KE_{\text{linear},\,x}\right)&=ma_z\frac{\mathrm{d}}{\mathrm{dt}}\left[\dot{R}_X-\left(a_x s\phi\ +a_y c\phi\ \right)\dot{\phi}+a_z\dot{\beta}_Y\right]\\&=ma_z\left[\ddot{R}_X-\ddot{\phi}\left(a_x s\phi+a_y c\phi\right)-\dot{\phi}^2\left(a_x c\phi-a_y s\phi\right)+a_z\ddot{\beta}_Y\right]\end{aligned} \tag{7.163}$$

$$\frac{\partial}{\partial\beta_Y}\left(KE_{\text{linear},\,x}\right)=\frac{\partial}{\partial\beta_Y}\left(\frac{1}{2}m\left[\dot{R}_X-\left(a_x s\phi\ +a_y c\phi\ \right)\dot{\phi}+a_z\dot{\beta}_Y\right]^2\right)=0 \tag{7.164}$$

$$\frac{\partial}{\partial\dot{\beta}_Y}\left(KE_{\text{linear},\,y}\right)=\frac{\partial}{\partial\dot{\beta}_Y}\left(\frac{1}{2}m\left[\dot{R}_Y+\left(a_x c\phi-a_y s\phi\right)\dot{\phi}-a_z\dot{\beta}_X\right]^2\right)=0 \tag{7.165}$$

$$\frac{d}{dt}\frac{\partial}{\partial\dot{\beta}_Y}\left(KE_{\text{linear},\,y}\right)=0 \tag{7.166}$$

$$\frac{\partial}{\partial\beta_Y}\left(KE_{\text{linear},\,y}\right)=\frac{\partial}{\partial\beta_Y}\left(\frac{1}{2}m\left[\dot{R}_Y+\left(a_x c\phi-a_y s\phi\right)\dot{\phi}-a_z\dot{\beta}_X\right]^2\right)=0 \tag{7.167}$$

The derivatives of each term in the angular kinetic energy terms are found one at a time:

$$\begin{aligned}\frac{\partial}{\partial\dot{\beta}_Y}\left(KE_{\text{ang},\,xx}\right)&=\frac{\partial}{\partial\dot{\beta}_Y}\left(\frac{1}{2}J_{xx}\left(\dot{\beta}_Y s\phi+\dot{\beta}_X c\beta_Y c\phi\right)^2\right)\\&=J_{xx}\left(\dot{\beta}_Y s\phi+\dot{\beta}_X c\beta_Y c\phi\right)(s\phi)\\&=J_{xx}\left(\dot{\beta}_Y\ s^2\phi+\dot{\beta}_X c\beta_Y c\phi s\phi\right)\end{aligned} \tag{7.168}$$

$$\begin{aligned}\frac{d}{dt}\frac{\partial}{\partial\dot{\beta}_Y}\left(KE_{\text{ang},\,xx}\right) &= J_{xx}\frac{d}{dt}\left(\dot{\beta}_Y\, s^2\phi + \dot{\beta}_X c\beta_Y c\phi s\phi\right) \\ &= J_{xx}\big[\ddot{\beta}_Y s^2\phi + 2\dot{\beta}_Y\dot{\phi} s\phi c\phi + \ddot{\beta}_X c\beta_Y c\phi s\phi - \dot{\beta}_X\dot{\beta}_Y s\beta_Y c\phi s\phi \\ &\quad - \dot{\beta}_X\dot{\phi} c\beta_Y s^2\phi + \dot{\beta}_X\dot{\phi} c\beta_Y c^2\phi\big]\end{aligned} \tag{7.169}$$

Since angles β_X and β_Y are assumed small, the trigonometric functions of these angles can be simplified:

$$\begin{aligned}&\frac{d}{dt}\frac{\partial}{\partial\dot{\beta}_Y}\left(KE_{\text{ang},\,xx}\right) \\ &\quad = J_{xx}\big[\ddot{\beta}_Y s^2\phi + 2\dot{\beta}_Y\dot{\phi} s\phi c\phi + \ddot{\beta}_X c\phi s\phi - \dot{\beta}_X\dot{\beta}_Y \beta_Y c\phi s\phi - \dot{\beta}_X\dot{\phi} s^2\phi \\ &\quad + \dot{\beta}_X\dot{\phi} c^2\phi\big]\end{aligned} \tag{7.170}$$

All terms that are second or higher order in β_X, β_Y, and their temporal derivatives are neglected, since these angles are small. Note that second order terms containing $\dot{\phi}$ are specifically kept, since ϕ is not small, and $\dot{\phi}$ is the actual rotor operation speed, which factors strongly into the dynamics.

$$\frac{d}{dt}\frac{\partial}{\partial\dot{\beta}_Y}\left(KE_{\text{ang},\,xx}\right) = J_{xx}\big[\ddot{\beta}_Y s^2\phi + 2\dot{\beta}_Y\dot{\phi} s\phi c\phi + \ddot{\beta}_X c\phi s\phi - \dot{\beta}_X\dot{\phi} s^2\phi + \dot{\beta}_X\dot{\phi} c^2\phi\big] \tag{7.171}$$

The other derivative of this term is:

$$\begin{aligned}\frac{\partial}{\partial\beta_Y}\left(KE_{\text{ang},\,xx}\right) &= \frac{\partial}{\partial\beta_Y}\left(\frac{1}{2}J_{xx}\left(\dot{\beta}_Y s\phi + \dot{\beta}_X c\beta_Y c\phi\right)^2\right) \\ &= J_{xx}\left(\dot{\beta}_Y s\phi + \dot{\beta}_X c\beta_Y c\phi\right)\left(-\dot{\beta}_X s\beta_Y c\phi\right) \\ &= J_{xx}\left[-\dot{\beta}_X\dot{\beta}_Y s\beta_Y s\phi c\phi - \dot{\beta}_X^2 s\beta_Y c\beta_Y c^2\phi\right]\end{aligned} \tag{7.172}$$

Note that with the small angle assumption on β_Y, this entire term is 3rd order in β_X, β_Y, and their derivatives, and can be completely neglected. The derivatives of the next angular kinetic energy term are found in the same way:

$$\begin{aligned}\frac{\partial}{\partial\dot{\beta}_Y}\left(KE_{\text{ang},\,yy}\right) &= \frac{\partial}{\partial\dot{\beta}_Y}\left(\frac{1}{2}J_{yy}\left(\dot{\beta}_Y c\phi - \dot{\beta}_X c\beta_Y s\phi\right)^2\right) \\ &= J_{yy}\left(\dot{\beta}_Y c\phi - \dot{\beta}_X c\beta_Y s\phi\right)c\phi = J_{yy}\left(\dot{\beta}_Y c^2\phi - \dot{\beta}_X c\beta_Y c\phi s\phi\right)\end{aligned} \tag{7.173}$$

$$\frac{d}{dt}\frac{\partial}{\partial \dot{\beta}_Y}\left(KE_{\text{ang, }yy}\right) = J_{yy}\,\frac{d}{dt}\left(\dot{\beta}_Y c^2\phi - \dot{\beta}_X c\beta_Y c\phi s\phi\right)$$
$$= J_{yy}\left[\ddot{\beta}_Y c^2\phi - 2\dot{\beta}_Y\dot{\phi}c\phi s\phi - \ddot{\beta}_X c\beta_Y c\phi s\phi + \dot{\beta}_X\dot{\beta}_Y s\beta_Y c\phi s\phi + \dot{\beta}_X\dot{\phi}c\beta_Y s^2\phi - \dot{\beta}_X\dot{\phi}c\beta_Y c^2\phi\right] \quad \textbf{(7.174)}$$

Since angles β_X and β_Y are assumed small, the trigonometric functions of these angles can be simplified:

$$\frac{d}{dt}\frac{\partial}{\partial \dot{\beta}_Y}\left(KE_{\text{ang, }yy}\right)$$
$$= J_{yy}\left[\ddot{\beta}_Y c^2\phi - 2\dot{\beta}_Y\dot{\phi}c\phi s\phi - \ddot{\beta}_X c\phi s\phi + \dot{\beta}_X\dot{\beta}_Y\beta_Y c\phi s\phi + \dot{\beta}_X\dot{\phi}s^2\phi - \dot{\beta}_X\dot{\phi}c^2\phi\right] \quad \textbf{(7.175)}$$

All terms that are second or higher order in β_X, β_Y, and their temporal derivatives are neglected, since these angles are small. Note that second order terms containing $\dot{\phi}$ are specifically kept, since ϕ is not small, and $\dot{\phi}$ is the actual rotor operation speed, which factors strongly into the dynamics.

$$\frac{d}{dt}\frac{\partial}{\partial \dot{\beta}_Y}\left(KE_{\text{ang, }yy}\right) = J_{yy}\left[\ddot{\beta}_Y c^2\phi - 2\dot{\beta}_Y\dot{\phi}c\phi s\phi - \ddot{\beta}_X c\phi s\phi + \dot{\beta}_X\dot{\phi}s^2\phi - \dot{\beta}_X\dot{\phi}c^2\phi\right] \quad \textbf{(7.176)}$$

The other derivative of this term is:

$$\frac{\partial}{\partial \beta_Y}\left(KE_{\text{ang, }yy}\right) = \frac{\partial}{\partial \beta_Y}\left(\frac{1}{2}J_{yy}\left(\dot{\beta}_Y c\phi - \dot{\beta}_X c\beta_Y s\phi\right)^2\right)$$
$$= J_{yy}\left(\dot{\beta}_Y c\phi - \dot{\beta}_X c\beta_Y s\phi\right)\left(\dot{\beta}_X s\beta_Y s\phi\right) \quad \textbf{(7.177)}$$
$$= J_{yy}\left[\dot{\beta}_Y\dot{\beta}_X s\beta_Y s\phi c\phi - \dot{\beta}_X^2 s\beta_Y c\beta_Y s^2\phi\right]$$

Note that with the small angle assumption on β_Y, this entire term is 3rd order in β_X, β_Y, and their derivatives, and can be completely neglected. The derivatives of the next angular kinetic energy term are found in the same way:

$$\frac{\partial}{\partial \dot{\beta}_Y}\left(KE_{\text{ang, }zz}\right) = \frac{\partial}{\partial \dot{\beta}_Y}\left(\frac{1}{2}J_{zz}\left(\dot{\phi} + \dot{\beta}_X s\beta_y\right)^2\right) = 0 \quad \textbf{(7.178)}$$

$$\frac{d}{dt}\frac{\partial}{\partial \dot{\beta}_Y}\left(KE_{\text{ang},\, zz}\right) = 0 \tag{7.179}$$

The other derivative of this term is:

$$\begin{aligned}\frac{\partial}{\partial \beta_Y}\left(KE_{\text{ang},\, zz}\right) &= \frac{\partial}{\partial \beta_Y}\left(\frac{1}{2}J_{zz}\left(\dot{\phi} + \dot{\beta}_X s\beta_y\right)^2\right) = J_{zz}\left(\dot{\phi} + \dot{\beta}_X s\beta_y\right)\left(\dot{\beta}_X c\beta_Y\right)\\ &= J_{zz}\left[\dot{\phi}\dot{\beta}_X c\beta_Y + \dot{\beta}_X^2 c\beta_Y s\beta_y\right]\end{aligned} \tag{7.180}$$

Using the small angle assumption on β_Y and eliminating the 3rd order term yields

$$\frac{\partial}{\partial \beta_Y}\left(KE_{\text{ang},\, zz}\right) = J_{zz}\dot{\phi}\dot{\beta}_X \tag{7.181}$$

The next term, the xy-angular-kinetic-energy term , does not contribute to the Lagrangian. Recall that the product of inertia J_{xy} is negligible for this thin disk system. Therefore, since the xy-angular-kinetic-energy term would contain this product of inertia, it and all of its derivatives are zero:

$$\frac{\partial}{\partial \dot{\beta}_Y}\left(KE_{\text{ang},\ xy}\right) = \frac{\partial}{\partial \dot{\beta}_Y}0 = 0 \tag{7.182}$$

$$\frac{d}{dt}\frac{\partial}{\partial \dot{\beta}_Y}\left(KE_{\text{ang},\ xy}\right) = 0 \tag{7.183}$$

$$\frac{\partial}{\partial \beta_Y}\left(KE_{\text{ang},\ xy}\right) = \frac{\partial}{\partial \beta_Y}(0) = 0 \tag{7.184}$$

The derivatives of the next angular kinetic energy term are found in the same way:

$$\begin{aligned}\frac{\partial}{\partial \dot{\beta}_Y}\left(KE_{\text{ang},\, xz}\right) &= \frac{\partial}{\partial \dot{\beta}_Y}\left[J_{xz}\left(\dot{\beta}_Y s\phi + \dot{\beta}_X c\beta_Y c\phi\right)\left(\dot{\phi} + \dot{\beta}_X s\beta_Y\right)\right]\\ &= J_{xz}\frac{\partial}{\partial \dot{\beta}_Y}\left[\dot{\beta}_Y\dot{\phi}s\phi + \dot{\beta}_X\dot{\phi}c\beta_Y c\phi + \dot{\beta}_X\dot{\beta}_Y s\beta_Y s\phi + \dot{\beta}_X^2 c\beta_Y s\beta_Y c\phi\right]\\ &= J_{xz}\left[\dot{\phi}s\phi + \dot{\beta}_X s\beta_Y s\phi\right]\end{aligned} \tag{7.185}$$

$$\begin{aligned}\frac{d}{dt}\frac{\partial}{\partial\dot{\beta}_Y}\left(KE_{\text{ang},\ xz}\right) &= J_{xz}\frac{d}{dt}\left[\dot{\phi}s\phi + \dot{\beta}_X s\beta_Y s\phi\right] \\ &= J_{xz}\left[\ddot{\phi}s\phi + \dot{\phi}^2 c\phi + \ddot{\beta}_X s\beta_Y s\phi + \dot{\beta}_X\dot{\beta}_Y c\beta_Y s\phi + \dot{\beta}_X\dot{\phi}s\beta_Y c\phi\right]\end{aligned} \tag{7.186}$$

Since angles β_X and β_Y are assumed small, the trigonometric functions of these angles can be simplified:

$$\frac{d}{dt}\frac{\partial}{\partial\dot{\beta}_Y}\left(KE_{\text{ang},\ xz}\right) = J_{xz}\left[\ddot{\phi}s\phi + \dot{\phi}^2 c\phi + \ddot{\beta}_X\beta_Y s\phi + \dot{\beta}_X\dot{\beta}_Y s\phi + \dot{\beta}_X\dot{\phi}\beta_Y c\phi\right] \tag{7.187}$$

All terms that are second or higher order in β_X, β_Y, and their temporal derivatives are neglected, since these angles are small. Note that second order terms containing $\dot{\phi}$ are specifically kept, since ϕ is not small, and $\dot{\phi}$ is the actual rotor operation speed, which factors strongly into the dynamics.

$$\frac{d}{dt}\frac{\partial}{\partial\dot{\beta}_Y}\left(KE_{\text{ang},\ xz}\right) = J_{xz}\left[\ddot{\phi}s\phi + \dot{\phi}^2 c\phi\right] \tag{7.188}$$

The other derivative of this term is:

$$\begin{aligned}\frac{\partial}{\partial\beta_Y}\left(KE_{\text{ang},\ xz}\right) &= \frac{\partial}{\partial\beta_Y}\left[J_{xz}\left(\dot{\beta}_Y s\phi + \dot{\beta}_X c\beta_Y c\phi\right)\left(\dot{\phi} + \dot{\beta}_X s\beta_Y\right)\right] \\ &= J_{xz}\frac{\partial}{\partial\beta_Y}\left[\dot{\beta}_Y\dot{\phi}s\phi + \dot{\beta}_X\dot{\phi}c\beta_Y c\phi + \dot{\beta}_X\dot{\beta}_Y s\beta_Y s\phi + \dot{\beta}_X^2 c\beta_Y s\beta_Y c\phi\right] \\ &= J_{xz}\left[-\dot{\beta}_X\dot{\phi}s\beta_Y c\phi + \dot{\beta}_X\dot{\beta}_Y c\beta_Y s\phi + \dot{\beta}_X^2 c^2\beta_Y c\phi - \dot{\beta}_X^2 s^2\beta_Y c\phi\right]\end{aligned} \tag{7.189}$$

Since angles β_X and β_Y are assumed small, the trigonometric functions of these angles can be simplified:

$$\frac{\partial}{\partial\beta_Y}\left(KE_{\text{ang},\ xz}\right) = J_{xz}\left[-\dot{\beta}_X\dot{\phi}\beta_Y c\phi + \dot{\beta}_X\dot{\beta}_Y s\phi + \dot{\beta}_X^2 c\phi - \dot{\beta}_X^2\beta_Y^2 c\phi\right] \tag{7.190}$$

The entire term is second order in β_X and β_Y, and can be neglected. The derivatives of the next angular kinetic energy term are found in the same way:

$$\begin{aligned}\frac{\partial}{\partial\dot\beta_Y}\left(KE_{\text{ang, }yz}\right) &= \frac{\partial}{\partial\dot\beta_Y}\left[J_{yz}\left(\dot\beta_Y c\phi - \dot\beta_X c\beta_Y s\phi\right)\left(\dot\phi + \dot\beta_X s\beta_Y\right)\right] \\ &= J_{yz}\frac{\partial}{\partial\dot\beta_Y}\left[\dot\beta_Y\dot\phi c\phi - \dot\beta_X\dot\phi c\beta_Y s\phi + \dot\beta_X\dot\beta_Y s\beta_y c\phi - \dot\beta_X^2 c\beta_Y s\beta_Y s\phi\right] \\ &= J_{yz}\left[\dot\phi c\phi + \dot\beta_X s\beta_Y c\phi\right]\end{aligned} \tag{7.191}$$

$$\begin{aligned}\frac{d}{dt}\frac{\partial}{\partial\dot\beta_Y}\left(KE_{\text{ang, }yz}\right) &= J_{yz}\frac{d}{dt}\left[\dot\phi c\phi + \dot\beta_X s\beta_Y c\phi\right] \\ &= J_{yz}\left[\ddot\phi c\phi - \dot\phi^2 s\phi + \ddot\beta_X s\beta_Y c\phi + \dot\beta_X\dot\beta_Y c\beta_Y c\phi - \dot\beta_X\dot\phi s\beta_Y s\phi\right]\end{aligned} \tag{7.192}$$

Since angles β_X and β_Y are assumed small, the trigonometric functions of these angles can be simplified:

$$\frac{d}{dt}\frac{\partial}{\partial\dot\beta_Y}\left(KE_{\text{ang, }yz}\right) = J_{yz}\left[\ddot\phi c\phi - \dot\phi^2 s\phi + \ddot\beta_X\beta_Y c\phi + \dot\beta_X\dot\beta_Y c\phi - \dot\beta_X\dot\phi\beta_Y s\phi\right] \tag{7.193}$$

All terms that are second or higher order in β_X, β_Y, and their temporal derivatives are neglected, since these angles are small. Note that second order terms containing $\dot\phi$ are specifically kept, since ϕ is not small, and $\dot\phi$ is the actual rotor operation speed, which factors strongly into the dynamics.

$$\frac{d}{dt}\frac{\partial}{\partial\dot\beta_Y}\left(KE_{\text{ang, }yz}\right) = J_{yz}\left[\ddot\phi c\phi - \dot\phi^2 s\phi\right] \tag{7.194}$$

The other derivative of this term is:

$$\begin{aligned}\frac{\partial}{\partial\beta_Y}\left(KE_{\text{ang, }yz}\right) &= \frac{\partial}{\partial\beta_Y}\left[J_{yz}\left(\dot\beta_Y c\phi - \dot\beta_X c\beta_Y s\phi\right)\left(\dot\phi + \dot\beta_X s\beta_Y\right)\right] \\ &= J_{yz}\frac{\partial}{\partial\beta_Y}\left[\dot\beta_Y\dot\phi c\phi - \dot\beta_X\dot\phi c\beta_Y s\phi + \dot\beta_X\dot\beta_Y s\beta_Y c\phi - \dot\beta_X^2 c\beta_Y s\beta_Y s\phi\right] \\ &= J_{yz}\left[\dot\beta_X s\beta_Y s\phi + \dot\beta_X\dot\beta_Y c\beta_Y c\phi + \dot\beta_X^2 s^2\beta_Y s\phi - \dot\beta_X^2 c^2\beta_Y s\phi\right]\end{aligned} \tag{7.195}$$

This term is at least second order in β_X and β_Y, and is neglected.

Combining the derivatives from (7.171), (7.176), (7.178), (7.183), (7.188) and (7.194) yields:

$$\begin{aligned}\frac{d}{dt}\frac{\partial}{\partial\dot{\beta}_Y}\left(KE_{\text{angular}}\right)\\ &= \frac{d}{dt}\frac{\partial}{\partial\dot{\beta}_Y}\left(KE_{\text{ang},\,xx}\right)+\frac{d}{dt}\frac{\partial}{\partial\dot{\beta}_Y}\left(KE_{\text{ang},\,yy}\right)+\frac{d}{dt}\frac{\partial}{\partial\dot{\beta}_Y}\left(KE_{\text{ang},\,zz}\right)\\ &+\frac{d}{dt}\frac{\partial}{\partial\dot{\beta}_Y}\left(KE_{\text{ang},\,xy}\right)+\frac{d}{dt}\frac{\partial}{\partial\dot{\beta}_Y}\left(KE_{\text{ang},\,xz}\right)+\frac{d}{dt}\frac{\partial}{\partial\dot{\beta}_Y}\left(KE_{\text{ang},\,yz}\right)\end{aligned} \tag{7.196}$$

$$\begin{aligned}\frac{d}{dt}\frac{\partial}{\partial\dot{\beta}_Y}\left(KE_{\text{angular}}\right)\\ &= J_{xx}\left[\ddot{\beta}_Y s^2\phi + 2\dot{\beta}_Y\dot{\phi}s\phi c\phi + \ddot{\beta}_X c\phi s\phi - \dot{\beta}_X\dot{\phi}s^2\phi + \dot{\beta}_X\dot{\phi}c^2\phi\right]\\ &+ J_{yy}\left[\ddot{\beta}_Y c^2\phi - 2\dot{\beta}_Y\dot{\phi}c\phi s\phi - \ddot{\beta}_X c\phi s\phi + \dot{\beta}_X\dot{\phi}s^2\phi - \dot{\beta}_X\dot{\phi}c^2\phi\right]\\ &+ J_{xz}\left[\ddot{\phi}s\phi + \dot{\phi}^2c\phi\right] + J_{yz}\left[\ddot{\phi}c\phi - \dot{\phi}^2s\phi\right]\end{aligned} \tag{7.197}$$

Recalling equation (7.33) allows the cancelation of several terms:

$$\begin{aligned}\frac{d}{dt}\frac{\partial}{\partial\dot{\beta}_Y}\left(KE_{\text{angular}}\right)\\ &= J\left[\ddot{\beta}_Y s^2\phi + 2\dot{\beta}_Y\dot{\phi}s\phi c\phi + \ddot{\beta}_X c\phi s\phi - \dot{\beta}_X\dot{\phi}s^2\phi + \dot{\beta}_X\dot{\phi}c^2\phi\right]\\ &+ J\left[\ddot{\beta}_Y c^2\phi - 2\dot{\beta}_Y\dot{\phi}c\phi s\phi - \ddot{\beta}_X c\phi s\phi + \dot{\beta}_X\dot{\phi}s^2\phi - \dot{\beta}_X\dot{\phi}c^2\phi\right]\\ &+ J_{xz}\left[\ddot{\phi}s\phi + \dot{\phi}^2c\phi\right] + J_{yz}\left[\ddot{\phi}c\phi - \dot{\phi}^2s\phi\right]\end{aligned} \tag{7.198}$$

$$\begin{aligned}\frac{d}{dt}\frac{\partial}{\partial\dot{\beta}_Y}\left(KE_{\text{angular}}\right)\\ &= J\left[\ddot{\beta}_Y s^2\phi\right] + J\left[\ddot{\beta}_Y c^2\phi\right] + J_{xz}\left[\ddot{\phi}s\phi + \dot{\phi}^2c\phi\right] + J_{yz}\left[\ddot{\phi}c\phi - \dot{\phi}^2s\phi\right]\end{aligned} \tag{7.199}$$

$$\frac{d}{dt}\frac{\partial}{\partial\dot{\beta}_Y}\left(KE_{\text{angular}}\right) = J\ddot{\beta}_Y + \ddot{\phi}\left[J_{xz}s\phi + J_{yz}c\phi\right] + \dot{\phi}^2\left[J_{xz}\mathrm{c}\phi - J_{yz}\mathrm{s}\phi\right] \tag{7.200}$$

The remaining derivatives from (7.172), (7.177), (7.180), (7.184), (7.189), and (7.195) form:

$$\begin{aligned}\frac{\partial}{\partial \beta_X}\left(KE_{\text{angular}}\right) &= \frac{\partial}{\partial \beta_X}\left(KE_{\text{ang, }xx}\right) + \frac{\partial}{\partial \beta_X}\left(KE_{\text{ang, }yy}\right) + \frac{\partial}{\partial \beta_X}\left(KE_{\text{ang, }zz}\right) \\ &+ \frac{\partial}{\partial \beta_X}\left(KE_{\text{ang, }xy}\right) + \frac{\partial}{\partial \beta_X}\left(KE_{\text{ang, }xz}\right) + \frac{\partial}{\partial \beta_X}\left(KE_{\text{ang, }yz}\right)\end{aligned} \tag{7.201}$$

$$\frac{\partial}{\partial \beta_X}\left(KE_{\text{angular}}\right) = J_{zz}\dot{\phi}\dot{\beta}_X \tag{7.202}$$

Next, the derivatives of the potential energy terms representing the elastic energy in the beam deflection are evaluated:

$$\frac{\partial}{\partial \dot{\beta}_Y}\left(PE_{\text{elastic, x}}\right) = \frac{\partial}{\partial \dot{\beta}_Y}\left(EI_{yy}\left[\frac{2\beta_Y^2}{L} - \frac{6R_X\beta_Y}{L^2} + \frac{6R_X^2}{L^3}\right]\right) = 0 \tag{7.203}$$

$$\frac{d}{dt}\frac{\partial}{\partial \dot{\beta}_Y}\left(PE_{\text{elastic, x}}\right) = 0 \tag{7.204}$$

$$\frac{\partial}{\partial \beta_Y}\left(PE_{\text{elastic, x}}\right) = \frac{\partial}{\partial \beta_Y}\left(EI_{yy}\left[\frac{2\beta_Y^2}{L} - \frac{6R_X\beta_Y}{L^2} + \frac{6R_X^2}{L^3}\right]\right) = EI_{yy}\left[\frac{4\beta_Y}{L} - \frac{6\mathrm{R}_{\mathrm{X}}}{L^2}\right] \tag{7.205}$$

$$\frac{\partial}{\partial \dot{\beta}_Y}\left(PE_{\text{elastic, y}}\right) = \frac{\partial}{\partial \dot{\beta}_Y}\left(EI_{xx}\left[\frac{2\beta_X^2}{L} + \frac{6R_Y\beta_X}{L^2} + \frac{6R_Y^2}{L^3}\right]\right) = 0 \tag{7.206}$$

$$\frac{d}{dt}\frac{\partial}{\partial \dot{\beta}_Y}\left(PE_{\text{elastic, y}}\right) = 0 \tag{7.207}$$

$$\frac{\partial}{\partial \beta_Y}\left(PE_{\text{elastic, y}}\right) = \frac{\partial}{\partial \beta_Y}\left(EI_{xx}\left[\frac{2\beta_X^2}{L} + \frac{6R_Y\beta_X}{L^2} + \frac{6R_Y^2}{L^3}\right]\right) = 0 \tag{7.208}$$

Having completed all the derivatives, they can be substituted back into equation (7.161) to get the equation of motion for angular motion about the x-axis:

$$\frac{d}{dt}\left(\frac{\partial \mathcal{L}}{\partial \dot{\beta}_Y}\right) = \frac{\partial \mathcal{L}}{\partial \mathrm{\beta}_{\mathrm{Y}}} \tag{7.209}$$

$$\begin{aligned}\frac{d}{dt}\frac{\partial}{\partial \dot{\beta}_Y}&\left(KE_{\text{linear}} + KE_{\text{angular}} - PE_{\text{elastic}}\right)\\ &= \frac{\partial}{\partial \beta_Y}\left(KE_{\text{linear}} + KE_{\text{angular}} - PE_{\text{elastic}}\right)\end{aligned} \qquad \textbf{(7.210)}$$

$$\begin{aligned}J\ddot{\beta}_Y + \ddot{\phi}[J_{xz}s\phi + J_{yz}c\phi] + \dot{\phi}^2[J_{xz}c\phi - J_{yz}s\phi]&\\ + ma_z\left[\ddot{R}_X - \ddot{\phi}(a_x s\phi + a_y c\phi) - \dot{\phi}^2(a_x c\phi - a_y s\phi) + a_z\ddot{\beta}_Y\right]&\\ = J_{zz}\dot{\phi}\dot{\beta}_X - EI_{yy}\left[\frac{4\beta_Y}{L} - \frac{6R_X}{L^2}\right]&\end{aligned} \qquad \textbf{(7.211)}$$

Combining terms makes the expression clearer:

$$\begin{aligned}(J + ma_z^2)\ddot{\beta}_Y + \ddot{\phi}[(J_{xz} - ma_x a_z)s\phi + (J_{yz} - ma_y a_z)c\phi]&\\ + \dot{\phi}^2[(J_{xz} - ma_x a_z)c\phi - (J_{yz} - ma_y a_z)s\phi] + ma_z\ddot{R}_X&\\ = J_{zz}\dot{\phi}\dot{\beta}_X - EI_{yy}\left[\frac{4\beta_Y}{L} - \frac{6R_X}{L^2}\right]&\end{aligned} \qquad \textbf{(7.212)}$$

7.3.5 Angular Z Motion

For angular motion about the z-axis, the governing equation is found from the Lagrangian as:

$$\frac{d}{dt}\left(\frac{\partial \mathcal{L}}{\partial \dot{\phi}}\right) = \frac{\partial \mathcal{L}}{\partial \phi} \qquad \textbf{(7.213)}$$

$$\frac{d}{dt}\left(\frac{\partial [KE - PE]}{\partial \dot{\phi}}\right) = \frac{\partial [KE - PE]}{\partial \phi} \qquad \textbf{(7.214)}$$

The derivatives of the linear kinetic energy terms, given in equation (7.14), are not zero for this case, because ϕ does appear in them. It is helpful to consider these derivatives together:

$$
\begin{aligned}
\frac{\partial}{\partial\dot{\phi}}\left(KE_{\text{linear},\,x}\right) &= \frac{\partial}{\partial\dot{\phi}}\left(\frac{1}{2}m\left[\dot{R}_X-\left(a_x s\phi\ +a_y c\phi\ \right)\dot{\phi}+a_z\dot{\beta}_Y\right]^2\right)\\
&= -m\left(a_x s\phi\ +a_y c\phi\ \right)\left[\dot{R}_X-\left(a_x s\phi\ +a_y c\phi\ \right)\dot{\phi}+a_z\dot{\beta}_Y\right]\\
&= m[-\dot{R}_X a_x s\phi-\dot{R}_X a_y c\phi+\dot{\phi}a_x^2 s^2\phi+\dot{\phi}a_y^2 c^2\phi+2\dot{\phi}a_x a_y s\phi c\phi\\
&-a_x a_z\dot{\beta}_Y s\phi-a_y a_z\dot{\beta}_Y c\phi]
\end{aligned}
\tag{7.215}
$$

$$
\begin{aligned}
\frac{\partial}{\partial\dot{\phi}}\left(KE_{\text{linear},\,y}\right) &= \frac{\partial}{\partial\dot{\phi}}\left(\frac{1}{2}m\left[\dot{R}_Y+\left(a_x c\phi-a_y s\phi\right)\dot{\phi}-a_z\dot{\beta}_X\right]^2\right)\\
&= m\left(a_x c\phi-a_y s\phi\right)\left[\dot{R}_Y+\left(a_x c\phi-a_y s\phi\right)\dot{\phi}-a_z\dot{\beta}_X\right]\\
&= m[\dot{R}_Y a_x c\phi-\dot{R}_Y a_y s\phi+\dot{\phi}a_x^2 c^2\phi+\dot{\phi}a_y^2 s^2\phi-2\dot{\phi}a_x a_y s\phi c\phi\\
&-a_x a_z\dot{\beta}_X c\phi+a_y a_z\dot{\beta}_X s\phi]
\end{aligned}
\tag{7.216}
$$

Combining the x and y terms yields:

$$
\begin{aligned}
\frac{\partial}{\partial\dot{\phi}}\left(KE_{\text{linear}}\right) &= \frac{\partial}{\partial\dot{\phi}}\left(KE_{\text{linear},\,x}\right)+\frac{\partial}{\partial\dot{\phi}}\left(KE_{\text{linear},\,y}\right)\\
&= \mathrm{m}\big[-\dot{R}_X a_x s\phi-\dot{R}_X a_y c\phi+\dot{\phi}a_x^2 s^2\phi+\dot{\phi}a_y^2 c^2\phi+2\dot{\phi}a_x a_y s\phi c\phi\\
&+\dot{R}_Y a_x c\phi-\dot{R}_Y a_y s\phi+\dot{\phi}a_x^2 c^2\phi+\dot{\phi}a_y^2 s^2\phi-2\dot{\phi}a_x a_y s\phi c\\
&+a_z\dot{\beta}_X(a_Y s\phi-a_x c\phi)-a_z\dot{\beta}_Y(a_x s\phi+a_y c\phi)\big]\\
&= m\big[-\dot{R}_X\left(a_x s\phi\ +a_y c\phi\ \right)+\dot{R}_Y\left(a_x c\phi-a_y s\phi\right)+\dot{\phi}\left(a_x^2+a_y^2\right)\\
&+a_z\dot{\beta}_X(a_Y s\phi-a_x c\phi)-a_z\dot{\beta}_Y(a_x s\phi+a_y c\phi)\big]
\end{aligned}
\tag{7.217}
$$

Then taking the time derivative gives:

$$
\begin{aligned}
&\frac{d}{dt}\frac{\partial}{\partial\dot{\phi}}(KE_{\text{linear}})\\
&\qquad = m\frac{d}{dt}\big[-\dot{R}_X(a_x s\phi\ + a_y c\phi) + \dot{R}_Y(a_x c\phi - a_y s\phi) + \dot{\phi}(a_x^2 + a_y^2)\\
&\qquad + a_z\dot{\beta}_X(a_y s\phi - a_x c\phi) - a_z\dot{\beta}_Y(a_x s\phi + a_y c\phi)\big]\\
&\qquad = m\big[-\ddot{R}_X(a_x s\phi\ + a_y c\phi) - \dot{R}_X\dot{\phi}(a_x c\phi - a_y s\phi)\\
&\qquad + \ddot{R}_Y(a_x c\phi - a_y s\phi) + \dot{R}_Y\dot{\phi}(-a_x s\phi - a_y c\phi) + \ddot{\phi}(a_x^2 + a_y^2)\\
&\qquad + a_z\ddot{\beta}_X(a_y s\phi - a_x c\phi) + a_z\dot{\beta}_X\dot{\phi}(a_y c\phi + a_z s\phi)\\
&\qquad - a_z\ddot{\beta}_Y(a_x s\phi + a_y c\phi) - a_z\dot{\beta}_Y\dot{\phi}(a_x c\phi - a_y s\phi)\big]\\
&\qquad = m\big[(\ddot{R}_Y - \dot{R}_X\dot{\phi} - a_z\dot{\beta}_Y\dot{\phi} - a_z\ddot{\beta}_X)(a_x c\phi - a_y s\phi)\\
&\qquad - (\ddot{R}_X + \dot{R}_Y\dot{\phi} + a_z\dot{\beta}_X\dot{\phi} - a_z\ddot{\beta}_Y)(a_x s\phi + a_y c\phi) + \ddot{\phi}(a_x^2 + a_y^2)\big]
\end{aligned}
\tag{7.218}
$$

The other derivatives are

$$
\begin{aligned}
\frac{\partial}{\partial\phi}(KE_{\text{linear},\,x}) &= \frac{\partial}{\partial\phi}\left(\frac{1}{2}m\big[\dot{R}_X - (a_x s\phi\ + a_y c\phi\ )\dot{\phi} + a_z\dot{\beta}_Y\big]^2\right)\\
&= -m(a_x c\phi - a_y s\phi\ )\dot{\phi}\big[\dot{R}_X - (a_x s\phi\ + a_y c\phi\ )\dot{\phi} + a_z\dot{\beta}_Y\big]\\
&= -m\big[\dot{R}_X\dot{\phi}(a_x c\phi - a_Y s\phi) + a_z\dot{\beta}_Y\dot{\phi}(a_x c\phi - a_y s\phi)\\
&\quad - \dot{\phi}^2(a_x^2 c\phi s\phi - a_x a_y s^2\phi + a_x a_y c^2\phi - a_y^2 s\phi c\phi)\big]
\end{aligned}
\tag{7.219}
$$

$$
\begin{aligned}
\frac{\partial}{\partial\phi}(KE_{\text{linear},\,y}) &= \frac{\partial}{\partial\phi}\left(\frac{1}{2}m\big[\dot{R}_Y + (a_x c\phi - a_y s\phi)\dot{\phi} - a_z\dot{\beta}_X\big]^2\right)\\
&= -\mathrm{m}(a_x s\phi + a_y c\phi)\dot{\phi}\big[\dot{R}_Y + (a_x c\phi - a_y s\phi)\dot{\phi} - a_z\dot{\beta}_X\big]\\
&= -\mathrm{m}\big[\dot{R}_Y\dot{\phi}(a_x s\phi + a_y c\phi) - a_z\dot{\beta}_X\dot{\phi}(\mathrm{a_x s\phi + a_y c\phi})\\
&\quad + \dot{\phi}^2(a_x^2 c\phi s\phi + a_x a_y c^2\phi - a_x a_y s^2\phi - a_y^2 c\phi s\phi)\big]
\end{aligned}
\tag{7.220}
$$

Which when combined, gives:

$$\begin{aligned}\frac{\partial}{\partial\phi}(KE_{\text{linear}}) = {} & -m[\dot{R}_X\dot{\phi}(a_x c\phi - a_Y s\phi) - \dot{\phi}^2(a_x^2 c\phi s\phi - a_x a_y s^2\phi + a_x a_y c^2\phi \\ & - a_y^2 s\phi c\phi) + a_z\dot{\beta}_Y\dot{\phi}(a_x c\phi - a_y s\phi)] - m[\dot{R}_Y\dot{\phi}(a_x s\phi + a_y c\phi) \\ & + \dot{\phi}^2(a_x^2 c\phi s\phi + a_x a_y c^2\phi - a_x a_y s^2\phi - a_y^2 c\phi s\phi) \\ & - a_z\dot{\beta}_X\dot{\phi}(a_x s\phi + a_y c\phi)] \\ = {} & -m[\dot{\phi}(\dot{R}_X + a_z\dot{\beta}_Y)(a_x c\phi - a_y s\phi) + \dot{\phi}(\dot{R}_Y \\ & - a_z\dot{\beta}_X)(a_x s\phi + a_y c\phi)]\end{aligned} \qquad \textbf{(7.221)}$$

The derivatives of each term in the angular kinetic energy terms are found one at a time:

$$\frac{\partial}{\partial\dot{\phi}}(KE_{\text{ang},\,xx}) = \frac{\partial}{\partial\dot{\phi}}\left(\frac{1}{2}J_{xx}\left(\dot{\beta}_Y s\phi + \dot{\beta}_X c\beta_Y c\phi\right)^2\right) = 0 \qquad \textbf{(7.222)}$$

$$\frac{d}{dt}\frac{\partial}{\partial\dot{\phi}}(KE_{\text{ang},\,xx}) = 0 \qquad \textbf{(7.223)}$$

The other derivative of this term is:

$$\begin{aligned}\frac{\partial}{\partial\phi}(KE_{\text{ang},\,xx}) &= \frac{\partial}{\partial\beta_Y}\left(\frac{1}{2}J_{xx}\left(\dot{\beta}_Y s\phi + \dot{\beta}_X c\beta_Y c\phi\right)^2\right) \\ &= J_{xx}\left(\dot{\beta}_Y s\phi + \dot{\beta}_X c\beta_Y c\phi\right)\left(\dot{\beta}_Y c\phi - \dot{\beta}_X c\beta_Y s\phi\right) \\ &= J_{xx}\left[\dot{\beta}_Y^2 s\phi c\phi + \dot{\beta}_X\dot{\beta}_Y c\beta_Y c^2\phi - \dot{\beta}_X\dot{\beta}_Y c\beta_Y s^2\phi\right]\end{aligned} \qquad \textbf{(7.224)}$$

Note that with the small angle assumption on β_Y, this entire term is 2nd order in β_X, β_Y, and their derivatives, and can be completely neglected:

$$\frac{\partial}{\partial\phi}(KE_{\text{ang},\,xx}) = 0 \qquad \textbf{(7.225)}$$

The derivatives of the next angular kinetic energy term are found in the same way:

$$\frac{\partial}{\partial\dot{\phi}}(KE_{\text{ang},\,yy}) = \frac{\partial}{\partial\dot{\phi}}\left(\frac{1}{2}J_{yy}\left(\dot{\beta}_Y c\phi - \dot{\beta}_X c\beta_Y s\phi\right)^2\right) = 0 \qquad \textbf{(7.226)}$$

$$\frac{d}{dt}\frac{\partial}{\partial\dot{\phi}}\left(KE_{\text{ang, }yy}\right)=0 \tag{7.227}$$

The other derivative of this term is:

$$\begin{aligned}\frac{\partial}{\partial\phi}\left(KE_{\text{ang, }yy}\right)&=\frac{\partial}{\partial\phi}\left(\frac{1}{2}J_{yy}\left(\dot{\beta}_Y c\phi-\dot{\beta}_X c\beta_Y s\phi\right)^2\right)\\&=J_{yy}\left(\dot{\beta}_Y c\phi-\dot{\beta}_X c\beta_Y s\phi\right)\left(-\dot{\beta}_Y s\phi-\dot{\beta}_X c\beta_Y c\phi\right)\\&=J_{yy}\left[-\dot{\beta}_Y^2 c\phi s\phi+\dot{\beta}_X\dot{\beta}_Y c\beta_Y s^2\phi-\dot{\beta}_X\dot{\beta}_Y c\beta_Y c^2\phi+\dot{\beta}_X^2 c^2\beta_Y c\phi s\phi\right]\end{aligned} \tag{7.228}$$

Note that with the small angle assumption on β_Y, this entire term is 2nd order in β_X, β_Y, and their derivatives, and can be completely neglected:

$$\frac{\partial}{\partial\phi}\left(KE_{\text{ang, }yy}\right)=0 \tag{7.229}$$

The derivatives of the next angular kinetic energy term are found in the same way:

$$\frac{\partial}{\partial\dot{\phi}}\left(KE_{\text{ang, }zz}\right)=\frac{\partial}{\partial\dot{\phi}}\left(\frac{1}{2}J_{zz}\left(\dot{\phi}+\dot{\beta}_X s\beta_y\right)^2\right)=J_{zz}\left(\dot{\phi}+\dot{\beta}_X s\beta_Y\right) \tag{7.230}$$

$$\frac{d}{dt}\frac{\partial}{\partial\dot{\phi}}\left(KE_{\text{ang, }zz}\right)=J_{zz}\left(\ddot{\phi}+\ddot{\beta}_X s\beta_Y+\dot{\beta}_X\dot{\beta}_Y c\beta_Y\right) \tag{7.231}$$

Since angles β_X and β_Y are assumed small, the trigonometric functions of these angles can be simplified:

$$\frac{d}{dt}\frac{\partial}{\partial\dot{\phi}}\left(KE_{\text{ang, }zz}\right)=J_{zz}\left(\ddot{\phi}+\ddot{\beta}_X\beta_Y+\dot{\beta}_X\dot{\beta}_Y\right) \tag{7.232}$$

All terms that are second or higher order in β_X, β_Y, and their temporal derivatives are neglected, since these angles are small.

$$\frac{d}{dt}\frac{\partial}{\partial\dot{\phi}}\left(KE_{\text{ang, }zz}\right)=J_{zz}\ddot{\phi} \tag{7.233}$$

The other derivative of this term is:

$$\frac{\partial}{\partial \phi}\left(KE_{\text{ang},\,zz}\right) = \frac{\partial}{\partial \beta_Y}\left(\frac{1}{2}J_{zz}\left(\dot{\phi} + \dot{\beta}_X s\beta_y\right)^2\right) = 0 \tag{7.234}$$

Recall that the product of inertia J_{xy} is negligible for this thin disk system. Therefore, since the xy-angular-kinetic-energy term would contain this product of inertia, it and all of its derivatives are zero:

$$\frac{\partial}{\partial \dot{\phi}}\left(KE_{\text{ang},\ xy}\right) = \frac{\partial}{\partial \dot{\phi}}0 = 0 \tag{7.235}$$

$$\frac{d}{dt}\frac{\partial}{\partial \dot{\phi}}\left(KE_{\text{ang},\ xy}\right) = 0 \tag{7.236}$$

$$\frac{\partial}{\partial \phi}\left(KE_{\text{ang},\ xy}\right) = \frac{\partial}{\partial \phi}0 = 0 \tag{7.237}$$

The derivatives of the next angular kinetic energy term are found in the same way:

$$\begin{aligned}\frac{\partial}{\partial \dot{\phi}}\left(KE_{\text{ang},\,xz}\right) &= \frac{\partial}{\partial \dot{\phi}}\left[J_{xz}\left(\dot{\beta}_Y s\phi + \dot{\beta}_X c\beta_Y c\phi\right)\left(\dot{\phi} + \dot{\beta}_X s\beta_Y\right)\right] \\ &= J_{xz}\frac{\partial}{\partial \dot{\beta}_Y}\left[\dot{\beta}_Y\dot{\phi}s\phi + \dot{\beta}_X\dot{\phi}c\beta_Y c\phi + \dot{\beta}_X\dot{\beta}_Y s\beta_Y s\phi + \dot{\beta}_X^2 c\beta_Y s\beta_Y c\phi\right] \\ &= J_{xz}\left[\dot{\beta}_Y s\phi + \dot{\beta}_X c\beta_Y c\phi\right]\end{aligned} \tag{7.238}$$

$$\begin{aligned}\frac{d}{dt}\frac{\partial}{\partial \dot{\phi}}\left(KE_{\text{ang},\ xz}\right) &= J_{xz}\frac{d}{dt}\left[\dot{\beta}_Y s\phi + \dot{\beta}_X c\beta_Y c\phi\right] \\ &= J_{xz}\left[\ddot{\beta}_Y s\phi + \dot{\beta}_Y\dot{\phi}c\phi + \ddot{\beta}_X c\beta_Y c\phi - \dot{\beta}_X\dot{\beta}_Y s\beta_Y c\phi - \dot{\beta}_X\dot{\phi}c\beta_Y s\phi\right]\end{aligned} \tag{7.239}$$

Since angles β_X and β_Y are assumed small, the trigonometric functions of these angles can be simplified:

$$\frac{d}{dt}\frac{\partial}{\partial \dot{\phi}}\left(KE_{\text{ang},\ xz}\right) = J_{xz}\left[\ddot{\beta}_Y s\phi + \dot{\beta}_Y\dot{\phi}c\phi + \ddot{\beta}_X c\phi - \dot{\beta}_X\dot{\beta}_Y\beta_Y c\phi - \dot{\beta}_X\dot{\phi}s\phi\right] \tag{7.240}$$

All terms that are second or higher order in β_X, β_Y, and their temporal derivatives are neglected, since these angles are small. Note that second order terms containing $\dot{\phi}$ are specifically kept, since ϕ is not small, and $\dot{\phi}$ is the actual rotor operation speed, which factors strongly into the dynamics.

$$\frac{d}{dt}\frac{\partial}{\partial\dot{\phi}}\left(KE_{\text{ang},\ xz}\right) = J_{xz}\left[\ddot{\beta}_Y s\phi + \dot{\beta}_Y\dot{\phi}c\phi + \ddot{\beta}_X c\phi - \dot{\beta}_X\dot{\phi}s\phi\right] \tag{7.241}$$

The other derivative of this term is:

$$\begin{aligned}\frac{\partial}{\partial\phi}\left(KE_{\text{ang},\ xz}\right) &= \frac{\partial}{\partial\phi}\left[J_{xz}\left(\dot{\beta}_Y s\phi + \dot{\beta}_X c\beta_Y c\phi\right)\left(\dot{\phi} + \dot{\beta}_X s\beta_Y\right)\right] \\ &= J_{xz}\frac{\partial}{\partial\phi}\left[\dot{\beta}_Y\dot{\phi}s\phi + \dot{\beta}_X\dot{\phi}c\beta_Y c\phi + \dot{\beta}_X\dot{\beta}_Y s\beta_Y s\phi + \dot{\beta}_X^2 c\beta_Y s\beta_Y c\phi\right] \\ &= J_{xz}\left[\dot{\beta}_Y\dot{\phi}c\phi - \dot{\beta}_X\dot{\phi}c\beta_Y s\phi + \dot{\beta}_X\dot{\beta}_Y s\beta_Y c\phi - \dot{\beta}_X^2 c\beta_Y s\beta_Y s\phi\ \right]\end{aligned} \tag{7.242}$$

Since angles β_X and β_Y are assumed small, the trigonometric functions of these angles can be simplified:

$$\frac{\partial}{\partial\phi}\left(KE_{\text{ang},\ xz}\right) = J_{xz}\left[\dot{\beta}_Y\dot{\phi}c\phi - \dot{\beta}_X\dot{\phi}s\phi + \dot{\beta}_X\dot{\beta}_Y\beta_Y c\phi - \dot{\beta}_X^2\beta_Y s\phi\right] \tag{7.243}$$

The terms that are 3rd order in β_X and β_Y, and can be neglected, leaving:

$$\frac{\partial}{\partial\phi}\left(KE_{\text{ang},\ xz}\right) = J_{xz}\left[\dot{\beta}_Y\dot{\phi}c\phi - \dot{\beta}_X\dot{\phi}s\phi\right] \tag{7.244}$$

The derivatives of the next angular kinetic energy term are found in the same way:

$$\begin{aligned}\frac{\partial}{\partial\dot{\phi}}\left(KE_{\text{ang}, yz}\right) &= \frac{\partial}{\partial\dot{\phi}}\left[J_{yz}\left(\dot{\beta}_Y c\phi - \dot{\beta}_X c\beta_Y s\phi\right)\left(\dot{\phi} + \dot{\beta}_X s\beta_Y\right)\right] \\ &= J_{yz}\frac{\partial}{\partial\dot{\phi}}\left[\dot{\beta}_Y\dot{\phi}c\phi - \dot{\beta}_X\dot{\phi}c\beta_Y s\phi + \dot{\beta}_X\dot{\beta}_Y s\beta_y c\phi - \dot{\beta}_X^2 c\beta_Y s\beta_Y s\phi\right] \\ &= J_{yz}\left[\dot{\beta}_Y c\phi - \dot{\beta}_X c\beta_Y s\phi\right]\end{aligned} \tag{7.245}$$

$$\begin{aligned}\frac{d}{dt}\frac{\partial}{\partial\dot{\phi}}\left(KE_{\text{ang, }yz}\right) &= J_{yz}\frac{d}{dt}\left[\dot{\beta}_Y c\phi - \dot{\beta}_X c\beta_Y s\phi\right] \\ &= J_{yz}\left[\ddot{\beta}_Y c\phi - \dot{\beta}_Y\dot{\phi} s\phi - \ddot{\beta}_X c\beta_Y s\phi + \dot{\beta}_X\dot{\beta}_Y s\beta_Y s\phi - \dot{\beta}_X\dot{\phi} c\beta_Y c\phi\right]\end{aligned} \tag{7.246}$$

Since angles β_X and β_Y are assumed small, the trigonometric functions of these angles can be simplified:

$$\frac{d}{dt}\frac{\partial}{\partial\dot{\phi}}\left(KE_{\text{ang, }yz}\right) = J_{yz}\left[\ddot{\beta}_Y c\phi - \dot{\beta}_Y\dot{\phi} s\phi - \ddot{\beta}_X s\phi + \dot{\beta}_X\dot{\beta}_Y\beta_Y s\phi - \dot{\beta}_X\dot{\phi} c\phi\right] \tag{7.247}$$

All terms that are second or higher order in β_X, β_Y, and their temporal derivatives are neglected, leaving since these angles are small. Note that second order terms containing $\dot{\phi}$ are specifically kept, since ϕ is not small, and $\dot{\phi}$ is the actual rotor operation speed, which factors strongly into the dynamics.

$$\frac{d}{dt}\frac{\partial}{\partial\dot{\phi}}\left(KE_{\text{ang, }yz}\right) = J_{yz}\left[\ddot{\beta}_Y c\phi - \dot{\beta}_Y\dot{\phi} s\phi - \ddot{\beta}_X s\phi - \dot{\beta}_X\dot{\phi} c\phi\right] \tag{7.248}$$

The other derivative of this term is:

$$\begin{aligned}\frac{\partial}{\partial\phi}\left(KE_{\text{ang, }yz}\right) &= \frac{\partial}{\partial\phi}\left[J_{yz}\left(\dot{\beta}_Y c\phi - \dot{\beta}_X c\beta_Y s\phi\right)\left(\dot{\phi} + \dot{\beta}_X s\beta_Y\right)\right] \\ &= J_{yz}\frac{\partial}{\partial\phi}\left[\dot{\beta}_Y\dot{\phi} c\phi - \dot{\beta}_X\dot{\phi} c\beta_Y s\phi + \dot{\beta}_X\dot{\beta}_Y s\beta_Y c\phi - \dot{\beta}_X^2 c\beta_Y s\beta_Y s\phi\right] \\ &= J_{yz}\left[-\dot{\beta}_Y\dot{\phi} s\phi - \dot{\beta}_X\dot{\phi} c\beta_Y c\phi - \dot{\beta}_X\dot{\beta}_Y s\beta_Y s\phi - \dot{\beta}_X^2 c\beta_Y s\beta_Y c\phi\right]\end{aligned} \tag{7.249}$$

Since angles β_X and β_Y are assumed small, the trigonometric functions of these angles can be simplified:

$$\frac{\partial}{\partial\phi}\left(KE_{\text{ang, }yz}\right) = J_{yz}\left[-\dot{\beta}_Y\dot{\phi} s\phi - \dot{\beta}_X\dot{\phi} c\phi - \dot{\beta}_X\dot{\beta}_Y\beta_Y s\phi - \dot{\beta}_X^2\beta_Y c\phi\right] \tag{7.250}$$

The terms that are 3rd order in β_X and β_Y, and can be neglected, leaving:

$$\frac{\partial}{\partial\phi}\left(KE_{\text{ang, }yz}\right) = J_{yz}\left[-\dot{\beta}_Y\dot{\phi} s\phi - \dot{\beta}_X\dot{\phi} c\phi\right] \tag{7.251}$$

Combining the derivatives from (7.223), (7.227), (7.233), (7.236), (7.241), and (7.248) yields:

$$\frac{d}{dt}\frac{\partial}{\partial\dot{\phi}}\left(KE_{\text{angular}}\right)$$

$$= \frac{d}{dt}\frac{\partial}{\partial\dot{\phi}}\left(KE_{\text{ang, }xx}\right) + \frac{d}{dt}\frac{\partial}{\partial\dot{\phi}}\left(KE_{\text{ang, }yy}\right) + \frac{d}{dt}\frac{\partial}{\partial\dot{\phi}}\left(KE_{\text{ang, }zz}\right) + \frac{d}{dt}\frac{\partial}{\partial\dot{\phi}}\left(KE_{\text{ang, }xy}\right) + \frac{d}{dt}\frac{\partial}{\partial\dot{\phi}}\left(KE_{\text{ang, }xz}\right) + \frac{d}{dt}\frac{\partial}{\partial\dot{\phi}}\left(KE_{\text{ang, }yz}\right) \tag{7.252}$$

$$\frac{d}{dt}\frac{\partial}{\partial\dot{\phi}}\left(KE_{\text{angular}}\right)$$

$$= 0 + 0 + J_{zz}\ddot{\phi} + 0 + J_{xz}\left[\ddot{\beta}_Y s\phi + \dot{\beta}_Y\dot{\phi}c\phi + \ddot{\beta}_X c\phi - \dot{\beta}_X\dot{\phi}s\phi\right] + J_{yz}\left[\ddot{\beta}_Y c\phi - \dot{\beta}_Y\dot{\phi}s\phi - \ddot{\beta}_X s\phi - \dot{\beta}_X\dot{\phi}c\phi\right] \tag{7.253}$$

The remaining derivatives from (7.225), (7.229), (7.234), (7.237), (7.244), and (7.251) form:

$$\frac{\partial}{\partial\phi}\left(KE_{\text{angular}}\right) = \frac{\partial}{\partial\phi}\left(KE_{\text{ang, }xx}\right) + \frac{\partial}{\partial\phi}\left(KE_{\text{ang, }yy}\right) + \frac{\partial}{\partial\phi}\left(KE_{\text{ang, }zz}\right) + \frac{\partial}{\partial\phi}\left(KE_{\text{ang, }xy}\right) + \frac{\partial}{\partial\phi}\left(KE_{\text{ang, }xz}\right) + \frac{\partial}{\partial\phi}\left(KE_{\text{ang, }yz}\right) \tag{7.254}$$

$$\frac{\partial}{\partial\phi}\left(KE_{\text{angular}}\right) = J_{xz}\left[\dot{\beta}_Y\dot{\phi}c\phi - \dot{\beta}_X\dot{\phi}s\phi\right] + J_{yz}\left[-\dot{\beta}_Y\dot{\phi}s\phi - \dot{\beta}_X\dot{\phi}c\phi\right] \tag{7.255}$$

All of the derivatives of the potential energy terms representing the elastic energy in the beam deflection are zero, because ϕ and $\dot{\phi}$ do not factor into the beam bending energy:

$$\frac{d}{dt}\frac{\partial}{\partial\dot{\phi}}\left(PE_{\text{elastic, }x}\right) = \frac{\partial}{\partial\phi}\left(PE_{\text{elastic, }x}\right) = \frac{d}{dt}\frac{\partial}{\partial\dot{\phi}}\left(PE_{\text{elastic, }y}\right) = \frac{\partial}{\partial\phi}\left(PE_{\text{elastic, }y}\right) = 0 \tag{7.256}$$

Having completed all the derivatives, they can be substituted back into equation (7.214) to get the equation of motion for angular motion about the z-axis:

$$\frac{d}{dt}\left(\frac{\partial L}{\partial\dot{\phi}}\right) = \frac{\partial L}{\partial\phi} \tag{7.257}$$

$$\frac{d}{dt}\frac{\partial}{\partial\dot{\phi}}\left(\mathrm{KE}_{\mathrm{linear}}+\mathrm{KE}_{\mathrm{angular}}-\mathrm{PE}_{\mathrm{elastic}}\right)=\frac{\partial}{\partial\phi}\left(\mathrm{KE}_{\mathrm{linear}}+\mathrm{KE}_{\mathrm{angular}}-\mathrm{PE}_{\mathrm{elastic}}\right) \tag{7.258}$$

$$\begin{aligned}
m\big[&(\ddot{R}_Y-\dot{R}_X\dot{\phi}-a_z\dot{\beta}_Y\dot{\phi}-a_z\ddot{\beta}_X)(a_x c\phi-a_y s\phi)\\
&-(\ddot{R}_X+\dot{R}_Y\dot{\phi}+a_z\dot{\beta}_X\dot{\phi}-a_z\ddot{\beta}_Y)(a_x s\phi+a_y c\phi)+\ddot{\phi}(a_x^2+a_y^2)\big]\\
&+J_{zz}\ddot{\phi}+J_{xz}\left[\ddot{\beta}_Y s\phi+\dot{\beta}_Y\dot{\phi}c\phi+\ddot{\beta}_X c\phi-\dot{\beta}_X\dot{\phi}s\phi\right]\\
&+J_{yz}\left[\ddot{\beta}_Y c\phi-\dot{\beta}_Y\dot{\phi}s\phi-\ddot{\beta}_X s\phi-\dot{\beta}_X\dot{\phi}c\phi\right]\\
&=-m\big[\dot{\phi}(\dot{R}_X+a_z\dot{\beta}_Y)(a_x c\phi-a_y s\phi)\\
&+\dot{\phi}(\dot{R}_Y-a_z\dot{\beta}_X)(a_x s\phi+a_y c\phi)\big]+J_{xz}\left[\dot{\beta}_Y\dot{\phi}c\phi-\dot{\beta}_X\dot{\phi}s\phi\right]\\
&+J_{yz}\left[-\dot{\beta}_Y\dot{\phi}s\phi-\dot{\beta}_X\dot{\phi}c\phi\right]\big]
\end{aligned} \tag{7.259}$$

Cancelling terms and rearranging gives:

$$\begin{aligned}
\ddot{\phi}\left[J_{zz}+m(a_x^2+a_y^2)\right]&+m(\ddot{R}_Y-a_z\ddot{\beta}_X)(a_x c\phi-a_y s\phi)\\
&-m(\ddot{R}_X-a_z\ddot{\beta}_Y)(a_x s\phi+a_y c\phi)+\ddot{\beta}_Y\left[J_{xz}s\phi+J_{yz}c\phi\right]\\
&+\ddot{\beta}_X\left[J_{xz}c\phi-J_{yz}s\phi\right]=0
\end{aligned} \tag{7.260}$$

REFERENCES

[1] Stodola, A., *Steam and Gas Turbines*. 1927, New York: McGraw-Hill Book Co., Inc. http://lccn.loc.gov/27016908

[2] Fennimore, A.M., T.D. Yuzvinsky, W.-Q. Han, M.S. Fuhrer, J. Cumings, and A. Zettl, *Rotational Actuators Based on Carbon Nanotubes.* Nature, 2003. **424**(6947): p. 408-410. http://dx.doi.org/10.1038/nature01823

[3] Bourlon, B., D.C. Glattli, C. Miko, L. Forro, and A. Bachtold, *Carbon Nanotube Based Bearing for Rotational Motions.* Nano Letters, 2004. **4**(4): p. 709-712. http://dx.doi.org/10.1021/nl035217g

[4] Subramanian, A., L.X. Dong, J. Tharian, U. Sennhauser, and B.J. Nelson, *Batch Fabrication of Carbon Nanotube Bearings.* Nanotechnology, 2007. **18**(7): p. 075703. http://dx.doi.org/10.1088/0957-4484/18/7/075703

[5] Jeffcott, H.H., *The Lateral Vibration of Loaded Shafts in the Neighbourhood of a Whirling Speed– the Effect of Want of Balance.* Philosophical Magazine, 1919. **37**(6): p. 304.

[6] Guillorn, M.A., M.L. Simpson, G.J. Bordonaro, V.I. Merkulov, L.R. Baylor, and D.H. Lowndes, *Fabrication of Gated Cathode Structures Using an in Situ Grown Vertically Aligned Carbon Nanofiber as a Field Emission Element.* Journal of Vacuum Science & Technology B: Microelectronics and Nanometer Structures, 2001. **19**(2): p. 573-578. http://dx.doi.org/10.1116/1.1358855

[7] Guillorn, M.A., T.E. McKnight, A. Melechko, V.I. Merkulov, P.F. Britt, D.W. Austin, D.H. Lowndes, and M.L. Simpson, *Individually Addressable Vertically Aligned Carbon Nanofiber-Based Electrochemical Probes.* Journal of Applied Physics, 2002. **91**(6): p. 3824-3828. http://dx.doi.org/10.1063/1.1448671

[8] Li, J., H.T. Ng, A. Cassell, W. Fan, H. Chen, Q. Ye, J. Koehne, J. Han, and M. Meyyappan, *Carbon Nanotube Nanoelectrode Array for Ultrasensitive DNA Detection.* Nano Letters, 2003. **3**(5): p. 597-602. http://dx.doi.org/10.1021/nl0340677

[9] Yang, X., M.A. Guillorn, D. Austin, A.V. Melechko, H. Cui, H.M. Meyer, V.I. Merkulov, J.B.O. Caughman, D.H. Lowndes, and M.L. Simpson, *Fabrication and Characterization of Carbon Nanofiber-Based Vertically Integrated Schottky Barrier Junction Diodes.* Nano Letters, 2003. **3**(12): p. 1751-1755. http://dx.doi.org/10.1021/nl0346631

[10] Ikuno, T., M. Katayama, K.-Y. Lee, T. Kuzuoka, J.-G. Lee, S.-i. Honda, H. Mori, and K. Oura, *Local Etching of Insulator-Coated Carbon Nanotubes Towards Passivated Nanoprobes* Japanese Journal of Applied Physics, 2004. **43**(7B): p. L987-L989. http://dx.doi.org/10.1143/JJAP.43.L987

[11] Koehne, J., J. Li, A.M. Cassell, H. Chen, Q. Ye, H.T. Ng, J. Han, and M. Meyyappan, *The Fabrication and Electrochemical Characterization of Carbon Nanotube Nanoelectrode Arrays.* Journal of Materials Chemistry, 2004. **14**(4): p. 676-684. http://dx.doi.org/10.1039/b311728f

[12] Peng, H.B. and J.A. Golovchenko, *Coulomb Blockade in Suspended Si[Sub 3]N[Sub 4]-Coated Single-Walled Carbon Nanotubes.* Applied Physics Letters, 2004. **84**(26): p. 5428-5430. http://dx.doi.org/10.1063/1.1765733

[13] Ye, Q., A.M. Cassell, H. Liu, K.J. Chao, J. Han, and M. Meyyappan, *Large-Scale Fabrication of Carbon Nanotube Probe Tips for Atomic Force Microscopy Critical Dimension Imaging Applications.* Nano Lett., 2004. **4**(7): p. 1301-1308. http://dx.doi.org/10.1021/nl049341r

[14] Zhang, L., *Controlled Transport of Latex Beads through Vertically Aligned Carbon Nanofiber Membranes.* Applied Physics Letters, 2002. **81**(1): p. 135. http://dx.doi.org/10.1063/1.1490142

[15] Melechko, A.V., T.E. McKnight, M.A. Guillorn, V.I. Merkulov, B. Ilic, M.J. Doktycz, D.H. Lowndes, and M.L. Simpson, *Vertically Aligned Carbon Nanofibers as Sacrificial Templates for Nanofluidic Structures.* Applied Physics Letters, 2003. **82**(6): p. 976-978. http://dx.doi.org/10.1063/1.1544058

[16] Hinds, B.J., N. Chopra, T. Rantell, R. Andrews, V. Gavalas, and L.G. Bachas, *Aligned Multiwalled Carbon Nanotube Membranes.* Science, 2004. **303**(5654): p. 62-65. http://dx.doi.org/10.1126/science.1092048

[17] Noy, A., H.G. Park, F. Fornasiero, J.K. Holt, C.P. Grigoropoulos, and O. Bakajin, *Nanofluidics in Carbon Nanotubes.* Nano Today, 2007. **2**(6): p. 22-29. http://dx.doi.org/10.1016/S1748-0132(07)70170-6

[18] Akita, S. and Y. Nakayama, *Mechanical and Electrical Properties of Multiwall Nanotube under Interlayer Sliding.* e-Journal of Surface Science and Nanotechnology, 2005. **3**: p. 86-93. http://dx.doi.org/10.1380/ejssnt.2005.86

[19] Rivera, J.L., C. McCabe, and P.T. Cummings, *Oscillatory Behavior of Double Nanotubes under Extension: A Simple Nanoscale Damped Spring.* Nano Lett., 2003. **3**(8): p. 1001-1005. http://dx.doi.org/10.1021/nl034171o

[20] Guo, W. and H. Gao, *Optimized Bearing and Interlayer Friction in Multiwalled Carbon Nanotubes.* Computer Modeling in Engineering & Sciences, 2005. **7**(1): p. 19-34. http://techscience.com/cgi/x_cmes?issue=v7n1&no=02

[21] Guo, W., Y. Guo, H. Gao, Q. Zheng, and W. Zhong, *Energy Dissipation in Gigahertz Oscillators from Multiwalled Carbon Nanotubes.* Physical Review Letters, 2003. **91**(12): p. 125501. http://dx.doi.org/10.1103/PhysRevLett.91.125501

[22] Guo, W., W. Zhong, Y. Dai, and S. Li, *Coupled Defect-Size Effects on Interlayer Friction in Multiwalled Carbon Nanotubes.* Physical Review B (Condensed Matter and Materials Physics), 2005. **72**(7): p. 075409-075410. http://dx.doi.org/10.1103/PhysRevB.72.075409

[23] Su, H., W.A. Goddard, III, and Y. Zhao, *Dynamic Friction Force in a Carbon Peapod Oscillator.* Nanotechnology, 2006. **17**(22): p. 5691-5695. http://dx.doi.org/10.1088/0957-4484/17/22/026

[24] Zhang, X.-H., U. Tartaglino, G.E. Santoro, and E. Tosatti, *Velocity Plateaus and Jumps in Carbon Nanotube Sliding.* Surface Science, 2007. **601**(18): p. 3693-3696. http://dx.doi.org/10.1016/j.susc.2007.05.034

[25] Zhang, S., W.K. Liu, and R.S. Ruoff, *Atomistic Simulations of Double-Walled Carbon Nanotubes (DWCNTs) as Rotational Bearings.* Nano Lett., 2004. **4**(2): p. 293-297. http://dx.doi.org/10.1021/nl0350276

[26] Omata, Y., Y. Yamagami, K. Tadano, T. Miyake, and S. Saito, *Nanotube Nanoscience: A Molecular-Dynamics Study.* Physica E: Low-dimensional Systems and Nanostructures, 2005. **29**(3-4): p. 454-468. http://dx.doi.org/10.1016/j.physe.2005.06.009

[27] Kuznetsov, S.S., Y.E. Lozovik, and A.M. Popov, *The Nanoactuator Based on a Carbon Nanotube.* Physics of the Solid State, 2007. **49**(5): p. 1004-1012. http://dx.doi.org/10.1134/S1063783407050320

[28] Cumings, J. and A. Zettl, *Low-Friction Nanoscale Linear Bearing Realized from Multiwall Carbon Nanotubes.* Science, 2000. **289**(5479): p. 602-604. http://dx.doi.org/10.1126/science.289.5479.602

[29] Kis, A., K. Jensen, S. Aloni, W. Mickelson, and A. Zettl, *Interlayer Forces and Ultralow Sliding Friction in Multiwalled Carbon Nanotubes.* Physical Review Letters, 2006. **97**(2): p. 025501-025504. http://dx.doi.org/10.1103/PhysRevLett.97.025501

[30] Yu, M.-F., B.I. Yakobson, and R.S. Ruoff, *Controlled Sliding and Pullout of Nested Shells in Individual Multiwalled Carbon Nanotubes.* Journal of Physical Chemistry B, 2000. **104**: p. 8764-8767. http://dx.doi.org/10.1021/jp002828d

[31] Steyn, J.L., *A Microfabricated Electroquasistatic Induction Turbine-Generator* Doctor of Philosophy thesis in Aeronautics and Astronautics. 2005, Cambridge, MA: Massachusetts Institute of Technology http://dspace.mit.edu/handle/1721.1/32463

[32] Savoulides, N., *Development of a MEMS Turbocharger and Gas Turbine Engine* Doctor of Philosophy thesis in Aeronautics and Astronautics. 2004, Cambridge, MA: Massachusetts Institute of Technology http://dspace.mit.edu/handle/1721.1/17815

[33] Lin, C.-C., *Development of a Microfabricated Turbine-Driven Air Bearing Rig* Doctor of Philosophy thesis in Mechanical Engineering. 1999, Cambridge, MA: Massachusetts Institute of Technology http://dspace.mit.edu/handle/1721.1/9393

[34] Yen, B., *A Fully-Integrated Multi-Watt Permanent Magnet Turbine Generator* Doctor of Philosophy thesis in Electrical Engineering. 2008, Massachusetts Institute of Technology http://dspace.mit.edu

[35] Dai, H., *Nanotube Growth and Characterization*, in *Carbon Nanotubes: Synthesis, Structure, Properties, and Applications*, M.S. Dresselhaus, G. Dresselhaus, and P. Avouris, Editors. 2001, Springer-Verlag: New York. p. 29-53. http://dx.doi.org/10.1007/3-540-39947-X_3

[36] Yuzvinsky, T.D., A.M. Fennimore, A. Kis, and A. Zettl, *Controlled Placement of Highly Aligned Carbon Nanotubes for the Manufacture of Arrays of Nanoscale Torsional Actuators.* Nanotechnology, 2006. **17**(2): p. 434-438. http://dx.doi.org/10.1088/0957-4484/17/2/015

[37] Subramanian, A., B.J. Nelson, L.X. Dong, and D.J. Bell. *Dielectrophoretic Nano-Assembly of Nanotube-Based Nems with Nanoelectrodes*. in *Proceedings of of the 6th IEEE International Symposium on Assembly and Task Planning*. 2005. Montreal, Quebec: IEEE. http://dx.doi.org/10.1109/ISATP.2005.1511473

[38] Miller, R.A., E.G. Nazarov, G.A. Eiceman, and A. Thomas King, *A MEMS Radio-Frequency Ion Mobility Spectrometer for Chemical Vapor Detection.* Sensors & Actuators: A. Physical, 2001. **91**(3): p. 301-312. http://dx.doi.org/10.1016/S0924-4247(01)00600-8

[39] Terry, S.C., J.H. Jerman, and J.B. Angell, *A Gas Chromatographic Air Analyzer Fabricated on a Silicon Wafer.* Electron Devices, IEEE Transactions on, 1979. **26**(12): p. 1880-1886. http://ieeexplore.ieee.org/iel5/16/31796/01480369.pdf?isnumber=31796&prod=JNL&arnumber=1480369&arnumber=1480369&arSt=+1880&ared=+1886&arAuthor=Terry%2C+S.C.%3B+Jerman%2C+J.H.%3B+Angell%2C+J.B.

[40] Wong, C.C., J.H. Flemming, D.R. Adkins, M.A. Plowman, and M. Center. *Evaluation of Mini/Micro-Pumps for Micro-Chem-Lab™*. in *Proceedings of the Fluids Engineering Division, ASME International Mechanical Engineering Congress and Exposition*. 1995: ASME. http://catalog.asme.org/ConferencePublications/PrintBook/1995_Proceedings_Fluids.cfm

[41] Freidhoff, C.B., R.M. Young, S. Sriram, T.T. Braggins, T.W. O'Keefe, J.D. Adam, H.C. Nathanson, R.R.A. Syms, T.J. Tate, M.M. Ahmad, S. Taylor, and J. Tunstall, *Chemical Sensing Using Nonoptical Microelectromechanical Systems.* Journal of Vacuum Science & Technology A: Vacuum, Surfaces, and Films, 1999. **17**: p. 2300. http://dx.doi.org/10.1116/1.581764

[42] Taylor, S., R.F. Tindall, and R.R.A. Syms, *Silicon Based Quadrupole Mass Spectrometry Using Microelectromechanical Systems.* Journal of Vacuum Science & Technology B: Microelectronics and Nanometer Structures, 2001. **19**: p. 557. http://dx.doi.org/10.1116/1.1359172

[43] Wilson, C.G. and Y.B. Gianchandani, *Spectral Detection of Metal Contaminants in Water Using an on-Chip Microglow Discharge.* Electron Devices, IEEE Transactions on, 2002. **49**(12): p. 2317-2322. http://dx.doi.org/10.1109/TED.2002.805608

[44] Weinberg, M., Personal Communication, May 5, 2006

[45] Epstein, A.H., S.D. Senturia, G. Anathasuresh, A. Ayon, K. Breuer, K.S. Chen, F. Ehrich, G. Gauba, R. Ghodssi, C. Groshenry, S. Jacobson, J.H. Lang, C.-C. Mehra, J. Mur Miranda, S. Nagle, D. Orr, E. Piekos, M.A. Schmidt, G. Shirley, S. Spearing, C. Tan, Y.-S. Tzeng, and I. Waitz, *Power MEMS and Microengines*, in *International Conference on Solid State Sensors and Actuators, 1997. (TRANSDUCERS'97)* 1997, IEEE: Chicago. http://dx.doi.org/10.1109/SENSOR.1997.635209

[46] Tsai, C.L. and A.K. Henning, *Surface Micromachined Turbines.* Solid State Sensors and Actuators, 1997. TRANSDUCERS'97 Chicago., 1997 International Conference on, 1997. **2**. http://dx.doi.org/10.1109/SENSOR.1997.635229

[47] Iijima, S., *Helical Microtubules of Graphitic Carbon.* Nature, 1991. **354**(6348): p. 56-58. http://dx.doi.org/10.1038/354056a0

[48] Dresselhaus, M. and M. Endo, *Relation of Carbon Nanotubes to Other Carbon Materials*, in *Carbon Nanotubes: Synthesis, Structure, Properties, and Applications*, M.S. Dresselhaus, G. Dresselhaus, and P. Avouris, Editors. 2001, Springer-Verlag: New York. p. 11-28. http://dx.doi.org/10.1007/3-540-39947-X_2

[49] Charlier, J.C., *Defects in Carbon Nanotubes.* Accounts of Chemical Research, 2002. **35**(12): p. 1063-1069. http://dx.doi.org/10.1021/ar010166k

[50] Iijima, S., T. Ichihashi, and Y. Ando, *Pentagons, Heptagon and Negative Curvature in Graphite Microtube Grouth.* Nature, 1992. **356**: p. 776. http://dx.doi.org/10.1038/356776a0

[51] Charlier, J.C., T.W. Ebbesen, and P. Lambin, *Structural and Electronic Properties of Pentagon-Heptagon Pair Defects in Carbon Nanotubes.* Physical Review B, 1996. **53**(16): p. 11108. http://dx.doi.org/10.1103/PhysRevB.53.11108

[52] Stone, A.J. and D.J. Wales, *Theoretical Studies of Icosahedral C60 and Some Related Species.* Chemical Physics Letters, 1986. **128**(5-6): p. 501-503. http://dx.doi.org/10.1016/0009-2614(86)80661-3

[53] Berber, S. and D. Tománek, *Stability Differences and Conversion Mechanism between Nanotubes and Scrolls.* Physical Review B, 2004. **69**(23): p. 233404. http://dx.doi.org/10.1103/PhysRevB.69.233404

[54] Feng, S.Q., D.P. Yu, G. Hub, X.F. Zhang, and Z. Zhang, *The Hrem Observation of Cross-Sectional Structure of Carbon Nanotubes.* Journal of Physics and Chemistry of Solids, 1997. **58**(11): p. 1887-1892. http://dx.doi.org/10.1016/S0022-3697(97)00085-1

[55] Zhang, X.F., X.B. Zhang, G. Van Tendeloo, S. Amelinckx, M. Op de Beeck, and J. Van Landuyt, *Carbon Nano-Tubes; Their Formation Process and Observation by Electron Microscopy.* Journal of Crystal Growth, 1993. **130**(3-4): p. 368-382. http://dx.doi.org/10.1016/0022-0248(93)90522-X

[56] Zhou, O., R.M. Fleming, D.W. Murphy, C.H. Chen, R.C. Haddon, A.P. Ramirez, and S.H. Glarum, *Defects in Carbon Nanostructures.* Science, 1994. **263**(5154): p. 1744-1747. http://dx.doi.org/10.1126/science.263.5154.1744

[57] Lavin, J.G., S. Subramoney, R.S. Ruoff, S. Berber, and D. Tománek, *Scrolls and Nested Tubes in Multiwall Carbon Nanotubes.* Carbon, 2002. **40**(7): p. 1123-1130. http://dx.doi.org/10.1016/S0008-6223(02)00050-7

[58] Melechko, A.V., V.I. Merkulov, T.E. McKnight, M.A. Guillorn, K.L. Klein, D.H. Lowndes, and M.L. Simpson, *Vertically Aligned Carbon Nanofibers and Related Structures: Controlled Synthesis and Directed Assembly.* Journal of Applied Physics, 2005. **97**(4): p. 041301-041339. http://dx.doi.org/10.1063/1.1857591

[59] Forró, L. and C. Schönenberger, *Physical Properties of Multi-Wall Nanotubes*, in *Carbon Nanotubes: Synthesis, Structure, Properties, and Applications*, M.S. Dresselhaus, G. Dresselhaus, and P. Avouris, Editors. 2001, Springer-Verlag: New York. p. 329-391. http://dx.doi.org/10.1007/3-540-39947-X_13

[60] Salvetat, J.-P., J.-M. Bonard, N.H. Thomson, A.J. Kulik, L. Forro, W. Benoit, and L. Zuppiroli, *Mechanical Properties of Carbon Nanotubes.* Applied Physics A: Materials Science & Processing, 1999. **69**(3): p. 255-260. http://dx.doi.org/10.1007/s003390050999

[61] Yakobson, B. and P. Avouris, *Mechanical Properties of Carbon Nanotubes*, in *Carbon Nanotubes: Synthesis, Structure, Properties, and Applications*, M.S. Dresselhaus, G. Dresselhaus, and P. Avouris, Editors. 2001, Springer-Verlag: New York. p. 287-327. http://dx.doi.org/10.1007/3-540-39947-X_12

[62] Che, J., T. Cagin, and W.A. Goddard, III, *Thermal Conductivity of Carbon Nanotubes.* Nanotechnology, 2000. **11**(2): p. 65-69. http://dx.doi.org/10.1088/0957-4484/11/2/305

[63] Chico, L., V.H. Crespi, L.X. Benedict, S.G. Louie, and M.L. Cohen, *Pure Carbon Nanoscale Devices: Nanotube Heterojunctions.* Physical Review Letters, 1996. **76**(6): p. 971. http://dx.doi.org/10.1103/PhysRevLett.76.971

[64] Huhtala, M., A.V. Krasheninnikov, J. Aittoniemi, S.J. Stuart, K. Nordlund, and K. Kaski, *Improved Mechanical Load Transfer between Shells of Multiwalled Carbon Nanotubes.* Physical Review B, 2004. **70**(4): p. 045404. http://dx.doi.org/10.1103/PhysRevB.70.045404

[65] Telling, R.H., C.P. Ewels, A.A. El-Barbary, and M.I. Heggie, *Wigner Defects Bridge the Graphite Gap.* Nature Materials, 2003. **2**(5): p. 333-337. http://dx.doi.org/10.1038/nmat876

[66] El-Barbary, A.A., R.H. Telling, C.P. Ewels, M.I. Heggie, and P.R. Briddon, *Structure and Energetics of the Vacancy in Graphite.* Physical Review B, 2003. **68**(14): p. 144107. http://dx.doi.org/10.1103/PhysRevB.68.144107

[67] Krasheninnikov, A.V. and K. Nordlund, *Stability of Irradiation-Induced Point Defects on Walls of Carbon Nanotubes.* Journal of Vacuum Science & Technology B: Microelectronics and Nanometer Structures, 2002. **20**(2): p. 728-733. http://dx.doi.org/10.1116/1.1463728

[68] Merkulov, V.I., A.V. Melechko, M.A. Guillorn, D.H. Lowndes, and M.L. Simpson, *Alignment Mechanism of Carbon Nanofibers Produced by Plasma-Enhanced Chemical-Vapor Deposition.* Applied Physics Letters, 2001. **79**(18): p. 2970-2972. http://dx.doi.org/10.1063/1.1415411

[69] Ren, Z.F., Z.P. Huang, J.W. Xu, J.H. Wang, P. Bush, M.P. Siegal, and P.N. Provencio, *Synthesis of Large Arrays of Well-Aligned Carbon Nanotubes on Glass.* Science, 1998. **282**(5391): p. 1105-1107. http://dx.doi.org/10.1126/science.282.5391.1105

[70] Ren, Z.F., Z.P. Huang, D.Z. Wang, J.G. Wen, J.W. Xu, J.H. Wang, L.E. Calvet, J. Chen, J.F. Klemic, and M.A. Reed, *Growth of a Single Freestanding Multiwall Carbon Nanotube on Each Nanonickel Dot.* Applied Physics Letters, 1999. **75**(8): p. 1086-1088. http://dx.doi.org/10.1063/1.124605

[71] Tu, Y., Z.P. Huang, D.Z. Wang, J.G. Wen, and Z.F. Ren, *Growth of Aligned Carbon Nanotubes with Controlled Site Density.* Applied Physics Letters, 2002. **80**(21): p. 4018-4020. http://dx.doi.org/10.1063/1.1482790

[72] Behler, K., S. Osswald, H. Ye, S. Dimovski, and Y. Gogotsi, *Effect of Thermal Treatment on the Structure of Multi-Walled Carbon Nanotubes.* Journal of Nanoparticle Research, 2006. **8**(5): p. 615-625. http://dx.doi.org/10.1007/s11051-006-9113-6

[73] Chen, S., J.Y. Huang, Z. Wang, K. Kempa, G. Chen, and Z.F. Ren, *High-Bias-Induced Structure and the Corresponding Electronic Property Changes in Carbon Nanotubes.* Applied Physics Letters, 2005. **87**(26): p. 263107-263103. http://dx.doi.org/10.1063/1.2155116

[74] Huang, J.Y., S. Chen, Z.F. Ren, G. Chen, and M.S. Dresselhaus, *Real-Time Observation of Tubule Formation from Amorphous Carbon Nanowires under High-Bias Joule Heating.* Nano Letters, 2006. **6**(8): p. 1699-1705. http://dx.doi.org/10.1021/nl0609910

[75] Huang, J.Y., S. Chen, S.H. Jo, Z. Wang, D.X. Han, G. Chen, M.S. Dresselhaus, and Z.F. Ren, *Atomic-Scale Imaging of Wall-by-Wall Breakdown and Concurrent Transport Measurements in Multiwall Carbon Nanotubes.* Physical Review Letters, 2005. **94**(23): p. 236802-236804. http://dx.doi.org/10.1103/PhysRevLett.94.236802

[76] Jensen, K., W. Mickelson, W. Han, and A. Zettl, *Current-Controlled Nanotube Growth and Zone Refinement.* Applied Physics Letters, 2005. **86**(17): p. 173107-173103. http://dx.doi.org/10.1063/1.1920427

[77] Yazyev, O.V., I. Tavernelli, U. Rothlisberger, and L. Helm, *Early Stages of Radiation Damage in Graphite and Carbon Nanostructures: A First-Principles Molecular Dynamics Study.* Physical Review B (Condensed Matter and Materials Physics), 2007. **75**(11): p. 115418-115415. http://dx.doi.org/10.1103/PhysRevB.75.115418

[78] Yakobson, B.I., C.J. Brabec, and J. Bernholc, *Nanomechanics of Carbon Tubes: Instabilities Beyond Linear Response.* Physical Review Letters, 1996. **76**(14): p. 2511-2514. http://dx.doi.org/10.1103/PhysRevLett.76.2511

[79] Yakobson, B.I., M.P. Campbell, C.J. Brabec, and J. Bernholc, *High Strain Rate Fracture and C-Chain Unraveling in Carbon Nanotubes.* Computational Materials Science, 1997. **8**(4): p. 341-348. http://dx.doi.org/10.1016/S0927-0256(97)00047-5

[80] Soule, D.E. and C.W. Nezbeda, *Direct Basal-Plane Shear in Single-Crystal Graphite.* Journal of Applied Physics, 1968. **39**(11): p. 5122-5139. http://dx.doi.org/10.1063/1.1655933

[81] Charlier, J.-C. and J.-P. Michenaud, *Energetics of Multilayered Carbon Tubules.* Physical Review Letters, 1993. **70**(12): p. 1858-1861. http://dx.doi.org/10.1103/PhysRevLett.70.1858

[82] Falvo, M.R. and R. Superfine, *Mechanics and Friction at the Nanometer Scale.* Journal of Nanoparticle Research, 2000. **2**(3): p. 237-248. http://dx.doi.org/10.1023/A:1010017130136

[83] Greenwood, J.A. and J.B.P. Williamson, *Contact of Nominally Flat Surfaces.* Proceedings of the Royal Society of London. Series A, Mathematical and Physical Sciences (1934-1990), 1966. **295**(1442): p. 300-319. http://www.jstor.org/pss/2415421

[84] Falvo, M.R., R.M. Taylor, A. Helser, V. Chi, F.P. Brooks, Jr., S. Washburn, and R. Superfine, *Nanometre-Scale Rolling and Sliding of Carbon Nanotubes.* Nature, 1999. **397**(6716): p. 236-238. http://dx.doi.org/10.1038/16662

[85] Liu, J., A.G. Rinzler, H. Dai, J.H. Hafner, R.K. Bradley, P.J. Boul, A. Lu, T. Iverson, K. Shelimov, C.B. Huffman, F. Rodriguez-Macias, Y.-S. Shon, T.R. Lee, D.T. Colbert, and R.E. Smalley, *Fullerene Pipes.* Science, 1998. **280**(5367): p. 1253-1256. http://dx.doi.org/10.1126/science.280.5367.1253

[86] Akita, S. and Y. Nakayama, *Interlayer Sliding Force of Individual Multiwall Carbon Nanotubes.* Japanese Journal of Applied Physics, 2003. **42**: p. 4830-4833. http://dx.doi.org/10.1143/JJAP.42.4830

[87] Rivera, J.L., C. McCabe, and P.T. Cummings, *The Oscillatory Damped Behaviour of Incommensurate Double-Walled Carbon Nanotubes.* Nanotechnology, 2005. **16**(2): p. 186-198. http://dx.doi.org/10.1088/0957-4484/16/2/003

[88] Yu, M.F., M.J. Dyer, G.D. Skidmore, H.W. Rohrs, X.K. Lu, K.D. Ausman, J.R. Von Ehr, and R.S. Ruoff, *Three-Dimensional Manipulation of Carbon Nanotubes under a Scanning Electron Microscope.* Nanotechnology, 1999. **10**(3): p. 244-252. http://dx.doi.org/10.1088/0957-4484/10/3/304

[89] Yu, M.-F., O. Lourie, M.J. Dyer, K. Moloni, T.F. Kelly, and R.S. Ruoff, *Strength and Breaking Mechanism of Multiwalled Carbon Nanotubes under Tensile Load.* Science, 2000. **287**(5453): p. 637-640. http://dx.doi.org/10.1126/science.287.5453.637

[90] Collins, P.G., M.S. Arnold, and P. Avouris, *Engineering Carbon Nanotubes and Nanotube Circuits Using Electrical Breakdown.* Science, 2001. **292**: p. 706-709. http://dx.doi.org/10.1126/science.1058782

[91] Cumings, J.P., A.K. Zettl, S.G. Louie, and M.L. Cohen. *Telescoped Multiwall Nanotube and Manufacture Thereof.* United States Patent No. 6,874,668, Apr. 5, 2005 http://v3.espacenet.com/textdoc?DB=EPODOC&IDX=EP0664438&F=0

[92] Zettl, A. and J. Cumings. *Sharpened Nanotubes, Nanobearings, and Nanosprings*. in *Electronic Properties of Novel Materials-Molecular Nanostructures: XIV International Winterschool/Euroconference.* 2000: AIP Conference Proceedings. http://dx.doi.org/10.1063/1.1342568

[93] Cumings, J., P.G. Collins, and A. Zettl, *Peeling and Sharpening Multiwall Nanotubes.* Nature, 2000. **406**(6796): p. 586. http://dx.doi.org/10.1038/35020698

[94] Zettl, A.K., A.M. Fennimore, and T.D. Yuzvinsky. *Rotational Actuator or Motor Based on Carbon Nanotubes.* United States Patent No. 7,053,520, May 30, 2006 http://v3.espacenet.com/textdoc?DB=EPODOC&IDX=US2005017598&F=0

[95] Allinger, M.L., F. Li, and L. Yan, *Molecular Mechanics. The Mm3 Force Field for Alkenes.* Journal of Computational Chemistry, 1990. **11**(7): p. 848-867. http://dx.doi.org/10.1002/jcc.540110708

[96] Guo, Y., N. Karasawa, and W. Goddard, *Prediction of Fullerene Packing in C 60 and C 70 Crystals.* Nature, 1991. **351**(6326): p. 464-467. http://dx.doi.org/10.1038/351464a0

[97] Kolmogorov, A.N. and V.H. Crespi, *Smoothest Bearings: Interlayer Sliding in Multiwalled Carbon Nanotubes.* Physical Review Letters, 2000. **85**(22): p. 4727-4730. http://dx.doi.org/10.1103/PhysRevLett.85.4727

[98] Lennard-Jones, J.E., *Cohesion.* Proceedings of the Physical Society, 1931. **43**: p. 461-482. http://dx.doi.org/10.1088/0959-5309/43/5/301

[99] Wong, E.W., P.E. Sheehan, and C.M. Lieber, *Nanobeam Mechanics: Elasticity, Strength, and Toughness of Nanorods and Nanotubes.* Science, 1997. **277**(5334): p. 1971. http://dx.doi.org/10.1126/science.277.5334.1971

[100] Waters, J.F., P.R. Guduru, M. Jouzi, J.M. Xu, T. Hanlon, and S. Suresh, *Shell Buckling of Individual Multiwalled Carbon Nanotubes Using Nanoindentation.* Applied Physics Letters, 2005. **87**(10): p. 103109-103103. http://dx.doi.org/10.1063/1.2012530

[101] Childs, D.W., *Turbomachinery Rotordynamics: Phenomena, Modeling, and Analysis*. 1993, New York: Wiley-Interscience. http://lccn.loc.gov/92035452

[102] Charlier, J.-C. and S. Iijima, *Growth Mechanisms of Carbon Nanotubes*, in *Carbon Nanotubes: Synthesis, Structure, Properties, and Applications*, M.S. Dresselhaus, G. Dresselhaus, and P. Avouris, Editors. 2001, Springer-Verlag: New York. p. 55-81. http://dx.doi.org/10.1007/3-540-39947-X_4

[103] Huang, Z.P., J.W. Xu, Z.F. Ren, J.H. Wang, M.P. Siegal, and P.N. Provencio, *Growth of Highly Oriented Carbon Nanotubes by Plasma-Enhanced Hot Filament Chemical Vapor Deposition.* Applied Physics Letters, 1998. **73**: p. 3845. http://dx.doi.org/10.1063/1.122912

[104] Wen, J.G., Z.P. Huang, D.Z. Wang, J.H. Chen, S.X. Yang, Z.F. Ren, J.H. Wang, L.E. Calvet, J. Chen, and J.F. Klemic, *Growth and Characterization of Aligned Carbon Nanotubes from Patterned Nickel Nanodots and Uniform Thin Films.* Journal of Materials Research, 2001. **16**(11): p. 3246-3253. http://dx.doi.org/10.1557/JMR.2001.0447

[105] Li, W.Z., J.G. Wen, and Z.F. Ren, *Effect of Temperature on Growth and Structure of Carbon Nanotubes by Chemical Vapor Deposition.* Applied Physics A: Materials Science & Processing, 2002. **74**(3): p. 397-402. http://dx.doi.org/10.1007/s003390201284

[106] Huang, Z.P., D.L. Carnahan, J. Rybczynski, M. Giersig, M. Sennett, D.Z. Wang, J.G. Wen, K. Kempa, and Z.F. Ren, *Growth of Large Periodic Arrays of Carbon Nanotubes.* Applied Physics Letters, 2003. **82**(3): p. 460-462. http://dx.doi.org/DOI:10.1063/1.1539299

[107] Wang, Y., J. Rybczynski, D.Z. Wang, K. Kempa, Z.F. Ren, W.Z. Li, and B. Kimball, *Periodicity and Alignment of Large-Scale Carbon Nanotubes Arrays.* Applied Physics Letters, 2004. **85**(20): p. 4741-4743. http://dx.doi.org/10.1063/1.1819992

[108] Bernstein, J., S. Cho, A.T. King, A. Kourepenis, P. Maciel, and M. Weinberg. *A Micromachined Comb-Drive Tuning Fork Rate Gyroscope*. in *Micro Electro Mechanical Systems, 1993 (MEMS '93): An Investigation of Micro Structures, Sensors, Actuators, Machines and Systems.* . 1993: Proceedings of the IEEE. http://dx.doi.org/10.1109/MEMSYS.1993.296932

[109] Bernstein, J.J. and M.S. Weinberg. *Comb Drive Micromechanical Tuning Fork Gyro.* European Patent No. 0,664,438, 1995 http://v3.espacenet.com/textdoc?DB=EPODOC&IDX=EP0664438&F=0

[110] Tang, W.C., T.C.H. Nguyen, M.W. Judy, and R.T. Howe, *Electrostatic-Comb Drive of Lateral Polysilicon Resonators.* SENSORS ACTUATORS., 1990. **21**(1): p. 328-331. http://dx.doi.org/10.1016/0924-4247(90)85065-C

[111] Dooyoung, H., S.T.Y. Huang, T. Jui-Che, H. Toshiyoshi, and M.C. Wu, *Low-Voltage, Large-Scan Angle MEMS Analog Micromirror Arrays with Hidden Vertical Comb-Drive Actuators.* Journal of Microelectromechanical Systems, 2004. **13**(2): p. 279-289. http://dx.doi.org/10.1109/JMEMS.2004.825314

[112] Van Kessel, P.F., L.J. Hornbeck, R.E. Meier, and M.R. Douglass, *A MEMS-Based Projection Display.* Proceedings of the IEEE, 1998. **86**(8): p. 1687-1704. http://dx.doi.org/10.1109/5.704274

[113] Geen, J.A. and D.W. Carow. *Micromachined Gyros.* United States Patent No. 6,122,961, Sept. 26, 2000 http://v3.espacenet.com/textdoc?DB=EPODOC&IDX=US6122961&F=0

[114] Mehregany, M., S.F. Bart, L.S. Tavrow, J.H. Lang, S.D. Senturia, and M.F. Schlecht, *A Study of Three Microfabricated Variable-Capacitance Motors.* Sensors & Actuators: A. Physical, 1990. **21**(1): p. 173-179. http://dx.doi.org/10.1016/0924-4247(90)85033-Z

[115] Tavrow, L.S., S.F. Bart, and J.H. Lang, *Operational Characteristics of Microfabricated Electric Motors.* Solid-State Sensors and Actuators, 1991. Digest of Technical Papers, TRANSDUCERS'91., 1991 International Conference on, 1991: p. 877-881. http://dx.doi.org/10.1109/SENSOR.1991.149026

[116] Bart, S.F., M. Mehregany, L.S. Tavrow, J.H. Lang, and S.D. Senturia, *Electric Micromotor Dynamics.* Electron Devices, IEEE Transactions on, 1992. **39**(3): p. 566-575. http://dx.doi.org/10.1109/16.123479

[117] Das, S., D.P. Arnold, I. Zana, J.W. Park, J.H. Lang, and M.G. Allen. *Multi-Watt Electric Power from a Microfabricated Permanent-Magnet Generator*. in *18th IEEE International Conference on Micro Electro Mechanical Systems, 2005. (MEMS 2005)* 2005: Proceedings of the IEEE. http://dx.doi.org/10.1109/MEMSYS.2005.1453923

[118] Woias, P., *Micropumps: Summarizing the First Two Decades.* Proceedings of SPIE, 2001. **4560**: p. 39. http://dx.doi.org/10.1117/12.443069

[119] Xu, Y., W.o. Choong, F. Eng Hock Tay, X.S. Zhang, Y.P. Kong, and T. Haiqing Gong, *Simulations of a Micro Valve and a Micro Pump*, in *Microfluidics and BioMEMS*, C.H. Mastrangelo and H. Becker, Editors. 2001, Proceedings of SPIE. http://dx.doi.org/10.1117/12.443070

[120] Wiberg, D.V., N.V. Myung, B. Eyre, K. Shcheglov, O.J. Orient, E. Moore, and P. Munz, *Liga-Fabricated Two-Dimensional Quadrupole Array and Scroll Pump for Miniature Gas Chromatograph/Mass Spectrometer.* Proceedings of SPIE, 2003. **4878**: p. 8. http://dx.doi.org/10.1117/12.520540

[121] Young, R.M., *Analysis of a Micromachine Based Vacuum Pump on a Chip Actuated by the Thermal Transpiration Effect.* Journal of Vacuum Science & Technology B: Microelectronics and Nanometer Structures, 1999. **17**: p. 280. http://dx.doi.org/10.1116/1.590551

[122] McNamara, S. and Y.B. Gianchandani, *On-Chip Vacuum Generated by a Micromachined Knudsen Pump.* Microelectromechanical Systems, Journal of, 2005. **14**(4): p. 741-746. http://dx.doi.org/10.1109/JMEMS.2005.850718

[123] Sen, M. and D. Wajerski, *Novel Pump for MEMS Applications.* Journal of Fluids Engineering, Transactions of the ASME, 1996. **118**(3): p. 624-627. http://dx.doi.org/10.1115/1.2817807

[124] Kilani, M.I., P.C. Galambos, Y.S. Haik, and C.J. Chen, *Design and Analysis of a Surface Micromachined Spiral-Channel Viscous Pump.* Journal of Fluids Engineering, 2003. **125**: p. 339. http://dx.doi.org/10.1115/1.1524582

[125] Wong, C.C., D. Chu, S.L. Liu, M.R. Tuck, Z. Mahmud, and V.A. Amatucci, *Rapid Prototyping of a Micro Pump with Laser Micromachining.* Proceedings of SPIE, 1995. **2642**: p. 156. http://dx.doi.org/10.1117/12.221164